

**APPLIED
COMPUTATIONAL
ELECTROMAGNETICS
SOCIETY
JOURNAL**

December 2019
Vol. 34 No. 12
ISSN 1054-4887

The ACES Journal is abstracted in INSPEC, in Engineering Index, DTIC, Science Citation Index Expanded, the Research Alert, and to Current Contents/Engineering, Computing & Technology.

The illustrations on the front cover have been obtained from the research groups at the Department of Electrical Engineering, The University of Mississippi.

THE APPLIED COMPUTATIONAL ELECTROMAGNETICS SOCIETY

<http://aces-society.org>

EDITORS-IN-CHIEF

Atef Elsherbeni

Colorado School of Mines, EE Dept.
Golden, CO 80401, USA

Sami Barmada

University of Pisa, ESE Dept.
56122 Pisa, Italy

ASSOCIATE EDITORS: REGULAR PAPERS

Mohammed Hadi

Kuwait University, EE Dept.
Safat, Kuwait

Alistair Duffy

De Montfort University
Leicester, UK

Wenxing Li

Harbin Engineering University
Harbin 150001, China

Maokun Li

Tsinghua University
Beijing 100084, China

Mauro Parise

University Campus Bio-Medico of Rome
00128 Rome, Italy

Yingsong Li

Harbin Engineering University
Harbin 150001, China

Riyadh Mansoor

Al-Muthanna University
Samawa, Al-Muthanna, Iraq

Antonio Musolino

University of Pisa
56126 Pisa, Italy

Abdul A. Arkadan

Colorado School of Mines, EE Dept.
Golden, CO 80401, USA

Salvatore Campione

Sandia National Laboratories
Albuquerque, NM 87185, USA

Wei-Chung Weng

National Chi Nan University, EE Dept.
Puli, Nantou 54561, Taiwan

Alessandro Formisano

Seconda Università di Napoli
81031 CE, Italy

Piotr Gas

AGH University of Science and Technology
30-059 Krakow, Poland

Long Li

Xidian University
Shaanxa, 710071, China

Marco Arjona López

La Laguna Institute of Technology
Torreon, Coahuila 27266, Mexico

Paolo Mezzanotte

University of Perugia
I-06125 Perugia, Italy

Luca Di Rienzo

Politecnico di Milano
20133 Milano, Italy

Lei Zhao

Jiangsu Normal University
Jiangsu 221116, China

Sima Noghianian

University of North Dakota
Grand Forks, ND 58202, USA

Qiang Ren

Beihang University
Beijing 100191, China

Nunzia Fontana

University of Pisa
56122 Pisa, Italy

Atif Shamim

King Abdullah University of Science and Technology (KAUST)
Thuwal 23955, Saudi Arabia

Stefano Selleri

DINFO – University of Florence
50139 Florence, Italy

ASSOCIATE EDITORS: EXPRESS PAPERS

Lijun Jiang

University of Hong Kong, EEE Dept.
Hong, Kong

Shinichiro Ohnuki

Nihon University
Tokyo, Japan

Kubilay Sertel

The Ohio State University
Columbus, OH 43210, USA

Steve J. Weiss

US Army Research Laboratory
Adelphi Laboratory Center (RDRL-SER-M)
Adelphi, MD 20783, USA

Jiming Song

Iowa State University, ECE Dept.
Ames, IA 50011, USA

Amedeo Capozzoli

Univerita di Napoli Federico II, DIETI
I-80125 Napoli, Italy

Yu Mao Wu

Fudan University
Shanghai 200433, China

Maokun Li

Tsinghua University, EE Dept.
Beijing 100084, China

EDITORIAL ASSISTANTS

Matthew J. Inman

University of Mississippi, EE Dept.
University, MS 38677, USA

Shanell Lopez

Colorado School of Mines, EE Dept.
Golden, CO 80401, USA

Madison Le

Colorado School of Mines, EE Dept.
Golden, CO 80401, USA

Allison Tanner

Colorado School of Mines, EE Dept.
Golden, CO 80401, USA

EMERITUS EDITORS-IN-CHIEF

Duncan C. Baker

EE Dept. U. of Pretoria
0002 Pretoria, South Africa

Allen Glisson

University of Mississippi, EE Dept.
University, MS 38677, USA

Ahmed Kishk

Concordia University, ECS Dept.
Montreal, QC H3G 1M8, Canada

Robert M. Bevensee

Box 812
Alamo, CA 94507-0516, USA

Ozlem Kilic

Catholic University of America
Washington, DC 20064, USA

David E. Stein

USAF Scientific Advisory Board
Washington, DC 20330, USA

EMERITUS ASSOCIATE EDITORS

Yasushi Kanai

Niigata Inst. of Technology
Kashiwazaki, Japan

Alexander Yakovlev

University of Mississippi, EE Dept.
University, MS 38677, USA

Levent Gurel

Bilkent University
Ankara, Turkey

Mohamed Abouzahra

MIT Lincoln Laboratory
Lexington, MA, USA

Ozlem Kilic

Catholic University of America
Washington, DC 20064, USA

Erdem Topsakal

Mississippi State University, EE Dept.
Mississippi State, MS 39762, USA

Sami Barmada

University of Pisa, ESE Dept.
56122 Pisa, Italy

Fan Yang

Tsinghua University, EE Dept.
Beijing 100084, China

Rocco Rizzo

University of Pisa
56123 Pisa, Italy

William O'Keefe Coburn

US Army Research Laboratory
Adelphi, MD 20783, USA

EMERITUS EDITORIAL ASSISTANTS

Khaled ElMaghoub

Trimble Navigation/MIT
Boston, MA 02125, USA

Christina Bonnington

University of Mississippi, EE Dept.
University, MS 38677, USA

Anne Graham

University of Mississippi, EE Dept.
University, MS 38677, USA

Kyle Patel

Colorado School of Mines, EE Dept.
Golden, CO 80401, USA

Mohamed Al Sharkawy

Arab Academy for Science and Technology, ECE Dept.
Alexandria, Egypt

DECEMBER 2019 REVIEWERS: REGULAR PAPERS

Ramin Aghajafari	Andrew Peterson
Kiran Ajetroa	Jagdishkumar Rathod
Khair Al Shamaileh	C.J. Reddy
Stamatios Amanatiadis	Vince Rodriguez
Hristos Anastassiu	Daniele Romano
Ahmed Attiya	Imaculate Rosaline
Huaguang Bao	Kamalesh Sainath
Ankan Bhattacharya	Sayeed Sajal
lahcene Boukelkoul	Birsen Saka
Fangyuan Chen	Rashid Saleem
Bernhard Hoenders	Mahdi Salimitorkamani
Tianqi Jiao	Yan Shi
Fatih Kaburcuk	Ashish Singh
Kenichi Kagoshima	Matt Stephanson
Yasushi Kanai	Chalasani Subba Rao
Joshua Kast	Arul Subramanian
Rafal Lech	Sellakkutti Suganthi
Wen-Jiao Liao	Rensheng Sun
Neetu Marwah	Christopher Trueman
Ramesh Munirathinam	Wei-Chung Weng
Mohankumar N.	Qi Wu
Yuvaraj N.	Alex Yuffa
Santhosh Babu Pallipalayam	Xiaoyan Zhang
Xiao-Min Pan	Yujuan Zhao
Panagiotis Papakanellos	

TABLE OF CONTENTS – REGULAR PAPERS

A Fast Gridless Sparse Method for Robust DOA Estimation in the Presence of Gain-phase Errors
Wencan Peng, Chenjiang Guo, Min Wang, Yuteng Gao, and Xia Zhao 1788

A p -norm-like Constraint LMS Algorithm for Sparse Adaptive Beamforming
Wanlu Shi and Yingsong Li 1797

Efficient Wideband MRCS Simulation for Radar HRRP Target Recognition Based on
MSIB and PCA
Yunqin Hu and Ting Wan 1804

Novel Reduced Matrix Equation Constructing Method Accelerates Iterative Solution
of Characteristic Basis Function Method
Zhonggen Wang, Qiang Chen, WenYan Nie, and Han Lin 1814

ASM-FDTD Combine the Prony’s Method to Simulate the EMP Propagation in Tunnel
Yun-Fei Mao, Hong-Bing Wu, Jia-Hong Chen, and Xu-Wei Su..... 1821

High Isolated X-Band MIMO Array Using Novel Wheel-Like Metamaterial
Decoupling Structure
Jianfeng Jiang, Yinfeng Xia, and Yingsong Li 1829

A Low-Profile Circularly Polarized Magnetic-Electric Dipole Antenna Array
Pingyuan Zhou, Mang He, Wen Tian, and Chuanfang Zhang 1837

Broadband Conformal End-fire Monopole Log-periodic Antenna Array
Chao Chen, Jiandan Zhong, and Yi Tan 1845

A Low Mutual Coupling Two-Element MIMO Antenna with a Metamaterial Matrix Loading
Ping Xu, Shengyuan Luo, Yinfeng Xia, Tao Jiang, and Yingsong Li 1851

Four-Element Planar MIMO Antenna for Indoor Communications with High Isolation
Mohamed M. Morsy 1857

Optimization of a Dual-Band, Printed Octafilar Antenna
Joseph D. Majkowski 1862

Study of Bandwidth and Resonant Frequency of a Rectangular Superconducting Thin Film Patch Antenna at Temperatures near T_c Abdelkrim Belhedri, Abderraouf Messai, Tayeb A. Denidni, and Boualem Mekimah	1871
Autoencoder Based Optimization for Electromagnetics Problems Sami Barmada, Nunzia Fontana, Dimitri Thomopoulos, and Mauro Tucci	1875
Characterization of Atmospheric Absorption in the 60 GHz Frequency Band Using a Multi-Pole Material Model Müberra Arvas, Ercumend Arvas, and Mohammad A. Alsunaidi	1881
A Tunable Trisection Bandpass Filter with Constant Fractional Bandwidth Based on Magnetic Coupling Mingye Fu, Qianyin Xiang, and Quanyuan Feng	1888
An Improved E-Plane Waveguide Power Divider Design for 94GHz Dual-Pyramidal Horn Antenna Xiaoyan Zhang, Yuting Chen, Yan Xie, and Lingfeng Liu	1897
Electric Field and SAR Distribution in the Vicinity of Orthodontic Brace Exposed to the Cell Phone Radiation Dejan B. Jovanovic, Dragan Dj. Krasic, Vladimir B. Stankovic, Nenad N. Cvetkovic, and Dragan D. Vuckovic	1904
Miniaturized Frequency Selective Radome Operating in the X-Band with Wideband Absorption Hamza Ahmad, MuhibUr Rahman, Shahid Bashir, Wajid Zaman, and Fauziahanim Che Seman	1915
Eddy Currents Induced in Two Parallel Round Conductors Tomasz Szczegieliński, Paweł Jabłoński, Dariusz Kusiak, and Zygmunt Piątek	1922
Efficient Computational Model of Phase Noise and its Applicability to Assess the Performance of Digital Modulation Techniques Asmaa E. Farahat and Khlaid F. A. Hussein.....	1931

A Fast Gridless Sparse Method for Robust DOA Estimation in the Presence of Gain-phase Errors

Wencan Peng¹, Chenjiang Guo¹, Min Wang², Yuteng Gao¹, and Xia Zhao¹

¹ School of Electronics and Information, Northwestern Polytechnical University, Xi'an, 710129, China
wcanpeng@163.com, ciguo@nwpu.edu.cn, ytgao2002@163.com, zhaoxia908@126.com

² National Lab of Radar Signal Processing, Xidian University, Xi'an, 710071, China
wangmin@xidian.edu.cn

Abstract – A new gridless sparse method (GLSM) is proposed to estimate the direction of arrival (DOA) and gain-phase errors simultaneously for a uniform linear array (ULA). We convert angular space to frequency space and establish a data model in the frequency domain. First, the cost function based on the covariance fitting criterion is transformed into a semidefinite programming (SDP) problem to estimate DOA and noise variance without previous calibration information. Second, gain errors are calculated by the estimated noise variance and the covariance matrix. Third, phase errors are obtained by decomposition of the covariance matrix, which has been pre-processed by a space smoothing technique. Finally, DOA estimation is improved further after the array errors are fully calibrated. Compared with traditional methods, the proposed method is robust to correlations of signal sources, and parameters are estimated without joint iteration. Moreover, there is no need for discrete grid points in the angular space, which results in grid mismatches and computation loads, so the proposed method is more accurate and faster. Simulation results verify the effectiveness of the proposed method.

Index Terms – Direction of arrival, gain and phase errors, gridless sparse method, semidefinite programming.

I. INTRODUCTION

The direction of arrival (DOA) estimation is one of the most important topics in array signal processing. Many high resolution DOA algorithms have been proposed, such as multiple signal classification (MUSIC) [1], estimation of signal parameters via rotational invariance techniques (ESPRIT) [2], maximum likelihood [3] and Capon [4]. Recently, DOA estimation performance has been further improved by sparse reconstruction algorithms. To study the sparsity of DOAs, a spatial domain is usually discretized to create a dictionary to sparsely represent the DOAs [5-7]. The

l_1 -based singular value decomposition (L1_SVD) algorithm [5], based on an overcomplete basis, handles the DOA estimation problem through SVD and a second-order cone (SOC) framework. The method in [6] based on the covariance fitting criteria estimates the source power and the corresponding DOAs by an iteration process. However, those on-grid methods assume that the true DOAs are located on a fixed set of grid points, so grid mismatch is inevitable. The off-grid methods [8-10] and gridless methods [11-12] are used to solve the grid mismatch problem. Additionally, the latter completely overcome this problem by operating in the continuous domain. A novel off-grid method [10] is proposed via successive nonconvex sparsity approximation penalties on the sparse signals and jointly estimates the sparse signals and grid offset parameters. The method proposed in [11] is a grid-free sparse method. DOAs and noise variance are solved by semidefinite programming (SDP) and convex optimization. However, all those subspace and sparse methods have the common assumption of ideal array manifolds. In practice, the array manifold is often affected by unknown array perturbations, such as gain and phase uncertainties, mutual coupling and sensor location errors [13-15]. Our paper focuses on the gain and phase errors of antenna arrays.

To deal with array gain-phase perturbations, array calibration algorithms are usually classified into two groups. The first group is called active calibration algorithms [16-18]. These methods require that all the DOAs are precisely known. With the use of calibration sources, the array can be calibrated well. However, it is hard to accurately determine the DOAs of the calibration sources in practice [19]. The second group is called self-calibration algorithms, which are more desirable. They can estimate both the array perturbations and DOA without knowing the exact locations of calibration sources. In [20], the method was proposed by Weiss and Friedlander and called the WF method for convenience. DOAs and gain-phase errors are estimated

by an alternative iteration method in the case of uncorrelated sources. However, convergence to the global optimum cannot be guaranteed when the phase error is large. In [21] and [22], non-iterative methods based on the WF method for phase errors are proposed. These methods have the benefit that the term of gain-phase errors is eliminated from the array manifold by the Hadamard product, and DOAs and gain-phase errors are solved independently. However, they have the disadvantages that the computation is complicated, the case of coherent signals is not considered, and they are not applicable to a uniform linear array (ULA). The method in [23] is a sparse-based method to achieve a joint estimation of DOA and array perturbations, which is based on a spatial dictionary, so it encounters the following problems: increased computational loads and errors caused by discretization. In [24], an on-grid method (ONGM) based on the covariance fitting criteria is proposed to estimate the DOA and gain-phase error simultaneously by alternate iteration. It performs well in cases of uncorrelated sources and coherent sources. However, the main drawbacks of ONGM are converging to suboptimal solutions in the case of large phase errors and high computational complexity.

Inspired by [24], we propose a gridless sparse method (GLSM) to deal with the DOA estimation problem of gain-phase errors. The covariance fitting criteria have sound statistical motivation and are robust to coherent signal sources [6, 25]. Moreover, according to [26], covariance fitting is related to the l_1 _norm minimization, which is robust to correlation. We consider the same covariance fitting criteria as the ONGM method, but the covariance fitting problem is transformed into an SDP problem and solved by SDPT3 or other SDP solvers [27-28] for estimating DOA and noise variance in the frequency domain. Then, the gain perturbations are estimated by using the covariance matrix and the estimated noise covariance, and phase errors are estimated by a common method with estimated DOAs. Finally, we use SDP solvers again to further improve DOA estimation after the gain-phase errors are compensated. Compared with the ONGM method [24], the proposed method overcomes some drawbacks. First, no discretization scheme is adopted, which avoids grid mismatch. Second, parameters are estimated with no iteration, so it does not fall into local optimality in the case of large phase errors and has better estimation performance. Third, the proposed method does not depend on the grid size and the number of iterations; thus, it can be faster than the ONGM method when a dense sampling grid is used in ONGM for high estimation precision. Simulation results show the effectiveness of the proposed method.

II. DATA MODEL

Consider that K narrowband far-field signals impinge on M isotropic sensors from different incident angles $\boldsymbol{\theta} = [\theta_1, \dots, \theta_K]^T$. The array spacing is half-wavelength and N is the number of snapshots. We convert the angular domain to the frequency domain to avoid discretizing the spatial angles.

We denote $f_k = (\sin(\theta_k) + 1) / 2 \in [0, 1)$, $k = 1, \dots, K$, and the relation $\boldsymbol{\theta} \leftrightarrow \mathbf{f}$ is one-to-one. We assume that $K \leq M - 1$ in the following discussion. The steering matrix can thus be represented as $\mathbf{A}(\mathbf{f}) = [\mathbf{a}(f_1), \dots, \mathbf{a}(f_K)]$, with $\mathbf{a}(f_k) = [1, e^{j2\pi f_k}, \dots, e^{j2(M-1)\pi f_k}]^T$. f_k is the frequency of the uniformly sampled complex sinusoid $\mathbf{a}(f_k)$, so $\mathbf{f} = [f_1, \dots, f_K]^T$ is the frequency parameter. Considering the gain-phase errors, the received signals at the ULA along the x-axis can be expressed as:

$$\mathbf{Y} = \boldsymbol{\Gamma} \mathbf{A}(\mathbf{f}) \mathbf{S} + \mathbf{N}, \quad (1)$$

where $\boldsymbol{\Gamma} = \text{diag}([\gamma_1, \gamma_2, \dots, \gamma_M]^T)$ denotes the gain-phase error diagonal matrix. Define $\gamma_m \triangleq \alpha_m e^{j\phi_m}$, and α_m and ϕ_m denote the gain error and phase error, respectively, of the m th sensor. In addition, we assume that $\alpha_1 = 1$, $\phi_1 = 0$, the noise \mathbf{N} is additive white Gaussian noise and that the source signal \mathbf{S} is independent of the noise.

The covariance matrix \mathbf{R} can be written as:

$$\mathbf{R}(\mathbf{f}, \mathbf{p}, \boldsymbol{\sigma}, \boldsymbol{\Gamma}) = \boldsymbol{\Gamma} \mathbf{A}(\mathbf{f}) \text{diag}(\mathbf{p}) \mathbf{A}^H(\mathbf{f}) \boldsymbol{\Gamma}^H + \text{diag}(\boldsymbol{\sigma}), \quad (2)$$

where $\mathbf{p} = [p_1, \dots, p_K]^T$ is the source power and $\boldsymbol{\sigma} = [\sigma^2, \dots, \sigma^2]_{M \times 1}^T$ denotes the noise variance.

For simplicity, note,

$$\mathbf{C}(\mathbf{f}, \mathbf{p}) = \mathbf{A}(\mathbf{f}) \text{diag}(\mathbf{p}) \mathbf{A}^H(\mathbf{f}). \quad (3)$$

The (m, l) th element of \mathbf{C} is:

$$C_{m,l} = \sum_{k=1}^K p_k^2 a_m(f_k) a_l^*(f_k) = \sum_{k=1}^K p_k^2 e^{j2\pi(m-l)f_k}. \quad (4)$$

It is easy to see that $\mathbf{C} \geq 0$ and \mathbf{C} is a (Hermitian) Toeplitz matrix.

The sample covariance matrix can be expressed as:

$$\hat{\mathbf{R}} = \mathbf{Y} \mathbf{Y}^H / N. \quad (5)$$

III. THE PROPOSED METHOD

A. Robust DOA estimation

We consider the following cost function based on covariance fitting criterion [6, 25]:

$$g(\mathbf{f}, \mathbf{p}, \boldsymbol{\sigma}, \boldsymbol{\Gamma}) = \left\| \mathbf{R}^{-1/2} (\hat{\mathbf{R}} - \mathbf{R}) \hat{\mathbf{R}}^{-1/2} \right\|_F^2, \quad (6)$$

where $\|\cdot\|_F$ represents the Frobenius norm for matrices and the l_2 _norm for vectors. According to [11], the

minimization of the criterion in (6) is a large-snapshot realization of the ML estimator. A simple calculation is as follows:

$$\begin{aligned} g(\mathbf{f}, \mathbf{p}, \boldsymbol{\sigma}, \boldsymbol{\Gamma}) &= \text{tr}[\mathbf{R}^{-1/2}(\hat{\mathbf{R}} - \mathbf{R})\hat{\mathbf{R}}^{-1}(\hat{\mathbf{R}} - \mathbf{R})\mathbf{R}^{-1/2}] \\ &= \text{tr}[(\mathbf{R}^{-1}\hat{\mathbf{R}} - \mathbf{I})(\mathbf{I} - \hat{\mathbf{R}}^{-1}\mathbf{R})] \\ &= \text{tr}(\mathbf{R}^{-1}\hat{\mathbf{R}}) + \text{tr}(\hat{\mathbf{R}}^{-1}\mathbf{R}) - 2M, \end{aligned} \quad (7)$$

where $\text{tr}(\bullet)$ denotes the trace of matrices. In the presence of noise \mathbf{R}^{-1} exists while $\hat{\mathbf{R}}^{-1}$ exists under the condition $N \geq M$. \mathbf{I} denotes the identity matrix. The unknown parameters \mathbf{f} , \mathbf{p} , $\boldsymbol{\sigma}$ and $\boldsymbol{\Gamma}$ are nonlinear in relation to \mathbf{R} , so it is challenging to minimize g . To calculate those parameters in (7), it is necessary to reparameterize \mathbf{R} for reducing the number of parameters. According to (3), \mathbf{C} is a (Hermitian) Toeplitz matrix, so it can be expressed as $\mathbf{C} = T(\mathbf{u})$ depending on the first row \mathbf{u} . Substitute $\mathbf{C} = T(\mathbf{u})$ into (2) to obtain:

$$\mathbf{R}(\mathbf{u}, \boldsymbol{\sigma}, \boldsymbol{\Gamma}) = \boldsymbol{\Gamma}T(\mathbf{u})\boldsymbol{\Gamma}^H + \text{diag}(\boldsymbol{\sigma}). \quad (8)$$

According to [6], the cost function in (6) is convex and has a unique global minimum. Problem (7) can thus be formulated as the following SDP problem:

$$\begin{aligned} \min_{\mathbf{f}, \mathbf{u}, \{\boldsymbol{\sigma} \succeq \mathbf{0}\}} \quad & \text{tr}(\mathbf{R}^{-1}\hat{\mathbf{R}}) + \text{tr}(\hat{\mathbf{R}}^{-1}\mathbf{R}) \\ \text{subject to} \quad & T(\mathbf{u}) \succeq \mathbf{0}, \end{aligned} \quad (9)$$

where $\boldsymbol{\sigma} \succeq \mathbf{0}$ represents that $\sigma_m \geq 0$ for all m , then we show the following equivalence:

$$\begin{aligned} (9) \Leftrightarrow \min_{\mathbf{f}, \mathbf{u}, \{\boldsymbol{\sigma} \succeq \mathbf{0}\}} \quad & \text{tr}\left(\hat{\mathbf{R}}^{\frac{1}{2}}\mathbf{R}^{-1}\hat{\mathbf{R}}^{\frac{1}{2}}\right) + \text{tr}(\hat{\mathbf{R}}^{-1}\mathbf{R}) \\ \text{subject to} \quad & T(\mathbf{u}) \succeq \mathbf{0}. \end{aligned} \quad (10)$$

The parameters of \mathbf{R}^{-1} in (10) are in the denominator, which does not satisfy the condition of CVX, so we introduce parameter \mathbf{Z} , satisfying the constraint condition $\mathbf{Z} \geq \hat{\mathbf{R}}^{\frac{1}{2}}\mathbf{R}^{-1}\hat{\mathbf{R}}^{\frac{1}{2}}$,

$$\begin{aligned} \min_{\mathbf{Z}, \mathbf{f}, \mathbf{u}, \{\boldsymbol{\sigma} \succeq \mathbf{0}\}} \quad & \text{tr}(\mathbf{Z}) + \text{tr}(\hat{\mathbf{R}}^{-1}\mathbf{R}) \\ \text{subject to} \quad & T(\mathbf{u}) \succeq \mathbf{0} \text{ and } \mathbf{Z} \geq \hat{\mathbf{R}}^{\frac{1}{2}}\mathbf{R}^{-1}\hat{\mathbf{R}}^{\frac{1}{2}} \\ \Leftrightarrow \min_{\mathbf{Z}, \mathbf{f}, \mathbf{u}, \{\boldsymbol{\sigma} \succeq \mathbf{0}\}} \quad & \text{tr}(\mathbf{Z}) + \text{tr}(\hat{\mathbf{R}}^{-1}\mathbf{R}) \\ \text{subject to} \quad & \begin{bmatrix} \mathbf{Z} & \hat{\mathbf{R}}^{\frac{1}{2}} \\ \hat{\mathbf{R}}^{\frac{1}{2}} & \mathbf{R} \\ & & T(\mathbf{u}) \end{bmatrix} \succeq \mathbf{0}. \end{aligned} \quad (11)$$

Substitute $\mathbf{R} = \boldsymbol{\Gamma}T(\mathbf{u})\boldsymbol{\Gamma}^H + \text{diag}(\boldsymbol{\sigma})$ into (11),

$$\begin{aligned} \min_{\mathbf{Z}, \mathbf{f}, \mathbf{u}, \{\boldsymbol{\sigma} \succeq \mathbf{0}\}} \quad & \text{tr}(\mathbf{Z}) + \text{tr}(\boldsymbol{\Gamma}^H\hat{\mathbf{R}}^{-1}\boldsymbol{\Gamma}T(\mathbf{u})) + \text{Re}(\text{diag}(\hat{\mathbf{R}}^{-1})^H)\boldsymbol{\sigma} \\ \text{subject to} \quad & \begin{bmatrix} \mathbf{Z} & \hat{\mathbf{R}}^{\frac{1}{2}} \\ \hat{\mathbf{R}}^{\frac{1}{2}} & \boldsymbol{\Gamma}T(\mathbf{u})\boldsymbol{\Gamma}^H + \text{diag}(\boldsymbol{\sigma}) \\ & & T(\mathbf{u}) \end{bmatrix} \succeq \mathbf{0}. \end{aligned} \quad (12)$$

We assume that $(\hat{\mathbf{u}}, \hat{\boldsymbol{\sigma}})$ is the solution of the SDP problem (12) with initial/estimated $\hat{\mathbf{f}}$. The SDP is implemented using CVX with the SDPT3 solver [27-28]. Because $T(\hat{\mathbf{u}})$ is a positive semidefinite Toeplitz matrix, it can be decomposed to:

$$T(\hat{\mathbf{u}}) = \mathbf{V}\hat{\mathbf{P}}\mathbf{V}^H, \quad (13)$$

where \mathbf{V} denotes the eigenvector matrix and $\hat{\mathbf{P}}$ is a diagonal matrix and denotes the eigenvalues of $T(\hat{\mathbf{u}})$.

The frequency parameter $\hat{\mathbf{f}}$ can be determined by the largest K eigenvalues. Then, the DOA estimates $\hat{\boldsymbol{\theta}}$ corresponding to $\hat{\mathbf{f}}$ as:

$$\hat{\boldsymbol{\theta}} = \arcsin(2\hat{\mathbf{f}} - 1). \quad (14)$$

We know that $\text{rank}(\mathbf{C}) = K \leq M - 1$, and it is natural to determine that $\text{rank}(T(\hat{\mathbf{u}})) = K \leq M - 1$, which means that $T(\hat{\mathbf{u}})$ is rank-deficient. Therefore, the prior knowledge $K \leq M - 1$ makes the solutions $\hat{\boldsymbol{\theta}}$ and $\hat{\mathbf{P}}$ unique.

B. Gain error estimation

From (2), (3) and (4), it is clear that,

$$R_{m,l} = \begin{cases} \gamma_m \gamma_l^* C_{m,l}, & m \neq l \\ \gamma_m \gamma_m^* \sum_{k=1}^K p_k^2 + \sigma^2, & m = l \end{cases}, \quad (15)$$

when $m=l$, the main diagonal element $R(m, m)$ is that,

$$R(m, m) = \alpha_m^2 \sum_{k=1}^K p_k^2 + \sigma^2. \quad (16)$$

$\hat{\boldsymbol{\sigma}}$ is estimated by (12), and the gain errors can be estimated as:

$$\hat{\alpha}_m = \text{sqrt}\left(\frac{\hat{R}(m, m) - \hat{\boldsymbol{\sigma}}^2}{\hat{R}(1, 1) - \hat{\boldsymbol{\sigma}}^2}\right), \quad m = 1, \dots, M, \quad (17)$$

where $\hat{R}(1, 1)$ is the first element of the main diagonal of \mathbf{R} and is taken as a reference because $\alpha_1 = 1$.

C. Phase error estimation

In this section, we introduce a forward and backward space smoothing method to reduce the

correlation between signal sources [24]. \mathbf{J}_M is an M order exchange matrix where the reverse-diagonal elements are 1, and the rest of the elements are 0. We construct a new covariance matrix:

$$\tilde{\mathbf{R}} = \mathbf{R} + \mathbf{J}_M \mathbf{R}^* \mathbf{J}_M, \quad (18)$$

where \mathbf{R}^* is the complex conjugate matrix of \mathbf{R} . The noise subspace $\mathbf{U} = [\mathbf{U}_{K+1}, \mathbf{U}_{K+2}, \dots, \mathbf{U}_{K+M}]$ can be obtained by the characteristic decomposition of $\tilde{\mathbf{R}}$. It is worth noting that the space smoothing algorithm is a dimensionality reduction algorithm, which is essentially a process of restoring the rank of the covariance matrix. Therefore, in general, the dimension of the modified covariance matrix is smaller than that of the original covariance matrix, that is to say, the performance of estimating coherent signals is obtained by reducing the degree of freedom of the covariance matrix. However, in order to satisfy the dimension for estimating phase errors, we do not divide \mathbf{R} and \mathbf{R}^* into multiple sub-arrays to make $\tilde{\mathbf{R}}$ reach the optimal case of full rank. Thus, we may further improve the performance of the proposed method in the case of coherent signals in the future.

The phase errors can be estimated as [20]:

$$\hat{\phi} = \text{angle}(\mathbf{w}), \quad (19)$$

$$\mathbf{w} = \frac{(\mathbf{B})^{-1} \mathbf{h}}{\mathbf{h}^T (\mathbf{B})^{-1} \mathbf{h}} \quad \mathbf{h} = [1, 0, \dots, 0]^T, \quad (20)$$

$$\mathbf{B} = \sum_{k=1}^K [\text{diag}(\mathbf{a}(\hat{\mathbf{f}}_k))]^H \mathbf{U} \mathbf{U}^H \text{diag}(\mathbf{a}(\hat{\mathbf{f}}_k)), \quad (21)$$

where $\hat{\phi} \triangleq [\hat{\phi}_1, \dots, \hat{\phi}_M]^T$ and $\text{angle}(\cdot)$ denotes the phase of a complex number.

Consequently, the proposed method is summarized as follows:

Step 1: Set $\Gamma_0 = \mathbf{I}$ and $(\hat{\mathbf{u}}, \hat{\sigma})$ is estimated by (12).

Step 2: $\hat{\mathbf{f}}$ and $\hat{\boldsymbol{\theta}}$ are estimated by (13) and (14), i.e., GLSM1.

Step 3: Gain errors are estimated by (17).

Step 4: Phase errors are estimated by (19).

Step 5: Set $\hat{\mathbf{F}} = \text{diag}([\hat{\alpha}_1 e^{j\hat{\phi}_1}, \dots, \hat{\alpha}_M e^{j\hat{\phi}_M}]^T)$, and $\hat{\mathbf{f}}$ and $\hat{\boldsymbol{\theta}}$ are re-estimated by (12), (13) and (14), i.e., GLSM2.

IV. CONNECTION TO PRIOR ART

A. Relation with the ONGM method

The GLSM method proposed in this paper has some similarities with the ONGM in [24]. Both methods adopt the same covariance fitting criteria for DOA, a similar method for gain error estimation, and the same method for phase error estimation. However, the following three main differences make their performances very different. The first is that GLSM

is based on the continuous frequency domain, while ONGM depends on the grid of the angular space. Note that the covariance matrix \mathbf{R} is approximated in ONGM by discretizing the range of the angle, where it is no guarantee that the true DOAs are located on the grids. Thus, the modelling error, which is dependent on the grid density, is one possible reason for the inaccuracy of ONGM estimation. The second is that the DOA estimate of ONGM is obtained directly from the solution of the covariance fitting optimization problem [11], while GLSM obtains the frequency estimation by the Vandermonde decomposition of $T(\hat{\mathbf{u}})$. Therefore, the DOA estimation of ONGM is bound by the grid, which is referred to as an on-grid issue. The third is that parameters of ONGM are estimated via iterative processing, while parameters of GLSM are estimated with no iteration. Alternating iteration processing causes ONGM to easily fall into local optimality in the case of large phase errors.

B. Complexity analysis

In this section, we compare the computational complexity of the GLSM method with the ONGM method [24]. ONGM is an iterative algorithm whose computational complexity is equal to the complexity of each iteration times the number of iterations; therefore, the major computational complexity of the ONGM algorithm is $O\{(\tilde{K}^2 M^3 + 2\tilde{K} M^4 + M^5)T\}$, where \tilde{K} denotes the grid size and T denotes the number of iterations, which is difficult to quantify and varies in different scenarios. We define J_1 as the variable size and $J_2 \times J_2$ as the dimension of the positive semidefinite matrix in the semidefinite constraint of an SDP [11]. According to reference [29], we know that the SDP can be solved in $O(J_1^2 J_2^{2.5})$ flops. In the GLSM method, J_1 equals M^2 and J_2 equals M , so the complexity of the GLSM method is $O(M^{6.5})$. Obviously, the order on M for GLSM is higher than that for ONGM. However, the grid size \tilde{K} is much greater than the number of sensors, M . Additionally, the computational complexity from phase errors is much higher in the ONGM method, which needs to execute $O(\tilde{K} T M^3)$ flops. In contrast, we need to run once to obtain the phase errors in the GLSM method. Therefore, the GLSM method can be faster than the ONGM method.

V. NUMERICAL SIMULATIONS

The gain errors $\{\alpha_m\}_{m=1}^M$ and phase errors $\{\phi_m\}_{m=1}^M$ of the sensors are generated by [21]:

$$\alpha_m = 1 + \sqrt{12} \sigma_\alpha \zeta_m, \quad (22)$$

$$\phi_m = \sqrt{12} \sigma_\phi \eta_m, \quad (23)$$

Where ζ_m and η_m are independent and identically distributed random variables distributed uniformly over $[-0.5, 0.5]$. Additionally, σ_α and σ_ϕ are the standard deviations of α_m and ϕ_m , respectively [22]. In the following simulations, $\sigma_\alpha = 0.1$. For all Monte Carlo experiments, the number of trials is 200. It is known from (17) that the estimation of the gain errors is independent of the phase error and DOA, and the gain errors do not affect the accuracy of the DOA, so we omit the performance of the gain error estimation in the following simulations.

The RMSE of DOA and phase errors are measured in (24) and (25), respectively:

$$\text{RMSE}_\theta = \left[\frac{1}{200K} \sum_{k=1}^K \sum_{i=1}^{200} (\hat{\theta}_k^i - \theta_k)^2 \right]^{1/2}, \quad (24)$$

$$\text{RMSE}_\phi = \left[\frac{1}{200M} \sum_{m=1}^M \sum_{i=1}^{200} (\hat{\phi}_m^i - \phi_m)^2 \right]^{1/2}. \quad (25)$$

A. Effect of DOA separation

We consider $K=2$ uncorrelated sources. The sample number is 200, the signal-to-noise ratio (SNR) is 20 dB and $\sigma_\phi = 20^\circ$. The grid size of the ONGM method is 180. Figure 1 shows the space spectra of the WF method, the L1_SVD method, the ONGM method, and the GLSM method under two different DOA separation cases. The proposed method without calibration is referred to as GLSM1, and GLSM2 represents the proposed method with calibration. L1_SVD1 is without gain-phase errors, and L1_SVD2 is with gain-phase errors.

It can be seen from Fig. 1 (a) that when two signals are not close to each other ($\text{DOA} = [5^\circ \ 20^\circ]$), the performance of the L1_SVD method with gain-phase errors severely deteriorates and has only one sharp peak. In contrast, the other three methods can accurately estimate DOA. When the DOA separation of the two signals is reduced ($\text{DOA} = [17^\circ \ 20^\circ]$), Fig. 1 (b) shows that the WF method almost completely fails, and the ONGM method only has one peak. In contrast, the proposed method can still distinguish the two closed signals. In addition, the calibration technique of the proposed method improves the estimation accuracy (GLSM1 vs. GLSM2).

B. Effect of phase errors

We consider $K=3$ sources from directions $\theta = [10, 25, 60]^\top$. The sample number is 200 and SNR is 20 dB. The grid size of the ONGM method is 180. Based on 200 Monte Carlo runs, the RMSE of DOA and gain-phase error estimates versus the standard deviation of the phase error σ_ϕ are obtained by the WF method, the ONGM method and the proposed method.

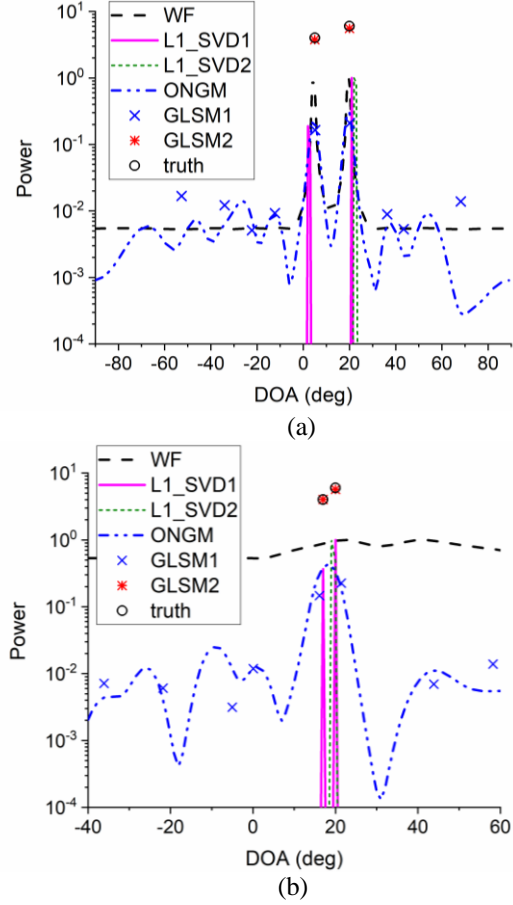


Fig. 1. Space spectrum of four algorithms: (a) $\text{DOA} = [5^\circ \ 20^\circ]$, and (b) $\text{DOA} = [17^\circ \ 20^\circ]$.

Figure 2 (a) and Fig. 2 (b) show that when the sources are uncorrelated, the ONGM method and the WF method are similar in the performance of DOA estimation and phase error estimation. Moreover, the performance of the two algorithms gradually deteriorates with increasing phase error because both algorithms easily fall into local optima when the phase errors are large. In contrast, the GLSM algorithm shows good stability to DOA and phase error estimation as the phase error increases from small to large, and the estimation accuracy is obviously higher than the first two algorithms. When the signal sources are coherent (source 2 is a replica of source 1), the WF algorithm is completely invalid in DOA estimation and phase error estimation. The estimation performance of the ONGM method and GLSM method are similar and obviously better than those of the WF method because GLSM and ONGM are based on the covariance fitting criterion, which is robust to the correlated sources, and both of them reduce the influence of signal correlation through the exchange matrix in the process of solving the phase error.

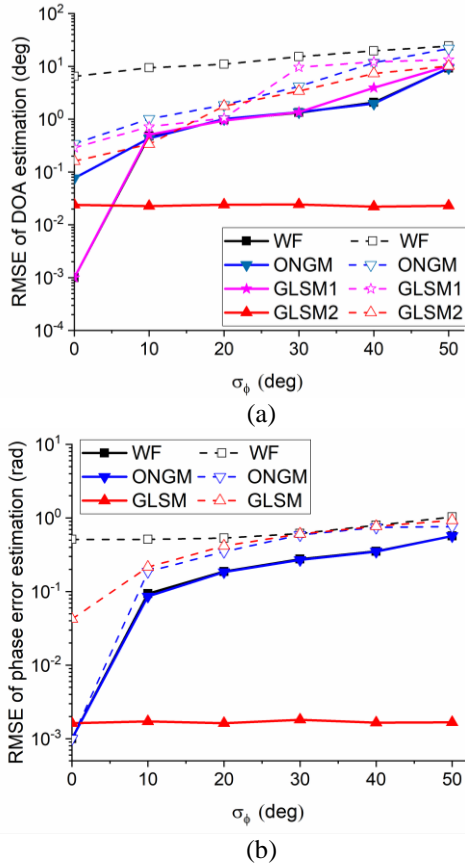
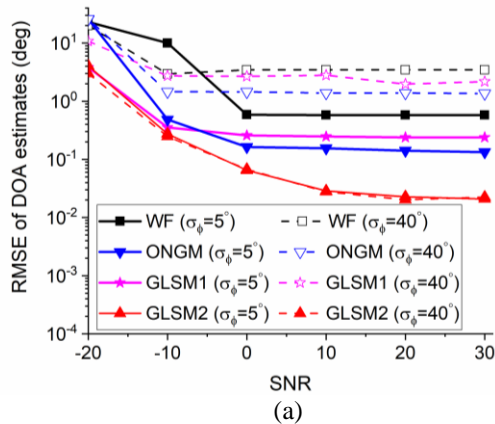


Fig. 2. RMSE versus σ_ϕ (a) RMSE of DOA estimation versus σ_ϕ , and (b) RMSE of phase error estimation versus σ_ϕ . (The dashed and solid plots represent the cases of coherent signal sources and uncorrelated signal sources, respectively).

C. Effect of SNR

We consider three sources from directions by direction 10° , 25° and 60° . The number of samples is



200 and the varying SNR is from -20 dB to 30 dB. The grid number of the ONGM method is 180. Based on 200 Monte Carlo runs, the RMSE of DOA and phase error estimates versus SNR are obtained by the WF method, the ONGM method and the proposed method.

First, some simulations are performed to consider the effect of SNR in the case of uncorrelated signal sources. We show the results in two different phase error cases: $\sigma_\phi = 5^\circ$ and $\sigma_\phi = 40^\circ$. Figure 3 (a) and Fig. 3 (b) show that in the case of small phase error ($\sigma_\phi = 5^\circ$), the estimation performance of the three algorithms improves as the SNR increases. Moreover, the curve of the proposed method is constantly lower than that of the WF method and the ONGM method. When the phase error is large ($\sigma_\phi = 40^\circ$), the performance of the WF algorithm and ONGM algorithm is difficult to further improve with increasing SNR, and the GLSM algorithm still maintains good estimation performance.

Then, some simulations are performed to consider the effect of SNR in the case of coherent sources (source 2 is a replica of source 1). The different simulation conditions from the uncorrelated sources case are two phase error cases ($\sigma_\phi = 5^\circ$ and $\sigma_\phi = 15^\circ$). Figure 4 (a) and Fig. 4 (b) show that in the case of coherent signal sources, the WF method is invalid regardless of how the SNR increases. In contrast, as the SNR increases, the phase error is smaller, the performance of the ONGM method and the GLSM method is better, and the GLSM method performs better than the ONGM method.

D. Effect of array length

We study the performance with respect to the array length M . Two uncorrelated sources impinge on the array with DOAs 10° and 25° . We set SNR=20 dB, $\sigma_\phi = 10^\circ$, and vary M from 5 to 40. Moreover, we consider two grid size cases (180 grids and 360 grids) for the ONGM method.

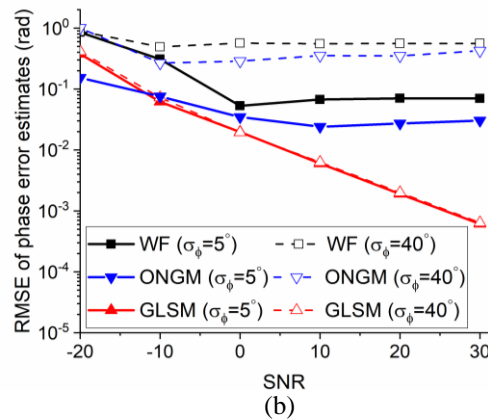


Fig. 3. RMSE versus SNR (the signal sources are uncorrelated). (a) RMSE of DOA estimates versus SNR. (b) RMSE of phase estimates versus SNR.

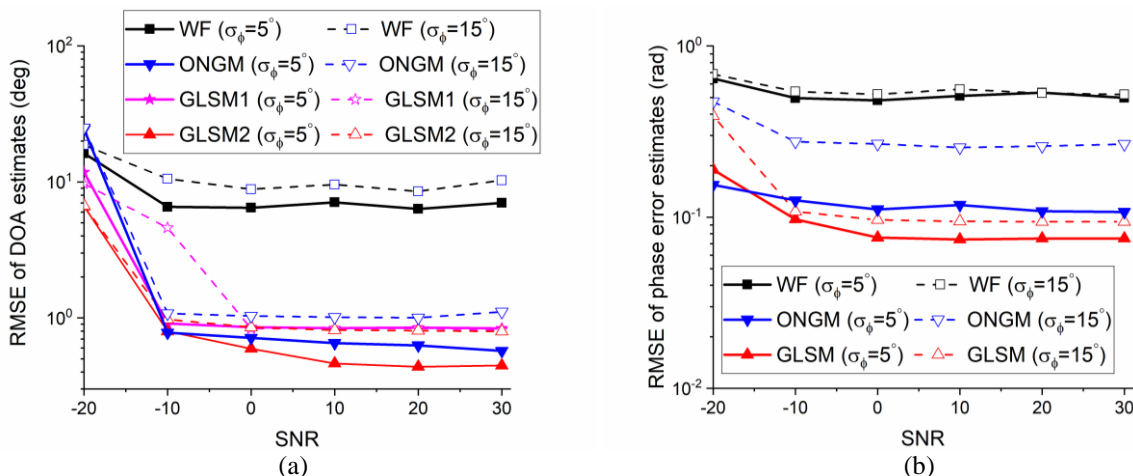


Fig. 4. RMSE versus SNR (Source 2 is a replica of source 1). (a) RMSE of DOA estimates versus SNR. (b) RMSE of phase error estimates versus SNR.

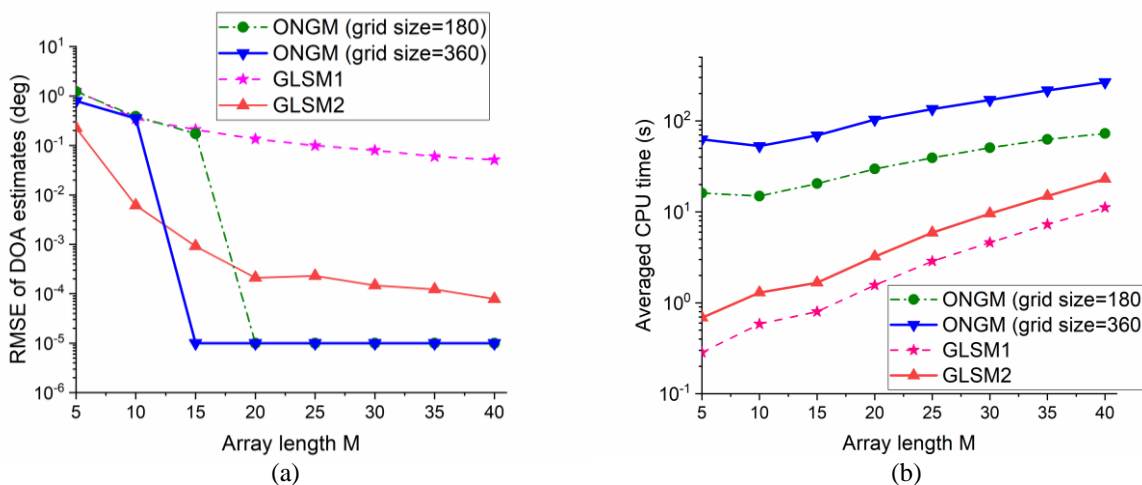


Fig. 5. (a) RMSE of DOA estimates of GLSM with an M -element ULA compared with ONGM. (b) CPU time usage of GLSM and ONGM.

Figure 5 (a) shows that the RMSEs of the GLSM method and the ONGM method improve with the array length. More specifically, when $M > 12$, the performance of the ONGM method with 360 grids is better than the GLSM method. Moreover, the more grids, the better the performance of the ONGM method is. Figure 5 (b) shows that the average CPU time usage of these two methods increases with an increasing number of array elements. However, the average CPU running time used by the GLSM method to complete one estimation is significantly lower than that of the ONGM method.

VI. CONCLUSION

In this paper, we propose a fast method to simultaneously estimate DOA and gain-phase errors in the continuous range without a grid mismatch

problem. This method does not require the existence of a calibration source and calibration information. Monte Carlo runs show that utilizing the covariance fitting criterion and the SDP, the proposed algorithm overcomes the shortcomings of the ONGM method in the case of severe gain-phase error perturbations when signal sources are uncorrelated. Moreover, the proposed method has the advantages of low computational complexity and high resolution compared to existing methods.

REFERENCES

- [1] R. Schmidt, "Multiple emitter location and signal parameter estimation," *IEEE Trans. Antennas Propag.*, vol. 34, no. 3, pp. 276-280, 1986.
- [2] R. Roy and T. Kailath, "ESPRIT-estimation of

- signal parameters via rotational invariance techniques,” *Adapt. Antennas Wirel. Commun.*, vol. 37, no. 7, pp. 224-235, 2009.
- [3] S. A. Vorobyov, A. B. Gershman, and K. M. Wong, “Maximum likelihood direction-of-arrival estimation in unknown noise fields using sparse sensor arrays,” *IEEE Trans. Signal Process.*, vol. 53, no. 1, pp. 34-43, 2005.
- [4] J. Capon, “High-resolution frequency-wave-number spectrum analysis,” *Proc. IEEE*, vol. 57, no. 8, pp. 1408-1418, 1969.
- [5] D. Malioutov, M. Cetin, and A. S. Willsky, “A sparse signal reconstruction perspective for source localization with sensor arrays,” *IEEE Trans. Signal Process.*, vol. 53, no. 8, pp. 3010-3022, 2005.
- [6] P. Stoica, P. Babu, and J. Li, “SPICE: A sparse covariance-based estimation method for array processing,” *IEEE Trans. Signal Process.*, vol. 59, no. 2, pp. 629-638, 2011.
- [7] M. Muzi, N. Tedeschi, L. Scorrano, V. Ferrara, and F. Frezza, “Single-snapshot time-domain direction of arrival estimation under bayesian group-sparse hypothesis and vector sensor antennas,” *Appl. Comput. Electromagn. Soc. J.*, vol. 33, no. 8, pp. 822-827, 2018.
- [8] H. Cui, H. Duan, and H. Liu, “Off-grid DOA estimation using temporal block sparse Bayesian inference,” in *2016 IEEE International Conference on Digital Signal Processing (DSP)*, 2016, pp. 204-207.
- [9] Z. Yang, L. Xie, and C. Zhang, “Off-grid direction of arrival estimation using sparse bayesian inference,” *IEEE Trans. Signal Process.*, vol. 61, no. 1, pp. 38-43, 2013.
- [10] X. Zhang, T. Jiang, Y. Li, and X. Liu, “An off-grid DOA estimation method using proximal splitting and successive nonconvex sparsity approximation,” *IEEE Access*, vol. 7, pp. 66764-66773, 2019.
- [11] Z. Yang, L. Xie, and C. Zhang, “A discretization-free sparse and parametric approach for linear array signal processing,” *IEEE Trans. Signal Process.*, vol. 62, no. 19, pp. 4959-4973, 2014.
- [12] Z. Yang and L. Xie, “On gridless sparse methods for multi-snapshot direction of arrival estimation,” *Circuits, Syst. Signal Process.*, vol. 36, no. 8, pp. 3370-3384, 2017.
- [13] A. L. Swindlehurst and T. Kailath, “A performance analysis of subspace-based method in the presence of model errors, Part I: The MUSIC algorithm,” *Signal Process. IEEE Trans.*, vol. 40, no. 7, pp. 1758-1774, 1992.
- [14] A. L. Swindlehurst and T. Kailath, “A performance analysis of subspace-based methods in the presence of model errors, Part I: The MUSIC algorithm,” *IEEE Trans. Signal Process.*, vol. 40, no. 7, pp. 1758-1774, 1992.
- [15] A. Azarbar, G. R. Dadashzadeh, and H. R. Bakhshi, “2-D DOA estimation with matrix pencil method in the presence of mutual coupling,” *Appl. Comput. Electromagn. Soc. J.*, vol. 27, no. 9, pp. 742-748, 2012.
- [16] Q. Cheng, Y. Hua, and P. Stoica, “Asymptotic performance of optimal gain-and-phase estimators of sensor arrays,” *IEEE Trans. Signal Process.*, vol. 48, no. 12, pp. 3587-3590, 2000.
- [17] B. P. Ng, J. P. Lie, M. H. Er, and A. Feng, “A practical simple geometry and gain/phase calibration technique for antenna array processing,” *IEEE Trans. Antennas Propag.*, vol. 57, no. 7, pp. 1963-1972, 2009.
- [18] W. Peng, Y. Gao, Y. Qu, and C. Guo, “Array calibration with sensor gain and phase errors using invasive weed optimization algorithm,” in *2017 Sixth Asia-Pacific Conference on Antennas and Propagation (APCAP)*, pp. 1-3, 2017.
- [19] A. Paulraj, R. Roy, and T. Kailath, “A subspace rotation approach to signal parameter estimation,” *Proc. IEEE*, vol. 74, no. 7, pp. 1044-1046, 1986.
- [20] A. J. Weiss and B. Friedlander, “Eigenstructure methods for direction finding with sensor gain and phase uncertainties,” *Circuits, Syst. Signal Process.*, vol. 9, no. 3, pp. 271-300, 1990.
- [21] A. Liu, G. Liao, C. Zeng, Z. Yang, and Q. Xu, “An eigenstructure method for estimating DOA and sensor gain-phase errors,” *IEEE Trans. Signal Process.*, vol. 59, no. 12, pp. 5944-5956, 2011.
- [22] S. Cao, Z. Ye, D. Xu, and X. Xu, “A hadamard product based method for DOA estimation and gain-phase error calibration,” *IEEE Trans. Aerosp. Electron. Syst.*, vol. 49, no. 2, pp. 1224-1233, 2013.
- [23] H. Liu, L. Zhao, Y. Li, X. Jing, and T. K. Truong, “A sparse-based approach for DOA estimation and array calibration in uniform linear array,” *IEEE Sens. J.*, vol. 16, no. 15, pp. 6018-6027, 2016.
- [24] W. Peng, C. Guo, M. Wang, and Y. Gao, “An improved gain-phase error self-calibration method for robust DOA estimation,” *Int. J. Microw. Wirel. Technol.*, pp. 1-9.
- [25] P. Stoica, P. Babu, and J. Li, “New method of sparse parameter estimation in separable models and its use for spectral analysis of irregularly sampled data,” *IEEE Trans. Signal Process.*, vol. 59, no. 1, pp. 35-47, 2011.
- [26] C. R. Rojas, D. Katselis, and H. Hjalmarsson, “A note on the SPICE method,” *IEEE Trans. Signal Process.*, vol. 61, no. 18, pp. 4545-4551, 2013.

- [27] K.-C. Toh, M. J. Todd, and R. H. Tütüncü, "SDPT3—A MATLAB software package for semidefinite programming, version 1.3," *Optim. Methods Softw.*, vol. 11, no. 1-4, pp. 545-581, 1999.
- [28] M. Grant, S. Boyd, and Y. Ye, "CVX: Matlab software for disciplined convex programming," 2009.
- [29] L. Vandenberghe and S. Boyd, "Semidefinite programming," *SIAM Rev.*, vol. 38, no. 1, pp. 49-95, 1996.



Wencan Peng was born in Hubei Province, China, in 1987. She received the B.S. degree in School of Measuring and Optical Engineering, Nanchang Hangkong University in Nanchang city, China, in 2010. Then, she received the M.S. degree in School of Electronics and

Information, Northwestern Polytechnical University in Xi'an city, China, in 2013. Now, She is pursuing the Ph.D. degree in School of Electronics and Information, Northwestern Polytechnical University. Her research interests include: array signal processing and array calibration.



Chenjiang Guo was born in Shannxi Province, China, in 1963. CIE Senior Member, Antenna Society Committee Member. He received the B.S., M.S. and Ph.D. in School of Electronics and Information, Northwestern Poly-

technical University in Xi'an City, China, in 1984, 1987 and 2007 respectively. He is a Professor in School of Electronics and Information NWPU. He has published more than 140 research papers. He research interests includes: array signal processing, theory and design of antenna.



Min Wang (IEEE Member), received the B.S. degree from Xidian Univ. China in 2000; M.S. and Ph.D. degree in Signal and Information Processing from Xidian Univ., Xi'an China, in 2003 and 2005 respectively. He is working with National Lab of Radar Signal Processing in Xidian University. His research interests include sparse signal processing, miliwave/Terahertz radar and high resolution radar imaging.



Yuteng Gao was born in Shannxi Province, China, in 1988. He received the B.S. and M.S degree in School of Electronics and Information, Northwestern Polytechnical University in Xi'an City, China, in 2010 and 2013 respectively. He is presently working on his Ph.D. degree in School of Electronics and Information, Northwestern Polytechnical University in Xi'an City, China. His research interests include millimeter wave, antenna design and radar imaging.



Xia Zhao was born in Ningxia, China, in 1978. She is now an Associate Professor in North Minzu University, and pursuing her Ph.D in Electromagnetic Field and Microwave Technology at Northwestern Polytechnical University. Her research interests concern: array signal processing and target localization.

A p -norm-like Constraint LMS Algorithm for Sparse Adaptive Beamforming

Wanlu Shi¹ and Yingsong Li^{1,2*}

¹ College of Information and Communication Engineering
Harbin Engineering University, Harbin, 150001, China
liyingsong@ieee.org

² Key Laboratory of Microwave Remote Sensing
National Space Science Center, Chinese Academy of Sciences
Beijing, 100190, China

Abstract — In this paper, a p -norm-like constraint normalized least mean square (PNL-CNLMS) algorithm is proposed for sparse adaptive beamforming. The proposed PNL-CNLMS algorithm inherits the good capacity of the conventional constrained least mean square (CLMS) algorithm in adaptive beamforming, i.e., forming ideal beam patterns. Also, the proposed PNL-CNLMS algorithm utilizes a p -norm-like constraint to exploit sparse property of the corresponding antenna array. In the derivation procedure, the Lagrange multiplier approach and the gradient descent method are utilized to obtain the devised updating equation. Numerical simulations reveal the superiority of the proposed PNL-CNLMS algorithm.

Index Terms — Array beamforming, constrained LMS algorithm, p -norm-like constraint, sparse adaptive beamforming.

I. INTRODUCTION

With the ability of forming the desired beampattern in the sector of interest while suppressing the influences from the unexpected interferences, adaptive beamforming has been an important application for array processing in the last decades. Because of the good capacity, adaptive beamforming is widely applied to radar, sonar, mobile communications, seismic sensing and other fields [1-2]. The strategy for an adaptive beamformer to acquire a better signal-to-interference-plus-noise ratio (SINR) is to form a main lobe in the interested direction to get a high gain, meanwhile, to form nulls to attenuate the interferences [3].

The wide spread linearly constrained minimum variance (LCMV) algorithm developed by Frost provides an excellent beamforming performance, which can provide the mentioned properties, i.e., dynamically adjusting the array weight vectors to adaptively capture the signals of interest (SOI) and suppress the

interferences [3]. Then, the normalized adaptive version of LCMV, namely the constraint normalized least-mean-square (CLMS) algorithm is developed in [4], through which the output power is minimized, and the unintended interferences are reduced. Meanwhile, the CLMS algorithm remains a maximum gain in the desired direction.

Always, however, in real-life applications, especially in radar system, enormous arrays are essentially needed for realizing the desired performance. Where the fact is, enormous arrays face the problem of limited power supply and insufficient computation ability. As conventional adaptive beamforming algorithms fail to meet the requirements of enormous arrays computations, sparse adaptive beamforming algorithms have been proposed [5-9] which aim to find sparse solution for adaptive beamforming with little effect on the beampattern capacity. The first proposed sparse adaptive beamforming algorithm is inspired by the Compressive Sensing [10] and the Least Absolutely Shrinkage and Selection Operator [11]. Then, with the development of sparse signal pressing [12-21], scholars use the zero attracting technique to exploit the sparse characteristics of the antenna array and force the minor entries of the weight vector towards zero [12-15].

Sparse signal processing algorithms exploit the sparse characteristics existing in many scenarios, which attributes to the fact that they have particular advantages on both convergence rate and performance. Sparse signal processing technique is a hot research point and has been widely investigated in recent years. From the representative zero-attracting LMS (ZA-LMS) algorithm, which introduces a zero-attractor into the traditional iteration equation of the LMS algorithm, an enormous number of algorithms have been studied for sparse system applications [13-22]. The zero-attractor forces all zero-filter taps to zero, so that the convergence rate is accelerated. However, the zero-attractor in the ZA-LMS, which is generate by the

l_1 -norm penalty, unable to distinguish dominant coefficients and attenuate all the coefficients. In this regard, the reweighted ZA-LMS (RZA-LMS) is proposed to introduce different zero attractors for different taps, i.e., the trivial coefficients are forced to zero more quickly.

Inspired by the zero-attractor techniques, an l_1 -norm CNLMS (L1-CNLMS) algorithm and a weighted l_1 -norm CNLMS (L1-WCNLMS) have been proposed for sparse adaptive beamforming [5]. Recently, many reweighted l_1 -norm penalties are proposed and considered in [12-15, 19-20], and a new reweighted l_1 -norm CNLMS (RL1-CNLMS) algorithm is proposed [8]. In [23-24], a p -norm-like diversity measure is proposed for sparse system identification, which holds a better performance than that of the l_1 -norm based algorithms, resulting in that it is possible to improve the l_1 -norm based sparse adaptive beamforming algorithms.

In this paper, we develop a p -norm-like constraint normalized least mean square (PNL-CNLMS) algorithm for sparse adaptive beamforming. Simulation results demonstrate that the proposed algorithms can get a better beamforming performance and use less antenna array elements.

II. ARRAY PROCESSING FUNDAMENTALS

In this paper, a planar antenna array is considered, in which the antenna elements are half wavelength spaced. Figure 1 is the model of an adaptive beamforming system, while Fig. 2 provides the array elements coordinate diagram. P_m ($m=1, 2, \dots, M$) is the positions of the sensors, and d is the interval between antenna elements, which is equal to half wavelength. The received signals have the directions of θ_s and θ_i ($i=1, 2, \dots, N$) which corresponds to the SOI and interferences, respectively. It is obvious that the objective of the adaptive beamforming algorithms is to generate main beam in θ_s and nulls in θ_i ($i=1, 2, \dots, N$). One of the basic assumptions for the system is that the receiving signals, including SOI and interferences are far-field narrow-band signals. In this way, the receiving signals can be regarded as plane waves. The sensor array is composed of M omnidirectional antennas, and each antenna corresponds to a so-called weight coefficient. Then, the designed sparse adaptive beamforming algorithm is used to find out the final sparse solution, i.e., to acquire the sparse weight vector. The optimal weight coefficients will be introduced in the next section.

Under the paradigm mentioned above, the receiving signals at time index k can be written as:

$$\mathbf{x}(k) = \mathbf{a}_s s(k) + \mathbf{a}_i \mathbf{i}(k) + \mathbf{n}(k). \quad (1)$$

Where \mathbf{a}_s and \mathbf{a}_i are the SOI and interferences steering matrix, $s(k)$ and $\mathbf{i}(k)$ are the complex signal envelope vectors $\mathbf{n}(k)$ is the zero-mean white Gaussian noise

vector. It should be pointed out that the SOI, interferences and the noise are assumed to be statistically independent.

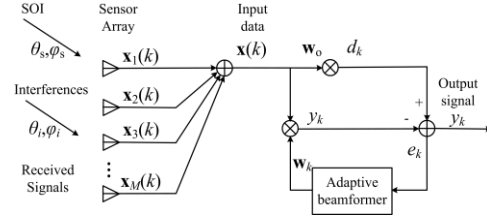


Fig. 1. Adaptive beamforming system.

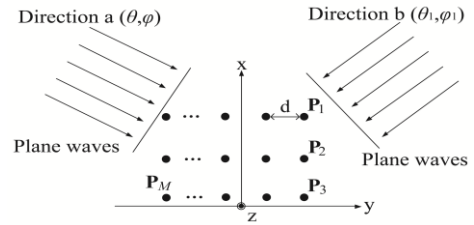


Fig. 2. Sensor array coordinate graph.

The output signal of the adaptive beamforming system then becomes:

$$y(k) = \mathbf{w}^H \mathbf{x}(k), \quad (2)$$

where \mathbf{w} represents the weight vector of the adaptive beamforming system.

For a given direction (θ, φ) , the beampattern is given by:

$$B(\theta, \varphi) = \mathbf{w}^H \exp \left\{ -j \frac{2\pi \mathbf{c}^T \mathbf{P}_m}{\lambda} \right\}, \quad (3)$$

where $\mathbf{c} = [-\sin\theta \cos\varphi, -\sin\theta \sin\varphi]^T$ is a unit vector and λ is the wavelength.

The output SINR of the adaptive beamformer is calculated by using:

$$\text{SINR} = \frac{\sigma_s^2 |\mathbf{w}^H \mathbf{a}_s|^2}{\mathbf{w}^H \mathbf{R}_{n+i} \mathbf{w}}. \quad (4)$$

In our notation, σ_s^2 is the power of SOI and \mathbf{R}_{n+i} denotes the interference-plus-noise covariance matrix which is given by:

$$\mathbf{R}_{n+i} = E \left\{ (\mathbf{i}(k) + \mathbf{n}(k)) (\mathbf{i}(k) + \mathbf{n}(k))^H \right\}, \quad (5)$$

where $E\{\cdot\}$ is the expectation operator and $(\cdot)^H$ represents the Hermitian operator.

III. THE CNLMS ALGORITHM

A. The CLMS algorithm

The well-known classical beamforming algorithm LCMV present a solution when the direction of SOI and interferences are given [1]. The weight vector in LCMV algorithm is expressed as:

$$\mathbf{w}_o = \mathbf{R}^{-1}\mathbf{C}(\mathbf{C}^H\mathbf{R}^{-1}\mathbf{C})^{-1}\mathbf{f}, \quad (6)$$

where \mathbf{R} , \mathbf{C} and \mathbf{f} are the covariance matrix of input signal, the constraint matrix, and the constraint vector, respectively. It should be pointed out that the constraint matrix \mathbf{C} contains the information of direction. In the constraint vector \mathbf{f} , the elements associated to the SOI are set to 1 and entries corresponding to interferences are selected as 0. Then the adaptive version of LCMV algorithm is proposed, namely the CLMS algorithm which can adaptively give the desired beam pattern according to the direction of SOI and interferences [4]. The objective of CLMS algorithm is to solve:

$$\min_{\mathbf{w}} E\left[|e_k|^2\right] \quad \text{subject to} \quad \mathbf{C}^H\mathbf{w} = \mathbf{f}, \quad (7)$$

with $d_k = \mathbf{w}_o^H \mathbf{x}_k$ and $e_k = d_k - \mathbf{w}^H \mathbf{x}_k$ denote the desired output signal and the estimation error, respectively.

To find out the solution of (7), the Lagrange multiplier method is utilized, and then (7) is transformed into the following cost function:

$$\zeta_{CLMS}(k) = E\left[|e_k|^2\right] + \lambda^H(\mathbf{C}^H\mathbf{w}_k - \mathbf{f}), \quad (8)$$

where λ is the Lagrange multiplier.

For the obtained cost function, namely (8), a close-form solution is unavailable. In this case, the gradient descent principle is utilized to iteratively seek for the solution. Then, the updating equation can be constructed as:

$$\mathbf{w}_{k+1} = \mathbf{w}_k - \mu \nabla_{\mathbf{w}} \zeta_{CLMS}(k), \quad (9)$$

where μ represents the step size in each iteration and $\nabla_{\mathbf{w}}$ is the gradient operation in terms of the weight vector.

To simplify the updating equation, the instantaneous estimation of the gradient vector is utilized. In this way, the gradient vector can be expressed as:

$$\hat{\nabla}_{\mathbf{w}} \zeta_{CLMS}(k) = -2e_k^* \mathbf{x}_k + \mathbf{C}\lambda_1. \quad (10)$$

From (7), one can get the constraint condition, i.e., $\mathbf{C}^H\mathbf{w} = \mathbf{f}$. Use this constraint condition, one can derive the updating function after several straight-forward calculations, which is given by:

$$\mathbf{w}_{k+1} = \mathbf{P}\left[\mathbf{w}_k + \mu e_k^* \mathbf{x}_k\right] + \mathbf{f}_c, \quad (11)$$

where

$$\mathbf{P} = \mathbf{I}_{N \times N} - \mathbf{C}(\mathbf{C}^H\mathbf{C})^{-1}\mathbf{C}^H, \quad (12)$$

which is the projection matrix with $\mathbf{I}_{N \times N}$ is the identity matrix, and \mathbf{f}_c is the constraint hyperplane which is given by:

$$\mathbf{f}_c = \mathbf{C}(\mathbf{C}^H\mathbf{C})^{-1}\mathbf{f}. \quad (13)$$

B. The CNLMS algorithm

In CLMS algorithm, it can be seen that the step size, which is also referred as convergence factor, is a constant. As a consequence, the convergence rate of CLMS algorithm can be accelerated. Minimize the

instantaneous posteriori squared error in terms of the step size [21]:

$$\frac{\partial [|e_{ip}(k)|^2]}{\partial \mu_k^*} = 0, \quad (14)$$

where

$$e_{ip}(k) = e_k (1 - \mu_k \mathbf{x}_k^H \mathbf{P} \mathbf{x}_k). \quad (15)$$

Solving (15), yields,

$$\mu_k = \frac{\mu_0}{\mathbf{x}_k^H \mathbf{P} \mathbf{x}_k + \varepsilon}. \quad (16)$$

In (16), ε is a small positive constant which can prevent overflowing when $\mathbf{x}_k^H \mathbf{P} \mathbf{x}_k$ is too small, and μ_0 is the initialized convergence factor.

Finally, the update function is obtained:

$$\mathbf{w}_{k+1} = \mathbf{P}\left[\mathbf{w}_k + \mu_k \frac{e_k \mathbf{x}_k}{\mathbf{x}_k^H \mathbf{P} \mathbf{x}_k + \varepsilon}\right] + \mathbf{f}_c. \quad (17)$$

C. The p -norm-like diversity measure

Different from the conventional Euclidean norm noted as $\|\cdot\|_p$ or L_p , the p -norm-like diversity measure is a general effective criterion developed in [24], which is expressed as:

$$\|\mathbf{x}\|_{p\text{-like}} = \sum_{j=1}^n |x(j)|^p, \quad 0 \leq p \leq 1. \quad (18)$$

As (18) shows, it is clearly to see that the so-called p -norm-like diversity measure is not a classical norm, but they have close connection to provide sparse solution and can be used for sparse array beamforming. In [24-25], numerical simulation results have shown that the p -norm-like diversity measure outperforms the conventional l_1 -norm optimal method for sparse system identification. Hence, in this paper the p -norm-like is utilized to exploit the sparsity characteristic of weight vector in adaptive beamforming algorithm.

D. Derivation of the PNL-CNLMS algorithm

The proposed PNL-CNLMS algorithm employs the p -norm-like diversity measure to develop the sparse adaptive beamforming algorithm, which is to solve:

$$\min_{\mathbf{w}} E\left[|e_k|^2\right] \quad \text{s.t.} \quad \begin{cases} \mathbf{C}^H\mathbf{w}_k = \mathbf{f}; \\ \|\mathbf{w}_k\|_{p\text{-like}} = z, \end{cases} \quad (19)$$

where z acts as the constraint factor which lies in the range (0, 1), while e_k , \mathbf{C} , \mathbf{w}_k and \mathbf{f} have the same meaning which are mentioned earlier in this paper.

Then, to solve (19), the Lagrange multiplier method is employed to acquire the objective function corresponding to (19):

$$\begin{aligned} \zeta_{p\text{-like}}(k) = & E\left[|e_k|^2\right] + \lambda_1^H(\mathbf{C}^H\mathbf{w}_k - \mathbf{f}) \\ & + \lambda_{p\text{-like}}[\|\mathbf{w}_k\|_{p\text{-like}} - z], \end{aligned} \quad (20)$$

where λ_1 and $\lambda_{p\text{-like}}$ are vector and scalar, respectively, which are the Lagrange multipliers.

Again, it is hard to obtain a close-form solution

for (20). Similar to (8), (9), and (10), instantaneous estimation is used to implement the gradient of (20), which yields:

$$\hat{\nabla}_{\mathbf{w}} \zeta_{p\text{-like}}(k) = -2e_k^* \mathbf{x}_k + \mathbf{C} \lambda_1 + \lambda_{p\text{-like}} \mathbf{Q}_{p\text{-like}}, \quad (21)$$

with

$$\mathbf{Q}_{p\text{-like}} = \frac{\partial \|\mathbf{w}_k\|_{p\text{-like}}}{\partial \mathbf{w}_k} = \frac{\text{sgn}(\mathbf{w}_k)}{|\mathbf{w}_k|^{1-p}}, \quad (22)$$

where $\text{sgn}(\cdot)$ is a sign function whose definition is:

$$\text{sgn}(x) = \begin{cases} 1, & x > 0 \\ -1, & x < 0, \\ 0, & x = 0 \end{cases} \quad (23)$$

Based on the principle of gradient descent concepts shown in (9), we can get the final updating equation given by:

$$\mathbf{w}_{k+1} = \mathbf{w}_k - \mu \hat{\nabla}_{\mathbf{w}} \zeta_{p\text{-like}}(k), \quad (24)$$

where $\hat{\nabla}_{\mathbf{w}} \zeta_{p\text{-like}}(k)$ is given in (21).

An upper bound is imposed on (22) to avert divergence when the entries of \mathbf{w}_k become zero. This is an essential step especially when the algorithm itself is aimed to exploit sparse characteristic of the weight vector. As a consequence, $\mathbf{Q}_{p\text{-like}}$ is expressed as:

$$\mathbf{Q}_{p\text{-like}} = \frac{\text{sgn}(\mathbf{w}_k)}{\varepsilon_{p\text{-like}} + |\mathbf{w}_k|^{1-p}}, \quad (25)$$

where $\varepsilon_{p\text{-like}}$ is a small positive constant.

The next task is to acquire the Lagrange multipliers. When the algorithm has converged, i.e., $\mathbf{w}_{k+1} = \mathbf{w}_k$, then we can rewrite the constraints in (19) to be:

$$\begin{cases} \mathbf{C}^H \mathbf{w}_{k+1} = \mathbf{C}^H \mathbf{w}_k = \mathbf{f}, \\ \mathbf{Q}_{p\text{-like}} \mathbf{w}_{k+1} = \mathbf{Q}_{p\text{-like}} \mathbf{w}_k = \|\mathbf{w}_k\|_{p\text{-like}} = z. \end{cases} \quad (26)$$

Take (21) into (24), and premultiplying (24) by \mathbf{C}^H and $\mathbf{Q}_{p\text{-like}}$ respectively, the Lagrange multipliers λ_1 and $\lambda_{p\text{-like}}$ are available:

$$\begin{cases} \lambda_1 = \mathbf{G}(2e_k^* \mathbf{x}_k - \lambda_{p\text{-like}} \mathbf{Q}_{p\text{-like}}), \\ \lambda_{p\text{-like}} = \left(\frac{-2}{n\mu} \right) z_e + \frac{2e_k^* \mathbf{Q}_{p\text{-like}}^H \mathbf{P} \mathbf{x}_k}{n}, \end{cases} \quad (27)$$

with

$$\begin{cases} z_e = (z - \mathbf{Q}_{p\text{-like}}^H \mathbf{w}_k), \\ \mathbf{G} = (\mathbf{C}^H \mathbf{C})^{-1} \mathbf{C}^H, \\ n = \|\mathbf{P} \mathbf{Q}_{p\text{-like}}\|_2^2. \end{cases} \quad (28)$$

Then consider the normalizing approach in [26], the final updating formulation for the proposed PNL-CNLMS algorithm can be written as:

$$\mathbf{w}_{k+1} = \mathbf{w}_k + \mu_k e_k^* \mathbf{W} + z_e \left(\frac{\mathbf{P} \mathbf{Q}_{p\text{-like}}}{\nu} \right), \quad (29)$$

where

$$\begin{cases} q = \mathbf{Q}_{p\text{-like}}^H \mathbf{P} \mathbf{x}_k, \\ v = \mathbf{Q}_{p\text{-like}}^H \mathbf{P} \mathbf{Q}_{p\text{-like}}, \\ \mu_k = \frac{\mu_0 \left[e_k - z_e \left(\frac{\mathbf{P} \mathbf{Q}_{p\text{-like}}}{\nu} \right) \mathbf{x}_k \right]}{e_k \mathbf{W}^H \mathbf{x}_k + \varepsilon_{p\text{-like}}}, \\ \mathbf{P} = \mathbf{I}_{N \times N} - \mathbf{C}(\mathbf{C}^H \mathbf{C})^{-1} \mathbf{C}^H, \\ \mathbf{W} = \mathbf{P} \left(\mathbf{x}_k - \frac{q \mathbf{Q}_{p\text{-like}}}{\nu} \right). \end{cases} \quad (30)$$

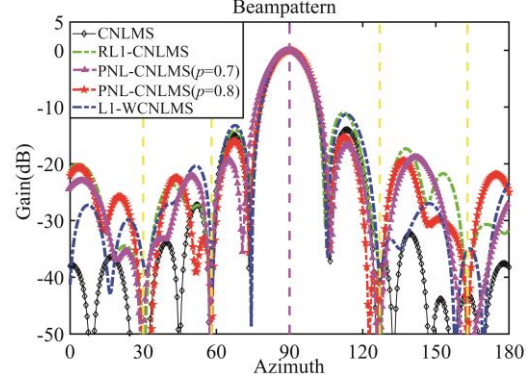


Fig. 3. Beampatterns of the proposed algorithms versus the CNLMS algorithm and the existing algorithms in [5, 8]. Purple line is the SOI, yellow lines are interferences.

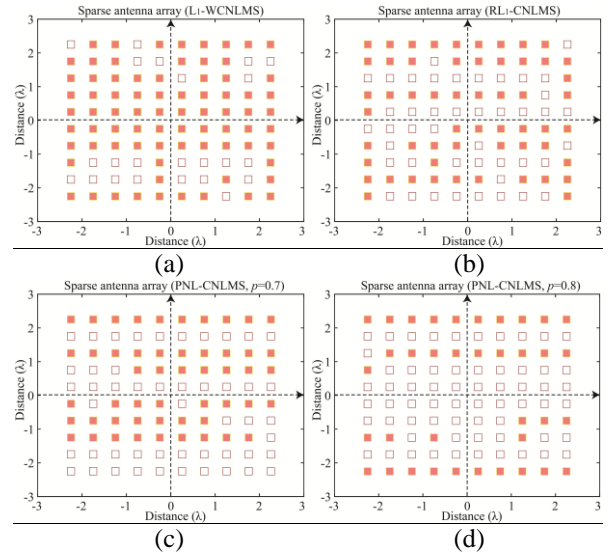


Fig. 4. Sparse arrays thinned by the proposed algorithms and the algorithm developed in [5]: (a) L_1 -WCNLMS in [5], (b) RL_1 -CNLMS algorithm in [8], (c) PNL-CNLMS algorithm with $p=0.7$, and (d) PNL-CNLMS algorithm with $p=0.8$.

IV. SIMULATION RESULTS

The proposed algorithm is expected to provide a better performance than the existing sparse adaptive beamforming algorithms [5, 8]. To evaluate its performance, several numerical simulations are carried out. The SOI as well as the interferences are QPSK signals from the azimuth of 90° , 30° , 58° , 127° and 163° , respectively, with an identical elevation angle of 45° . The signals are received by a rectangular array (RA) which contains 100 antenna elements with 10 rows and 10 columns. The signal-to-noise ratio (SNR) is set to 30 dB and the initialized convergence factor for L_1 -WCNLMS, RL_1 -CNLMS, CNLMS and PNL-CNLMS are 5×10^{-3} , 2×10^{-2} , 5×10^{-3} and 7×10^{-3} , respectively. The constraint factor z is selected as 0.8 uniformly. The iteration index is 6×10^3 , while ϵ_{p-like} is equal to 5×10^{-3} .

Figure 3 depicts the comparison of beam patterns. All the algorithms can form a main lobe in the direction of SOI and generate nulls to attenuate interferences which are similar with that of the non-sparse classical CNLMS beamforming algorithm. Nevertheless, the side lobe level (SLL) for the proposed PNL-CNLMS algorithm as well as the L_1 -WCNLMS and RL_1 -CNLMS algorithms are a little higher than the CNLMS algorithm. However, the proposed new algorithm shows lower SLL against the existing sparse adaptive beamforming algorithms. It is found that for $p=0.7$ and $p=0.8$, the proposed algorithm shows a better balance between array sparsity and beampattern performance.

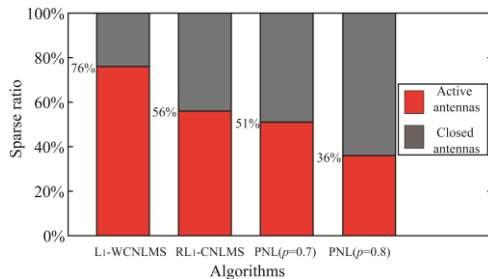


Fig. 5. Final sparse array ratio for the algorithms presented in Fig. 3 and Fig. 4.

Figure 4 illustrates the final thinned sensor array obtained by the proposed PNL-CNLMS algorithm and the existing adaptive sparse beamforming algorithms [5, 8]. In this paper, sparse ratio is defined as the percentage of active antenna elements taking account of the total antenna elements. The final sparse ratio is provided in Fig. 5. The figures indicate that all the algorithms hold the ability for realizing sparse adaptive beamforming. Nevertheless, the proposed algorithm can exploit a higher sparse level, it has a better performance in terms of beampattern in comparison with the existing algorithms, though the proposed algorithm has a better performance. This is because that the p -norm-like

diversity measure can effectively exploit the sparse characteristic than the L_1 -norm and the reweighted L_1 -norm. In addition, simulation results reveal that there is no particular correlation between parameter p and the sparsity of the antenna array. In a word, our proposed adaptive beamformer can turn off the trivial antenna elements in order to reduce the power supply and keep a similar performance in the RA beamforming.

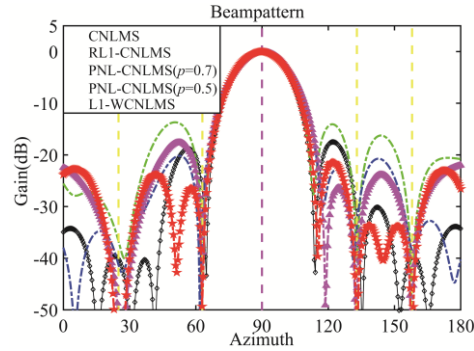


Fig. 6. Beampatterns of the proposed algorithms versus the CNLMS algorithm and the existing algorithms in [5, 8]. Purple line is the SOI, yellow lines are interferences.

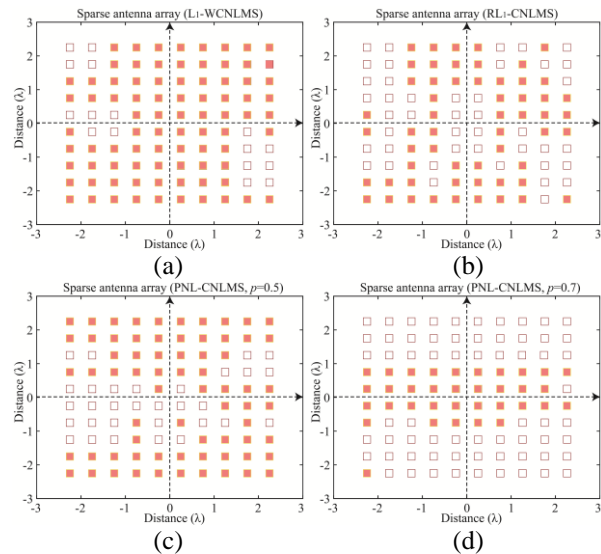


Fig. 7. Sparse arrays thinned by the proposed algorithms and the algorithm developed in [5]: (a) L_1 -WCNLMS in [5], (b) RL_1 -CNLMS algorithm in [8], (c) PNL-CNLMS algorithm with $p=0.5$, and (d) PNL-CNLMS algorithm with $p=0.7$.

Herein, to verify the effectiveness of the proposed algorithm, another example is presented. In this case, the directions of signals are 25° , 63° , 90° , 133° , and 158° , respectively. The elevation is set as 30° . $p=0.5$ and $p=0.7$ are selected, while other parameters are consistent with the first example. Figure 6 depicts the

beampatterns of the proposed algorithm and other related sparse beamforming algorithms. The finalized sparse array is illustrated in Fig. 7. In this example, the proposed algorithm can get the ideal beampattern based a sparse array. What's more, it is clearly seen that the proposed PNL-CNLMS algorithm can provide a compromise between beampattern and array sparsity.

V. CONCLUSION

In this paper, a p -norm-like constraint normalized least mean square (PNL-CNLMS) algorithm is proposed for sparse adaptive beamforming. Two experiments are provided in the simulation to discuss the performance of the proposed algorithm. The proposed PNL-CNLMS algorithm can provide a similar beampattern with that of the conventional non-sparse adaptive beamforming algorithm using less antenna elements. For the sake of comparison with the existing sparse adaptive beamforming algorithms, the proposed PNL-CNLMS algorithm has a better beamforming performance and provides higher sparse level, which verifies the superiority of the proposed algorithm. Besides, by adjusting the parameter p , a trade-off between beampattern and sparse array is achieved. Still, the proposed algorithm shows potential to be further improved, e.g., reduce the SLL. What's more, the convergence rate for the proposed algorithm can be improved if a variable parameter p is employed, and the task is how to exploit the sparsity. In the future, the proposed algorithm can be further developed under impulsive noise and it can be used for MIMO antenna arrays [27-34].

ACKNOWLEDGMENT

This work was partially supported by the National Key Research and Development Program of China (2016YFE111100), Key Research and Development Program of Heilongjiang (GX17A016), the Science and Technology innovative Talents Foundation of Harbin (2016RAXXJ044), the Natural Science Foundation of Beijing (4182077), China Postdoctoral Science Foundation (2017M620918 and 2019T120134), the Ph.D. Student Research and Innovation Fund of the Fundamental Research Funds for the Central Universities (3072019GIP0808), the Fundamental Research Funds for the Central University (HEUCFG201829 and 2072019CFG0801), and Natural Science Foundation of Heilongjiang Province, China (F2017004).

REFERENCES

- [1] H. L. Van Trees, *Detection, Estimation, and Modulation Theory, Part IV: Optimum Array Processing*, John Wiley & Sons, New York, NY, 2002.
- [2] J. Li and P. Stoica (Eds.), *Robust Adaptive Beamforming*, John Wiley & Sons, New York, NY, 2005.
- [3] O. L. Frost III, "An algorithm for linearly constrained adaptive array processing," *Proc. IEEE*, vol. 60, no. 8, pp. 926-935, Aug. 1972.
- [4] J. A. Apolinário, Jr., S. Werner, P. S. R. Diniz, and T. I. Laakso, "Constrained normalized adaptive filtering for CDMA mobile communications," *IEEE Signal Processing Conference*, Rhodes, Greece, Sept. 1998.
- [5] J. F. de Andrade, M. L. R. de Campos, and J. A. Apolinário, " L_1 -constrained normalized LMS algorithms for adaptive beamforming," *IEEE Transactions on Signal Processing*, vol. 63, no. 24, pp. 6524-6539, Dec. 2015.
- [6] W. Shi, Y. Li, and S. Luo, "Adaptive antenna array beamforming based on norm penalized NLMS algorithm," *2018 IEEE International Symposium on Antennas and Propagation and USNC-URSI Radio Science Meeting*, in press, Boston, America, July 2018.
- [7] W. Shi and Y. Li, "Norm-constrained NLMS for sparse controllable adaptive array beamforming," *2018 International Applied Computational Electromagnetics Society Symposium*, in press, Beijing, China, July 2018.
- [8] W. Shi, Y. Li, and J. Yin, "Improved constraint NLMS algorithm for sparse adaptive array beamforming control applications," *Applied Computational Electromagnetics Society Journal*, Accepted, Mar. 2019.
- [9] W. Shi, Y. Li, L. Zhao, and X. Liu, "Controllable sparse antenna array for adaptive beamforming," *IEEE Access*, vol. 7, pp. 6412-6423, Jan. 2019.
- [10] D. L. Donoho, "Compressed sensing," *IEEE Trans. Inf. Theory*, vol. 52, no. 4, pp. 1289-1306, Apr. 2006.
- [11] R. Tibshirani, "Regression shrinkage and selection via the lasso," *J. R. Stat. Soc. Ser. B-Stat. Methodol.*, vol. 58, no. 1, pp. 267-288, Jan. 1996.
- [12] Y. Chen, Y. Gu, and A. O. Hero, "Sparse LMS for system identification," *Proc. IEEE International Conference on Acoustic Speech and Signal Processing*, (ICASSP'09), pp. 3125-3128, Taipei, Taiwan, Apr. 2009.
- [13] O. Taheri and S. A. Vorobyov, "Sparse channel estimation with L_p -norm and reweighted L_1 -norm penalized least mean squares," *IEEE International Conference on Acoustic Speech and Signal Processing (ICASSP'11)*, pp. 2864-2867, Prague, Czech Republic, May 2011.
- [14] Y. Li, Z. Jiang, O. M. Omer-Osman, X. Han, and J. Yin, "Mixed norm constrained sparse APA algorithm for satellite and network echo channel estimation," *IEEE Access*, vol. 6, pp. 65901-65908, 2018.
- [15] W. Shi, Y. Li, and Y. Wang, "Noise-free

- maximum correntropy criterion algorithm in non-gaussian environment,” *IEEE Transactions on Circuits and Systems II: Express Briefs*, 10.1109/TCSII.2019.2914511, 2019.
- [16] Y. Gu, J. Jin, and S. Mei, “ l_0 -norm constraint LMS algorithm for sparse system identification,” *IEEE Signal Process. Lett.*, vol. 16, no. 9, pp. 774-777, 10.1109/LSP.2009.2024736, Sept. 2009.
- [17] Y. Li, Y. Wang, R. Yang, et al., “A soft parameter function penalized normalized maximum correntropy criterion algorithm for sparse system identification,” *Entropy*, vol. 19, no. 1, p. 45, 10.3390/e19010045, Jan. 2017.
- [18] Y. Li, Z. Jiang, W. Shi, X. Han, and B. Chen, “Blocked maximum correntropy criterion algorithm for cluster-sparse system identifications,” *IEEE Transactions on Circuits and Systems II: Express Briefs*, 10.1109/TCSII.2019.2891654, 2019.
- [19] D. Angelosante, J. A. Bazerque, and G. B. Giannakis, “Online adaptive estimation of sparse signals: Where RLS meets the l_1 -norm,” *IEEE Transactions on Signal Processing*, vol. 58, no. 7, pp. 3436-3447, Mar. 2010.
- [20] O. Taheri and S. A. Vorobyov, “Reweighted l_1 -norm penalized LMS for sparse channel estimation and its analysis,” *Elsevier Signal Processing*, vol. 104, pp. 70-79, May 2014.
- [21] Y. Li, Y. Wang, and T. Jiang, “Sparse-aware set-membership NLMS algorithms and their application for sparse channel estimation and echo cancelation,” *AEU - International Journal of Electronics and Communications*, vol. 70, no. 7, pp. 895-902, 2016.
- [22] Y. Li, Y. Wang, and T. Jiang, “Norm-adaption penalized least mean square/fourth algorithm for sparse channel estimation,” *Signal Processing*, vol. 128, pp. 243-251, Nov. 2016.
- [23] I. S. Caballero, C. J. P. Prieto, and A. A. Rodriguez, “Sparse deconvolution using adaptive mixed-Gaussian models,” *Signal Processing*, vol. 54, no. 2, pp. 161-172, Oct. 1996.
- [24] B. D. Rao and K. K. Delgado, “An affine scaling methodology for best basis selection,” *IEEE Transactions on Signal Processing*, vol. 47, no. 1, pp. 187-200, 1999.
- [25] F. Wu and F. Tong, “Gradient optimization p-norm-like constraint LMS algorithm for sparse system estimation,” *Signal Processing*, vol. 93, no. 4, pp. 967-971, Apr. 2013.
- [26] P. S. R. Diniz, *Adaptive Filtering: Algorithms and Practical Implementation*, New York, USA: Springer, 2010.
- [27] Q. Wu, Y. Li, Y. Zakharov, W. Xue, and W. Shi, “A kernel affine projection-like algorithm in reproducing kernel hilbert space,” *IEEE Transactions on Circuits and Systems II: Express Briefs*, 10.1109/TCSII.2019.2947317, 2019.
- [28] X. Zhang, T. Jiang, Y. Li, and X. Liu, “An off-grid DOA estimation method using proximal splitting and successive nonconvex sparsity approximation,” *IEEE Access*, vol. 7, pp. 66764-66773, 2019.
- [29] X. Zhang, T. Jiang, Y. Li, and Y. Zakharov, “A novel block sparse reconstruction method for DOA estimation with unknown mutual coupling,” *IEEE Communications Letters*, vol. 23, no. 10, pp. 1845-1848, 2019.
- [30] F. Liu, J. Guo, L. Zhao, G. L. Huang, Y. Li, and Y. Yin, “Dual-band metasurface-based decoupling method for two closely packed dual-band antennas,” *IEEE Transactions on Antennas and Propagation*, 10.1109/TAP.2019.2940316, 2019.
- [31] J. Guo, F. Liu, L. Zhao, Y. Yin, G. L. Huang, and Y. Li, “Meta-surface antenna array decoupling designs for two linear polarized antennas coupled in H-Plane and E-Plane,” *IEEE Access*, vol. 7, pp. 100442-100452, 2019.
- [32] S. Luo, Y. Li, Y. Xia, and L. Zhang, “A low mutual coupling antenna array with gain enhancement using metamaterial loading and neutralization line structure,” *Applied Computational Electromagnetics Society Journal*, vol. 34, no. 3, pp. 411-418, 2019.
- [33] S. Luo, Y. Li, C. Y. D. Sim, Y. Xia, and X. Liu, “MIMO antenna array based on metamaterial frequency selective surface,” *International Journal of RF and Microwave Computer-Aided Engineering*, Submitted, 2019.
- [34] T. Jiang, T. Jiao, and Y. Li, “A low mutual coupling MIMO antenna using periodic multi-layered electromagnetic band gap structures,” *Applied Computational Electromagnetics Society Journal*, vol. 33, no. 3, 2018.

Efficient Wideband MRCS Simulation for Radar HRRP Target Recognition Based on MSIB and PCA

Yunqin Hu* and Ting Wan

Department of Communication Engineering
Nanjing University of Posts and Telecommunications, Nanjing, 210009, China

*huyq@njupt.edu.cn

Abstract — In this paper, efficient wideband monostatic radar cross-section (MRCS) simulation is presented for radar high range resolution profile (HRRP) target recognition. Firstly, an efficient numerical approach is proposed for the wideband MRCS. The well-conditioned integral equation and the higher-order hierarchical divergence-conforming vector basis functions are utilized for the scattering field. The adaptive cross approximation (ACA) based matrix compression method is applied for efficient analysis of MRCS at a specific frequency point. The geometric theory of diffraction (GTD) based scattering model is utilized for MRCS over a wide frequency band. Secondly, the radar HRRP target identification is performed by using principal component analysis (PCA) on modified surrounding-line integral bispectrum (MSIB). The HRRP of target can be obtained by inverse fast Fourier transform (IFFT) of the spectral domain backscattering field within a certain frequency range. The one-dimensional MSIB features of HRRP are extracted to constitute eigenvectors for radar target recognition. To enhance the separation ability of radar target recognition, the MSIB is projected onto PCA space before recognition. Numerical examples prove that the proposed algorithm is feasible and efficient.

Index Terms — Adaptive cross approximation, geometric theory of diffraction, high range resolution profile, modified surrounding-line integral bispectrum, principal component analysis.

I. INTRODUCTION

The high range resolution profile (HRRP) carries information of target scattering centers distribution along the radar line-of-sight, reflecting details of target structure such as scatter centers' strength, scatter centers' position, target size, and so on. These target features have been shown to be highly discriminative. HRRP based radar target recognition has received extensive attention and research [1-3].

In the field of non-cooperative radar HRRP target recognition, various computational electromagnetics algorithms have been widely used in the prediction of

scattered electromagnetic fields of actual targets. Frequency domain surface integral equation (SIE) by the method of moments (MoM) is a powerful tool in full wave electromagnetic simulation, since it does not need to handle the absorbing boundary conditions and its computational domain is taken on the surface of the target. Most of the existing fast methods for surface integral equations, such as the multilevel fast multipole algorithm (MLFMA) [4], are based on the fact that when unknowns N are grouped in local spatial regions, the resulting blocks of the system impedance matrix \mathbf{Z} are rank deficient. It is noteworthy that in radar HRRP target recognition, the wideband monostatic radar cross-section (MRCS) must be simulated. Since the scattering field depends on both frequency and incident angle, most of the available iterative algorithms must be run at each incident angle and frequency point many times. Obviously, the repeated solution of linear systems is time-consuming and expensive.

Many efforts have been done to accelerate the wideband MRCS simulation. For monostatic scattering at a specific sample frequency point, two classes of methods are mainly studied. One is the interpolation method, including the asymptotic waveform evaluation (AWE) technique [5,6] and the cubic-spline method [7]. The other is the matrix compression method. When unknowns are spatially grouped, the rank deficient interaction submatrices between well-separated groups can be well approximated as the outer product of two lower rank matrices. For monostatic scattering, where there are many right-hand sides (RHS), the blocked RHS can be also well approximated by this low rank outer product form where each outer product approximant is computed using the adaptive cross approximation (ACA) [8]. For wideband scattering analysis, impedance matrix interpolation [9], asymptotic waveform evaluation (AWE) technique [10] and Taylor expansion based method [11] are studied to reduce the total simulation time.

The HRRP of target can be obtained by inverse fast Fourier transform (IFFT) to the simulated wideband MRCS. However, due to the shift sensitivity, the

translation invariance features reflecting the essential features of HRRP must be extracted from the original data before recognition. Fortunately, the bispectrum of HRRP has translation invariance while maintaining phase information and suppressing the additive white Gaussian noise (AWGN). However, using the bispectrum features for target recognition is inefficient, because it is a two-dimensional function and its data amount is the square of HRRP's. Many integral bispectrum methods have been developed to convert a bispectrum from two-dimensional to one-dimensional, including radially integrated bispectra (RIB) [12], axially integrated bispectra (AIB) [13], circularly integrated bispectra (CIB) [14] and surrounding-line integral bispectrum (SIB) [15]. Compared with the others, SIB is more preferred because its integration path contains all the information of bispectrum, with no missing or reusing any bispectrum information, and avoids any interpolation in the integration process. By choosing integral paths exactly consistent with the bispectrum symmetry, the modified surrounding-line integral bispectrum (MSIB) has less computational complexity than SIB [16].

This paper is organized as follows. In Section II, an efficient numerical approach is proposed for wideband MRCS. Firstly, the well-conditioned integral equation and the novel higher-order hierarchical divergence-conforming vector basis functions are utilized for efficient analysis of electromagnetic scattering. Then, the matrix compression method based on ACA and the scattering model based on the geometric theory of diffraction (GTD) are employed to improve the simulation efficiency of wideband MRCS. In Section III, the MSIB features of HRRP are extracted to constitute eigenvectors for target identification. To enhance the separation ability of radar target recognition, the MSIB features are projected onto the PCA space before recognition. Numerical simulations are used to demonstrate the feasibility and effectiveness of the approach in Section IV. Finally, the conclusion is given in Section V.

II. ANALYSIS OF WIDEBAND MRCS

A. Integral equation and basis function

The combined field integral equation (CFIE) has been used extensively for conducting bodies. For a homogenous dielectric object, the Poggio-Miller-Chang-Harrington-Wu-Tsai (PMCHWT) [17] formulation is widely used, because it can yield an accurate solution without the interior resonance corruption. However, PMCHWT suffers from poor convergence problems [18]. In this paper, the electric-magnetic current combined-field integral equation (JMCFIE) which provides better conditioned system matrix for iterative solution is utilized to analyze electromagnetic scattering from a homogeneous dielectric target.

Using the equivalence principle, the homogeneous dielectric scattering problem can be solved by considering two simple equivalent problems, an external equivalent problem in the free space denoted by D_1 and an internal equivalent problem in the unbounded homogeneous dielectric domain D_2 characterized by $(\epsilon_r, \mu_r, \sigma_r)$. Let \mathbf{n}_l denote the unit normal of the object surface pointing into domain D_l . A set of integral equations can be formulated for each equivalent problem. For the exterior equivalent problem, they are the electric field integral equation (EFIE) and the magnetic field integral equation (MFIE), denoted as EFIE_1 and MFIE_1 . For the internal equivalent problem, the integral equations for electric and magnetic field are denoted as EFIE_2 and MFIE_2 [19, 20]. In PMCHWT formulation, the EFIE_1 is combined with the EFIE_2 to form a combined equation. Similarly, the MFIE_1 is combined with the MFIE_2 to form another combined equation.

The well-conditioned JMCFIE formulation can be established by combining the interior and exterior equivalent problems as the following form [21]:

$$\begin{cases} \frac{1}{\eta_1} \text{EFIE}_1 + \mathbf{n}_1 \times \text{MFIE}_1 + \frac{1}{\eta_2} \text{EFIE}_2 + \mathbf{n}_2 \times \text{MFIE}_2 \\ -\mathbf{n}_1 \times \text{EFIE}_1 + \eta_1 \text{MFIE}_1 - \mathbf{n}_2 \times \text{EFIE}_2 + \eta_2 \text{MFIE}_2 \end{cases}, \quad (1)$$

where $\eta_l = \sqrt{\mu_l / \epsilon_l}$ ($l=1,2$).

In terms of the geometrical modeling and current discretization, traditional methods are low-order techniques using plane triangle patches and low-order basis functions, such as the Rao-Wilton-Glisson basis function (RWG). For electrically large size problems, the accuracy of solutions obtained by low-order techniques can only be improved slowly with the increase of unknowns, thus, the number of unknowns will be very large inevitably. To resolve such problems, the higher-order hierarchical divergence-conforming vector basis functions defined on curved triangular patches are used in this paper.

First, choose the curve Rao-Wilton-Glisson basis function (CRWG) as the lowest-order (order-0.5) divergence-conforming basis function. It can be expressed in normalized area coordinates (ξ_1, ξ_2, ξ_3) as:

$$\begin{aligned} \mathbf{f}_{1,0}^e(\mathbf{r}) &= \frac{1}{J} \left[(\xi_1 - 1) \frac{\partial \mathbf{r}}{\partial \xi_1} + \xi_2 \frac{\partial \mathbf{r}}{\partial \xi_2} \right] \\ \mathbf{f}_{2,0}^e(\mathbf{r}) &= \frac{1}{J} \left[\xi_1 \frac{\partial \mathbf{r}}{\partial \xi_1} + (\xi_2 - 1) \frac{\partial \mathbf{r}}{\partial \xi_2} \right] \\ \mathbf{f}_{3,0}^e(\mathbf{r}) &= \frac{1}{J} \left[\xi_1 \frac{\partial \mathbf{r}}{\partial \xi_1} + \xi_2 \frac{\partial \mathbf{r}}{\partial \xi_2} \right], \end{aligned} \quad (2)$$

where J is the element Jacobian and \mathbf{r} is the position vector of the point determined by normalized face coordinates on curved parametric triangular patch.

The novel higher-order bases are constructed by multiplying the corresponding order new orthogonal scalar polynomials with the lowest order bases [22, 23]. The order of basis function is 0.5 higher than that of polynomials. Without loss of generality, we consider basis functions associated with edge 1. The edge-based basis functions of order-3.5 associated with edge 1 can be expressed as:

$$\begin{aligned}\mathbf{f}_{1,1}^e(\mathbf{r}) &= \sqrt{3}(\xi_2 - \xi_3)\mathbf{f}_{1,0}^e(\mathbf{r}) \\ \mathbf{f}_{1,2}^e(\mathbf{r}) &= \frac{\sqrt{5}}{2}\left[3(\xi_2 - \xi_3)^2 - 1\right]\mathbf{f}_{1,0}^e(\mathbf{r}) \\ \mathbf{f}_{1,3}^e(\mathbf{r}) &= \frac{\sqrt{7}}{2}\left[5(\xi_2 - \xi_3)^3 - 3(\xi_2 - \xi_3)\right]\mathbf{f}_{1,0}^e(\mathbf{r}).\end{aligned}\quad (3)$$

As in Formula (2), the superscript of $\mathbf{f}_{i,j}^e$ denotes edge-based, the subscript i denotes the number of the edge and j denotes the order of hierarchical polynomials.

The face-based basis functions of order-3.5 associated with edge 1 can be expressed as:

$$\begin{aligned}\mathbf{f}_{1,01}^f(\mathbf{r}) &= 2\sqrt{3}\xi_1\mathbf{f}_{1,0}^e(\mathbf{r}) \\ \mathbf{f}_{1,02}^f(\mathbf{r}) &= 2\sqrt{3}\xi_1(5\xi_1 - 3)\mathbf{f}_{1,0}^e(\mathbf{r}) \\ \mathbf{f}_{1,11}^f(\mathbf{r}) &= 6\sqrt{5}\xi_1(\xi_2 - \xi_3)\xi_1\mathbf{f}_{1,0}^e(\mathbf{r}) \\ \mathbf{f}_{1,03}^f(\mathbf{r}) &= 2\sqrt{30}\xi_1(2 - 8\xi_1 + 7\xi_1^2)\mathbf{f}_{1,0}^e(\mathbf{r}) \\ \mathbf{f}_{1,12}^f(\mathbf{r}) &= 2\sqrt{30}(\xi_2 - \xi_3)\xi_1(7\xi_1 - 3)\mathbf{f}_{1,0}^e(\mathbf{r}) \\ \mathbf{f}_{1,21}^f(\mathbf{r}) &= 2\sqrt{210}(\xi_2^2 - 4\xi_2\xi_3 + \xi_3^2)\xi_1\mathbf{f}_{1,0}^e(\mathbf{r}).\end{aligned}\quad (4)$$

The superscript of $\mathbf{f}_{i,m}^f$ denotes face-based, the first subscript i denotes the number of the edge, and the sum of two digits of the second subscript is equal to the order of the polynomial.

The edge-based and face-based basis functions associated with edge 2 and edge 3 can be obtained by rotating the coordinates, $\xi_1 \rightarrow \xi_2 \rightarrow \xi_3 \rightarrow \xi_1$ in (3) and (4), and then multiplying the corresponding lowest-order basis in (2). Note that one of the three subsets of face-based functions should be discarded since a 2-D triangle element can have only two independent tangent vectors. The hierarchical divergence-conforming vector basis functions of order-3.5 include the vector basis functions of order-2.5 and order-1.5.

After expanding the equivalent surface current densities with the higher-order hierarchical divergence-conforming vector basis functions and using the Galerkin's testing procedure, the integral equation can be well tested leading to a matrix equation:

$$\mathbf{A} \cdot \mathbf{x} = \mathbf{b}, \quad (5)$$

where \mathbf{A} is the impedance matrix, \mathbf{x} is the unknown coefficient vector of the basis function, \mathbf{b} is the excitation vector generated by the incident wave.

Comparing with the low-order techniques, the

novel higher order hierarchical divergence-conforming vector basis function can greatly reduce the number of unknowns for a given problem. To reduce the memory requirement and computational complexity of MoM, the MLFMA is employed to complete the matrix-vector product of each iteration step. The FMM box size must be chosen to be a little bit larger than the average patch size [24].

B. ACA for MRCS

Iterative solvers may be quite satisfactory for only a few RHS such as bistatic problems, but for monostatic scattering with many required sampling angles, this part of the problem becomes expensive, because iterative solvers must be used to compute current solutions for each RHS excitation vector.

For analyzing the MRCS at a given operating frequency, the impedance matrix remains the same, whereas the RHS vector should be updated at each incident angle. The MRCS problem can be expressed in the following matrix form:

$$\mathbf{A} \cdot \mathbf{X} = \mathbf{B}, \quad (6)$$

where $\mathbf{B}=[\mathbf{b}_1, \mathbf{b}_2, \dots, \mathbf{b}_M,]$, $\mathbf{X}=[\mathbf{x}_1, \mathbf{x}_2, \dots, \mathbf{x}_M,]$ and M is the number of incident angles.

Like the impedance matrix, the blocked RHS is also low rank and can be compressed by the ACA method. Readers can see [8] for Bebendorf's ACA details. By using ACA, the blocked RHS can be approximated using low rank representations:

$$\mathbf{B} \approx \mathbf{U}_{ACA} \cdot \mathbf{V}_{ACA}. \quad (7)$$

The dimension of matrices \mathbf{U}_{ACA} and \mathbf{V}_{ACA} are $N \times k$ and $M \times k$, respectively. Generally, k is much smaller than M . By substituting (7) into (6), the linear equations can be rewritten as:

$$\mathbf{X} \approx (\mathbf{A}^{-1} \cdot \mathbf{U}_{ACA}) \cdot \mathbf{V}_{ACA}^H. \quad (8)$$

The iterative solution of linear equations $\mathbf{A}^{-1} \cdot \mathbf{U}_{ACA}$ is required at each principle eigenvectors. Compared with solving linear equations at each angle repeatedly, the ACA method is able to greatly reduce the computation time. The computational complexity of ACA is $k^2(N+M)$ and the memory requirement is $k(N+M)$.

C. GTD-based scattering model for wideband MRCS

In radar HRRP target recognition, MRCS must be simulated at multiple frequency sampling points over wideband. Since the impedance matrix depends on frequency, the above electromagnetic algorithm must be repeated at each frequency point. To improve simulation efficiency, a parametric scattering model based on the GTD is utilized for fast analysis of the scattered field over a wide frequency band.

In GTD method [25], the backscattering from a target, which can be modeled as a collection of ideal scattering centers, can be approximated as:

$$E^{sca}(f) = \sum_{m=1}^M b_m \left(j \frac{f}{f_c} \right)^{\alpha_m} e^{-j \frac{4\pi}{c} f r_m}, \quad (9)$$

where, M denotes the order of the model; b_m and r_m denotes the complex scattering amplitude and vertical distance of the m th scattering center; f_c is the center frequency of the test band; α_m is an integer multiple of 0.5, which reflects the scattering mechanism of the scattering center.

For real targets, when data are collected over a very narrow angular window, (9) still provides a very compact way to model their backscattering. However, when data collected over a broad angular window, if we want to model a complex target as a summation of ideal scattering centers, we have to use a different set of scattering centers for each different observation angle. The backscattering can be approximated as the summation of point scatterers multiplied by their respective aspect-dependent amplitude functions [26]:

$$E^{sca}(f, \theta, \varphi) = \sum_{m=1}^M b_m(\theta, \varphi) \left(j \frac{f}{f_c} \right)^{\alpha_m} e^{-j \frac{4\pi}{c} f r_m}. \quad (10)$$

The amplitude function $b_m(\theta, \varphi)$ for each scattering center accounts for angular dependence and must be stored. The parameters of GTD scattering center model can be extracted from the scattered field at partial sampling frequency points by using the matrix pencil method [27].

III. TARGET RECOGNITION BASED ON MSIB AND PCA

Suppose that the spectral backscatter field of N_F sampling frequency points at a specific sampling angle can be expressed as $\mathbf{X} = [X(1), X(2), \dots, X(N_F)]^T$. The HRRP can be obtained by IFFT:

$$\mathbf{x} = [x(1), x(2), \dots, x(N_F)]^T, \quad (11)$$

$$\mathbf{x}(n) = \text{IFFT}[\mathbf{X}(n)], \quad n = 1, 2, \dots, N_F. \quad (12)$$

The bispectrum of HRRP is defined as the Fourier transform of the third-order cumulant of HRRP sequence:

$$B(\omega_1, \omega_2) = X(\omega_1) X(\omega_2) X^*(\omega_1 + \omega_2), \quad (13)$$

$$X(\omega) = \sum_{\tau=-\infty}^{\infty} x(\tau) \exp(-j\omega\tau). \quad (14)$$

The bispectrum is translation invariant, while maintaining the phase information and inhibiting the AWGN theoretically. However, bispectrum is a two-dimensional function and its data amount is the square of HRRP's. If the two-dimensional bispectrum features is directly used in target recognition, a large amount of memory is needed for the target template library. In addition, the bispectrum has great information redundancy.

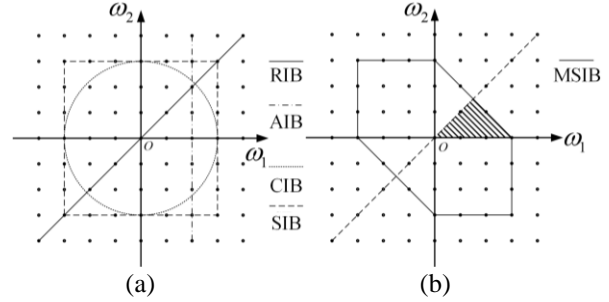


Fig. 1. Integral path of the different integrated bispectra: (a) RIB, AIB, CIB, SIB, and (b) MSIB.

To decrease the computational complexity of target recognition, many different integral bispectrum methods have been developed to convert a bispectrum from two-dimensional to one-dimensional. According to the integral path, four kinds of integral bispectrum are shown in Fig. 1 (a), with each point represents a value of bispectrum. The calculation of the integral bispectrum can be simplified by using the bispectrum symmetry.

According to the periodicity and symmetry of bispectrum, bispectrum in $0 \leq \omega_1 \leq \omega_2 \leq \omega_1 + \omega_2 \leq \pi$ contains all the information. As shown in Fig. 1 (b), the MSIB integrates along a closed hexagons centered at the origin. The MSIB does not omit or reuse any bispectrum values, so as to ensure that important information can be obtained for target recognition. The MSIB expression is:

$$\text{MSIB}(s) = \sum_{R_s} B(\omega_1, \omega_2), \quad s = 1, 2, \dots, m, \quad (15)$$

where R_s is an integral path and m is the total number of integral paths. Because the path of integration completely conforms to the bispectrum symmetry, it only needs to integrate along the section within the shaded area. This makes the time of extracting integral bispectrum features significantly saved.

Suppose the total number of targets is C . By simulating the backscattering responses of each target at n_c sampling angles, n_c training samples of MSIB will be obtained for target c , $c = 1, 2, \dots, C$. The training samples of these targets form a MSIB database $\mathbf{X} = \{\mathbf{x}_1, \dots, \mathbf{x}_i, \dots, \mathbf{x}_N\}$, where \mathbf{x}_i represents a MSIB vector of some target. The total number of training samples is $N = \sum_{c=1}^C n_c$. The MSIB can be used as feature vectors of targets, but bispectrums on many integration paths may be redundant, and some are even baneful for target classification.

The PCA is utilized to reduce the redundant information and the feature space dimension of MSIB before recognition [28]. PCA seeks the most expressive features for well representing different classes with minimum mean square error. The mean vector and the

covariant matrix of the training samples are defined as:

$$\boldsymbol{\mu} = \frac{1}{N} \sum_{n=1}^N \mathbf{x}_n, \quad (16)$$

$$\mathbf{C} = \frac{1}{N} \sum_{n=1}^N (\mathbf{x}_n - \boldsymbol{\mu}) \cdot (\mathbf{x}_n - \boldsymbol{\mu})^T, \quad (17)$$

where ‘ T ’ denotes the transpose. Then, compute the eigenvalue equation of the covariance matrix:

$$\mathbf{C}\mathbf{p} = \lambda\mathbf{p}. \quad (18)$$

Assume that the eigenvalues are arranged from maximum to minimum, $\lambda_1 \geq \lambda_2 \geq \dots \geq \lambda_m \geq 0$, and the corresponding eigenvectors are $\mathbf{p}_1, \mathbf{p}_2, \dots, \mathbf{p}_m$. The transformed matrix is constituted with the eigenvectors corresponding to the previous n_{PCA} eigenvalues:

$$\mathbf{A} = (\mathbf{p}_1, \mathbf{p}_2, \dots, \mathbf{p}_{n_{\text{PCA}}})^T, \quad n_{\text{PCA}} < m. \quad (19)$$

Each MSIB vector can be projected onto the n_{PCA} -dimensional PCA space by the following formula:

$$\mathbf{y}_i = \mathbf{A}(\mathbf{x}_i - \boldsymbol{\mu}). \quad (20)$$

In this way, the dimension of the MSIB vectors is decreased to n_{PCA} . Then, the radar recognition is performed by the maximal correlate coefficient template marching method (MCC-TMM) on the low-dimensional PCA space. The recognition accuracy depends on n_{PCA} . Generally, the larger the n_{PCA} , the higher the recognition accuracy, but there is no optimum selection rule to maximize the probability of correct recognition while retaining a small value [29]. This will be discussed in the next section.

IV. NUMERICAL SIMULATION

In this section, numerical examples are given to verify the valid and efficiency of the proposed method. In all examples, the inner-outer Flexible Generalized Minimal Residual (FGMRES) method is used for the iterative solution, where the inner and outer restart numbers are both taken to be 10, and the stop precision for the inner and outer iteration is 1.E-2 and 1.E-4, respectively.

Firstly, the accuracy and validity of the well-conditioned integral equation combined with the novel higher-order hierarchical divergence-conforming vector basis functions and the MLFMA are verified by a dielectrically coated warhead model ($\epsilon_r = 2.0$), as shown in Fig. 2. The incident plane wave is 3GHz and the incident angles are $\theta_i = 0^\circ$, $\phi_i = 0^\circ$. For composite conducting and dielectric object, the CFIE on the conductor surface and the JMCIE on the dielectric surface are combined, noted as JMCIE-CFIE. The novel higher-order hierarchical divergence-conforming vector basis functions and the MLFMA are utilized for efficient analysis. Corresponding to order-1.5, order-2.5 and order-3.5 hierarchical bases, 46390, 38598 and 35712 unknowns are generated from curvilinear triangular patches discretization, respectively. The bistatic RCS for

$\hat{\phi}\hat{\phi}$ -polarization at $\phi_s = 0^\circ$ is computed and compared with low-order RWG method. As shown in Fig. 3, there is an excellent agreement between novel higher-order bases and RWG bases.

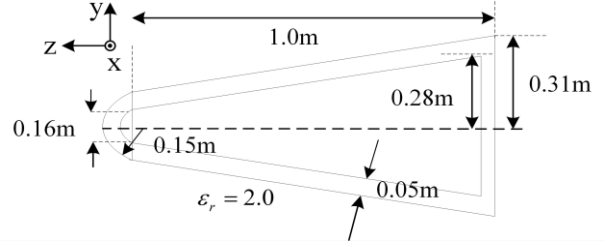


Fig. 2. Geometrical models for a dielectrically coated warhead.

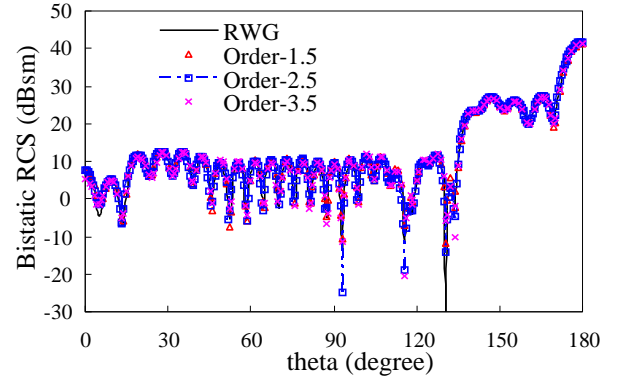


Fig. 3. Bistatic RCS for $\hat{\phi}\hat{\phi}$ -polarization of a dielectrically coated warhead at 3 GHz, with the RWG basis functions, order-1.5, order-2.5 and order-3.5 hierarchical basis functions.

Table 1: Memory requirements of MLFMA with different bases for dielectrically coated warhead

Bases	RWG	Order-1.5	Order-2.5	Order-3.5
Patch size (λ)	0.1	0.5	0.8	1.06
Total unknowns	222,168	46,390	38,598	35,712
MoM memory (MB)	376,576	16,418	11,366	9,730
Box size (λ)	0.25	0.8	1.0	1.3
Near field memory (MB)	1384.5	662.2	750.2	1041.6
Far field memory (MB)	1047.2	713.3	903.0	1228.9
MLFMA memory (MB)	2431.7	1347.9	1653.2	2270.5

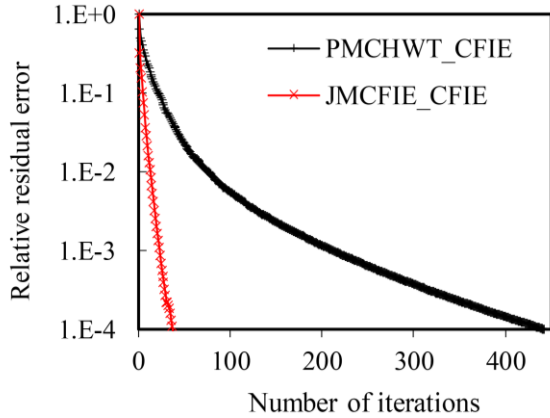


Fig. 4. Convergence histories of PMCHWT_CFIE and JMCFIE_CFIE solved with FGMRES for the dielectrically coated warhead.

The memory requirements of MLFMA are presented and compared between different bases in Table 1. With the increase of the order of higher-order basis functions, the total number of unknowns decreases, and the memory requirement of MoM greatly decreases, however, the near-field and far-field memory of MLFMA both increase. This is because, with the increase of the order of basis functions, the larger FMM box size is, and the larger the truncation term of MLFMA is, which leads to the low efficiency of MLFMA. After compromise consideration, order-1.5 and order-2.5 are more appropriate in the higher-order MLFMA. In the following numerical examples, the order of the hierarchical basis function is set to be 2.5. As shown in Fig. 4, the iterative convergence of JMCFIE-CFIE is plotted and compared with the traditional PMCHWT-CFIE. The latter needs 1829s and 444 iterative steps, while the former only needs 145s and 38 iterative steps. The result shows that the JMCFIE-CFIE has good iterative convergence characteristics.

Secondly, the accuracy and validity of the wideband MRCS algorithm are verified by a homogenous dielectric cylinder ($\epsilon_r = 2.0, \mu_r = 1.0$) of 2.5m length and 0.6m diameter. The incident plane wave is 5GHz. As shown in Fig. 5, the MRCS for $\hat{\theta}\hat{\theta}$ -polarization is computed by the ACA based matrix compression method and compared with direct solution at each incident angle by FEKO. It can be found there is an excellent agreement. For direct solution, the iterative solver must be used at each incident angle and the total number is 361. While, for the ACA based matrix compression method, the iteration solver is only used 21 times, since the number of columns in \mathbf{U}_{ACA} is 21. This demonstrates that the ACA based matrix compression method can efficiently analyze the MRCS problem. In this example, the amount of calculation has been reduced by about 17 times. As

shown in Fig. 6, the wideband backscattering for $\hat{\theta}\hat{\theta}$ -polarization of this dielectric cylinder is computed by the GTD-based scattering model and compared with the direct solution at each sampling frequency point by FEKO. Good agreement can be found between them. The backscattering is computed at 81 equal spaced frequencies from 0.1GHz to 0.5GHz in FEKO, while the number of sampling frequencies is 21 in the GTD-based scattering model. In this example, the amount of calculation has been reduced by about 4 times, and plenty of time is saved by using the GTD-based scattering model.

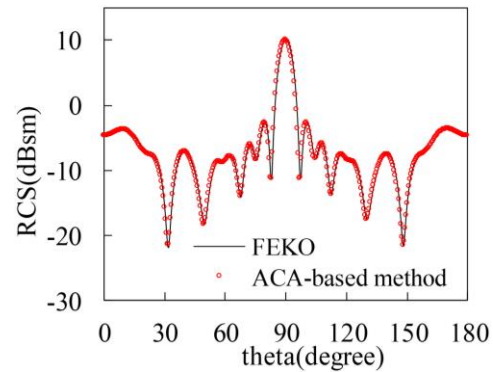


Fig. 5. MRCS for $\hat{\theta}\hat{\theta}$ -polarization of a dielectric cylinder ($\epsilon_r = 2.0, \mu_r = 1.0$) of 2.5m length and 0.6m diameter at 5GHz.

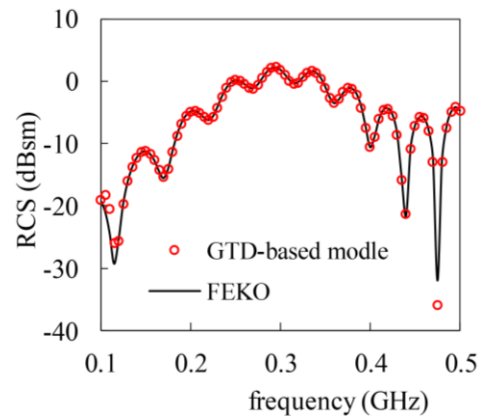


Fig. 6. Wideband MRCS for $\hat{\theta}\hat{\theta}$ -polarization of a dielectric cylinder ($\epsilon_r = 2.0, \mu_r = 1.0$) of 2.5m length and 0.6m diameter at $\theta = 0^\circ$.

Finally, numerical examples are given to verify the proposed radar recognition algorithm. Assume there are three known types of scaled aircraft models (i.e., $C=3$) including F15, F117 and VFY-218. The geometrical models and the geometry dimension for the three types of aircraft are shown in Fig. 7 and Table 2, respectively.

The $\hat{\theta}\hat{\theta}$ -polarization backscattering fields of these aircrafts are calculated by the proposed numerical approach in Section II. The elevation angle is fixed at 0° . The azimuth angle is changed continuously from 0° to 180° with an interval of 0.25° . At each azimuth angle, 161 frequency points from 1 to 5 GHz with a frequency step of 25 MHz are calculated. Thus, there are 721 HRRP corresponding to 721 azimuth angles for each target in the database, and the dimension of HRRP vector is 161.

With curvilinear triangular patches discretization, the unknown number of F15, F117 and VFY-218 for order-2.5 hierarchical basis functions is 187152, 153594 and 170898, respectively. The backscattering field of each aircraft at 21 frequency points uniformly distributed between 1G to 5G is calculated by the ACA based matrix compression method. Compared with solving linear equations repeatedly at 721 angles with direct solution, the iteration solver is only used 56, 41 and 48 times with the ACA accelerated method for F15, F117 and VFY-218, respectively. Plenty of iterative solution time can be saved. For wideband backscattering field, the GTD-based scattering model is established for each aircraft by using the backscattering field corresponding to 721 azimuth angles. Instead of computing at 161 frequency points with direct solution, the number of sampling frequency points is reduced to 21 by using the GTD-based scattering model. The computational efficiency has been improved by about 8 times. The HRRPs of each aircraft models are illustrated in Fig. 8. Figure 9 shows the bispectrums of F15 at $\varphi=0^\circ$ without and with AWGN (SNR=10dB), respectively. Figure 10 and Fig. 11 shows the bispectrums of F117 and VFY-218, respectively. It can be found from Fig. 9 to Fig. 11 that the estimation of bispectrum cannot completely suppress the AWGN. This is because when the length of pseudo-random sequence is limited, the third-order cumulant of Gaussian noise sequence approximately obeys the complex Gaussian distribution.

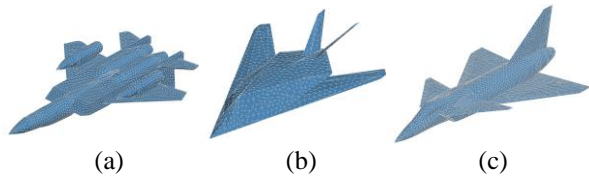


Fig. 7. Geometrical models for three known types of scaled aircraft: (a) F15, (b) F117, and (c) VFY-218.

Aircraft	Length	Width	Height
F15	7.1713	5.0248	1.5967
F117	7.628	5.1547	0.9384
VFY-218	7.7354	4.4522	2.057

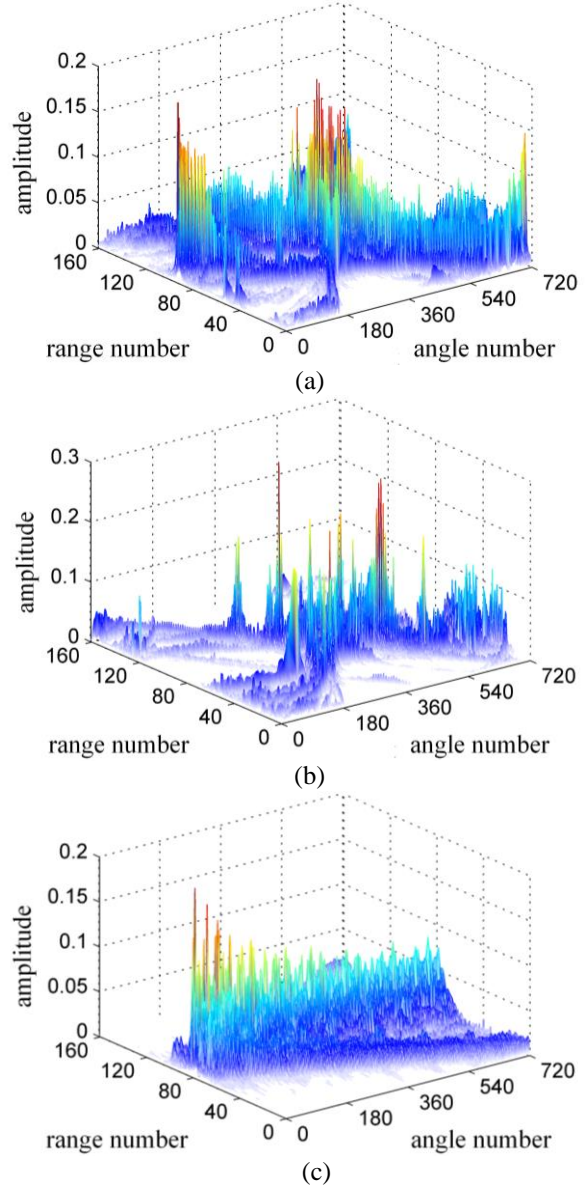


Fig. 8. HRRPs of the three aircraft models: (a) F15, (b) F117, and (c) VFY-218.

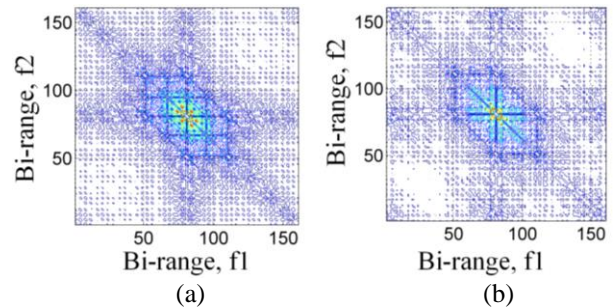


Fig. 9. Bispectrum for F15 at $\varphi=0^\circ$: (a) without noise, and (b) with AWGN (SNR=10dB).

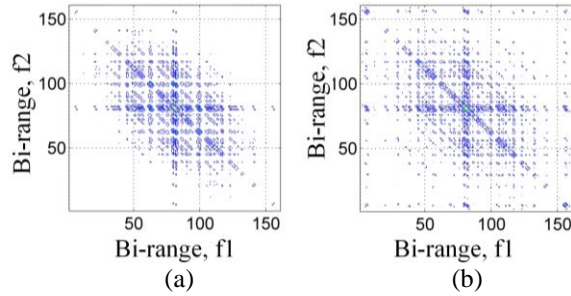


Fig. 10. Bispectrum for F117 at $\varphi=0^\circ$: (a) without noise, and (b) with AWGN (SNR=10dB).

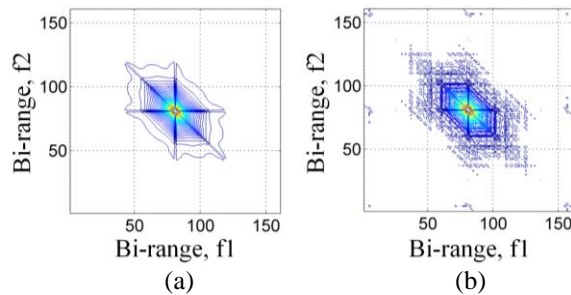


Fig. 11. Bispectrum for VFY-218 at $\varphi=0^\circ$: (a) without noise, and (b) with AWGN (SNR=10dB).

We uniformly choose one in every three of the 721 MSIBs as the training samples, leading to 241 training samples for each target. The rest of the MSIBs in the database are served as testing samples, providing totally 1440 testing samples. Figure 12 shows the average correct recognition rates (CRR) of MSIB_PCA with respect to n_{PCA} and the noise levels of AWGN. It can be found that the average CRR gradually improves as n_{PCA} increases. But when n_{PCA} reaches a certain value, the CRR remained unchanged. It can also be seen that the average CRR is constantly reduced when the level of Gaussian noise is increased.

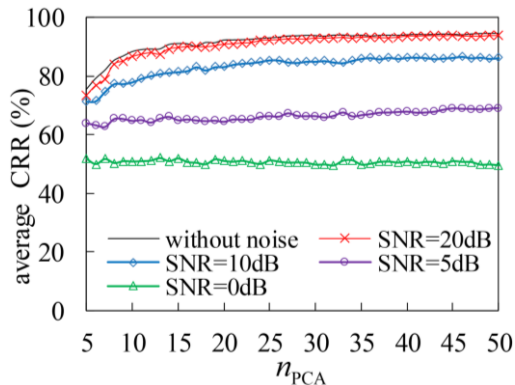


Fig. 12. The average CRR of three aircraft models with respect to n_{PCA} and the levels of AWGN.

To give insight into the confusion of the three aircraft in recognition process, Table 3 shows CRR when each aircraft is chosen as the testing target respectively. Here $n_{PCA}=50$. It can be noticed that the CRR is inversely proportional to the level of Gauss's noise, and it can be improved to a certain extent by projecting the MSIB features onto the lower-dimensional PCA space for recognition. It also can be found that the CRR of VFY-218 is higher than the other two. This is because the HRRPs of VFY-218 are obviously different, as shown in Fig. 5.

Table 3: Correct recognition rate of three aircraft models

		F15	F117	VFY-218
Without noise	MSIB	92.92	94.21	96.25
	MSIB_PCA	94.38	94.17	99.17
SNR=20dB	MSIB	92.62	93.58	96.25
	MSIB_PCA	92.71	92.5	98.75
SNR=10dB	MSIB	81.46	87.71	94.17
	MSIB_PCA	81.88	82.08	98.33
SNR=5dB	MSIB	55.00	57.08	88.33
	MSIB_PCA	60.42	56.88	93.96
SNR=0dB	MSIB	46.04	39.79	62.29
	MSIB_PCA	46.46	39.58	72.71

IV. CONCLUSION

In this paper, efficient wideband MRCS simulation has been presented for radar HRRP target recognition based on MSIB and PCA. Firstly, an efficient numerical approach has been proposed for the wideband MRCS from a target. The well-conditioned integral equation combined with the novel higher-order hierarchical divergence-conforming vector basis functions and the MLFMA has been utilized for efficient scattering analysis. The well-conditioned matrix equation can obtain rapid converging iterative solutions without preconditioning. Comparing with low-order techniques, the use of novel higher order hierarchical divergence-conforming vector basis function can greatly reduce the number of unknowns for a given problem. By using the low-rank property of the multiple RHS problem, the ACA based matrix compression method has been employed for efficient computation of MRCS. Compared with solving linear equations repeatedly at each angle with direct solution, the ACA based matrix compression method can greatly reduce the computation time. The GTD-based scattering model has been utilized for fast analysis of MRCS over a wide frequency band. By modeling a complex target as a summation of ideal scattering centers, large amount of calculation can be reduced. Finally, the one-dimensional MSIB features of HRRP have been extracted to constitute eigenvectors

for radar target recognition. To enhance the separation ability of radar target recognition, the MSIB features have been projected onto a lower-dimensional PCA space for recognition. Numerical examples prove that the proposed algorithm is feasible and efficient.

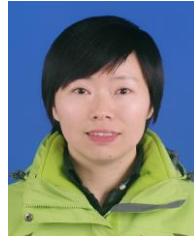
ACKNOWLEDGMENT

The work is supported by the National Natural Foundation of China (Grant No. 61401219). We would like to thank the sponsors.

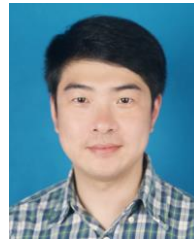
REFERENCES

- [1] S. P. Jacobs, *Automatic Target Recognition Using High-Resolution Radar Range Profiles*. Washington University, Washington, 1997.
- [2] L. Du, H. He, and L. Zhao, "Noise robust radar HRRP target recognition based on scatterer matching algorithm," *IEEE Sensors Journal*, vol. 16, no. 6, pp. 1743-1753, Mar. 2016.
- [3] H. W. Liu, B. Feng, and B. Chen, "Radar high-resolution range profiles target recognition based on stable dictionary learning," *IET Radar Sonar and Navigation*, vol. 10, no. 2, pp. 228-237, Feb. 2016.
- [4] J. M. Song, C. C. Lu, and W. C. Chew, "Multilevel fast multipole algorithm for electromagnetic scattering by large complex objects," *IEEE Trans. Antennas Propag.*, vol. 45, no. 10, pp. 1488-1493, 1997.
- [5] X. C. Wei, Y. J. Zhang, and E. P. Li, "The hybridization of fast multipole method with asymptotic waveform evaluation for the fast monostatic RCS computation," *IEEE Trans. Antennas Propag.*, vol. 52, no. 2, pp. 605-607, Feb. 2004.
- [6] R. D. Slone, J. F. Lee, and R. Lee, "Automating multipoint Galerkin AWE for a FEM fast frequency sweep," *IEEE Trans. Magn.*, vol. 38, no. 2, pp. 637-640, 2002.
- [7] Z. W. Liu, R. S. Chen, and J. Q. Chen, "Adaptive sampling cubic-spline interpolation method for efficient calculation of monostatic RCS," *Microw. Opt. Technol. Lett.*, vol. 50, no. 3, pp. 751-755, 2008.
- [8] J. Shaeffer, "Direct solve of electrically large integral equations for problem sizes to 1 M unknowns," *IEEE Trans. Antennas Propag.*, vol. 56, no. 8, pp. 2306-2313, 2008.
- [9] Z. H. Fan, Z. W. Liu, D. Z. Ding, and R. S. Chen, "Preconditioning matrix interpolation technique for fast analysis of scattering over broad frequency Band," *IEEE Trans. Antennas Propag.*, vol. 58, no. 7, pp. 2484-2487, 2010.
- [10] C. J. Reddy, M. D. Deshpande, C. R. Cockrell, and F. B. Beck, "Fast RCS computation over a frequency band using method of moments in conjunction with asymptotic waveform evaluation technique," *IEEE Trans. Antennas Propag.*, vol. 46, no. 8, pp. 1229-1233, Aug. 1998.
- [11] G. Hislop, N. A. Ozdemir, C. Craeye, and D. G. Ovejero, "MoM matrix generation based on frequency and material independent reactions (FMIR-MoM)," *IEEE Trans. Antennas Propag.*, vol. 60, no. 12, pp.5777-5786, Dec. 2012.
- [12] V. Chandran and S. L. Elgar, "Pattern recognition using invariants defined from higher order spectra-one-dimensional inputs," *IEEE Trans. Signal Proces.*, vol. 41, no. 1, pp. 205-212, Jan. 1993.
- [13] J. K. Tugnait, "Detection of non-Gaussian signals using integrated polyspectrum," *IEEE Trans. Signal Proces.*, vol. 42, no. 11, pp. 3137-3149, Nov. 1994.
- [14] X. J. Liao and Z. Bao, "Circularly integrated bispectra: Novel shift invariant features for high-resolution radar target recognition," *Electronics Letters*, vol. 34, no. 19, pp. 1879-1880, Sept. 1998.
- [15] V. Chandran and S. L. Elgar, "Pattern recognition using invariants defined from higher order spectra-one-dimensional inputs," *IEEE Trans. Signal Proces.*, vol. 41, no. 1, pp. 205-212, Jan. 1993.
- [16] V. Chandran and S. L. Elgar, "Pattern recognition using invariants defined from higher order spectra-one-dimensional inputs," *IEEE Trans. Signal Proces.*, vol. 41, no. 1, pp. 205-212, Jan. 1993.
- [17] Y. Q. Hu, J. J. Ding, D. Z. Ding, and R. S. Chen, "Analysis of electromagnetic scattering from dielectric objects above a lossy half space by multiresolution preconditioned MLFMA," *IET Microwaves, Antennas & Propagation*, vol. 4, no. 2, pp. 232-239, Feb. 2010.
- [18] P. Ylä-Oijala, M. Taskinen, and S. Järvenpää, "Analysis of surface integral equations in electromagnetic scattering and radiation problems," *Engineering Analysis with Boundary Elements*, vol. 32, pp. 196-209, 2008.
- [19] Y. Q. Hu, D. Z. Ding, Z. H. Fan, and R. S. Chen, "Well-conditioned MLFMA for electromagnetic scattering from dielectric objects above a lossy half-space," *Microwave and Optical Technology Letters*, vol. 52, no. 2, pp. 381-386, 2010.
- [20] R. S. Chen, Y. Q. Hu, Z. H. Fan, D. Z. Ding, D. X. Wang, and E. K. N. Yung, "An efficient surface integral equation solution to EM scattering by chiral objects above a lossy half space," *IEEE Trans. Antennas Propag.*, vol. 57, no. 11, pp. 3586-3593, 2009.
- [21] P. Ylä-Oijala and M. Taskinen, "Application of combined field integral equation for electromagnetic scattering by dielectric and composite objects," *IEEE Trans. Antennas Propag.*, vol. 53, no. 3, pp. 1168-1173, Mar. 2005.
- [22] R. D. Graglia, A. F. Peterson, F. P. Andriulli, "Curl-conforming hierarchical vector bases for triangles and tetrahedra," *IEEE Trans. Antennas*

- Propagat.*, vol. 59, no. 3, pp. 950-959, 2011.
- [23] L. P. Zha, Y. Q. Hu, and T. Su, "Efficient surface integral equation using hierarchical vector bases for complex EM scattering problems," *IEEE Trans. Antennas Propagat.*, vol. 60, no. 2, pp. 952-957, Feb. 2012.
- [24] Z. P. Nie, W. Ma, Y. Ren, Y. Zhao, J. Hu, and Z. Zhao, "A wideband electromagnetic scattering analysis using MLFMA with higher order hierarchical vector basis functions," *IEEE Trans. Antennas Propag.*, vol. 57, no. 10, pp. 3169-3178, Oct. 2009.
- [25] L. C. Potter, D. M. Chiang, R. Carriere, and M. J. Gerry, "A GTD-based parametric model for radar scattering," *IEEE Trans. Antennas Propagat.*, vol. 43, no. 10, pp. 1058-1067, Oct. 1995.
- [26] L. C. Trintinalia, R. Bhalla, and H. Ling, "Scattering center parameterization of wide-angle backscattered data using adaptive Gaussian representation," *IEEE Trans. Antennas Propagat.*, vol. 45, no. 11, pp. 1664-1668, 1997.
- [27] T. K. Sarkar and Odilon Pereira, "Using the matrix pencil method to estimate the parameters of a sum of complex exponentials," *IEEE Antennas and Propagation Magazine*, vol. 37, no. 1, pp. 48-55, 1995.
- [28] T. K. Moon and W. C. Stirling, *Mathematical Methods and Algorithms for Signal Processing*, Prentice Hall, 1999.
- [29] J. H. Jung and H. T. Kim, "Comparisons of four feature extraction approaches based on Fisher's linear discriminant criterion in radar target recognition," *Journal of Electromagnetic Waves and Applications, PIER*, vol. 21, no. 2, pp. 251-265, 2007.



Yunqin Hu received Ph.D. degree in Information and Communication Engineering from Nanjing University of Science and Technology. During 2014, she was with the Electrical and Computer Engineering of Iowa State University as a visiting scholar. She is currently a Lecturer with the Communication Engineering of Nanjing University of Posts and Telecommunications. Her current research interests include computational electromagnetics, antennas and electromagnetic scattering and propagation in complex media.



Ting Wan received the Ph.D. degree in Information and Communication Engineering from Nanjing University of Science and Technology. He is currently an Associate Professor of Nanjing University of Posts and Telecommunications. His research interests include computational electromagnetics, electromagnetic scattering and radiation, and electromagnetic modeling of microwave/millimeter wave integrated circuits.

Novel Reduced Matrix Equation Constructing Method Accelerates Iterative Solution of Characteristic Basis Function Method

Zhonggen Wang^{1*}, Qiang Chen², WenYan Nie³, and Han Lin¹

¹School of Electrical and Information Engineering
Anhui University of Science and Technology, Huainan, 232001, China
zgwang@ahu.edu.cn*, hanlin@aust.edu.cn

²Department of Electrical and Communications Engineering
Tohoku University, Sendai, 980-8579, Japan
chenq@ecei.tohoku.ac.jp

³School of Mechanical and Electrical Engineering
Huainan Normal University, Huainan, 232001, China
wynie5240@163.com

Abstract — In this paper, a new construction method of reduced matrix equation is proposed to improve the iterative solution efficiency of characteristic basis function method (CBFM). Firstly, the singular value decomposition (SVD) technique is applied to compress the incident excitations and these new excitations retained on each block after SVD are defined as the excitation basis functions (EBFs). Then, the characteristic basis functions (CBFs) of each block are solved from these EBFs. Lastly, these EBFs and CBFs are used as the testing functions and the basis functions to construct the reduction matrix equation, respectively. The diagonal sub-matrices of the reduced matrix constructed by the proposed method are all identity matrices. Thus, the condition of the reduced matrix is improved resulting in a smaller number of iterations required for the solution of the reduced matrix equation. The numerical results validate the accuracy of the proposed method. Compared with the traditional CBFM, the iterative solution efficiency of the reduced matrix equation constructed by the proposed method is significantly improved.

Index Terms — Characteristic basis functions, characteristic basis function method, reduced matrix equation, singular value decomposition, testing functions.

I. INTRODUCTION

The method of moments (MoM) is known as an effective method to solve the electromagnetic scattering problems. However, the computational time and memory requirement of MoM increase significantly while dealing with large problems. In order to mitigate these problems, a number of acceleration algorithms have been proposed, such as fast multipole method (FMM) [1],

multilevel fast multipole method (MLFMM) [2-4], adaptive integral method (AIM) [5], adaptive cross approximation (ACA) algorithm [6,7], precorrected-fast Fourier transform (P-FFT) [8] method, and fast dipole method (FDM) [9]. These methods effectively utilize the matrix-vector products (MVPs) and can handle large number of unknowns. Another essentially different family of techniques reduces the number of degrees of freedom (DoFs) by employing macro basis functions and domain-decomposition schemes, instead of utilizing the rapid computation of the MVPs. This family of techniques includes domain decomposition method (DDM) [10-12], synthetic function expansion technique (SFX) [13], accurate sub-entire-domain (ASED) basis function method [14], characteristic mode (CM) [15,16], and characteristic basis function method (CBFM) [17-19]. Among these techniques, the CBFM has been successfully and widely applied to printed circuits and scattering problems. The main computational of the CBFM consists of three parts: characteristic basis functions (CBFs) generation; reduced matrix construction; and reduced matrix equation solution. In recent years, several techniques have been proposed to improve the performance of the CBFM. In [20], multistep angular-derived CBFs generation technique has been proposed to reduce the singular value decomposition (SVD) time of generating the CBFs. In [21], the ACA-SVD has been adapted to efficiently generate the CBFs, which reduces both the time of generating the initial CBFs and the SVD time of initial CBFs. In [22], an improved primary CBFM (IP-CBFM) has been proposed to reduce the amount of memory used for reduced matrix by combining the secondary CBFs with the primary CBFs. In [23], the high level CBFs have been proposed to

improve the iterative solution efficiency of CBFM. Furthermore, some hybrid methods have been presented, such as CBFM-FMM [24], CBFM-MLFMM [25], CBFM-ACA [26], and CBFM-FDM [27] to accelerate the vector-matrix-vector products (VMVPs) in the construction of the reduced matrix. To some extent, these methods can save time and reduce the storage requirement. However, the size of reduced matrix in CBFM increases when analyzing the electrically large problems. Therefore, the solution of the reduced matrix equation should be performed by an iterative method. In this paper, a new construction method of reduced matrix equation is proposed to improve the iterative solution efficiency of CBFM. The diagonal sub-matrices of the reduced matrix constructed by the proposed method are all identity matrices, which improve the condition of reduced matrix and reduce the number of iterations.

II. CHARACTERISTIC BASIS FUNCTION METHOD

The CBFM divides the target into M blocks, where each block is solved as an independent domain. For each block, the CBFs can be obtained as:

$$\mathbf{Z}_{ii}^e \cdot \mathbf{J}_i^{\text{CBFs}} = \mathbf{E}_i, \quad (1)$$

where \mathbf{Z}_{ii}^e denotes the self-impedance of the extended block i , with dimensions $N_i^{eb} \times N_i^{eb}$, for $i = 1, 2, \dots, M$. The N_i^{eb} represents the number of Rao-Wilton-Glisson (RWG) basis functions belonging to the extended block i , \mathbf{E}_i is the excitation matrix with dimensions $N_i^{eb} \times N_{\text{pws}}$, and N_{pws} is the number of incident excitations. In order to eliminate the redundant information in $\mathbf{J}_i^{\text{CBFs}}$ caused by overestimation, the SVD is used to reduce the redundancy of the initial CBFs. This factorization yields the following result:

$$\mathbf{J}_i^{\text{CBFs}} = \mathbf{U}_i \mathbf{W}_i \mathbf{V}_i^T, \quad (2)$$

where \mathbf{U}_i and \mathbf{V}_i are orthogonal matrices with dimensions $N_i^{eb} \times N_i^{eb}$ and $N_{\text{pws}} \times N_{\text{pws}}$, respectively, and \mathbf{W}_i is a diagonal matrix with dimensions $N_i^{eb} \times N_{\text{pws}}$. The superscript T denotes the transpose operation. Suppose, the same number B of CBFs is retained on each block after SVD, where B is smaller than N_{pws} , the surface current of the target can be expressed as a linear combination of these CBFs as:

$$\mathbf{J} = \begin{bmatrix} \mathbf{J}_1 \\ \vdots \\ \mathbf{J}_i \\ \vdots \\ \mathbf{J}_M \end{bmatrix} = \sum_{k=1}^B a_1^k \begin{bmatrix} \mathbf{J}_1^k \\ [0] \\ \vdots \\ [0] \end{bmatrix} + \dots + \sum_{k=1}^B a_M^k \begin{bmatrix} [0] \\ \vdots \\ [0] \\ \vdots \\ [\mathbf{J}_M^k] \end{bmatrix}, \quad (3)$$

where a_i^k are the unknown expansion coefficients and \mathbf{J}_i^k is the k th CBF of block i . The Galerkin method [28] is used to determine the unknown expansion coefficients and a $BM \times BM$ reduced matrix for the BM unknown expansion coefficients is obtained. Then the reduced matrix equation $\mathbf{Z}^R \cdot \boldsymbol{\alpha} = \mathbf{E}^R$ can be constructed as follow:

$$\begin{bmatrix} \mathbf{Z}_{11}^R & \mathbf{Z}_{12}^R & \dots & \mathbf{Z}_{1M}^R \\ \mathbf{Z}_{21}^R & \mathbf{Z}_{22}^R & \dots & \mathbf{Z}_{2M}^R \\ \vdots & \vdots & \ddots & \vdots \\ \mathbf{Z}_{M1}^R & \mathbf{Z}_{M2}^R & \dots & \mathbf{Z}_{MM}^R \end{bmatrix} \begin{bmatrix} \boldsymbol{\alpha}_1 \\ \boldsymbol{\alpha}_2 \\ \vdots \\ \boldsymbol{\alpha}_M \end{bmatrix} = \begin{bmatrix} \mathbf{E}_1^R \\ \mathbf{E}_2^R \\ \vdots \\ \mathbf{E}_M^R \end{bmatrix}, \quad (4)$$

where $\boldsymbol{\alpha}_i = (\boldsymbol{\alpha}_i^1, \boldsymbol{\alpha}_i^2, \dots, \boldsymbol{\alpha}_i^B)^T$ represent the unknown weights of the CBFs on block i , \mathbf{E}_i^R is the excitation vector, and \mathbf{Z}_{ij}^R is the sub-matrix containing the coupling terms between blocks i and j . The each element of the sub-matrix can be written as:

$$\begin{aligned} \mathbf{Z}_{ij}^R(m, n) &= \langle \mathbf{F}_{i,m}, L(\mathbf{F}_{j,n}) \rangle \\ &= \left\langle \sum_{p=1}^{N_i} \mathbf{J}_i(p, m) \mathbf{f}_{i,p}(\mathbf{r}), L \left(\sum_{q=1}^{N_j} \mathbf{J}_j(q, n) \mathbf{f}_{j,q}(\mathbf{r}) \right) \right\rangle \\ &= \sum_{p=1}^{N_i} \sum_{q=1}^{N_j} \mathbf{J}_i(p, m)^* \langle \mathbf{f}_{i,p}(\mathbf{r}), L(\mathbf{f}_{j,q}(\mathbf{r})) \rangle \mathbf{J}_j(q, n), \\ &= \sum_{p=1}^{N_i} \sum_{q=1}^{N_j} \mathbf{J}_i(p, m)^* \mathbf{Z}_{ij}(p, q) \mathbf{J}_j(q, n) \end{aligned} \quad (5)$$

where $\langle \mathbf{F}_{i,m}, L(\mathbf{F}_{j,n}) \rangle$ denotes the coupling term between the m th CBF on block i and n th CBF on block j . $\mathbf{F}_{i,m}$ and $\mathbf{F}_{j,n}$ are the m th and n th CBFs on blocks i and j , respectively. $\mathbf{f}_{i,p}(\mathbf{r})$, and $\mathbf{f}_{j,q}(\mathbf{r})$ are the p th and q th RWG basis functions on blocks i and j , respectively. $\mathbf{Z}_{ij}(p, q)$ stands for the coupling term between the p th RWG on block i and q th RWG on block j . The coefficient $\mathbf{J}_i(p, m)$ denotes the value of the m th CBF, included on the block i , and sampled at the center of the p th RWG. N_i and N_j are the numbers of RWG basis functions on blocks i and j , respectively. Equation (5) enables us to express the coupling terms between the CBFs of two blocks as a simple product between matrices:

$$\mathbf{Z}_{ij}^R = \mathbf{J}_i^H \mathbf{Z}_{ij} \mathbf{J}_j, \quad (6)$$

where H stands for conjugated transpose, \mathbf{Z}_{ij} is the matrix containing the coupling terms between the RWGs on blocks i and j . Likewise, the voltage vector is then computed as:

$$\mathbf{E}_i^R = \mathbf{J}_i^H \mathbf{E}_i. \quad (7)$$

It can be found from Eqs. (5), (6), and (7) that the CBFs (\mathbf{J}_i) are used as higher level testing and basis functions in terms of RWG basis functions in the process of constructing the reduced matrix equation. For moderate size problems, the reduced matrix equation (Eq. (4)) can be solved via a single LU-decomposition and one matrix-vector product per excitation. However, for large size problems, the dimensions of the reduced matrix become so large that an iterative method should be used to solve the reduced matrix equation.

III. NEW REDUCED MATRIX EQUATION CONSTRUCTION METHOD

Firstly, the SVD is applied to deal with the excitation matrix before generating the CBFs:

$$\mathbf{E}_i = \mathbf{U}\mathbf{W}\mathbf{V}^T, \quad (8)$$

where \mathbf{U} and \mathbf{V} are the orthogonal matrices of dimensions $N_i^{eb} \times N_i^{eb}$ and $N_{pws} \times N_{pws}$, respectively. \mathbf{W} is an $N_i^{eb} \times N_{pws}$ diagonal matrix whose elements are the singular values of \mathbf{E}_i . Setting an appropriate threshold (typically 0.001), a new set of incident excitations will be obtained retaining only those with relative singular values above the threshold. Hence, a new excitation matrix named \mathbf{E}_i^{new} is obtained and the number of excitations is decreased. These new excitations are defined as the new testing functions of the block and denoted as excitation basis functions (EBFs). For simplicity, it is assumed that all the blocks contain the same number K of EBFs. The dimensions of \mathbf{E}_i^{new} are $N_i^{eb} \times K$, and K is always smaller than N_{pws} . Replacing \mathbf{E}_i in Eq. (1) with \mathbf{E}_i^{new} , a new equation can be constructed as follows:

$$\mathbf{Z}_{ii}^e \mathbf{J}_i^{new} = \mathbf{E}_i^{new}. \quad (9)$$

By solving Eq. (9), K CBFs (\mathbf{J}_i^{new}) can be obtained on each block and are defined as the new basis functions. The total number of matrix equation solutions is $M \cdot K$, which is smaller than $M \cdot N_{pws}$ in the CBFM as $K \ll N_{pws}$. The time required to generate the CBFs in the proposed method is reduced compared to the traditional CBFM. By using the EBFs and CBFs as the testing and the basis functions, the coupling terms between the CBFs of two blocks can be rewritten as:

$$\mathbf{Z}_{ij}^{Rnew} = (\mathbf{E}_i^{new})^H \mathbf{Z}_{ij} \mathbf{J}_j^{new}, \quad (10)$$

where \mathbf{E}_i^{new} is an unitary matrix. When $i = j$, $\mathbf{Z}_{ii}^{Rnew} = (\mathbf{E}_i^{new})^H \mathbf{E}_i^{new} = \mathbf{I}$, where \mathbf{I} represents the identity matrix. Eq. (4) can be rewritten as:

$$\begin{bmatrix} \mathbf{I} & \mathbf{Z}_{12}^{Rnew} & \cdots & \mathbf{Z}_{1M}^{Rnew} \\ \mathbf{Z}_{21}^{Rnew} & \mathbf{I} & \cdots & \mathbf{Z}_{2M}^{Rnew} \\ \vdots & \vdots & \ddots & \vdots \\ \mathbf{Z}_{M1}^{Rnew} & \mathbf{Z}_{M2}^{Rnew} & \cdots & \mathbf{I} \end{bmatrix} \begin{bmatrix} \mathbf{a}_1 \\ \mathbf{a}_2 \\ \vdots \\ \mathbf{a}_M \end{bmatrix} = \begin{bmatrix} \mathbf{E}_1^{Rnew} \\ \mathbf{E}_2^{Rnew} \\ \vdots \\ \mathbf{E}_M^{Rnew} \end{bmatrix}, \quad (11)$$

where $\mathbf{E}_i^{Rnew} = (\mathbf{E}_i^{new})^H \mathbf{E}_i^{new}$, it can be seen from Eq. (11) that the sub-matrix containing the coupling terms between the CBFs of each block becomes the identity matrix because of the orthogonal properties of the EBFs. Compared with the traditional CBFM, the condition number of the reduced matrix is improved, and the number of iterations required in the solution process is reduced accordingly.

IV. NUMERICAL RESULTS

In this section, three test samples are presented to demonstrate the accuracy and efficiency of the proposed method. All simulations are executed on a PC with an Intel(R) Core(TM) i5-6200 CPU with 2.3 GHz (only one core was used) and 48 GB RAM. The bi-conjugated stabilized gradient (BiCGStab) is selected as iterative solver with a residual error of 0.001. The relative error Err is introduced and defined as follows:

$$Err = \left(\frac{|\text{RCS}_x - \text{RCS}_{\text{FEKO}}|}{|\text{RCS}_{\text{FEKO}}|} \right) \times 100\%, \quad (12)$$

where RCS_{FEKO} are the simulation results from the software FEKO, and RCS_x are results computed by the traditional CBFM or the proposed method.

Firstly, the scattering problem of a PEC plate with a side length of 2 m is considered at a frequency of 500 MHz. The geometry is divided into 8246 triangular patches with an average length of $\lambda/10$ leading to 15286 unknowns. The geometry is divided into 9 blocks, with each block extended by $\Delta=0.15\lambda$ in all directions. For both methods, 800 incident excitations are set. The total numbers of CBFs and the relative errors of two methods under different SVD thresholds are shown in Table 1. It can be seen from the table that the relative error of the proposed method converges faster with reducing SVD threshold than the traditional CBFM. In order to compare the iterative solution efficiency of the two methods, the reduced matrix dimensions of the proposed method and the traditional CBFM are 865×865 and 872×8721 when the SVD thresholds are selected as 0.002 and 0.001, respectively. The condition number of CBFM matrix is 11009, while the condition number of the proposed method matrix is only 2219. Figure 1 illustrates the iterative convergence of the two methods. It can be seen from the figure that the proposed method achieves a good convergence. In order to confirm the higher convergence of the proposed method, the observation of the eigenvalues distributions is presented in Fig. 2. The

figure shows that the convergence of the iterative solutions of the proposed method improves as the eigenvalues move away from the origin. The bistatic RCS in horizontal polarization calculated by the two methods are shown in Fig. 3. It is clear from the RCS curves that the results calculated by the proposed method agree well with the one by FEKO, and also the one by CBFM. The total number of iterations of CBFM is 63, while the one of proposed method is only 37. Thus, a 41% of iterations number reduction is obtained.

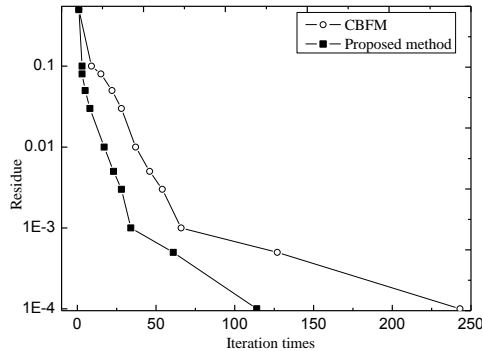


Fig. 1. Iteration times at different residues of two methods.

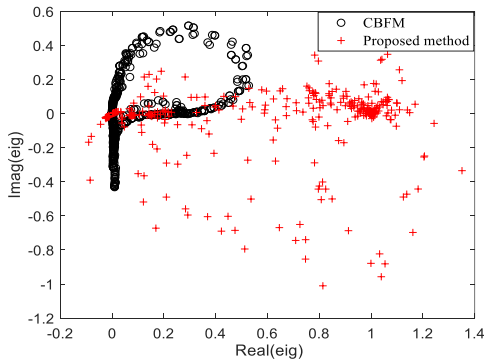


Fig. 2. Eigenvalues distribution of two methods.

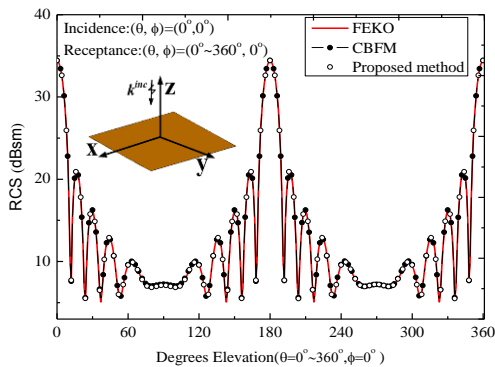


Fig. 3. Bistatic RCS of a PEC plate in horizontal polarization.

Next, the scattering problem of a PEC missile with a length of 1 m, a wingspan of 0.64 m, and a height of 0.22 m is considered at a frequency of 3 GHz. The total number of unknowns is 85217, and the geometry is divided into 52 blocks. Each block is excited by using multiple 800 incident excitations. The CBFs produced by the CBFM and the proposed method are 6025 and 6194, respectively. The condition number of CBFM matrix is 68341, and of proposed method matrix is only 7213. The average number of iterations of the conventional CBFM is 607 by using the iterative BiCGStab method without using the preconditioning techniques, while the proposed method requires only 299 iterations. The CPU time spent in the solution of the reduced matrix equation is reduced from 311.9 second with CBFM to 161.2 second in the proposed method. The bistatic RCS in horizontal polarization calculated by the two methods are depicted in Fig. 4. It can be seen from the figure that the RCS curve of proposed method is in a good agreement with that of traditional CBFM. A good agreement with the result of FEKO is also achieved except around $\theta = 115^\circ$ and $\theta = 69^\circ$.

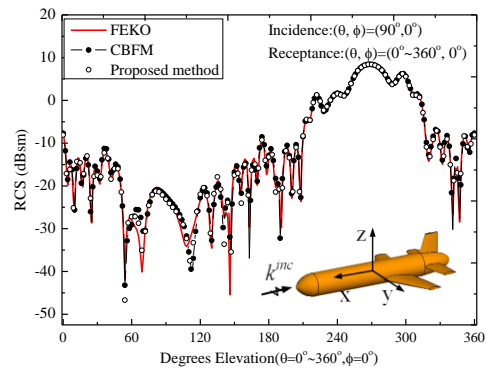


Fig. 4. Bistatic RCS of a PEC missile in horizontal polarization.

Finally, the monostatic RCS of a cone-sphere with gap (referenced from [29]) at a frequency of 10 GHz is calculated. Total 181 observation directions for $\theta = 90^\circ$ and ranging from $\phi = 0^\circ$ to $\phi = 180^\circ$ are considered. The number of unknowns is 158881, while 11949 and 11832 CBFs are obtained for the CBFM and the proposed method, respectively. The sparse approximate inverse preconditioner is applied to accelerate the iterative solution of reduced matrix equation. The average number of iterations per direction is 59.7 for the traditional CBFM, while this number is reduced to 32.1 iterations when the proposed method is applied. A substantial reduction in the CPU-time is obtained because of the better conditioned reduced matrix. Figure 5 shows a comparison of the results obtained by applying FEKO, CBFM, and the proposed method for monostatic RCS in

horizontal polarization. It can be observed from the figure that the results obtained by the proposed method agree well with that obtained by the FEKO.

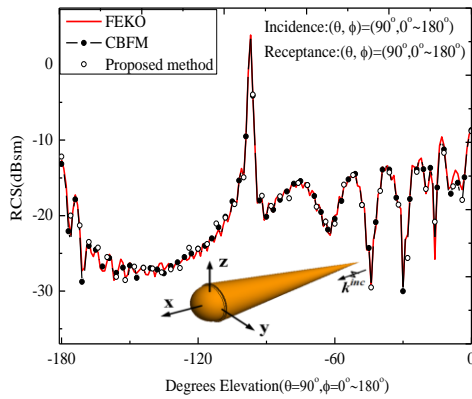


Fig. 5. Monostatic RCS of the cone-sphere with gap in horizontal polarization.

The CPU-times of the above three test examples using the CBFM and the proposed method are summarized in Table 2. Compared with the CBFM, the CPU-time of CBFs generation using the proposed method is reduced because the number of matrix equation solutions is significantly reduced. Moreover, the reduced matrix solution time is reduced because of the better conditioned system of equation using the proposed method. The CBFs generation time and the reduced matrix solving time are remarkably reduced and the gains are about 19.3% and 45.1%, respectively.

V. CONCLUSION

A new construction method of reduced matrix

equation is proposed in this paper to improve the iterative solution efficiency of characteristic basis function method (CBFM). In the proposed method, the excitation basis functions (EBFs) are first constructed by using the singular value decomposition (SVD) technique. Then, the characteristic basis functions (CBFs) are obtained by using the EBFs. These EBFs and CBFs are defined as the testing and the basis functions, respectively. The diagonal sub-matrices of the reduced matrix constructed by the new testing and basis functions are all identity matrices, which improves the condition of reduced matrix. Thus, the total number of iterations to achieve reasonable results is significantly reduced. Numerical simulations are conducted to validate the performance of the proposed method. The results demonstrate that the number of iterations required by the proposed method is noticeably less than that by the traditional CBFM due to the better conditioned system of equation. Furthermore, the proposed method can also be combined with MLFFM, AIM, P-FFT, FDM and other algorithms to further improve the efficiency of the characteristic basis function method for analyzing the electromagnetic scattering characteristics of electrically large targets.

ACKNOWLEDGMENT

This work was supported by the Natural Science Foundation of Anhui Province [Grant Number 1808085MF166, 1808085QF197]; the Postdoctoral Science Foundation of Anhui Province [grant number 2017B214]; the Overseas Visiting and Training Program for Outstanding Young Talents of Anhui Province [Grant Number gxgwx2018025]; the Natural Science Foundation of Anhui Provincial Education Department [grant number KJ2016A669].

Table 1: The total CBFs number and the relative error of two methods under different SVD threshold

SVD Threshold		0.8	0.5	0.1	0.05	0.01	0.005	0.002	0.001
CBFM	CBFs Number	20	112	369	446	623	699	796	872
	Err(%)	68.85	34.82	16.01	7.62	1.58	0.96	0.82	0.51
Proposed Method	CBFs Number	28	171	421	492	679	756	865	912
	Err(%)	56.09	18.71	5.12	3.14	0.86	0.61	0.57	0.49

Table 2: CPU time of the CBFM and proposed method for different calculation steps

Problems	Method	Impedance Matrix Calculation (s)	CBFs Generation (s)	Reduced Matrix Calculation (s)	Solving Matrix (s)	Total Time (s)
Plate	CBFM	239.1	747.7	84.1	0.8	1071.7
	Proposed Method	242.9	479.7	83.3	0.5	806.4
Missile	CBFM	2205.6	6675.4	986.7	311.9	10179.6
	Proposed Method	2209	5749.8	994.9	137.2	9090.9
Cone-Sphere with Gap	CBFM	5040.3	21240.7	4516.3	277.2×181	80970.5
	Proposed Method	5048.2	19661.8	4373.6	160.5×181	58134.1

REFERENCES

- [1] R. Coifman, V. Rokhlin, and S. Wandzura, "The fast multipole method for the wave equation: A pedestrian prescription," *IEEE Antennas Propag Mag.*, vol. 53, no. 3, pp.7-12, 1993.
- [2] M. Chen, R. S. Chen, and X. Q. Hu, "Augmented MLFMM for analysis of scattering from PEC object with fine structures," *Applied Computational Electromagnetics Society (ACES) Journal*, vol. 26, no. 5, pp. 418-428, 2011.
- [3] X. M. Pan, S. L. Huang, and X. Q. Sheng, "Wide angular sweeping of dynamic electromagnetic responses from large Targets by MPI parallel skeletonization," *IEEE Trans. Antennas Propag.*, vol. 66, no. 3, pp. 1619-1623, 2018.
- [4] Y. N. Liu, X. M. Pan, and X. Q. Sheng, "Skeletonization accelerated MLFMA solution of volume integral equation for plasmonic structures," *IEEE Trans. Antennas Propag.*, vol. 66, no. 3, pp. 1590-1594, 2018.
- [5] E. Bleszynski, M. Bleszynski, and T. Jaroszewicz, "Adaptive integral method for solving large-scale electromagnetic scattering and radiation problems," *Radio Science*, vol. 31, no. 5, pp. 1225-1251, 1996.
- [6] K. Zhao, M. N. Vouvakis, and J. F. Lee, "The adaptive cross approximation algorithm for accelerated method of moments computations of EMC," *IEEE Transactions on Electromagnetic Compatibility*, vol. 47, no. 4, pp. 763-773, 2005.
- [7] Z. Liu, R. Chen, J. Chen, and Z. Fan, "Using adaptive cross approximation for efficient calculation of monostatic scattering with multiple incident angles," *Applied Computational Electromagnetics Society (ACES) Journal*, vol. 26, no. 4, pp. 325-333, 2011.
- [8] J. R. Phillips and J. K. White, "A precorrected-FFT method for electrostatic analysis of complicated 3-D structures," *IEEE Trans. Comput. Aided Des. Integr. Circuits Syst.*, vol. 16, no. 10, pp. 1059-1072, 1997.
- [9] X. Chen, C. Gu, Z. Niu, Y. Niu, and Z. Li, "Fast dipole method for electromagnetic scattering from perfect electric conducting targets," *IEEE Trans. Antennas Propag.*, vol. 60, no. 2, pp. 1186-1191, 2012.
- [10] Z. Peng, X. Wang, and J. F. Lee, "Integral equation based domain decomposition method for solving electromagnetic wave scattering from non-penetrable objects," *IEEE Trans Antennas Propag.*, vol. 59, no. 9, pp. 3328-3338, 2011.
- [11] J. Hu, R. Zhao, M. Tian, *et al.*, "Domain decomposition method based on integral equation for solution of scattering from very thin conducting cavity," *IEEE Trans. Antennas Propag.*, vol. 62, no.10, pp. 5344-5348, 2014.
- [12] A. Freni, P. De Vita, P. Pirinoli, *et al.*, "Fast-factorization acceleration of MoM compressive domain-decomposition," *IEEE Trans. Antennas Propag.*, vol. 59, no. 12, pp. 4588-4599, 2011.
- [13] L. Matekovits, V. A. Laza, and G. Vecchi, "Analysis of large complex structures with the synthetic-functions approach," *IEEE Trans Antennas Propag.*, vol. 55, no. 9, pp. 2509-2521, 2007.
- [14] W. B. Lu, T. J. Cui, Z. G. Qian, *et al.*, "Accurate analysis of large-scale periodic structures using an efficient sub-entire-domain basis function method," *IEEE Trans. Antennas Propag.*, vol. 52, no. 11, pp. 3078-3085, 2004.
- [15] F. G. Hu and C. F. Wang, "Integral equation formulations for characteristic modes of dielectric and magnetic bodies," *IEEE Trans. Antennas Propag.*, vol. 64, no. 11, pp. 4770-4776, 2016.
- [16] L. Guan, Z. He, D. Z. Ding, and R. S. Chen, "Efficient characteristic mode analysis for radiation problems of antenna arrays," *IEEE Trans. Antennas Propag.*, vol. 67, no. 1, pp. 199-206, 2019.
- [17] V. V. S. Prakash and R. Mittra, "Characteristic basis function method: A new technique for efficient solution of method of moments matrix equations," *Microw. Opt. Technol. Lett.*, vol. 36, no. 2, pp. 95-100, 2003.
- [18] E. Lucente, A. Monorchio, and R. Mittra, "An iteration free MoM approach based on excitation independent characteristic basis functions for solving large multiscale electromagnetic scattering problems," *IEEE Trans. Antennas Propag.*, vol. 56, no. 4, pp. 999-1007, 2008.
- [19] Y. F. Sun, K. Lu, and G. H. Wang, "Analysis of electromagnetic scattering from dielectric objects using multilevel characteristic basis function method," *Chinese Journal of Radio Science*, vol. 28, no. 1, pp. 92-96, 2013.
- [20] C. Delgado, M. F. Catedra, and R. Mittra, "Efficient multilevel approach for the generation of characteristic basis functions for large scatters," *IEEE Trans. Antennas Propag.* vol. 56, no. 7, pp. 2134-2137, 2008.
- [21] X. Chen, C. Gu, Z. Niu, Y. Niu, and Z. Li, "Efficient iterative solution of electromagnetic scattering using adaptive cross approximation enhanced characteristic basis function method," *IET Microwaves, Antennas & Propagation*, vol. 9, no. 3, pp. 217-223, 2015.
- [22] T. Tanaka, Y. Inasawa, Y. Nishioka, and H. Miyashita, "Improved primary characteristic basic function method for monostatic radar cross section analysis of specific coordinate plane," *IEICE Transactions on Electronics*, vol. E99-C, no. 1, pp. 28-35, 2016.

- [23] E. García, C. Delgado, and F. Cátedra, "A novel and efficient technique based on the characteristic basis functions method for solving scattering problems," *IEEE Trans. Antennas Propag.*, vol. 67, no.5, pp. 3241-3248, 2019.
- [24] C. Craeye, "A fast impedance and pattern computation scheme for finite antenna arrays," *IEEE Trans. Antennas Propag.*, vol. 54, no. 10, pp. 3030-3034, 2006.
- [25] E. García, C. Delgado, I. González, and M. F. Catedra, "An iterative solution for electrically large problems combining the characteristic basis function method and the multilevel fast multipole algorithm," *IEEE Trans. Antennas Propag.*, vol. 56, no. 8, pp. 2363-2371, 2008.
- [26] R. Maaskant and R. Mittra, "Fast analysis of large antenna arrays using the characteristic basis function method and the adaptive cross approximation algorithm," *IEEE Trans. Antennas Propag.* vol. 56, no. 11, pp. 3440-3451, 2008.
- [27] X. Chen, Z. Li, Z. Niu, and C. Gu, "A hybrid fast dipole method and adaptive modified characteristic basis function method for electromagnetic scattering from perfect electric conducting targets," *J Electromagn Waves Appl.*, vol. 25, no. 14, pp. 1940-1952, 2011.
- [28] B. G. Galerkin, "On electrical circuits for the approximate solution of the Laplace equation," *Vestnik Inzh.*, vol. 19, pp. 897-908, 1915.
- [29] A. C. Woo, H. T. G. Wang, M. J. Schuh, and M. L. Sanders, "Benchmark radar targets for the validation of computational electromagnetics programs," *IEEE Antennas Propag. Mag.*, vol. 35, no. 6, pp. 84-89, 1993.



Zhonggen Wang received the Ph.D. degree in Electromagnetic Field and Microwave Technique from the Anhui University of China (AHU), Hefei, P. R. China, in 2014. Since 2014, he has been with the School of Electrical and Information Engineering, Anhui University of Science and Technology, where he is currently an Associate Professor. Since 2018, he is currently with the Department of Communications Engineering, Tohoku University, Sendai, Japan, as a Visiting Scholar. His research interests include computational electromagnetics, array antennas, and reflectarrays.



Qiang Chen received the B.E. degree from Xidian University, Xi'an, China, in 1986, and the M.E. and D.E. degrees from Tohoku University, Sendai, Japan, in 1991 and 1994, respectively. He is currently a Chair Professor with the Electromagnetic Engineering Laboratory, Department of Communications Engineering, Tohoku University. His current research interests include antennas, microwave and millimeter wave, electromagnetic measurement, and computational electromagnetics. He is a member of the Institute of Electronics, Information and Communication Engineers (IEICE). He is currently the Chair of the IEICE Technical Committee on Wireless Power Transfer. He was the Secretary and the Treasurer of the IEEE Antennas and Propagation Society Tokyo Chapter in 1998, the Secretary of the Technical Committee on Electromagnetic Compatibility of the IEICE from 2004 to 2006, and the Secretary of the Technical Committee on Antennas and Propagation of the IEICE from 2008 to 2010. He was an Associate Editor of the IEICE Transactions on Communications from 2007 to 2012.



Wenyan Nie received the B.S. and M.S degrees from Anhui University of Science and Technology in 2007 and 2012, respectively. She is currently an Associate Professor at Huainan Normal University. Her research interests include computational electromagnetic methods, antenna theory and design.



Han Lin is a Lecturer at Anhui University of Science and Technology. She received the Ph.D. degree in Electromagnetic Field and Microwave Technique from the Nanjing University of Aeronautics and Astronautics, Nanjing, P. R. China, in 2015. Her research interests include computational electromagnetic methods, antenna theory and design.

ASM-FDTD Combine the Prony's Method to Simulate the EMP Propagation in Tunnel

Yun-Fei Mao, Hong-Bing Wu, Jia-Hong Chen, and Xu-Wei Su

China Satellite Maritime Tracking and Control Department
 Jiangyin, 2144000, China
 myf4494@163.com, hongbing@163.com, stone_cjh@sina.com, suxuwei1983@163.com

Abstract — The aliasing problem in ASM-FDTD is presented in detail, to overcome the problem of the ASM-FDTD method to simulate the Electromagnetic pulse (EMP) propagation in periodic tunnel structure, the prony's method is employed to model the time domain field of the ASM-FDTD. The solution of the aliasing problem is achieved through evaluating of the exponential models at intermediate spectral points with interpolation, and the computational resource is also saved for the later time response. The accuracy of the approach is verified by comparing the results with the MW-FDTD which is calculated by parallel computing.

Index Terms — Aliasing problem, array scanning method (ASM), finite-difference time domain (FDTD), periodic structures, tunnel.

I. INTRODUCTION

EMP propagation in tunnel is a significant subject to study, the interest mainly comes from two aspects. First is the electromagnetic protection against the EMP weapons, second is the ultra-wideband (UWB) communication in tunnel. The well-known finite-difference time-domain (FDTD) technique is an ideal method due to its accuracy and flexibility, but the main problem is the high memory requirement and heavy computational burden when deal with these large-scale problems [1]-[12]. A successful technique to deal with this problem is MW-FDTD [13] which requires a relatively small FDTD computational mesh along with the pulse, this technique is applicable only when the significant pulse energy exists over a small part of the propagation path at any instant time. However, when a long distance is simulated, much computer resources are required. The ASM-FDTD [14]-[16] method is a novel technique, combining the spectral FDTD method [17] to model the excitation of infinite periodic structures. Tunnel system is periodic in one dimension. By considering the influence of the steel-bar structure in the around reinforce concrete, and the impressed excitation sources is often introduced at the sectional surfaces. So the ASM-FDTD technique can be dealt

with, as a result, only a single periodic cell of the periodic tunnel structure needs to be considered. The computational resources are reduced.

However, in the implementation of the ASM-FDTD technique, it involves the aliasing problems which is similar to the Discrete Fourier Transform (DFT). And it is difficult to distinguish the overlapping signals. To overcome the problem, it needs to increase the number of spectral sampling points in Brillouin zone or to enlarge the size of periodic cell, which requires a lot of computational resources. Another problem is a long time running is needed when simulating the long distant tunnel structure.

The Prony's method [18] is a technique to model the sampled data as a linear superposition of complex exponentials. In the present paper, the Prony's method is combined with the ASM-FDTD method, by using the periodic sources with different phase shift. Results show that they are agree very well with each other, which means the laws of the integral field could be expressed by a set of exponential parameter values simply. Firstly we obtain the exponential parameter values from a short time-domain response of the integral field with respect to every spectral points, then the exponential models is used to extrapolate the later time response of the integral field, so a large computation time will be reduced. On the other hand, based on the known parameter values corresponding to the finite spectral sampled points, we could estimate the parameter values at every spectral point in Brillouin zone approximately, by using interpolation method. Thus the integral fields at every spectral point are also obtained by the exponential models analytically and the aliasing problem can be solved.

This paper is organized as follows. In Section II, the Fourier transform (FT) property of the ASM-FDTD is presented, the details of the aliasing problem is made clear systematically according to the FT theory. In Section III we outline the application of Prony's method to fit the exponential model to the integral field and show the exponential parameter values versus the spectral sampling points. In Section IV, the estimation

of the parameter values by interpolation and the solution to the aliasing problem are described. The final results of the problem are compared with the MW-FDTD method.

II. FOURIER TRANSFORM PROPERTY OF ASM

In time domain, $E_{tot}^{\infty}(r, r_0, k_z, t)$ is the total electric field at r in the infinite periodic structure along the z direction produced by a set of sources at $r_0 + m\alpha 1_z$ ($m=0, \pm 1, \dots$) with a phase shift $\exp(-jk_z\alpha)$. Between the adjacent sources and $E_{tot}(r, r_0 + n\alpha 1_z, k_z, t)$ is the field at r in the same periodic environment produced by a single source at $r_0 + n\alpha 1_z$, according to the superposition principle we can obtain:

$$\begin{aligned} E_{tot}^{\infty}(r, r_0, k_z, t) &= \sum_{n=-\infty}^{\infty} E_{tot}(r, r_0 + n\alpha 1_z, k_z, t) \\ &= \sum_{n=-\infty}^{\infty} E_{tot}(r, r_0 + n\alpha 1_z, t) e^{-jk_z n\alpha} \end{aligned} \quad (1)$$

where α is the period along the z direction and k_z is the phasing parameter. Multiply both side of (1) with $e^{-jk_z m\alpha}$ and integrate from π/α to $-\pi/\alpha$ with k_z , following the orthogonal property of the complex exponential function we have:

$$E_{tot}(r, r_0 - m\alpha 1_z, t) = \frac{\alpha}{2\pi} \int_{-\pi/\alpha}^{\pi/\alpha} E_{tot}^{\infty}(r, r_0, k_z, t) e^{-jk_z m\alpha} dk_z. \quad (2)$$

In an infinite periodic structure,

$$E_{tot}(r, r_0 - m\alpha 1_z, t) = E_{tot}(r + m\alpha 1_z, r_0, t). \quad (3)$$

Substitute (3) into (2),

$$E_{tot}(r + m\alpha 1_z, r_0, t) = \frac{\alpha}{2\pi} \int_{-\pi/\alpha}^{\pi/\alpha} E_{tot}^{\infty}(r, r_0, k_z, t) e^{-jk_z m\alpha} dk_z. \quad (4)$$

So $E_{tot}(r + m\alpha 1_z, r_0, t)$ at $r_0 + m\alpha 1_z$ produced by a single source at r in $n=0$ periodic cell can be calculated by $E_{tot}^{\infty}(r, r_0, k_z, t)$ which could be obtained by spectral FDTD with the periodic condition:

$$E_{tot}^{\infty}(r + \alpha 1_z, r_0, k_z, t) = E_{tot}^{\infty}(r, r_0, k_z, t) e^{-jk_z \alpha}. \quad (5)$$

From (1) we can find that $E_{tot}^{\infty}(r, r_0, k_z, t)$ is periodic with period $2\pi/\alpha$:

$$E_{tot}^{\infty}(r, r_0, k_z + i \frac{2\pi}{\alpha}, t) = E_{tot}^{\infty}(r, r_0, k_z, t), \quad i=0, 1, \dots \quad (6)$$

the property of conjugation,

$$E_{tot}^{\infty}(r, r_0, -k_z, t) = E_{tot}^{\infty}(r, r_0, k_z, t)^*. \quad (7)$$

For brevity we set:

$$\alpha = f_0, T_0 = 1/f_0, k_z = 2\pi\tau, \quad (8)$$

$$E_{tot}(r + n\alpha 1_z, r_0, t) = G(nf_0), E_{tot}^{\infty}(r, r_0, k_z, t) = g(\tau). \quad (9)$$

Substitute them into (4) and (6):

$$G(nf_0) = \frac{1}{T_0} \int_{-T_0/2}^{T_0/2} g(\tau) e^{-j2\pi n f_0 \tau} d\tau, \quad (10)$$

$$g(\tau + iT_0) = g(\tau) \quad (i=0, \pm 1, \dots). \quad (11)$$

By using the simple left endpoint rule of numerical integration, from (10) we have:

$$G_d(nf_0) = \frac{1}{N} \sum_{k=-N/2}^{N/2-1} g(kT) e^{-j2\pi n k/N}, \quad (12)$$

where $T = T_0/N$ is the sampling interval and N is the number of sampling points, substitute (8) and (9) into (12):

$$E_{tot}(r + n\alpha 1_z, r_0, t) = \frac{1}{N} \sum_{k=-N/2}^{N/2-1} E_{tot}^{\infty}(r, r_0, \frac{k}{N\alpha}, t) e^{-j2\pi n k/N}. \quad (13)$$

For the property of (7) that only half of the sampling points need to be computed here.

Suppose that $h(\tau)$ is the sampling function and its Fourier transform (FT) is $H(f)$, which can be shown:

$$h(\tau) = \sum_{k=-\infty}^{\infty} \delta(\tau - kT) \Leftrightarrow H(f) = \frac{1}{T} \sum_{k=-\infty}^{\infty} \delta(f - \frac{k}{T}), \quad (14)$$

$g(\tau)$ is a periodic continuous function, its FT is $G(f)$ can be expressed as:

$$G(f) = \sum_{n=-\infty}^{\infty} G(nf_0) \delta(f - nf_0). \quad (15)$$

Sample $g(\tau)$ with $h(\tau)$, the result is $g(\tau)h(\tau)$ and its FT can be expressed as [19]:

$$GH(f) = \sum_{n=-\infty}^{\infty} a_n \delta(f - nf_0), \quad (16)$$

$$\begin{aligned} a_n &= \frac{1}{T_0} \sum_{k=-N/2}^{N/2-1} g(kT) e^{-j2\pi n k/N} \\ &= \frac{G_d(nf_0)}{T} \end{aligned} \quad (17)$$

According to the convolution theorem, from (14) and (15) we have:

$$\begin{aligned} GH(f) &= \sum_{n=-\infty}^{\infty} G(nf_0) \delta(f - nf_0) * H(f) \\ &= \sum_{m=-\infty}^{\infty} \left[\sum_{n=-\infty}^{\infty} \frac{1}{T} G(nf_0) \delta(f - nf_0 - mNf_0) \right] \end{aligned} \quad (18)$$

Form (16) and (18) we get:

$$GH(\gamma f_0) = a_{\gamma} \quad (\gamma = 0, \pm 1, \dots), \quad (19)$$

$$GH(\gamma f_0) = \frac{1}{T} \sum_{m=-\infty}^{\infty} G[(\gamma + mN)f_0]. \quad (20)$$

So,

$$Ta_{\gamma} = \sum_{m=-\infty}^{\infty} G[(\gamma + mN)f_0]. \quad (21)$$

Substitute Ta_{γ} into (17) we finally get:

$$G_d(\gamma f_0) = \sum_{m=-\infty}^{\infty} G[(\gamma + mN)f_0]. \quad (22)$$

By considering the scaling factor T in (20) we can find $G_d(\gamma f_0)$ or $GH(\gamma f_0)$ is the final result we get according to the numerical integration and the DFS respectively. It is not the field of the observation point in the γ th cell we wanted, but a superposition of the field at a set of periodic observation points with period Nf_0 , which can be shown in Fig. 1 along z direction in space domain with the consideration of $f_0 = \alpha$. The mark \circ denote the observation points at positive z direction and \ominus denote the points at negative direction

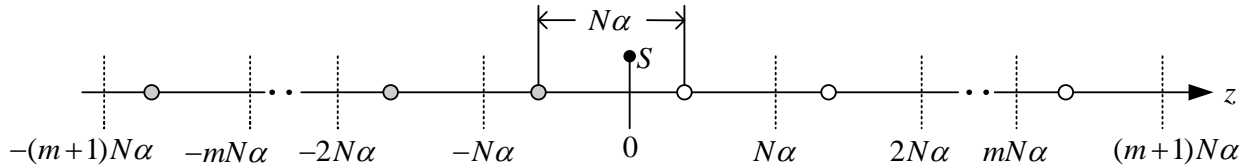


Fig. 1. Aliasing problem in space domain.

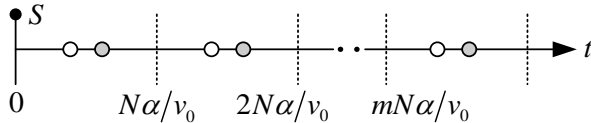


Fig. 2. Aliasing problem in time domain

To lessen the aliasing problem, the interval of the points in time domain shown in Fig. 2 should be apart from each other as much as possible, it can be achieved by increasing N or enlarging α , both of them will heavily increase the computational requirements. The effective interval T_d is its least distant to the adjacent points. From (23) and Fig. 2, any sampling point at cell γ except $\gamma \leq N/2$, the T_d can be shown as:

$$T_d = \min[2 \bmod(\gamma, N/2), N - 2 \bmod(\gamma, N/2)] \alpha / v_0. \quad (24)$$

We will get $T_{d \max} = N\alpha / (2v_0)$ when set the sampling points at $\gamma = (2m+1)N/4$. A further analysis shows that the two symmetric points overlap with each other when $\gamma = mN/2$, if the periodic cell is symmetric itself and both r_0 and r are at symmetric position, the field of the two symmetrical sampling points will be exactly equal, then the output of ASM-FDTD will be accurately double to the standard FDTD method, the effective interval will be $T_d = N\alpha / v_0$, and a minimum aliasing error will appear. But if $G(\gamma f_0)$ is infinite duration in time domain, the period of $N\alpha$ should tend to infinite to avoid the aliasing problem and there will be no advantage of ASM-FDTD.

if the source is set at the origin, where reveals the aliasing problem clearly in the ASM-FDTD.

Suppose the velocity of propagation is v_0 , convert (22) into time domain we obtain:

$$G_d(|\gamma| f_0 / v_0) = \sum_{m=-\infty}^{\infty} G[|\gamma + mN| f_0 / v_0]. \quad (23)$$

(23) can be shown by Fig. 2, here the mark \circ and \ominus denote the points in time domain corresponded to the observation points' position in Fig. 1, they are symmetric with each other at the points of $|mN\alpha| / (2v_0)$.

III. PRONY'S METHOD ANALYSIS AND EXTRAPOLATION

We now outline the Prony's method to fit the deterministic exponential model to the integral field $E_{tot}^{\infty}(r, r_0, k_z, t)$ in (2) with respect to every spectral sampling points k_z , which can be concisely expressed as the form:

$$\hat{E}_{tot}^{\infty}(r, r_0, k_z, t) = \sum_{m=1}^M h_m(k_z) e^{s_m(k_z)t}, \quad (25)$$

both $h_m(k_z)$ and $s_m(k_z)$ are complex here. The structure of the tunnel in the ASM-FDTD is periodic in the z direction shown in Fig. 3. The top curved interface is dealt with Conformal FDTD (CFDTD) [20], outside of the soil is truncated by convolution PML (CPML) [21] and the infinite periodic structure is truncated in the z direction with the PBC.

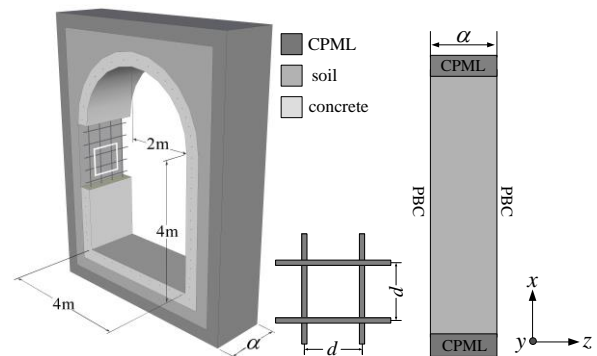


Fig. 3. Geometry of the periodic tunnel structure.

The parameters for the soil are dielectric constant $\varepsilon_r = 10.0$ and conductivity $\delta = 1.0e-3$ s/m. For the concrete $\varepsilon_{rc} = 6.0$ and $\delta_c = 5.0e-4$ s/m with the thickness $w = 0.2666$ m, the interval of the steel bar contained in the middle of concrete is $d = 0.1333$ m, the top vaulted part is a semicircle with the radius $r = 2.0$ m.

In the waveguide system [22], the excitation source is usually introduced robustly according to the propagation model such as TE10 and TM11. Though in this case we can't get the analytical model of the wave propagation, the way that the excitation sources induced in the waveguide system can still be employed here. It can be shown as:

$$E_{tan}^{n+1}(i, j, k_s) = E_{tan}^n(i, j, k_s) + f(i, j, k_s)g(t), \quad (26)$$

the subscript 'tan' denotes the E-field distributed in a transverse cross section at $z = k_s \Delta z$ of the tunnel structure in Fig. 3, $f(i, j, k_s)$ is the function of the field distribution and $g(t)$ refers to the time function determine the bandwidth of the sources. Here we set $f(i, j, k_s)$ as the model of TE10 in waveguide with the size of $a \times b = 4.0 \text{ m} \times 6.0 \text{ m}$. Though the model doesn't satisfy the boundary condition of the tunnel, we can consider that after some length propagation the model will be in a steady state which approach TE10 propagation model of the tunnel itself.

In ASM-FDTD the spectral points are sampled as the midpoint rule of integration that:

$$k_z = \xi_i = \frac{\pi}{\alpha} \left[-1 + \frac{2i-1}{N} \right], \quad (27)$$

the number of sampling points $N = 80$, for the property (7) of ASM-FDTD we compute the $E_{tot}^\infty(r, r_0, k_z, t)$ with respect to $\xi_i < 0$, period of the single cell $\alpha = 0.4$ m, $g(t)$ in (26) set to be a differential Gaussian electric pulse that $g(t) = E_0(t-t_0)\exp(4\pi(t-t_0)^2/\tau^2)$ with $\tau = 3.0$ ns, $E_0 = 1000$ V/m and $t_0 = 2\tau$, $f(i, j, k_s)$ located at the $x-y$ plane with $z = \alpha/2$, Yee cell size is given by $\Delta x = \Delta y = \Delta z = 0.01333$ m and the time step is $\Delta t = 22.16$ ps. The simulation is performed for 40000 time steps and a probe is placed at $(a/2, b/2, \alpha/2)$ to sample the y-component of the E-field.

In the Prony's method with respect to every spectral sampling point k_z in Brillouin zone, we set the model order $M = 18$, the analyzed data sampled since the 10000th time step to ensure the propagation model to settle down, the samples between 10000 to 15000 are used for estimating the exponential models, and the rest are used for prediction comparison, the sampling interval is 22 time steps that 227 modeling samples are

obtained. Figures 4 (a) and (b) show the comparisons of the extrapolation results based on the exponential models to the original result of TD field $E_{tot}^\infty(r, r_0, k_z, t)$ in ASM-FDTD for $\xi_i \alpha / \pi = -0.7625$ and $\xi_i \alpha / \pi = -0.2625$ in (27) respectively, from which we can find that they are in good agreement. It can be seen that in the implementation of the ASM-FDTD to simulate the EMP propagation in the periodic tunnel structure, the total field $E_{tot}^\infty(r, r_0, k_z, t)$ can be expressed as a linear superposition of complex exponentials with high accuracy, so we just determine the models of exponential from a finite early-time response, the later time response can be obtained by extrapolation from the exponential models. In this case, if the simulation had been stopped at 15000 time steps instead of the 40000 time steps, saving about 63% in terms of simulation time will be obtained, and this percentage would be much greater as the simulation time steps increase.

To further verify the accuracy of the exponential models, in (13) we set $n = 50$, Fig. 5 shows a comparison between the final numerical integration results obtained based on the exponential models and the ASM-FDTD method. From the figure, we can see they agree well with each other. And we find the aliasing problem in ASM-FDTD apparently, with a further analysis from Fig. 2 we know that the main waveform in the figure consist of the field at the probes of $(\gamma = 50, m = 5)$ and $(\gamma = 50, m = -6)$ in (22), which are 180m and -172m far away off the excitation source along the z direction respectively.

In equation (25), $h_m(k_z)$ and $s_m(k_z)$ can be defined as:

$$\begin{aligned} h_m(k_z) &= A_m(k_z) \exp(j\theta_m(k_z)) \\ s_m(k_z) &= \sigma_m(k_z) + j\omega_m(k_z) \end{aligned}, \quad (28)$$

A_m is the amplitude of the complex exponential, θ_m is the initial phase in radians, σ_m is the damping factor, and ω_m is the frequency. The model order $M = 18$, for concisely expressed we select two representative terms, Fig. 6 shows the parameters versus to the sampling spectral points corresponding to the order $m = 1$ and $m = 2$. In fact for the analyzed data is real, the complex exponentials must occur in complex conjugate pairs of equal amplitude, so the $M/2$ terms of the orders are significant. We can see the parameter $\omega_m(k_z)$ presents a very well continuous linear character, $A_m(k_z)$ and $\sigma_m(k_z)$ changes with different orders. Some discontinuous appear in those curves just at the points with the amplitude is low or the damping factor is high. For the parameter $\theta_m(k_z)$, it is so oscillatory of some orders even when the amplitude values are great.

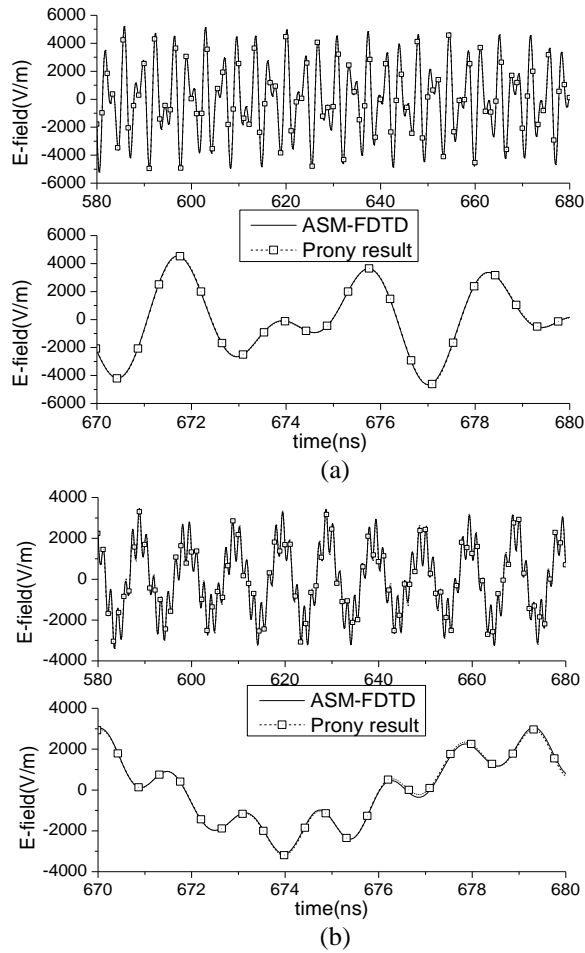


Fig. 4. Comparison of the integral field in ASM-FDTD and the exponential model result for: (a) $\xi_i \alpha / \pi = -0.7625$ and (b) $\xi_i \alpha / \pi = -0.2625$.

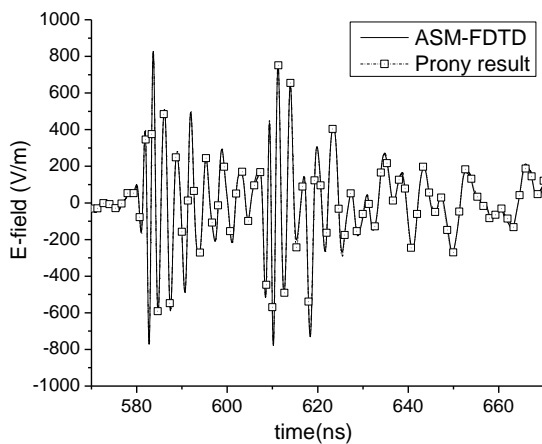


Fig. 5. Comparison of the $E_{tot}(r + n\alpha_{1z}, r_0, t)$ computed from the original time response and extrapolated time response with the exponential models.

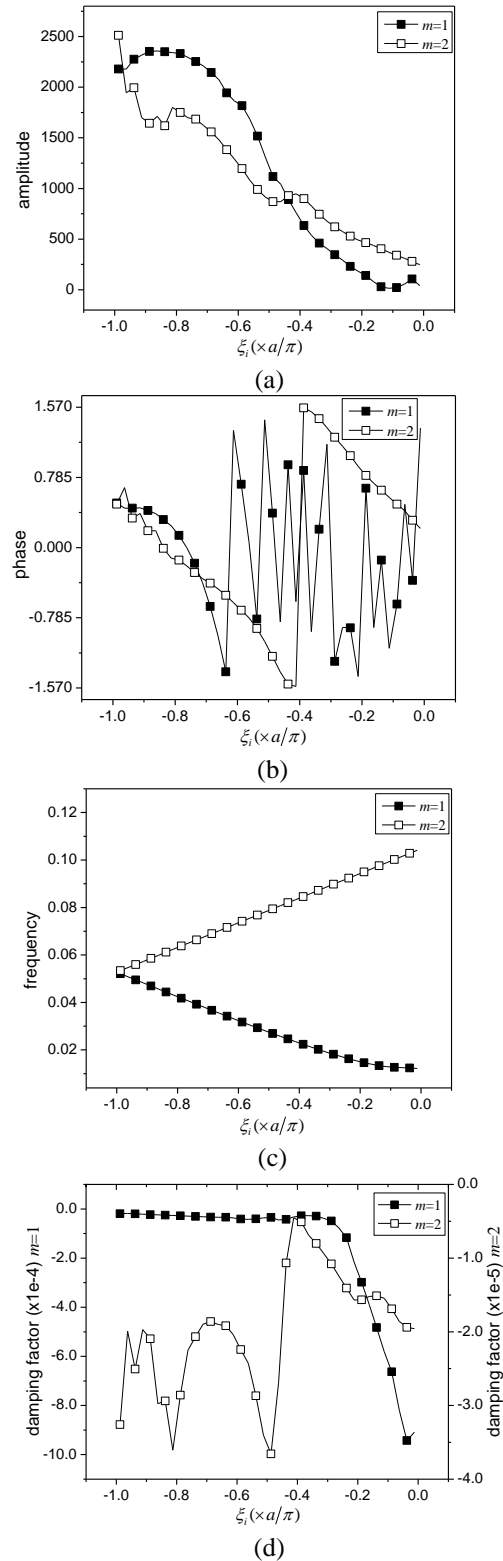


Fig. 6. Parameters of the exponential models versus the sampling spectral points in Brillouin zone, for expressing concisely here we set $\Delta t = 1$.

IV. ALIASING PROBLEM SOLVED BY INTERPOLATION

The aliasing problem in ASM-FDTD can be overcome by increasing the number of spectral sampling points with the cost of computational requirement. In Section III, we find that the integral field correspond to the sampling points can be represented by sums of damped exponentials, so if we obtain the parameters of the exponentials at every spectral points, the aliasing problem can then be solved. In this section we will estimate the parameters through interpolation, and then solve the aliasing problem in the ASM-FDTD. Cubic spline interpolation is employed here for its smooth graph and continuously turning tangent.

Figure 6 show the parameters of the exponential models versus the sampling spectral points, one point should be emphasized here is the parameter of phase, which is obtained by the function of inverse tangent. Correspond to the order $m=2$ we can obtain a smoother phase plots by unwrapping, but to the order of $m=1$ there are too many discontinuities that we can't set a correct jump tolerance to get the right unwrapped result. Furthermore the phase θ_m in (28) is at the range of $[-\pi, \pi]$, but the phase we get by inverse tangent is at $[-\pi/2, \pi/2]$, so it needs to combine other information such as the phase obtained by inverse cosine or sine to convert the phase from the range of $[-\pi/2, \pi/2]$ to the range of $[-\pi, \pi]$. So, we transform the equation in (28) to:

$$h_m(k_z) = p(k_z) + jq(k_z), \quad (29)$$

which can avoid the above problem properly. The parameters $p(k_x)$ and $q(k_z)$ corresponding to the order $m=1$ and $m=2$ are shown in Fig. 7.

Set the endpoint condition of the interpolation to be:

$$\begin{aligned} \rho_0 &= \rho_1 \\ \rho_{M+1} &= \rho_M \end{aligned} \quad (30)$$

Take the imaginary part of the amplitude as example, the resulting curve of interpolation is shown in Fig. 8. The other parameters have the same smooth results as the figure shown.

Based on the above analysis, a probe is set at $(a/2, b/2, l_z/2)$, according to the conclusion in Section II, we can set the number of sampling points:

$$N_{interp} = \frac{4(l-l_0)}{\alpha} \quad (l > l_0). \quad (31)$$

The first waveform of $n = N_{interp}/4$ in (13) is the transient field we want. Of course we can also set other algorithm according (23) just ensure $n\alpha = l - l_0$ and the effective interval in (24) is broad enough.

Figure 5 shows the aliasing results consist of the

field with probes of 180m and -172m distant to the excitation sources, follow the above criterions we set $N_{interp} = 360$ and $n = 90$. Figure 9 shows the comparison between the picked-up result and the MW-FDTD method where the length of window to be set 20m to lessen the truncation error. As seen from the figures, these results are consistent well to each other.

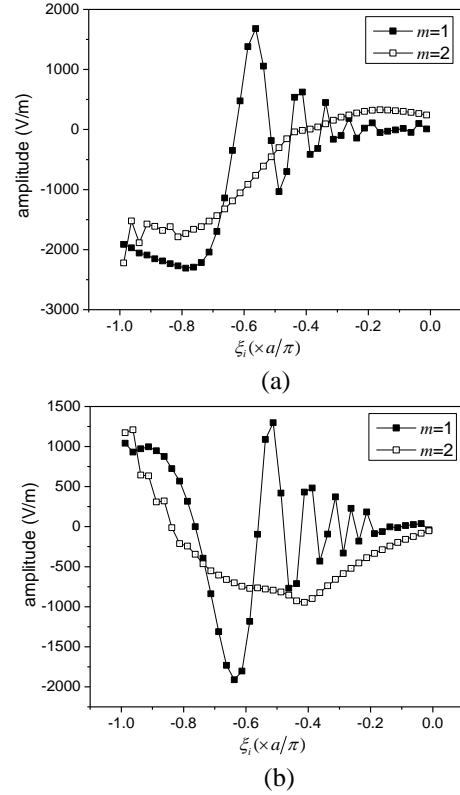


Fig. 7. Parameter of the complex amplitude versus the sampling spectral points in Brillouin zone: (a) the real part and (b) the imaginary part.

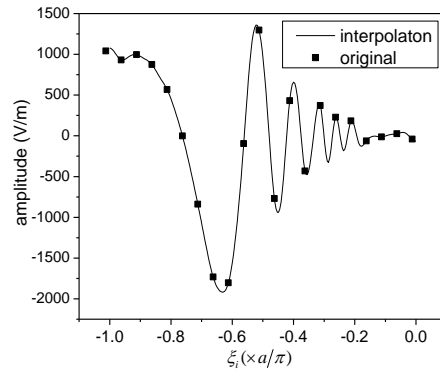


Fig. 8. The cubic spline interpolation result based on the imaginary part of the amplitude.

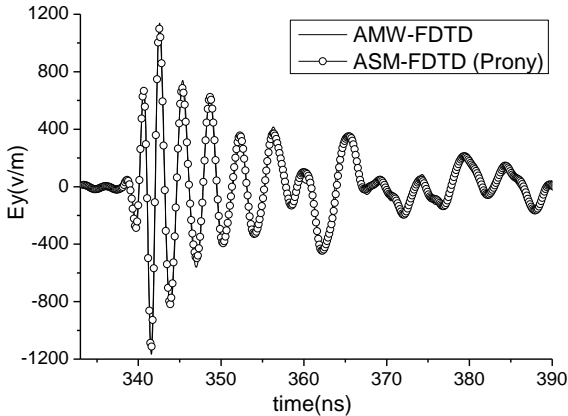


Fig. 9. Comparison of picked-up result from the aliasing output of ASM-FDTD with the MW-FDTD result.

V. CONCLUSION

In this paper, the aliasing problem in the ASM-FDTD has been presented in detail. To overcome the problem, the Prony's method is employed to fit an exponential model with the total field of ASM-FDTD and a good agreement is observed. By extrapolating the total field based on the exponential model and interpolating the exponential parameters correspond to the spectral points in Brillouin zone, the computational requirement is drastically reduced and the aliasing problem is solved. Results show good agreement with the MW-FDTD. This method can also be applied to deal with the aliasing problem in the implementation of the ASM-FDTD to simulate some other periodic structures, and some other interpolation methods and curve-fitting approximation [23] maybe more appropriate for this problem.

ACKNOWLEDGMENT

This work was supported by Chinese National Science Foundation under Grant No. 60971063.

REFERENCES

- [1] D. G. Dudley, M. Lienar, S. F. Mahmud, and P. Degauque, "Wireless propagation in tunnels," *IEEE Antennas Propag. Magazine*, vol. 49, pp. 11-26, 2007.
- [2] Y. P. Zhang, "Novel model for propagation loss prediction in tunnels," *IEEE Trans. Veh. Technol.*, vol. 52, pp. 1308-1314, 2003.
- [3] E. Heyman, R. Kastner, and R. W. Ziolkowski, "Hybrid Ray-FDTD moving window approach to pulse propagation," *Journal of Computational Physics*, vol. 138, pp. 480-500, 1997.
- [4] J. F. Liu, X. L. Xi, G. B. Wan, and L. L. Wang, "Simulation of electromagnetic wave propagation through plasma sheath using the moving window finite-difference time-domain method," *IEEE Trans. on Plasma Science*, vol. 39, pp. 852-855, 2011.
- [5] G. S. Ching, M. Ghorraishi, M. Landmann, and H. Sakamoto, "Wideband polarimetric directional propagation channel analysis inside an arched tunnel," *IEEE Trans. Antennas Propagat.*, vol. 57, pp. 760-767, 2009.
- [6] K. Guan, Z. Zhong, B. Ai, and C. Briso-Rodriguez, "Complete propagation model in tunnels," *IEEE Antennas and Wireless Propagation Letters*, vol. 12, pp. 741-743, 2013.
- [7] K. S. Yee, "Numerical solution of initial boundary value problems involving Maxwell's equations in isotropic media," *IEEE Trans. Antennas Propagat.*, vol. 14, pp. 302-307, 1966.
- [8] A. Taflov and S. C. Hagness, *Computational Electrodynamics: The Finite-Difference Time-Domain Method*. 2nd ed., Boston, MA: Artech House, 2000.
- [9] J. W. Schuster, K. C. Wu, R. R. Ohs, and R. J. Luebbers, "Application of moving window FDTD to predicting path loss over forest covered irregular terrain," *Antennas and Propagation Society International Symposium*, pp. 1607-1610, 2004.
- [10] Y. Wu and I. Wassell, "Introduction to the segmented finite-difference time-domain method," *IEEE Trans. on Magnetics*, vol. 45, pp. 1364-1367, 2009.
- [11] M. M. Rana and A. S. Mohan, "Segmented locally one dimensional FDTD method for EM propagation inside large complex tunnel environments," *IEEE Trans. on Magnetics*, vol. 48, pp. 223-226, 2012.
- [12] F. Akleman and L. Sevgi, "Realistic surface modeling for a Finite Difference Time Domain wave propagator," *IEEE Trans Antennas Propagat.*, vol. 51, no.7, July 2003.
- [13] Y. Xiaoshuan and B. Chen, "Application of MW-FDTD to simulate the electromagnetic pulse (EMP) propagation in tunnel," *CEEM'2009*, pp. 200-203, 2009.
- [14] R. Qiang, J. Chen, F. Caploino, and D. R. Jackson, "ASM-FDTD: A technique for calculating the field of a finite source in the presence of an infinite periodic artificial material," *IEEE Microw. Wireless Compon. Lett.*, vol. 17, no. 4, Apr. 2007.
- [15] R. Qiang, J. Chen, and F. Yang, "FDTD simulation of infrared FSS transmission spectrum from oblique incidence," in *Proc. IEEE Antennas Propag. Soc. Int. Symp.*, pp. 2715-2718, June 2006.
- [16] B. A. Munk and G. A. Burrell, "Plane-wave expansion for arrays of arbitrarily oriented piecewise linear elements and its application in

determining the impedance of a single linear antenna in a lossy half-space," *IEEE Trans. Antennas Propag.*, vol. AP-27, no. 5, pp. 331-343, May 1979.

- [17] A. Aminian and Y. Rahmat-Sammii, "Spectral FDTD: A novel technique for the analysis of oblique incident plane wave on periodic structures," *IEEE Trans. Antennas Propag.*, vol. 54, no. 6, pp. 1818-1825, June 2006.
- [18] S. L. Marple, *Digital Spectral Analysis with Applications*. Englewood Cliffs, NJ: Prentice-Hall, Inc., Ch. 11, 1987.
- [19] E. O. Brigham, *The Fast Fourier Transform*. Englewood Cliffs, NJ: Prentice-Hall, Inc., Ch. 5-6, 1974.
- [20] W. Yu and R. Mittra, "A conformal finite difference time domain technique for modeling curved dielectric surfaces," *IEEE Microw. and Wireless Compon. Lett.*, vol. 11, no. 1, Jan. 2001.
- [21] J. Alan Roden and S. D. Gedney, "Convolution PML: An efficient FDTD implementation of the CPF-CPML for arbitrary media," *Microw. and Optl. Technol. Lett.*, vol. 27, no. 5, Dec. 5, 2000.
- [22] A. Taflove, *Computational Electrodynamics: The Finite-Difference Time-Domain Method*. Boston, MA: Artech House, Ch. 5, 1995.
- [23] A. K. Shaw, "Optimal identification of discrete-time systems from impulse response data," *IEEE Trans Signal Processing*, vol. 42, no. 1, Jan. 1994.



Yun-Fei Mao was born in Zhejiang Province, China, in 1984. He received the B.S. degrees, the M.S. degree and the Ph.D. degree in Electric systems from Nanjing Engineering Institute, Nanjing, China, in 2006, 2009 and 2013 respectively. He is currently working in China Satellite Maritime Tracking and Control Department, Yuan Wang III, Jiangyin 214400, China. His research interests include computational electromagnetic and electro-magnetic tracking.



Hong-Bing Wu was born in Jiangsu Province, China, in 1987. He is currently working in China Satellite Maritime Tracking and Control Department, Jiangyin 214400, China. His research interests include inertial navigation and electromagnetic tracking.



Jia-Hong Chen was born in Jiangsu, China, in 1969. He received the B.S. and M.S. degrees in National University of Defense Technology, Changsha, China, in 1982 and 1987, respectively, and the Ph.D. degree in Control Engineering from Xi'an Jiao Tong University, Xi'an, China. His research interests include electromagnetics and electromagnetic tracking.



Xu-Wei Su was born in Hubei Province, China, in 1983. He received the B.S. in Xidian University, Xi'an, China, in 2001. He is currently working in China Satellite Maritime Tracking and Control Department, Jiangyin 214400, China. His research interests include electromagnetics and electromagnetic tracking.

High Isolated X-Band MIMO Array Using Novel Wheel-Like Metamaterial Decoupling Structure

Jianfeng Jiang¹, Yinfeng Xia¹, and Yingsong Li^{1,2,*}

¹ College of Information and Communication Engineering
Harbin Engineering University, Harbin 150001, China

² Key Laboratory of Microwave Remote Sensing, National Space Science Center
Chinese Academy of Sciences, Beijing 100190, China

*liyingsong@ieee.org

Abstract — A compact broadband antenna array with two identical antenna elements is proposed to realize high isolation that is realized via integrating a new wheel-like meta-material structure into the closely set antenna elements. The wheel-like meta-material decoupling structure is settled between the two antenna elements to reduce the coupling from the nearby antenna element. The proposed antenna array is designed, optimized, fabricated and measured in a chamber. The achieved results verify that the developed antenna is able to provide a wide bandwidth ranging from 8 GHz to 12 GHz. Using the developed wheel-like meta-material decoupling structure, not only the designed antenna array maintains performance of MIMO array, but also the coupling is reduced to be less than -20 dB within the X-band. Therefore, the proposed antenna array is a suitable candidate for X-band MIMO radar system applications to get a high isolation between the elements.

Index Terms — High isolation, low mutual coupling, meta-material, MIMO antenna, wideband.

I. INTRODUCTION

With the rapid evolution of the wireless communications and radar technology, the bandwidth requirements for these systems become to be wider and wider to obtain high data speed and resolution [1,2]. Thus, the wideband technology has been paid lots of attentions and gotten significant evolutions [3,4]. However, in wideband systems, reflection and diffraction can cause multipath fading problems, and hence, many researchers have moved to study MIMO technology to find out solutions for these problems. On the other hand, the MIMO technology can also improve the channel capacity and system reliability [5-7]. As a result, the combination of broadband technology and MIMO technology has drawn great concern in recent years.

In fact, with the increasing number of the antennas

in the MIMO system, the distance between the antenna elements becomes to be narrow in the miniaturized devices, resulting in serious coupling affect from neighbored antenna elements [8-9]. To maintain the independence of each antenna elements in the MIMO system within a limited space, it is one of the urgent difficulties to overcome mutual coupling from the adjacent antenna elements. Therefore, the many recent research works are mainly focused on designing miniaturized MIMO antenna array integrating with decoupling structure.

In order to implement a high isolation MIMO antenna array, the defected ground structure (DGS) can change the current path on the ground plane to equal the combination of inductance and capacitance, modifying the electric field distribution between the transmission line and the ground plane to achieve the purpose of decoupling [10-12]. Also, the neutralization lines and other decoupling network have been presented to achieve the good isolation by introducing counter phased current against the excited antenna in development of the MIMO antenna array [13-16]. Recently, the meta-material structures have been considered to reduce the isolation between the adjacent antenna elements. The meta-material is a class of artificial composite structural material that can respond to external electromagnetic fields, which includes left-hand material, Electromagnetic Band Gap (EBG) structure, the Frequency Selective Surface (FSS) and so on. In [17-20], EBG structure have been proposed to reduce the mutual coupling using the suppression of surface waves. In [21-23], the FSS is suspended over the antenna array to increase isolation performance. However, these meta-materials cannot cover a wide bandwidth for X-band communication applications.

In this article, a compact wideband MIMO antenna with a novel wheel-like meta-material structure is presented and analyzed numerically and experimentally. The designed MIMO antenna array is made up of

two identical rectangular patch antennas on the same substrate, and the proposed wheel-like meta-material structure, which has three cells, is inserted into the middle of the antenna elements. The proposed MIMO antenna array is created, modeled, optimized, fabricated and measured to verify the effectiveness of the proposed MIMO array. The results show that the proposed MIMO antenna array can cover the frequency band of 8 GHz and 12 GHz, with omnidirectional radiation patterns and high isolation of 20 dB.

This paper is organized as follows: in Section II, the configuration of the MIMO antenna array and meta-material structure are proposed. Section III analyzes and discusses the simulated and measured results of the developed MIMO antenna array. Finally, a conclusion is given in Section IV.

II. DESIGN OF THE PROPOSED WIDEBAND MIMO ANTENNA ARRAY

A. The proposed MIMO antenna array structure

The configuration of the proposed MIMO antenna array is modeled in HFSS 13.0 and is shown in Fig. 1. As shown in Fig. 1, the dimensions of antenna array are $26 \times 18 \times 1.6 \text{ mm}^3$, and the two patch antenna elements are printed on a substrate with permittivity of 4.4, a loss tangent of 0.02 and a thickness of $h=1.6 \text{ mm}$. The proposed antenna is fed by microstrip line with a width of 3 mm.

In order to obtain wide bandwidth, a stub is integrated with the ground plane. Fig. 2 shows that the stub can increase the bandwidth. Furthermore, there are two small gaps in each patch antenna element to obtain the good matching by controlling the width and length of gaps.

Finally, the proposed MIMO antenna array is optimized using the HFSS to let the MIMO array operate at the X-band, and the optimized dimension of the MIMO array is listed in Table 1.

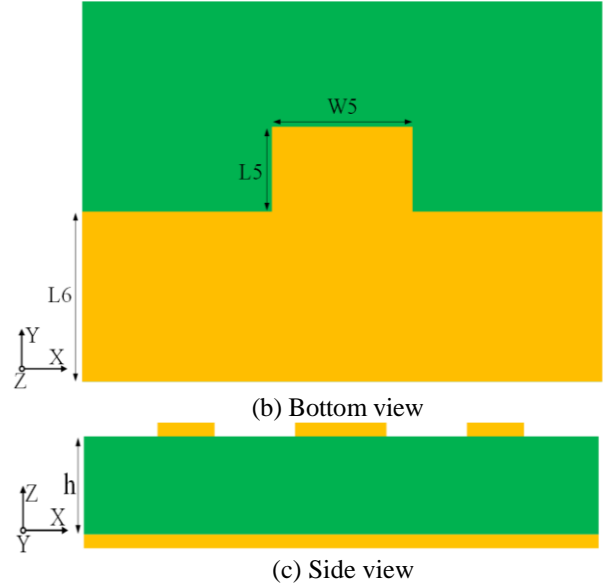
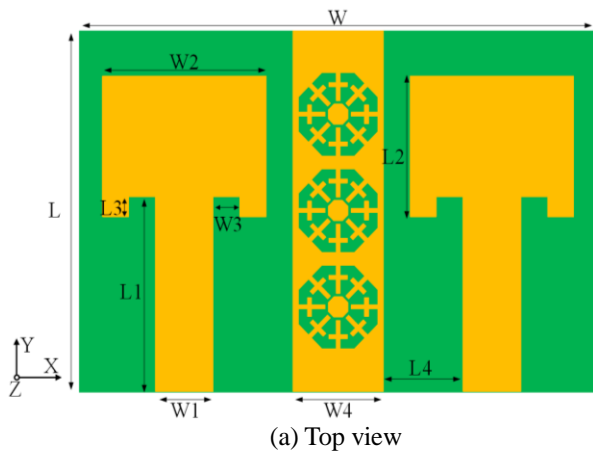


Fig. 1. Geometry structure of the proposed MIMO antenna array integrating with wheel-like meta-material structure.

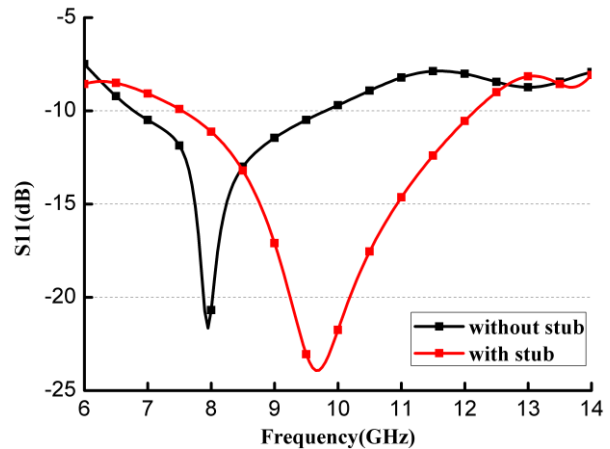


Fig. 2. S_{11} of the wideband MIMO antenna array with and without stub.

Table 1: Optimized dimensions of the MIMO antenna array (Unit: mm)

Parameters	W	W1	W2	W3	W4
Values	26	3	8.5	1.4	4.5
Parameters	W5	L	L1	L2	L3
Values	7	18	9.7	7	1
Parameters	L4	L5	L6	h	
Values	4.25	4	8	1.6	

B. Meta-material decoupling structure

In Fig. 1, there is a wheel-like meta-material

structure between the proposed antenna elements. However, there is still having surface wave interferences that will affect the performance of the other antenna elements. If the influences of surface waves can be reduced, the characteristics of the MIMO antenna array will be improved. One effective method is to increase the distance between the two antennas, but this method does not meet the trend of miniaturization of electronic devices and is limited by the space in the portable devices. On the other hand, adding a decoupling network in the MIMO antenna array to suppress the propagation of surface waves has attracted much more attention in recent years. As we know, the meta-material structure has the property of suppressing surface waves, and hence, it can be used in the MIMO antenna array to reduce the mutual coupling between the MIMO antenna elements and can maintain good performance with closely antenna elements.

A meta-material decoupling cell used in the proposed MIMO antenna array is shown in Fig. 3, which is comprised of a copper patch with an octagon slot, eight crosses and a small octagon patch in the center. The diagonal length (W7) of the largest octagon slot is 4.5 mm and the diagonal length (W8) of the small octagon is 1.1 mm. The eight identical crosses are connected to the sides of the octagonal slot, the width (v) of the crosses is 0.2 mm. In addition, the length (L9) of the crosses is 1.4 mm, and the width (W9) of the crosses is 0.95 mm.

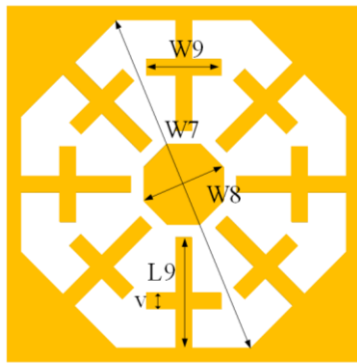


Fig. 3. Geometry structure of the proposed wheel-like meta-material cell.

In order to better validate the effectiveness of the proposed wheel-like meta-material cell, the meta-material cell is investigated by HFSS, and its effective parameters, such as equivalent permittivity ϵ and equivalent permeability μ , can be calculated from S-parameters [24], which is presented in formula (1) - (4):

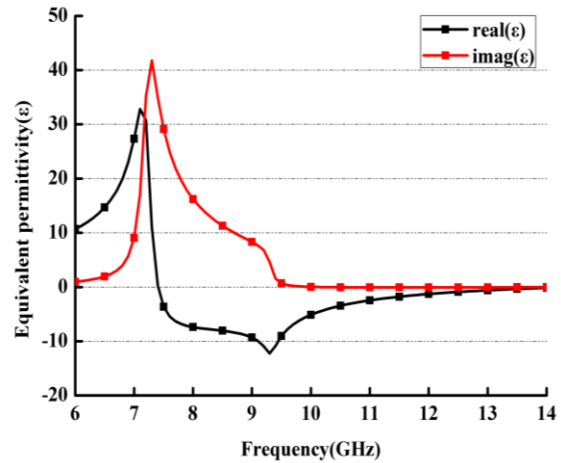
$$z = \pm \sqrt{\frac{(1+S_{11})^2 - S_{21}^2}{(1-S_{11})^2 - S_{21}^2}}, \quad (1)$$

$$e^{jnk d} = \frac{S_{21}}{1 - S_{11} \frac{z-1}{z+1}}, \quad (2)$$

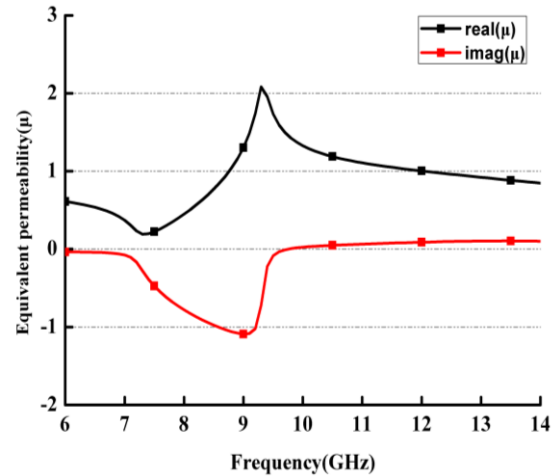
$$\epsilon = \frac{n}{z}, \quad (3)$$

$$\mu = n \cdot z, \quad (4)$$

where k is the wave number in free space, d is the thickness of the meta-material structure cell, n is the refractive index, z is the wave impedance, ϵ is the equivalent permittivity, and μ is the equivalent permeability.



(a) Equivalent permittivity



(b) Equivalent permeability

Fig. 4. Equivalent permittivity and permeability of the proposed meta-material cell.

Therefore, the equivalent permittivity and permeability of the meta-material cell can be calculated and shown in Fig. 4. It is noticed that the designed cell has a negative permittivity and positive permeability in entire X-band, which means that the designed meta-

material cell can meet the meta-material properties. According to the equation (5),

$$k^2 = \omega^2 \mu \epsilon, \quad (5)$$

which is the dispersive equation of plane electromagnetic waves, it can be concluded that k has no solution, result in suppressing the propagation of surface waves and achieving the purpose of decoupling. Thus, the proposed meta-material structure can be suitable for improve the isolation of X-band MIMO antenna array.

III. ANALYSES RESULTS

The proposed wideband MIMO antenna array is constructed and analyzed based on the HFSS 13.0. To further verify the analysis effectiveness, the proposed antenna array is fabricated and presented in Fig. 5. The measured results were obtained using vector network analyzer (VNA) E5063A.

The simulation and measurement S-parameters including the reflection coefficient (S_{11}) and transmission coefficient (S_{12}) are shown in Fig. 6. It is noted that the proposed wideband MIMO antenna array without the proposed wheel-like meta-material decoupling structure has a bandwidth ranging from 8 GHz to 12 GHz. By using the proposed wheel-like meta-material decoupling structure, the bandwidth of the proposed MIMO antenna array moves to 7 GHz-12 GHz. That is to say that the operating frequency band moves to low frequency, and there is another resonance mode is appeared because of the resonance of the proposed wheel-like meta-material decoupling structure. It is noticed that mutual coupling that is measured using S_{12} is reduce from -13 dB to less than -20 dB in the operating band of the proposed MIMO antenna array. The MIMO antenna can cover the X-band if we consider S_{11} is less than -10 dB. It is also found that the resonance frequency is 9.7 GHz for the MIMO antenna array without the wheel-like meta-material decoupling structure, while there are two resonance frequencies locating at 9.7 GHz and 10.35 GHz, respectively.

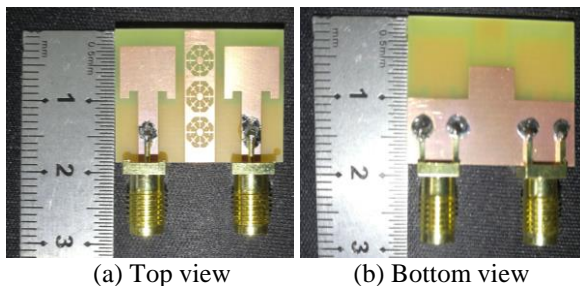
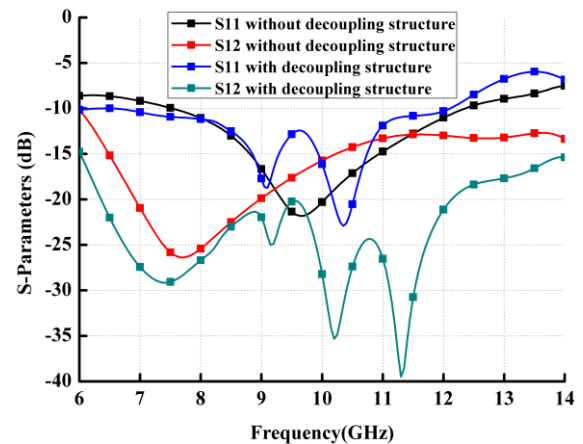


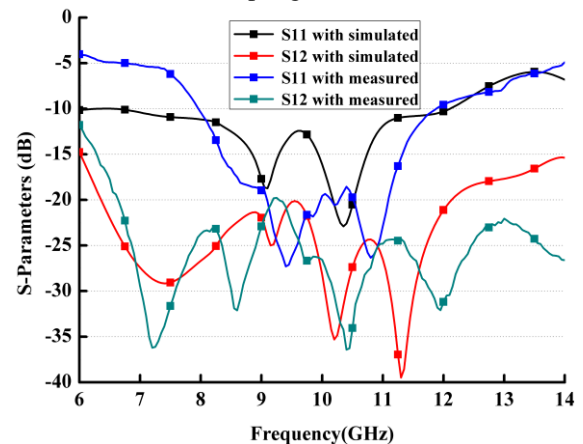
Fig. 5. Photograph of the fabricated broadband MIMO antenna.

Figure 6 (b) depicts the comparison of the simulation and measurement of the S-parameters for

proposed MIMO antenna array with the wheel-like meta-material decoupling structure. In the X-Band, S_{11} is still less than -10 dB from the measurement, while the S_{12} is less than -20 dB. It is found that the two resonance frequencies are shifted to the high frequency, which may be caused by the inaccuracy of the dimensions of the fabrication. However, the simulated and the measured results meet well in the operating band, which tells us that the proposed wheel-like meta-material decoupling structure can effectively reduce the mutual coupling between the antenna elements and maintains the bandwidth of the MIMO antenna array.



(a) With/without the proposed wheel-like meta-material decoupling structure



(b) Simulated and measured S-parameters of the proposed MIMO antenna array

Fig. 6. S_{11} and S_{12} of the wideband MIMO antenna array.

Figure 7 shows the xoz -plane and yoz -plane radiation patterns of the designed MIMO antenna array with comparison of the simulated and measured results. In the measurement, one antenna element is fed, while the other one is terminated. The measurements agree well with the simulation, which show an acceptable agreement with simulations. It was observed that

the radiation pattern in the xoz-plane is almost omnidirectional in Fig. 7. In the yoz-plane, the radiation patterns are tended to be quasi-directional ones which is similar to the conventional monopole antenna. But the antenna pattern gradually deteriorates with the frequency increasing, and there are some distortions in the high frequency, which are tolerable changes at 10 GHz and 12 GHz shown in Figs. 7 (b) and (c). The reason may be that the added decoupling structure gives a little effects on the direction of the electric field, resulting in the antenna radiation performance to be affected.

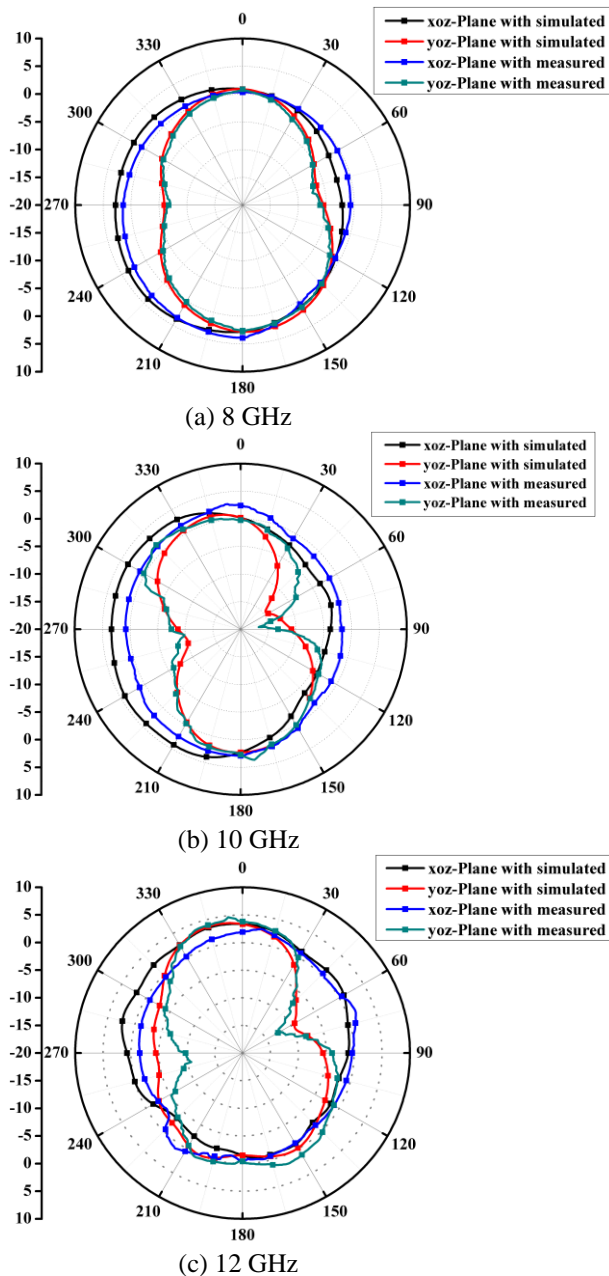


Fig. 7. The simulated and measured radiation patterns.

In Fig. 8, the gain of the proposed MIMO antenna with wheel-like meta-material structure ranges from 2.67 dBi to 4.62 dBi over the X-band, and the variation in the gain values is found to be less than 2 dBi. Moreover, the maximum gain is 4.62 dBi at 10 GHz, and the minimum gain is 2.67 dBi at 9.4 GHz. The reason may be that the impedance does not match at 9.4 GHz, resulting in part of the energy to be reflected on the feedline and not to be effectively radiated from the antenna.

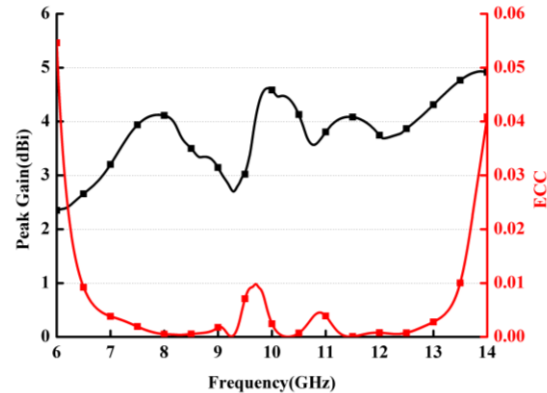


Fig. 8. Gain and ECC of the proposed MIMO antenna array.

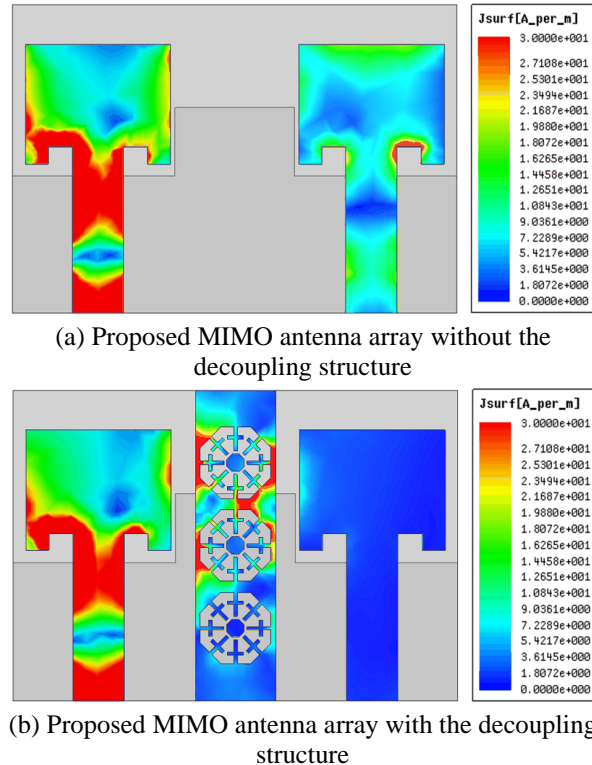


Fig. 9. Surface current distribution on the proposed MIMO antenna array at 11GHz.

The envelope correlation coefficient (ECC) is also important parameter to verify the performance of MIMO antenna. Using the equation in [25], we know that the ECC must be zero in ideal, which is not possible in free space environment. In Fig. 8, the obtained ECC for proposed MIMO antenna array with wheel-like meta-material structure is less than 0.01 within the X-band, which indicates that there is very low correlation between the two ports.

To better demonstrate the effectiveness of the proposed meta-material decoupling structure, the current distribution on the antenna is shown in Fig. 9. In Fig. 9 (a), the current distributions on the proposed MIMO antenna without meta-material decoupling structure is presented, which coupled to the adjacent antenna element when the left antenna is excited. After integrating the proposed meta-material decoupling structure into the middle of the two antenna elements, the surface current on the right antenna is observed to be significantly reduced in Fig. 9 (b). Thus, it is concluded that the proposed wheel-like meta-material decoupling structure can block the surface waves from the left antenna to the right antenna.

IV. CONCLUSION

A compact wideband MIMO antenna array based on wheel-like meta-material structure with the size of $26 \times 18 \times 1.6 \text{ mm}^3$ has been proposed for X-band communication applications. To suppress mutual coupling between the proposed MIMO antenna elements, a wheel-like meta-material decoupling structure is developed and integrated into the middle of the MIMO antenna array. The MIMO antenna array is designed, simulated, optimized, fabricated and measured, and the results demonstrated that the proposed MIMO antenna array has a wide bandwidth to cover the entire X-band with a fractional bandwidth of 40% and provides a high isolation that is better than 20dB. In addition, the peak gain ranges from 2.67 dBi to 4.62 dBi within the X-band. Moreover, ECC is less than 0.01. Hence, the proposed antenna array is suitable for X-band MIMO radar systems. In the future, the proposed technique can be used for developing the dual-band or dual-polarization low mutual coupling MIMO arrays [26-27], beamforming [28], direction of arrival (DOA) [29-30] using adaptive methods [31-37].

ACKNOWLEDGMENTS

This paper is supported by the National Key Research and Development Program of China (2016YFE0111100), Key Research and Development Program of Heilongjiang (GX17A016), China Post-doctoral Science Foundation (2017M620918, 2019T120134), the Fundamental Research Funds for the Central Universities (HEUCFG201829, 2072019CFG0801).

REFERENCES

- [1] T. Kaiser, F. Zheng, and E. Dimitrov, "An overview of ultra-wide-band systems with MIMO," *Proceedings of the IEEE*, vol. 97, no. 2, pp. 285-312, 2009.
- [2] Y. Li, W. Li, and W. Yu, "A multi-band/UWB MIMO/diversity antenna with an enhance isolation using radial stub loaded resonator," *Applied Computational Electromagnetics Society Journal*, vol. 28, no. 1, pp. 8-20, 2013.
- [3] A. Iqbal, O. A. Saraereh, A. W. Ahmad, and S. Bashir, "Mutual coupling reduction using F-shaped stubs in UWB-MIMO antenna," *IEEE Access*, vol. 6, pp. 2755-2759, 2018.
- [4] L. Liu, S. Cheung, and T. Yuk, "Compact MIMO antenna for portable devices in UWB applications," *IEEE Transactions on Antennas and Propagation*, vol. 61, no. 8, pp. 4257-4264, 2013.
- [5] S. Luo, Y. Li, Y. Xia, G. Yang, L. Sun, and L. Zhao, "Mutual coupling reduction of a dual-band antenna array using dual-frequency metamaterial structure," *Applied Computational Electromagnetics Society Journal*, vol. 34, no. 3, pp. 403-410, 2019.
- [6] Y. Kong, Y. Li, and W. Yu, "A minimized MIMO-UWB antenna with high isolation and triple band-notched functions," *Frequenz*, vol. 70, no. 11-12, pp. 463-471, 2016.
- [7] S. Luo, Y. Li, Y. Xia, and L. Zhang, "A low mutual coupling antenna array with gain enhancement using metamaterial loading and neutralization line structure," *Applied Computational Electromagnetics Society Journal*, vol. 34, no. 3, pp. 411-418, 2019.
- [8] J. Li, X. Zhang, Z. Wang, X. Chen, J. Chen, Y. Li, and A. Zhang, "Dual-band eight-antenna array design for MIMO applications in 5G mobile terminals," *IEEE Access*, vol. 7, pp. 71636-71644, 2019.
- [9] T. Jiang, T. Jiao, and Y. Li, "A low mutual coupling MIMO antenna using periodic multi-layered electromagnetic band gap structures," *Applied Computational Electromagnetics Society Journal*, vol. 33, no. 3, 2018.
- [10] R. Anitha, V. P. Sarin, P. Mohanan, and K. Vasudevan, "Enhanced isolation with defected ground structure in MIMO antenna," *Electronics Letters*, vol. 50, no. 24, pp. 1784-1786, 2014.
- [11] C. Luo, J. Hong, and L. Zhong, "Isolation enhancement of a very compact UWB-MIMO slot antenna with two defected ground structures," *IEEE Antennas and Wireless Propagation Letters*, vol. 14, pp. 1766-1769, 2015.
- [12] N. Kishore, A. Prakash, and V. Tripathi, "A multiband microstrip patch antenna with defected ground structure for its applications," *Microwave*

- and *Optical Technology Letters*, vol. 58, no. 12, pp. 2814-2818, 2016.
- [13] A. Najam, Y. Duroc, and S. Tedjni, "UWB-MIMO antenna with novel stub structure," *Progress In Electromagnetics Research C*, vol. 19, pp. 245-257, 2011.
- [14] J. Li, Q. Chu, Z. Li, and X. Xia, "Compact dual band-notched UWB MIMO antenna with high isolation," *IEEE Transactions on Antennas and Propagation*, vol. 61, no. 9, pp. 4759-4766, 2013.
- [15] S. Zhang and G. F. Pedersen, "Mutual coupling reduction for UWB MIMO antennas with a wideband neutralization line," *IEEE Antennas and Wireless Propagation Letters*, vol. 15, pp. 166-169, 2016.
- [16] H. Huang and J. Wu, "Decoupled dual-antenna with three slots and a connecting line for mobile terminals," *IEEE Transactions on Antennas and Propagation*, vol. 14, pp. 1730-1733, 2015.
- [17] Q. Li, A. Feresidis, M. Mavridou, and P. Hall, "Miniaturized double-layer EBG structures for broadband mutual coupling reduction between UWB monopoles," *IEEE Transactions on Antennas and Propagation*, vol. 63, no. 3, pp. 1170-1173, 2015.
- [18] T. Jiang, T. Jiao, and Y. Li, "Array mutual coupling reduction using L-loading E-shaped electromagnetic band gap structures," *International Journal of Antennas and Propagation*, vol. 2016, pp. 1-9, 2016.
- [19] F. Yang, K. Ma, Y. Qian, and T. Itoh, "A uniplanar compact photonic-bandgap (UC-PBG) structure and its applications for microwave circuit," *IEEE Transactions on Microwave Theory and Techniques*, vol. 47, no. 8, pp. 1509-1514, 1999.
- [20] K. Niraj and K. Usha, "MIMO antenna H-plane isolation enhancement using UC-EBG structure and metal line strip for WLAN applications," *Radioengineering*, vol. 28, no. 2, pp. 399-406, 2019.
- [21] Y. Ranga, L. Matekovits, K. P. Esselle, and A. R. Weily, "Multioctave frequency selective surface reflector for ultrawideband antennas," *IEEE Antennas and Wireless Propagation Letters*, vol. 10, pp. 219-222, 2011.
- [22] X. Zhu, X. Yang, Q. Song, and B. Lui, "Compact UWB-MIMO antenna with metamaterial FSS decoupling structure," *EURASIP Journal on Wireless Communications and Networking*, 2017.
- [23] A. Mansoor and R. Amiri, "Mutual coupling reduction of closely spaced MIMO antenna using frequency selective surface based on meta-materials," *Applied Computational Electromagnetics Society Journal*, vol. 32, no. 12, pp. 1064-1068, 2017.
- [24] X. Chen, T. M. Grzegorzczuk, B. Wu, J. Pacheco, and J. Kong, "Robust method to retrieve the constitutive effective parameters of metamaterials," *Physical Review E*, vol. 70, no. 1, 2004.
- [25] R. Tian, B. K. Lau, and Z. Ying, "Multiplexing efficiency of MIMO antennas," *IEEE Antennas and Wireless Propagation Letters*, vol. 10, pp. 183-186, 2011.
- [26] F. Liu, J. Guo, L. Zhao, G.L. Huang, Y. Li, and Y. Yin, "Dual-band metasurface-based decoupling method for two closely packed dual-band antennas," *IEEE Transactions on Antennas and Propagation*, 10.1109/TAP.2019.2940316.
- [27] J. Guo, F. Liu, L. Zhao, Y. Yin, G. L. Huang, and Y. Li, "Meta-surface antenna array decoupling designs for two linear polarized antennas coupled in H-plane and E-plane," *IEEE Access*, vol. 7, pp. 100442-100452, 2019.
- [28] W. Shi, Y. Li, L. Zhao, and X. Liu, "Controllable sparse antenna array for adaptive beamforming," *IEEE Access*, vol. 7, pp. 6412-6423, 2019.
- [29] X. Zhang, T. Jiang, Y. Li, and X. Liu, "An off-grid DOA estimation method using proximal splitting and successive nonconvex sparsity approximation," *IEEE Access*, vol. 7, pp. 66764-66773, 2019.
- [30] X. Zhang, T. Jiang, Y. Li, and Y. Zakharov, "A novel block sparse reconstruction method for DOA estimation with unknown mutual coupling," *IEEE Communications Letters*, vol. 23, no. 10, pp. 1845-1848, 2019.
- [31] W. Shi, Y. Li, and Y. Wang, "Noise-free maximum correntropy criterion algorithm in non-gaussian environment," *IEEE Transactions on Circuits and Systems II: Express Briefs*, 10.1109/TCSII.2019.2914511.
- [32] Y. Li, Z. Jiang, W. Shi, X. Han, and B. Chen, "Blocked maximum correntropy criterion algorithm for cluster-sparse system identifications," *IEEE Transactions on Circuits and Systems II: Express Briefs*, 10.1109/TCSII.2019.2891654.
- [33] Y. Li, Z. Jiang, O. M. O. Osman, X. Han, and J. Yin, "Mixed norm vonstrained sparse APA algorithm for satellite and network echo channel estimation," *IEEE Access*, vol. 6, pp. 65901-65908, 2018.
- [34] Y. Li, Y. Wang, and T. Jiang, "Norm-adaption penalized least mean square/fourth algorithm for sparse channel estimation," *Signal Processing*, vol. 28, pp. 243-251, 2016.
- [35] Y. Li, Y. Wang, and T. Jiang, "Sparse-aware set-membership NLMS algorithms and their application for sparse channel estimation and echo cancelation," *AEU-International Journal of Electronics and Communications*, vol. 70, no. 7, pp. 895-902, 2016.

- [36] Y. Li, Z. Jiang, Z. Jin, X. Han, and J. Yin, "Cluster-sparse proportionate NLMS algorithm with the hybrid norm constraint," *IEEE Access*, vol. 6, pp. 47794-47803, 2018.
- [37] Q. Wu, Y. Li, Y. Zakharov, W. Xue, and W. Shi, "A kernel affine projection-like algorithm in reproducing kernel hilbert space," *IEEE Transactions on Circuits and Systems II: Express Briefs*, 10.1109/TCSII.2019.2947317.

A Low-Profile Circularly Polarized Magnetic-Electric Dipole Antenna Array

Pingyuan Zhou, Mang He, Wen Tian, and Chuanfang Zhang

School of Information and Electronics
Beijing Institute of Technology, Beijing, 100081, China
py_zhou@bit.edu.cn, hemang@bit.edu.cn, 714380548@qq.com, zcf@bit.edu.cn

Abstract — A low-profile circularly polarized (CP) magneto-electric dipole (MED) antenna array is presented in this paper. By tilting the vertical walls of a MED with two protruded stubs being orthogonal to the horizontal patches and by using a staircase-shaped feeding strip, a wideband CP MED antenna is formed. In comparison to the conventional MED, the profile of the antenna is reduced from $0.25\lambda_c$ to only $0.07\lambda_c$ at the center frequency of the operating band. The sequentially rotated feeding (SRF) network is employed to construct a 2×2 array with enhanced 3 dB axial-ratio (AR) bandwidth. The overall size of the array is as compact as $1.33\lambda_c \times 1.33\lambda_c \times 0.07\lambda_c$, and the measured results show that the usable overlapped bandwidth of the reflection coefficient $|S_{11}| < -10$ dB and $AR < 3$ dB is 31.2%, covering 1.76 GHz to 2.41 GHz. The peak gain of the array is 12.9 dBic with the gain variation being less than 3 dB within the 1.85-2.32 GHz band, and the front-back-ratio (FBR) is greater than 20 dB. The proposed array is promising in the applications for portable and individual communication devices for wireless communications.

Index Terms — Circularly polarized antenna, magneto-electric dipole antenna, small size, wideband.

I. INTRODUCTION

As a type of wideband complementary antenna, the magneto-electric dipole (MED), which was first proposed by Luk in 2006, has attracted widespread interests in recent years [1-15]. The MED antenna has many advantages such as wide bandwidth, symmetrical beam, low cross-polarization level, and stable gain, etc. However, the traditional MED antenna usually has a relatively high profile of about 0.25 wavelengths at the center frequency of the operating band, which may limit its application in many portable communication systems.

A lot of works have been conducted to lower the profile of the MED antenna. In [2], the height of a wideband MED is reduced to $0.2\lambda_c$ by attaching two extra inverted-L-shaped wires above the shorted bowtie patches. In [3,4], a horizontal planar dipole and a pair of vertical folded patches are used to further reduce the antenna profile to $0.17\lambda_c$, and 55% 10 dB impedance

bandwidth is reached. In [5], the profile of the MED is lowered to $0.156\lambda_c$ by bending the vertical shorted patch to a triangular shape, and a very wide bandwidth of 86.2% is obtained. A new MED with the height of $0.16\lambda_c$ is presented in [6], although the structure of the antenna is much simple than those in [2-5], the antenna still has wide impedance bandwidth of 45%. In [7], by replacing the traditional quarter-wave vertical shorted patch with a bent one of an obtuse-triangle-shaped cross section, the antenna's profile is lowered down to $0.097\lambda_c$, at the expense of reduced -10 dB $|S_{11}|$ bandwidth of 28.2%. The thickness of the MED is reduced to only $0.035\lambda_c$ in [8], but the bandwidth decreases to 20.7% and the FBR rises to 16 dB. [9-11] give the dielectric substrate loaded or substrate integrated MED, and the profiles of the antennas can be reduced to the order of 0.08 to $0.11\lambda_c$. However, these antennas suffer from complexity in construction of the ground reflector and in assembling process, relatively high fabrication cost and sensitivity to environments, narrow bandwidth, and reduced gain in comparison with the air-support metal MED antennas.

In contrast to the linearly polarized antennas, wideband CP antennas are often required in many communication systems to avoid multipath effects and mitigate the polarization mismatch. Recently, [12-15] have presented several wideband CP MED antennas. In [12], a CP MED antenna is designed by combing two bowtie patch antennas with two electric dipoles. It is fed by a Wilkinson power divider, and 33% overlapped -10 dB $|S_{11}|$ and 3 dB AR bandwidth is achieved, but the height of the antenna is $0.25\lambda_c$. In [13], a $0.21\lambda_c$ -thick wideband crossed-dipole loaded CP MED is proposed, and the usable bandwidth is 26.8%. In [14], two symmetric electric dipoles, two vertical patches, and a cavity with two gaps are combined to provide 65.1% overlapped CP bandwidth, but the antenna's profile is as high as $0.27\lambda_c$. In [15], two L-probe fed CP MED antennas, operating respectively at the microwave and millimeter-wave bands, possess the overlapped bandwidths of 47.7% with the $0.29\lambda_c$ profile and 41% with the $0.15\lambda_c$ -profile. Although wide CP bandwidths have been obtained in [12-15], the heights of the MED antennas are still quite high; this is undesirable for some

portable devices.

In this paper, a low-profile wideband CP MED antenna array is proposed for portable or individual wireless devices, in which compactness and light-weight is one of the most important requirements. Based on the proposed single-fed CP MED antenna with wide impedance bandwidth, which has a much lower profile of $0.07\lambda_c$ as compared with the traditional $0.25\lambda_c$ -thick MED antenna, a 2×2 array is constructed by using the sequentially rotated feeding (SRF) technique. The use of SRF network [16,17] further enhances the polarization purity and AR bandwidth, and the overlapped AR < 3 dB and $|S_{11}| < -10$ dB bandwidth can be greater than 30%. Within the operating band, the gain variation is less than 3 dB from 1.85 to 2.32 GHz, showing a 22.5% 3 dB gain bandwidth.

II. ANTENNA ELEMENT

A. Antenna configuration

The geometry of the proposed MED antenna element is shown in Fig. 1. Two metallic patches with each dimension of $L_1 \times W_1$ and being parallel to the ground, together with two attached stubs with the each size of $L_2 \times W_2$ protruding along the y -direction, form an electric dipole (ED). The position of the stub measured from the inner edge of the patch is W_3 , and the gap width between the inner edge of the two arms of the ED is S . In Fig. 1 (c), two inclined metallic patches connect the inner edges of the two horizontal patches to the ground, in which α denotes the included angle between the slanted patches and ground, and H is the height of the antenna. Similar to the conventional MED antenna [1], [7], the shorted inclined-patches, the ground, and the aperture between the ED's two arms, form an equivalent magnetic dipole (MD). The feeding line of the antenna is a staircase-shaped metallic strip, as shown in Fig. 1 (d), which consists of four parts. The first part is a vertical strip with the length of l_1 , and it connects to the intersection line of the horizontal patch and the inclined shorted patch. The second part is a horizontal strip with the length of l_2 , and the third part, with the length being l_3 , is parallel to another inclined shorted patch. The first three parts share the same width of W_{f1} . The fourth part of the feeding line is a vertical strip with the shape of an inverted trapezoid. The lengths of the top and bottom bases, and the height of the trapezoid are W_{f1} , W_{f2} , and l_4 , respectively. The antenna element can be fed by connecting the inner conductor of a SMA connector to the bottom base of the trapezoid and attaching the outer conductor to the ground. The third part (l_3) works as a microstrip line and the distance between the line and inclined-patch can be determined by the basic formula for microstrip line design. It is noted that in this section the size of the ground is set to $G=150$ mm ($0.95\lambda_c$) for analysis the properties of the single MED antenna element.

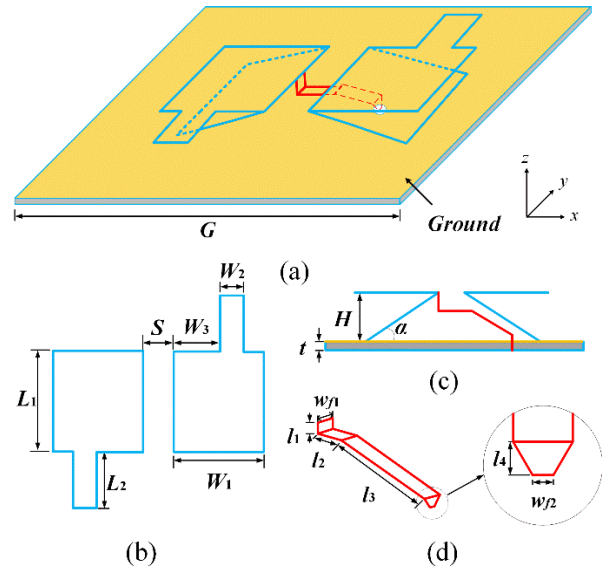


Fig. 1. Configuration of the proposed MED antenna element. (a) Perspective view, (b) top view, (c) side view, and (d) the feeding strip. Optimal dimensions of the antenna element (unit: mm): $L_1=51$, $L_2=13$, $W_1=51$, $W_2=10$, $W_3=25$, $S=6$, $H=10$, $G=150$, $l_1=2$, $l_2=6$, $l_3=17.3$, $l_4=2$, $t=1$, $w_{f1}=2.1$, $w_{f2}=1.3$. $\alpha=20.3^\circ$.

B. Operating principles

As shown in Fig. 1, it is apparent that both the equivalent electric currents of ED and the equivalent magnetic currents of the MD are y -directed. In the xz -plane, both the electric field radiated from the ED and that from the MD have the same shape of figure “O”, although they are spatially orthogonal. In addition, there is an inherent 90° phase difference between these two sets of electric fields since one of them is radiated from an ED and the other one is produced by an equivalent MD [18]. Thus, good CP radiation can be generated in the entire xz -plane. However, if we consider the presence of the ground plane, in the xz -plane the electric field from the ED will be shorted at the ground plane because it is tangential to the ground; while the electric field from the MD will not since it is normal to the ground. Therefore, given the existence of ground plane, the total electric field in the upper half xz -plane is the superposition of the field from the ED with the shape of half figure “8” and that from the MD with the shape of half figure “O”. This indicates that low AR can be kept in the upper half xz -plane except the region near the ground plane.

In the yz -plane, the electric fields from the ED and MD are still orthogonal in space and quadrature in phase but both radiation patterns are like figure “8”. The electric field from the ED will be enhanced near the ground, because it is vertically polarized with respect to the ground plane in the yz -plane; while the electric field from the MD will be shorted since it has only tangential

component to the ground. So, the total radiated electric field in the upper half yz -plane is still the sum of the field from the MD with the shape of half figure “8” and the field from the ED with the approximate shape of half figure “O”. It is seen that the proposed MED antenna can produce good CP and symmetrical radiation in the upper half space over a wide frequency range, if the ED and MD are excited with nearly the same magnitude.

To better understand the operating principle, the current distributions on the ED patches and the electric field vectors in the gap at different time instants within one period T are shown in Fig. 2. At the instant $t=0$, the current on the ED patches is dominated along $+y$ -axis, while the electric field in the gap is minimized, which indicates that the ED is strongly excited. At $t=T/4$, the electric field in the gap is strong along $-x$ -axis, while the current on the ED patches is weak, which means the MD is strongly excited at this instant. As seen in Figs. 2 (c) and (d), in the next half period, the current and electric field distributions repeat the ones at $t=0$ and $t=T/4$ but with opposite directions. It is clear that the circulation of the electric current and field in one period meets the requirement for possible CP radiation.

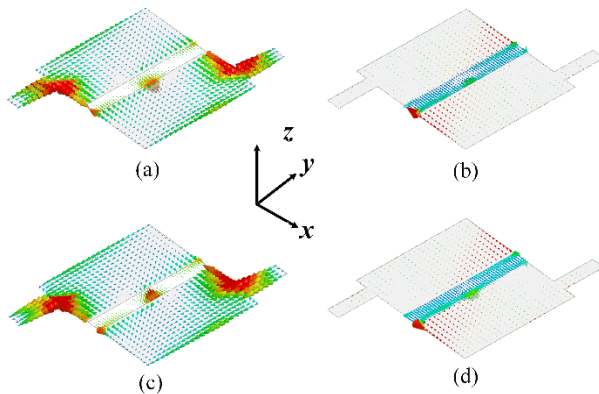


Fig. 2. Current and electric field distributions of the proposed antenna at different time instants: (a) $t=0$, (b) $t=T/4$, (c) $t=T/2$, and (d) $t=3T/4$.

C. Antenna element performance and parametric studies

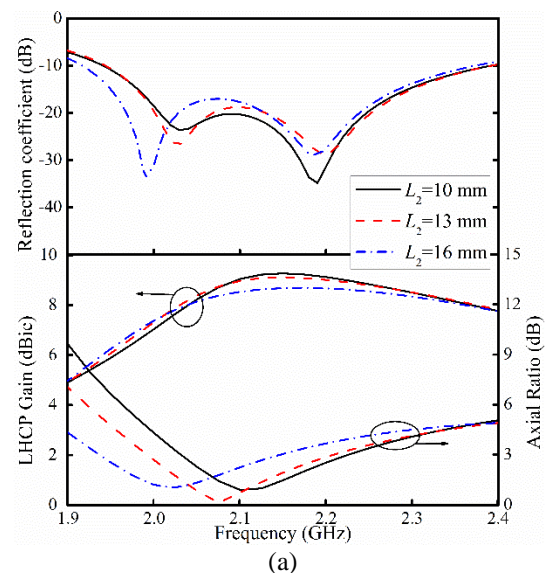
From Fig. 1, two resonant frequencies can be predicted existing in the structure of the antenna. The ED determines the lower resonant frequency f_L since it has a long current path, and the higher one f_H is dependent of the effective length and width of the equivalent MD. The electric current length of the ED is mainly affected by L_1+L_2 , the effective length and width of the MD is determined by the parameters L_1 , S , and W_1 , while S also significantly affects the coupling between the ED and MD. Therefore, parametric studies are carried out on the three key sizes of L_2 , W_1 and S in order to optimize the performance of the antenna, and only one parameter

varies while the others are kept unchanged in each of the following analyses, and the final optimum geometrical sizes for the MED antenna are listed in the caption of Fig. 1.

The variations of $|S_{11}|$, AR and gain of the antenna versus L_2 are shown in Fig. 3 (a). It is seen that both AR and $|S_{11}|$ are sensitive to the variation of L_2 . When L_2 increases, f_L is shifted downward since the current path of the ED is elongated, whereas f_H almost remains unchanged. The minimal AR frequency is lowered as well, which results in misalignment of the AR and $|S_{11}|$ bandwidths. Besides, the peak gain decreases by 0.6 dB or so as L_2 is increased from 10 mm to 16 mm. Thus, in order to obtain a wide overlapped AR and $|S_{11}|$ bandwidth and high gain, the stub length L_2 is set to 13 mm.

Figure 3 (b) shows the effects of the arm length of the ED on the performance of the antenna. It is observed that the two resonant frequencies are shifted downward with the increased W_1 , which indicates that the current path along the ED and the effective length of the MD are both elongated by increasing W_1 . The antenna appears to be mismatched at low frequency, and the AR and $|S_{11}|$ operating bands become misaligned. Moreover, f_H shifts downward more strongly than f_L does, which means that W_1 has more significant effects on the MD.

The effects of gap width S between two ED patches on the antenna's performance is illustrated in Fig. 3 (c). It is clearly that the large S will cause the higher resonant frequency move upward significantly, while the low resonant frequency remains almost unchanged. But when S increases, the coupling between the two arms of the ED becomes weak, and impedance mismatch is seen near the frequency of f_L . The AR and gain of the antenna are almost not affected by changing S , which indicates that the excitation magnitude and phase relationship between the ED and MD is almost independent of S .



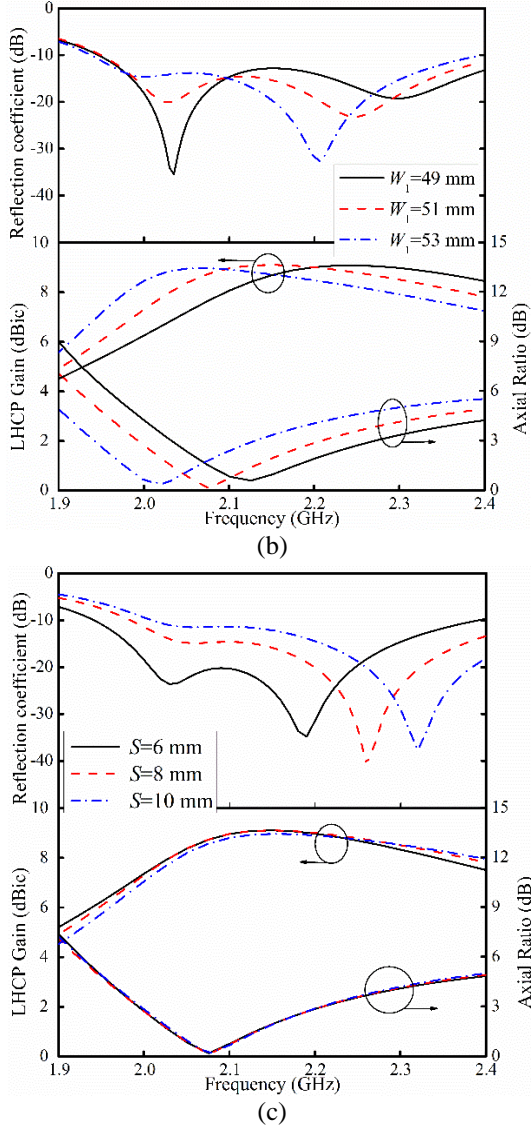


Fig. 3. Effects of different geometrical parameters on the performance of the MED antenna element: (a) L_2 , (b) W_1 , and (c) S .

With the optimum geometrical sizes, the MED antenna has 20.3% overlapped $|S_{11}| < -10$ dB bandwidth from 1.95 GHz to 2.39 GHz and 10.5% $AR < 3$ dB bandwidth from 1.99 GHz to 2.21 GHz, respectively. The peak gain of the antenna is 9.11 dBic, and the variation of the gain is less than 3 dB from 1.97 GHz to beyond 2.5 GHz.

III. ANTENNA ARRAY DESIGN AND PERFORMANCE

A 2×2 array is constructed by four proposed MED antenna elements, denoted by A1 to A4, and the layout of the array is shown in Fig. 4. The four antenna elements are placed above the top surface (as the ground plane of

the antenna) of a double-sided copper clad laminate, and the SRF network is etched on the bottom surface to excite the array. The relative permittivity, loss tangent, and thickness of the dielectric substrate are $\epsilon_r=3.5$, $\tan\delta=0.002$, and $t=1$ mm, respectively. The SRF network is composed of two-stage Wilkinson power dividers to provide wideband and stable power division ratio and phase difference between the antenna elements. Each antenna element is excited by connecting the output of the power divider to the inverted trapezoid, i.e., the fourth part at the end of the feeding strip, through a metal probe. For a left-handed circular polarization (LHCP) design, the elements A1 to A4 rotate clockwise, and the feeding phase for each element is 90° lag to that of the former one. The spacing between two neighbor elements is $D=84$ mm ($0.58\lambda_c$), so the overall size of the array is about 190 mm \times 190 mm \times 11 mm ($1.33\lambda_c \times 1.33\lambda_c \times 0.07\lambda_c$).

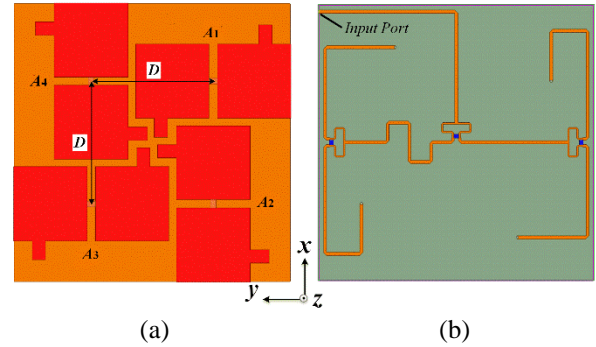


Fig. 4. Layout of the 2×2 array: (a) top view and (b) SRF network composed of two-stage Wilkinson power dividers.

Parametric studies of L_2 , W_1 and S are carried out to study their effects on the performance of the array. The variations of the AR and $|S_{11}|$ of the array versus L_2 are shown in Fig. 5 (a). The relationship between L_2 and the two resonant frequencies is complicated in array environment. When L_2 increases, owing to the stronger mutual coupling between antenna elements, f_L shifts upwards first and then moves to lower frequency slightly while f_H is increased continuously, so the two resonant frequencies depart from each other. Meanwhile, the AR is seen slightly increased at high frequency, and the gain of the array decreases quickly if L_2 is enlarged to 16 mm.

As shown in Fig. 5 (b), when W_1 is increased from 49 mm to the optimum value of 51 mm, f_H shifts down from 2.25 GHz to 2.2 GHz, and the impedance matching is improved. The lower resonant frequency f_L shifts upward slightly; and as W_1 increases to 53 mm, f_H moves to a higher frequency with f_L being almost unchanged. Meanwhile, a large loss of gain of the array at higher frequency is observed. Based on these findings, it is evident that overlarge value of W_1 cannot be chosen to construct the compact array, since large W_1 leads to small

edge-to-edge spacing between the antenna elements and then causes strong mutual coupling.

Figure 5 (c) gives the effects of S on the array's performance. It can be seen that continuously increased S does not lower down the two resonant frequencies monotonically as the single antenna does because mutual coupling among the antenna elements is strong due to the large S . At the same time, it is also observed that the gain is reduced at the high frequency band with the increased S .

With the optimum geometrical sizes of the antenna element, the 2×2 array has a more than 35% $|S_{11}| < -10$ dB bandwidth from 1.76 GHz to 2.50 GHz, an AR < 3 dB bandwidth of 33% from 1.74 GHz to 2.42 GHz, and 3 dB gain bandwidth of 22.5% from 1.88 GHz to 2.37 GHz.

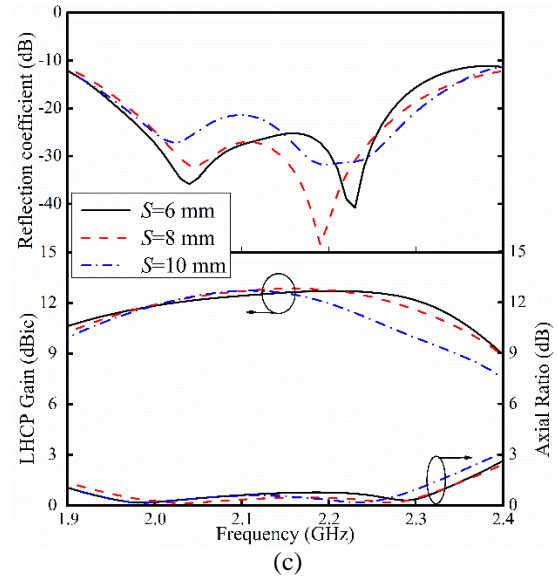
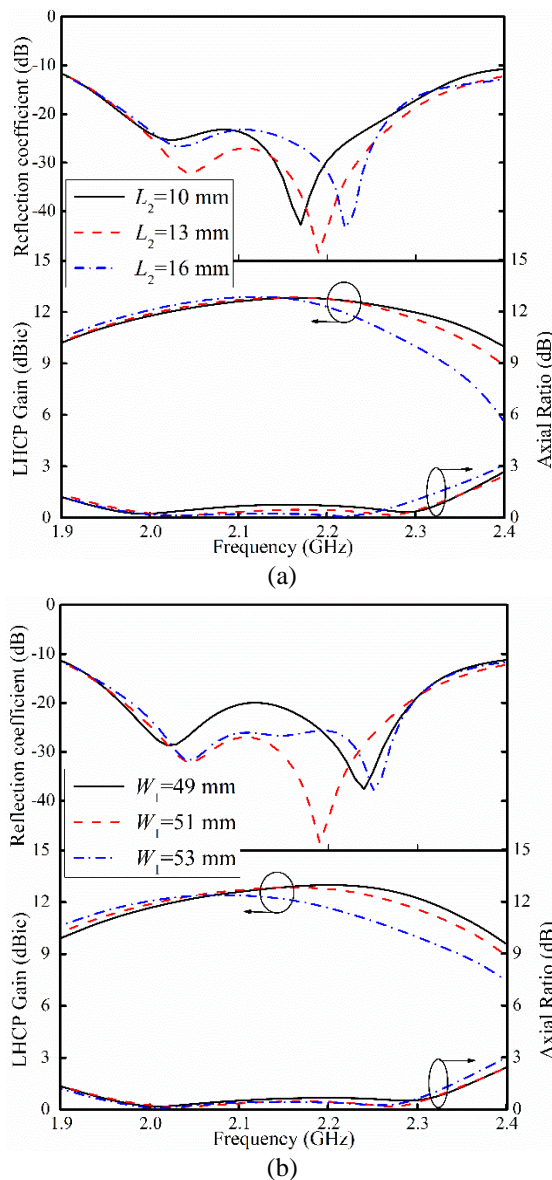


Fig. 5. Effects of different geometrical parameters on the performance of the MED antenna array: (a) L_2 , (b) W_1 , and (c) S .

V. EXPERIMENTAL VERIFICATION

A 2×2 CP MED array is fabricated, as shown in Fig. 6. The array element has the optimum dimensions listed in the caption of Fig. 1, and the inter-element spacing is 84 mm. All the MED elements and feeding structure are made of copper sheets with the thickness of 0.3 mm, and each antenna element is fixed to a 190 mm \times 190 mm substrate by four metal screws.

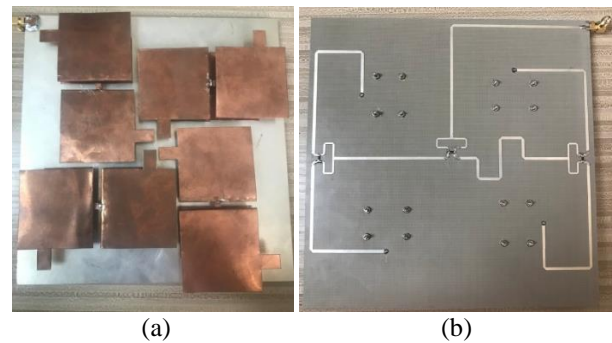


Fig. 6. The fabricated prototype of the antenna array: (a) top view and (b) two-stage Wilkinson power divider.

The simulated and measured $|S_{11}|$ and AR of the antenna array are presented in Fig. 7. The measured $|S_{11}|$ agrees well with the simulated results, and the $|S_{11}|$ is less than -10 dB from 1.76 GHz to 2.50 GHz. Agreement of the measured and simulated AR shows good LHCP performance of the array, and the measured 3 dB AR bandwidth is about 32.7% from 1.74 GHz to 2.42 GHz.

Thus, the overlapped $|S_{11}|$ and AR bandwidth is 31.2%, ranging from 1.76 GHz to 2.41 GHz.

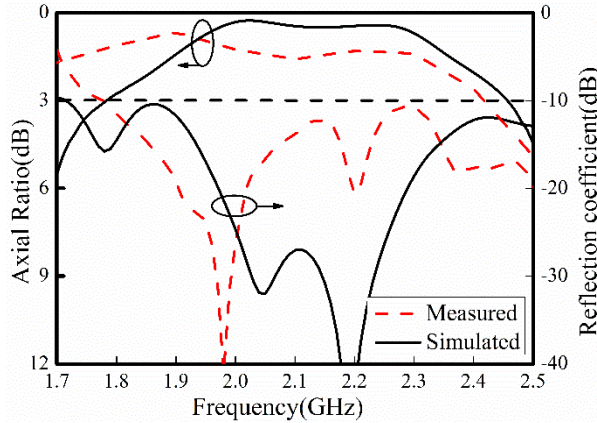


Fig. 7. Simulated and measured reflection coefficient, and axial ratio of the proposed array antenna.

The simulated and measured gain of the antenna array, along with the calculated total efficiency, are illustrated in Fig. 8. The measured peak gain is about 12.9 dBic, and the minimum gain is above 8 dBic within the overlapped bandwidth. The variation of gain is less than 3 dB from 1.85 to 2.32 GHz, showing a bandwidth of 22.5%, which is slightly narrower than the simulated one of 23.1% (1.88-2.37 GHz). It is noted that the maximum difference between the measured results and the simulated ones is about 2 dB, which may be caused by the imprecision of the handmade antenna elements, uncertainties in the measurements, and the losses in the feeding network. The simulated array efficiency is greater than 55% within the entire overlapped bandwidth and more than 72% within the 3 dB gain bandwidth.

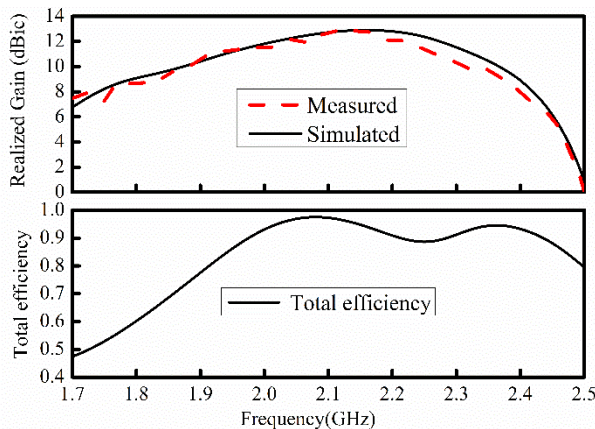


Fig. 8. Simulated and measured realized gain of the array, and simulated total efficiency of the proposed array antenna.

Figure 9 depicts the measured radiation patterns of

the array at 1.9, 2.1, and 2.3 GHz, from which good LHCP performance is observed. The simulated results are also plotted for comparison, showing good agreement with the measured ones in the xoz - and yoz -planes. In both planes, the FBR is over 20 dB at each frequency, and the corresponding 3 dB beam-widths in the xoz - and yoz -planes are measured 44.2° and 44.8° at 1.9 GHz, 39.6° and 37.3° at 2.1 GHz, and 37.9° and 36.8° at 2.3 GHz, respectively.

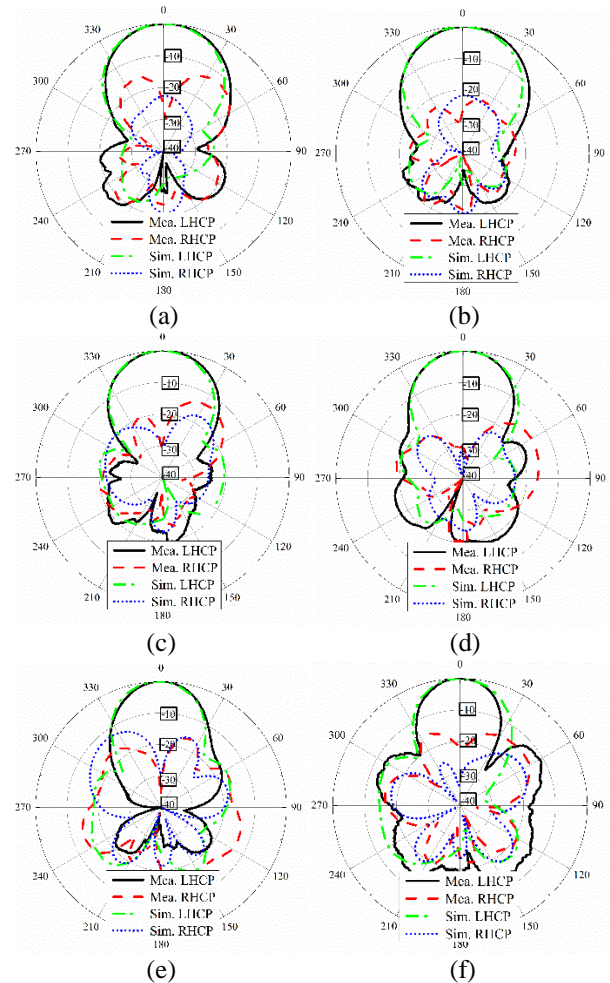


Fig. 9. Simulated and measured radiation patterns of the proposed array antenna at: (a) 1.9GHz at xz -plane, (b) 1.9GHz at yz -plane, (c) 2.1GHz at xz -plane, (d) 2.1GHz at yz -plane, (e) 2.3GHz at xz -plane, and (f) 2.3GHz at yz -plane.

The performance comparison of the proposed CP MED array with other 2×2 arrays that also use the SRF technique is shown in Table 1. Since we did not find other pure metal MED-type 2×2 array designs, it is noted that the comparison arrays listed in Table 1 are all printed on dielectric substrates or substrate-loaded [19-24]. It is seen that the proposed array has wider overlapped

-10 dB $|S_{11}|$ and 3 dB AR bandwidth and high gain as compared with these arrays of similar volume sizes. To the best of our knowledge, with similar usable bandwidth,

the proposed antenna array has the smallest size among the pure metal MED arrays.

Table 1: Measured results comparisons of the proposed array and other 2×2 arrays with SRF

Array	Overall Size	-10 dB $ S_{11} $ Bandwidth	3 dB AR Bandwidth	Overlapped Bandwidth	Peak Gain
[19]	$1.45\lambda_c \times 1.45\lambda_c \times 0.028\lambda_c$	15.9%	11.8%	11.8%	12.5 dBic
[20]	$1.32\lambda_c \times 1.32\lambda_c \times 0.065\lambda_c$	36.5%	28.8%	28.8%	13.2 dBic
[21]	$1.82\lambda_c \times 1.82\lambda_c \times 0.040\lambda_c$	>19%	12.7%	12.7%	12.0 dBic
[22]	$1.50\lambda_c \times 1.50\lambda_c \times 0.060\lambda_c$	20.8%	17.6%	17.6%	11.5 dBic
[23]	$1.67\lambda_c \times 1.67\lambda_c \times 0.060\lambda_c$	6.0%	6.8%	6.0%	10.5 dBic
[24]	$2.03\lambda_c \times 2.03\lambda_c \times 0.106\lambda_c$	29.5%	16.2%	16.2%	12.9 dBic
Proposed	$1.33\lambda_c \times 1.33\lambda_c \times 0.070\lambda_c$	34.7%	32.7%	31.2%	12.9 dBic

VI. CONCLUSION

A compact low-profile CP MED antenna array, which is composed of pure metallic structures, is proposed in this paper. The profile of the array is only $0.07\lambda_c$, which is much lower than other pure metal designs of the MED-type. The lateral size of the array is also as small as $1.33\lambda_c \times 1.33\lambda_c$. The measured -10 dB $|S_{11}|$ bandwidth is about 35% (1.76-2.5GHz), the 3 dB AR bandwidth is nearly 33% (1.7-2.41 GHz), and the 3 dB gain bandwidth is 22.5% (1.87-2.29GHz) with the peak gain of 12.9 dBic. The proposed array is promising in the applications for portable and individual communication devices.

ACKNOWLEDGMENT

The research and publication of this article was funded by the National Natural Science Foundation of China under Grant [61471040].

REFERENCES

- [1] K. M. Luk and H. Wong, "A new wideband unidirectional antenna element," *Int. J. Microw. Opt. Technol.*, vol. 1, no. 1, pp. 35-44, June 2006.
- [2] H. Wong, K. M. Mak, and K. M. Luk, "Wideband shorted bowtie patch antenna with electric dipole," *IEEE Trans. Antennas Propag.*, vol. 56, no. 7, pp. 2098-2101, July 2008.
- [3] L. Ge and K. M. Luk, "A magneto-electric dipole antenna with low-profile and simple structure," *IEEE Antennas Wireless Propag. Lett.*, vol. 12, pp. 140-142, 2013.
- [4] L. Ge and K. M. Luk, "A low-profile magneto-electric dipole antenna," *IEEE Trans. Antennas Propag.*, vol. 60, no. 4, pp. 1684-1689, Apr. 2012.
- [5] He K, Gong S, and Gao F, "Low-profile wideband unidirectional patch antenna with improved feed structure," *Electronics Lett.*, vol. 51, no. 4, pp. 317-319, 2015.
- [6] K. M. Luk and B. Wu, "The magneto-electric dipole-a wideband antenna for base stations in mobile communications," *Proc. IEEE*, vol. 100, no.7, pp. 2297-2307, 2012.
- [7] C. Ding and K. M. Luk, "Low-profile magneto-electric dipole antenna," *IEEE Antennas Wireless Propag. Lett.*, vol. 15, pp.1642-1644, 2016.
- [8] M. Li and K.-M. Luk, "A low-profile, low-backlobe and wideband complementary antenna for wireless application," *IEEE Trans. Antennas Propag.*, vol. 63, no. 1, pp. 7-14, Jan. 2015.
- [9] M. Li and K.-M. Luk, "A low-profile wideband planar antenna," *IEEE Trans. Antennas Propag.*, vol. 61, no. 9, pp. 4411-4418, Sep. 2013.
- [10] C. Y. Shuai and G. M. Wang, "Substrate-integrated low-profile unidirectional antenna," *IET Microw. Antennas Propag.*, vol. 12, no. 2, pp. 185-189, Feb. 2018.
- [11] H. W. Lai and H. Wong, "Substrate integrated magneto-electric dipole antenna for 5G wi-fi," *IEEE Trans. Antennas Propag.*, vol. 63, no. 2, pp. 870-874, Feb. 2015.
- [12] K. M. Mak and K. M. Luk, "A circularly polarized antenna with wide axial ratio beamwidth," *IEEE Trans. Antennas Propag.*, vol. 57, no. 10, pp. 3309-3312, Oct. 2009.
- [13] S. X. Ta and I. Park, "Crossed dipole loaded with magneto-electric dipole for wideband and wide-beam circularly polarized radiation," *IEEE Antennas Wireless Propag. Lett.*, vol. 14, pp. 358-361, 2015.
- [14] K. Kang, Y. Shi, and C. H. Liang, "A wideband circularly polarized magneto electric dipole antenna," *IEEE Antennas Wireless Propag. Lett.*, vol. 16, pp. 1647-1650, 2017.
- [15] M. Li and K. M. Luk, "A wideband circularly polarized antenna for microwave and millimeter-wave applications," *IEEE Trans. Antennas Propag.*, vol. 62, no. 4, pp. 1872-1879, Apr. 2014.
- [16] P.S. Hall, J. S. Dachele, and J. R. James, "Design principles of sequentially fed wide bandwidth circularly polarized microstrip antennas," in *Proc.*

- Inst. Elect. Eng.*, vol. 136, no. 5, pp. 381-389, Oct. 1989.
- [17] P. S. Hall, "Application of sequential feeding to wide bandwidth, circularly polarised microstrip patch arrays," in *Proc. Inst. Elect. Eng.*, vol. 136, no. 5, pp. 390-398, Oct. 1989.
- [18] C. A. Balanis, *Antenna Theory: Analysis and Design*. 3rd Edition, John Wiley and Sons, New York, 2005.
- [19] K. Ding, C. Gao, T. Yu, D. Qu, and B. Zhang, "Gain-improved broadband circularly polarized antenna array with parasitic patches," *IEEE Antennas Wireless Propag. Lett.*, vol. 16, pp. 1468-1471, 2017.
- [20] W. Hu, D. Inserra, G. Wen, and Z. Chen, "Wideband low axial ratio and high-gain sequentially rotated antenna array," *IEEE Antennas Wireless Propag. Lett.*, vol. 17, no. 12, pp. 2264-2268, Dec. 2018.
- [21] C. Deng, Y. Li, Z. Zhang, and Z. Feng, "A wideband sequential-phase fed circularly polarized patch array," *IEEE Trans. Antennas Propag.*, vol. 62, no. 7, pp. 3890-3893, July 2014.
- [22] W. Yang, J. Zhou, Z. Yu, and L. Li, "Bandwidth- and gain-enhanced circularly polarized antenna array using sequential phase feed," *IEEE Antennas Wireless Propag. Lett.*, vol. 13, pp. 1215-1218, 2014.
- [23] Y. Li, Z. Zhang, and Z. Feng, "A sequential-phase feed using a circularly polarized shorted loop structure," *IEEE Trans. Antennas Propag.*, vol. 61, no. 3, pp. 1443-1447, Mar. 2013.
- [24] M. Akbari, S. Gupta, and A. R. Sebak, "Sequential feeding networks for subarrays of circularly polarized patch antenna," *2016 IEEE Int. Symp. Antennas Propag. (APSURSI)*, Fajardo, pp. 587-588, 2016.

Broadband Conformal End-fire Monopole Log-periodic Antenna Array

Chao Chen, Jiandan Zhong, and Yi Tan

College of Communication Engineering
Chengdu University of Information Technology, Chengdu, 610225, China
tang59690508@163.com, heke79382@163.com, colorfulyn@163.com

Abstract — The paper presented a broadband conformal end-fire monopole log-periodic dipole antenna array that can cover 2GHz-18GHz and have a good end-fire radiation pattern. The proposed monopole log-periodic antenna has a simple feed network, which uses slot microstrip lines as the feed network. The monopoles are designed on both sides of the copper substrate according to certain rules. The proposed 2G-18GHz conformal monopole log-periodic antenna array that consists of a metal cylinder, antennas fixed in metal inverted cone, and twelve monopole log-periodic antenna arrays. Two types monopole log-period antenna arrays conforming to a metal cylinder consisting of 2GHz-6GHz monopole log-periodic antenna unit and 6GHz-18GHz antenna unit 30° evenly placed in a wedge-shaped groove of a metal cylinder. The measured results show that the 2GHz-18GHz end-fire antenna array are available and have good end-fire radiation.

Index Terms — Conformal antenna, end-fired, monopole log-periodic antenna array, metal cylinder.

I. INTRODUCTION

In 1957, Rumsey first proposed non-frequency-variable antennas, and developed various types of broadband antennas [1]. In 1960, Dwight Isbell of the University of Illinois proposed a log-period array of antennas [2]. In 1961, R. L. Carrel used the transmission line theory to propose the equivalent circuit of the log-periodic antenna [3]. For nearly 60 years, the design rules for log-period dipole antennas (LPDA) have been based primarily on the results of two researchers, Isbell and Carrel [3-6].

From the analysis of LPDA antenna array structure, the research on LPDA mainly focuses on three aspects: (1) designing a wide-band feeding structure [7,8]; (2) changing the shape of the dipole unit [9,10]; (3) combine broadband feed networks with new vibrator unit structures [11,12]. From the perspective of LPDA antenna array performance, the research mainly focuses on three aspects: (1) low profile [13]; (2) dual polarization [14]; (3) miniaturization technology [15]. Since the longest and the shortest vibrators of the logarithmic period

antenna array determine the lowest frequency and the highest frequency of the LPDA antenna array, the bandwidth of the antenna is determined. The broadband monopole log-periodic is designed according to the principle that is proposed in [16]. In today's increasing miniaturized electronic devices, how to reduce the size of the antenna in the case of satisfying the antenna performance. Generally, the method of miniaturizing the antenna is mainly (1) loading method; (2) dipole folding method; (3) dipole tilt method; (4) reducing feed structure; but the antenna is generally miniaturized while having a wide frequency band width and reduced gain, etc.

In this paper, we designed 2G-6GHz end-fire monopole antenna array and 6G-18GHz end-fire monopole antenna array. The designed end-fire monopole log-periodic antenna array uses the slot line as the feed circuit. The monopoles are printed on both sides of the dielectric plate according to a certain rule, and then the dielectric plate having the monopole is placed between the groove lines. These sheet metal pieces are monopole oscillators and have a trapezoidal distribution. These novel complementary monopoles form a novel monopole log-periodic antenna array. In the design of the monopole log-periodic antenna array, the monopole oscillator is in the form of a substrate plane, which avoids the processing error in a small distance and causes the coincidence of the adjacent monopole to affect the performance of the antenna array. At the same time, the radiation area of the antenna array is expanded. 2GHz-6GHz monopole log-periodic antenna unit and 6GHz-18GHz antenna unit 30° evenly placed in a wedge-shaped groove of a metal cylinder. The measured results show that the 2GHz-18GHz end-fire antenna array are available and have good end-fire radiation.

II. ANTENNA DESIGN AND ANALYSIS

The end-fire monopole antenna array is shown in Fig. 1. The relationship between the parameters of the monopole log-periodic antenna array is as follows:

$$tg\theta = \frac{H_1}{R_1} = \frac{H_2}{R_2}, \quad (1)$$

$$\sqrt{\tau} = \frac{H_n}{H_{n-1}}, \quad (2)$$

$$h = \sqrt{\tau}/(\Delta\tau)^2 \times H_n, \quad (3)$$

where τ is the scale factor, $\Delta\tau$ is the introduced parameter and θ is the opening angle of the unipolar log periodic antenna array.

As can be seen from Fig. 1, H_1 is the height of the monopole with the lowest frequency. The dielectric plate printed with the monopole is placed on the two sides of the slot line, so that, the feed phase of the adjacent monopole is opposite. The substrate with monopole drivers is Rogers RO4350 substrate with dielectric constant of 3.66, loss tangent of 0.004 and its thickness is 0.5mm. The substrate with feeding network is Rogers RO 3210 with dielectric constant of 10.2, loss tangent of 0.003 and its thickness is 1mm.

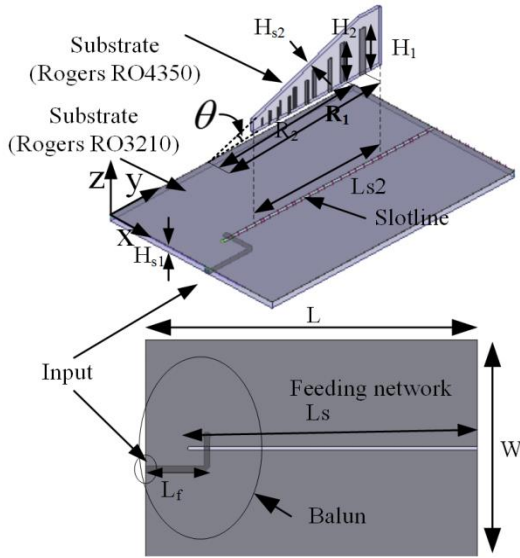


Fig. 1 Overall view of the monopole log-periodic end-fire antenna array with parameter definitions.

The feeding network is microstrip-to-slotline transition, which can provide the balance input for monopoles. The slotline has a characteristic impedance of 80Ω . The microstrip-to-slotline transition has a characteristic impedance of 50Ω . In the design of the feeding network, a microstrip stub and slot stub are inserted to improve the impedance matching. The equivalent circuit of the microstrip-to-slotline transition is shown in Fig. 2. The open-circuit microstrip stub and the short-circuit slotline are represented as follows:

$$Z_{oc} = -jZ_{mso} \cot(\phi_{mso}), \quad (4)$$

and

$$Z_{sc} = +jZ_{sls} \tan(\phi_{sls}). \quad (5)$$

The proposed monopole log-periodic antenna array consists of microstrip-to-slotline transition as the feeding part and twelve monopoles oriented vertically over ground whose lengths and spacing are decided by log-periodic design principles (formula 1,2,3).

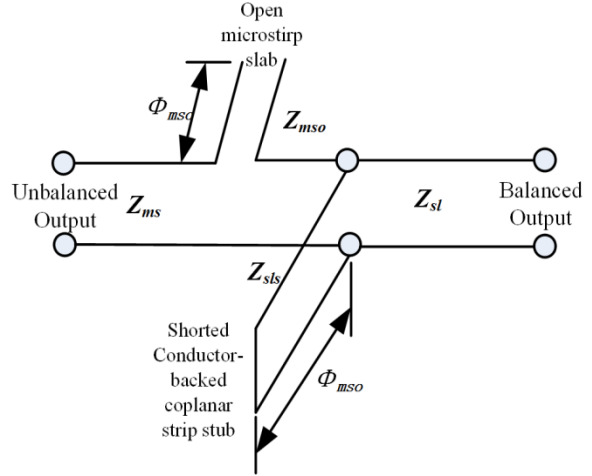


Fig. 2. Equivalent circuit of microstrip-to-slotline transition.

Each of these monopoles attached to both sides of the slotline serves as a driver for the antenna. Also, attached to this slotline are horizontal microstrip lines with their images, and form open-circuited transmission lines. The lengths of these monopoles are related with their first resonance occurs at a frequency which is related to the resonant frequencies of adjacent monopoles by the square root of the design ratio τ . If the longest monopole has a resonant frequency f_0 , the monopole immediately in front of it will have a higher resonant frequency $f_0/\sqrt{\tau}$. The entire array is fed at one point by placing a generator on the slotline. The open-circuited monopoles present an impedance to transmission line.

To experimentally verify the proposed end-fire monopole log-periodic antenna, two types of antennas based on the previously design principle is fabricated and assembled. The design of antennas are optimized by using ANSYS Electronics Desktop v16.1. An Agilent N5230A network analyzer and microwave anechoic chamber were used for measurements.

A. Design of 2GHz-6GHz monopole log-periodic antenna

According to the design principle, the 2GHz-6GHz monopole log-periodic antenna is fabricated and assembled in Fig. 3. The dimensions of 2GHz-6GHz monopole log-periodic antenna are revealed in Table 1.

ANSYS Electronic Desktop v16.1, based on the finite-element method (FEM), was used for the simulations of the 2GHz-6GHz end-fire monopole log-periodic antenna. An Agilent N5230A network was used for the measurement of the prototype. As shown in Fig. 4, the measured and simulated reflection coefficients of the optimized antenna were found to be in closed agreement. The measured bandwidth for the -10dB reflection coefficient covers 2GHz-6GHz.

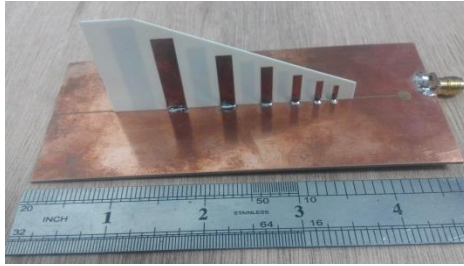


Fig. 3. Fabricated 2GHz-6GHz end-fire monopole log-periodic antenna

Table 1: Dimensions of 2GHz-6GHz end-fire monopole log-periodic antenna (mm)

H_1	H_2	H_{s1}	H_{s2}	W
30.6	26.5	1	0.5	50
L	θ	L_s	L_{s2}	L_f
120	16.2°	107.8	74.5	15

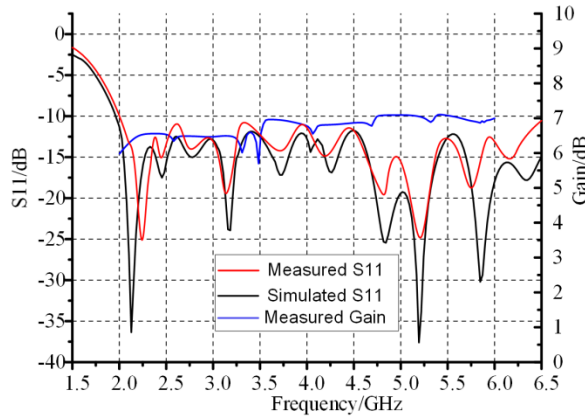


Fig. 4. Reflection coefficient and measured gain in the end-fire direction of the 2GHz-6GHz monopole log-periodic antenna.

The simulation result closely resembles the measured result at the operating bandwidth validating the design principle of the broadband end-fire monopole log-periodic antenna. The measured gain in the end-fire direction was found to be 6dB-7dB across the operating bandwidth, as shown in Fig. 4. The antenna exhibits high gain throughout the operating band, the antenna is suitable for transmitting and receiving applications in the wideband wireless communication systems.

Figure 5 shows the simulated and measured radiation patterns of the proposed antenna. It can be seen that the measured radiation patterns agree well with the simulated ones. The measured half-power beam width (HPBW) is in the range of 30°-45° in YOZ plane and 45°-65° in XOY plane. And the proposed antenna has a good end-fire

radiation pattern.

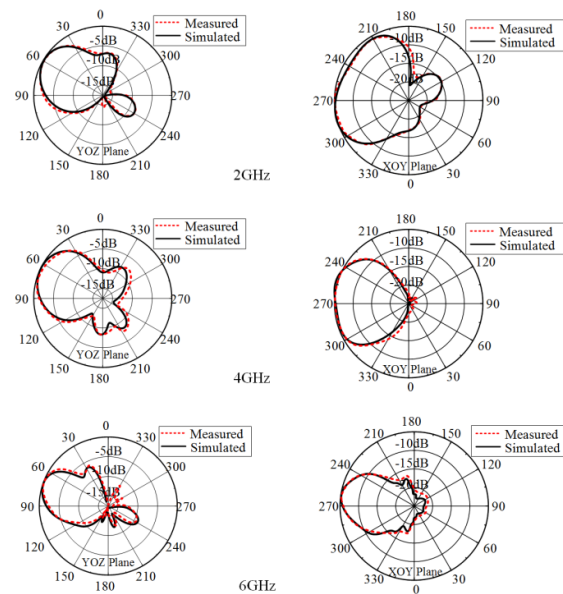


Fig. 5. Simulated and measured normalized radiation pattern of the monopole log-periodic antenna at 2GHz, 4GHz, 6GHz.

B. Design of 6GHz-18GHz monopole log-periodic antenna

According to the design principle, the 6GHz-18GHz monopole log-periodic antenna is fabricated and assembled in Fig. 6. The dimensions of 6GHz-18GHz monopole log-periodic antenna are revealed in Table 2.

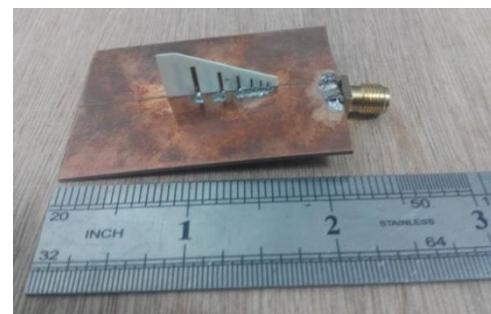


Fig. 6. Fabricated 6GHz-18GHz end-fire monopole log-periodic antenna

Table 2: Dimensions of 6GHz-18GHz end-fire monopole log-periodic antenna (mm)

H_1	H_2	H_{s1}	H_{s2}	W
8	6.8	1	0.5	30
L	θ	L_s	L_{s2}	L_f
45	16°	39	23.6	8

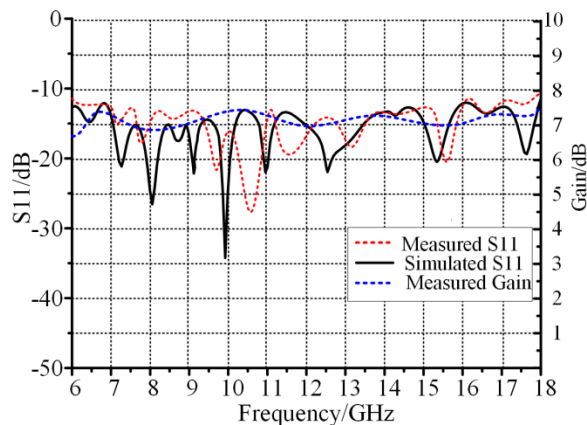


Fig. 7. Reflection coefficient and measured gain in the end-fire direction of the 6GHz-18GHz monopole log-periodic antenna.

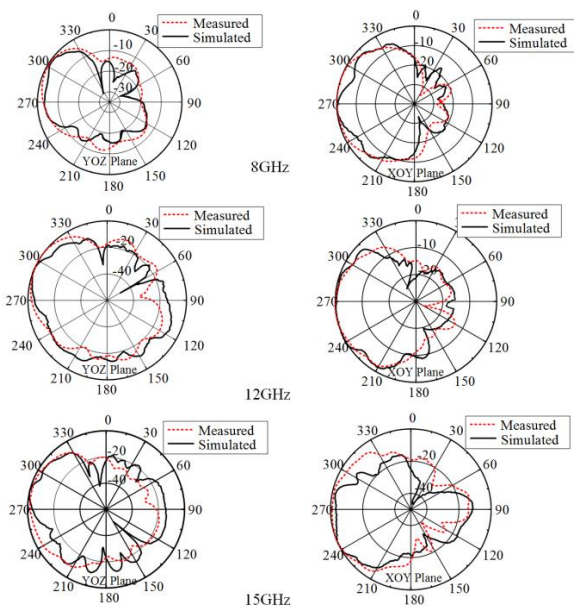


Fig. 8. Simulated and measured normalized radiation pattern of the monopole log-periodic antenna at 8GHz, 12GHz, 15GHz.

ANSYS Electronic Desktop v16.1, based on the finite-element method (FEM), was used for the simulations of the 6GHz-18GHz end-fire monopole log-periodic antenna. An Agilent N5230A network was used for the measurement of the prototype. As shown in Fig. 7, the measured and simulated reflection coefficients of the optimized antenna were found to be in closed agreement.

As shown in Fig. 7, the measured bandwidth for -10dB reflection coefficient covers 6GHz-18GHz. The simulation result closely resembles the measured result at the operating bandwidth validating the design

principle of the broadband end-fire monopole log-periodic antenna. The measured gain in the end-fire direction was found to be 6.5dB-7.5dB across the operating bandwidth. The antenna exhibits high gain throughout the operating band, the antenna is suitable for transmitting and receiving applications in the wideband wireless communication systems.

Figure 8 shows the simulated and measured radiation patterns of the proposed antenna. It can be seen that the measured radiation patterns agree well with the simulated ones. And the antenna has good end-fire radiation pattern.

III. MONOPOLE LOG-PERIODIC ANTENNA ARRAY RADIATION PATTERN ON METAL CYLINDER

The 2G-18GHz conformal monopole log-periodic antenna array consists of a metal cylinder, a fixed antenna metal inverted cone, and twelve monopole log-periodic antenna arrays. Two types of monopole log-period antenna arrays conforming to a metal cylinder consisting of a 2GHz-6GHz monopole log-periodic antenna unit and a 6GHz-18GHz antenna unit 30° evenly placed in a wedge-shaped groove of a metal cylinder as shown in Fig. 9 (a). The composition is shown in Fig. 9. To verify the performance of the new unipolar log-periodic antenna array, we tested conformal monopole log-periodic antenna array as shown in Fig. 10.

The top of the monopole dielectric plate of the monopole log-periodic antenna array is flush with the surface of the metal cylinder. Adding a dielectric sleeve outside the antenna keeps the appearance of the metal cylinder smooth, so that the monopole log-periodic antenna array conforms to the metal cylinder without affecting the aerodynamic distribution.

Since the monopole log-periodic antenna array is applied to the direction finding, only one monopole is considered to be fed, and the other monopole are matched with the resistance of 50 ohms. Due to the symmetry of the monopole log-periodic antenna array from 2 GHz to 18 GHz, we tested only two of the new 2 GHz to 18 GHz unipolar log-periodic antenna arrays as shown in Fig. 9 (b). As shown in Fig. 11, the monopole log-periodic antenna array has good end-fire radiation characteristics. The monopole log-periodic antenna array has good end-fire radiation characteristics.

Due to the influence of the metal cylinder and the antenna floor, the monopole log-periodic antenna array has an approximation. It can be seen from Fig. 11, due to the influence of the gap of the feeding circuit, the radiation pattern of the high frequency band of the antenna array is depressed and the side lobes are increased at the high frequency point. However, the radiation patterns of the antenna elements at different angles in the antenna array can cover the axial direction of the metal cylinder, which meets the target of the antenna array radiation, and has a good application

prospect on the metal body.

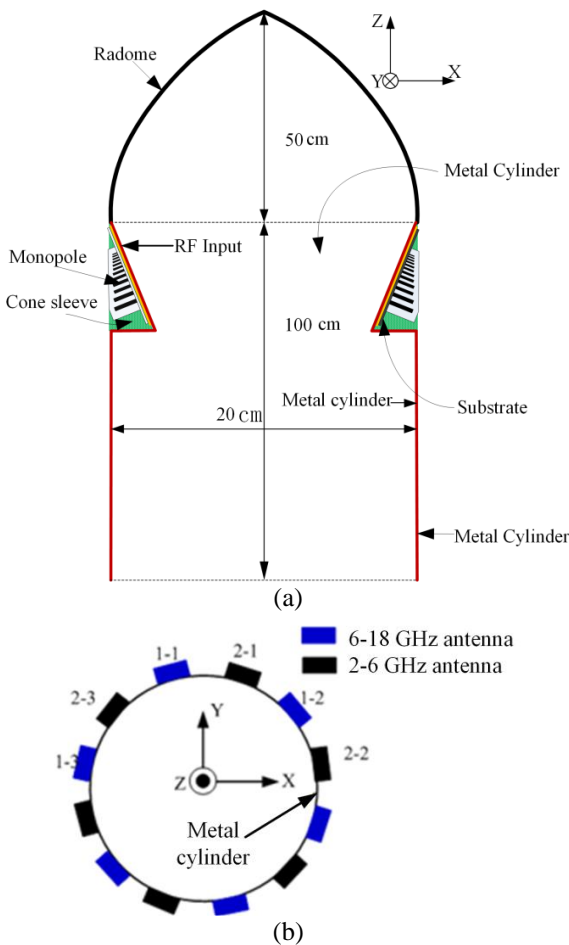


Fig. 9. Conformal monopole log-periodic antenna array on metal cylinder: (a) side view and (b) top view.

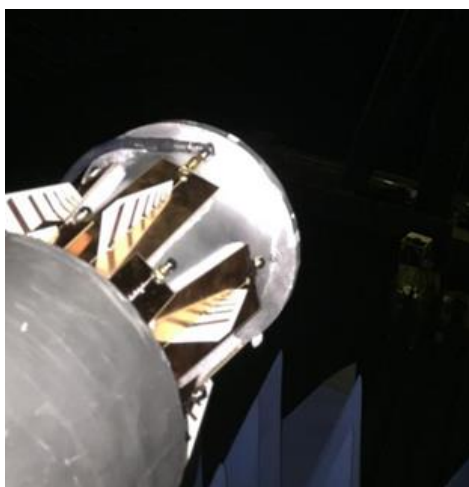


Fig. 10. 2 GHz-18 GHz monopole antenna array test picture.

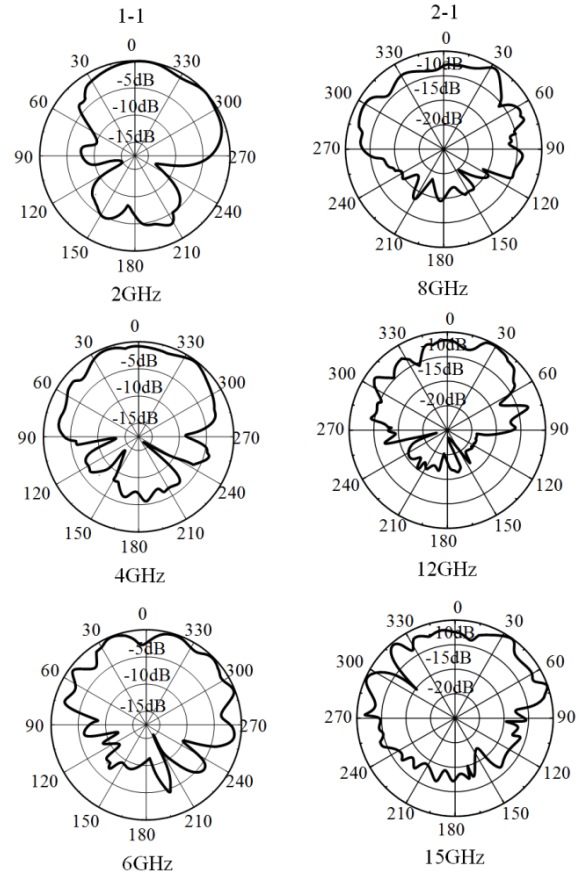


Fig. 11. Radiation pattern of XOZ plane.

IV. CONCLUSIONS

The paper uses two monopole log-periodic antenna arrays (2GHz-6GHz, 6GHz-18GHz monopole log-periodic antenna array) to form an end-fired directional antenna array covering 2GHz-18GHz. Two monopole log-periodic antenna arrays are alternately embedded in an inverted conical metal body. While maintaining the aerodynamic layout, the conformality of metal cylinder is realized. The measurement results show that the proposed antenna array can cover from the 2GHz to 18GHz. The conformal end-fired antenna array has good end-fire radiation characteristics and meets the requirements of the direction finding. According to its advantages, the proposed antenna is a good candidate for ultra wideband wireless communications, phase antenna array systems.

ACKNOWLEDGMENT

This research was supported by the microwave anechoic chamber, University of electronic Science and Technology of China, which provided the measurement conditions. And thanks Dr. Y.H. Sun for the help in the design of antennas.

REFERENCES

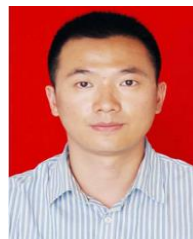
- [1] V. H. Rumsey, "Frequency independent antennas," *1958 IRE International Convention Record*, vol. 5, pp. 114-118, 1966.
- [2] D. E. Isbell, "Log-periodic dipole arrays," *IRE Trans. Antennas Propag.*, AP-8:260-267, 1960.
- [3] R. L. Carrel, "The design of log-periodic antennas," *[J]. IRE Int. Conent. Rec.*, vol. 9, no. 1, pp. 61-75, 1961.
- [4] P. J. Gibson, "The Vivaldi aerial," *9th Eur. Microw. Conf.*, Brighton, U.K., pp. 101-105, 1979.
- [5] D. Schaubert, E. Kollberg, et al., "Endfire tapered slot antennas on dielectric substrates," *IEEE Trans. Antennas Propag.*, vol. 33, pp. 1392-1400, 1985.
- [6] N. Fourikis, N. Lioutas, and N. V. Shuley, "Parametric study of the co-and cross-polarization characteristics of tapered planar and antipodal slotline antennas," *IEE Proceedings of Microw. Antennas Propag.*, vol. 140, pp. 17-22, 1993.
- [7] Z. Li, et al., "A novel wideband end-fire conformal antenna array mounted on a dielectric cone," *Applied Computational Electromagnetics Society Journal*, vol. 31, pp. 933-942, 2016.
- [8] G. A. Casula, et al., "Evolutionary design of a wide band flat wire antenna for WLAN and Wi-Fi applications," *Applied Computational Electromagnetics Society Journal*, vol. 29, pp. 547-557, 2014.
- [9] Y. Sun, et al., "Wide bandwidth endfire antenna with log-period directors," *Applied Computational Electromagnetics Society Journal*, vol. 30, pp. 1173-1179, 2015.
- [10] S. Weiss, K. Coburn, and O. Kilic, "FEKO simulation of a wedge mounted four element array antenna," *Applied Computational Electromagnetics Society Journal*, vol. 577-583, 2009.
- [11] P. Wang, "Analysis of radiation characteristics of conformal end-fire antenna mounted on a large conducting cylinder," *Applied Computational Electromagnetics Society Journal*, vol. 31, pp. 943-952, 2016.
- [12] S. Hoseyni, et al., "A compact design and new structure of monopole antenna with dual band notch characteristic for UWB applications," *Applied Computational Electromagnetics Society Journal*, vol. 31, pp. 797-805, 2016.
- [13] N. Angkawisittpan and A. Siritariwat, "A dual frequency monopole antenna with double spurlines for PCS and bluetooth applications," *Applied Computational Electromagnetic Society*, vol. 31, pp. 976-981, 2016.
- [14] M. M. Fakharian, P. Rezaei, and V. Sharbati, "A planar monopole antenna with switchable dual band-notched UWB/dual-band WLAN applications," *Applied Computational Electromagnetics Society Journal*, vol. 31, pp. 381-387, 2016.
- [15] M. NejatiJahromi, M. Nagshvarian-Jahromi, and M. Rahman, "A new compact planar antenna for switching between UWB, narrow band and UWB with tunable-notch behaviors for UWB and WLAN applications," *Applied Computational Electromagnetics Society Journal*, vol. 33, pp. 400-406, 2018.
- [16] Y. Sun, Y. Huang, G. Wen, et al., "A 6-18 GHz log-periodic monopole end-fire antenna based on microstrip-to-slotline transition," *Antennas and Propagation & USNC/URSI National Radio Science Meeting, 2017 IEEE International Symposium on. IEEE*, pp. 1541-1542, 2017.



Chao Chen was born in China, in 1979. He received his M.S degree in Sichuan University in 2005. He is currently an Associate Professor in Chengdu University of Information Technology. His research and industrial experience covers a broad spectrum of electromagnetics, including RF, Microwave, Millimeter wave Integrated Circuits and Systems design for Wireless Communication, Navigation, Identification, Mobile TV applications, RFIC/MMIC/MMMIC device modeling, System on Chip (SoC) and System in Package (SiC) Design.



Jiandan Zhong received his M.S. and Ph.D. degrees in Chengdu University of Information Technology in 2010 and University of Electronic Science and Technology of China in 2017. He is now Lecturer with College of Communication Engineering, Chengdu University of Information Technology. His current research interests include wideband antennas, patch antennas and wireless communication and signal and information processing.



Yi Tan is now Lecturer with College of Communication Engineering, Chengdu University of Information Technology. His research activities are electromagnetic meta-material and its application in microwave engineering area, FDTD and CAD analysis for the metamaterial model and characteristics.

A Low Mutual Coupling Two-Element MIMO Antenna with a Metamaterial Matrix Loading

Ping Xu^{1,2}, Shengyuan Luo², Yinfeng Xia¹, Tao Jiang¹, and Yingsong Li^{1,3}

¹ College of Information and Communication Engineering
Harbin Engineering University, Harbin 150001, China
jiangtao@hrbeu.edu.cn

² Naval Research Academy, PLA (NVRA), Shanghai 200235, China

³ Key Laboratory of Microwave Remote Sensing
National Space Science Center, Chinese Academy of Sciences, Beijing 100190, China
liyingsong@ieee.org

Abstract — A low mutual coupling two-element multiple-input multiple-output (MIMO) antenna with a loading metamaterial structure is proposed numerically and experimentally. The proposed MIMO antenna operating at 5.5 GHz consists of a two-element patch antenna array and a metamaterial structure which is to reduce the coupling between the two patch antenna elements for a small radar applications. In this design, the edge-to-edge distance between two patch elements is set to be 2 mm, which is closely installed and uses the same ground plane. The proposed metamaterial structure blocks the propagation of the electromagnetic waves from the original propagation path along the substrate. The numerical and experimental results demonstrate that the mutual coupling between the antenna elements is reduced to less than -20 dB in the operating band.

Index Terms — Isolation enhancement, metamaterial, MIMO antenna array, mutual decoupling.

I. INTRODUCTION

With the evolution of the advanced wireless communication technologies, the demand of the high data rate, high throughput and high capacity is important to the communication systems, which promote the scholars and industrial companies to develop better communication techniques. Recently, the multiple-input multiple-output MIMO technology and massive MIMO techniques have been seen as the most advantage techniques to improve the communication quality [1-3]. Thus, the MIMO antenna changes to be the important techniques for receiving and transmitting signals. Comparing with the traditional MIMO antenna array technology, the massive MIMO antenna array technology can serve more than hundreds of users and

terminals simultaneously, which need to arrange more antenna elements in the limited physical space for the miniaturization of the portable terminals [4-6]. The edge-to-edge distance between the elements in the massive MIMO antenna array is only a fraction of the wavelength, and hence, the mutual coupling in massive MIMO antenna array is inevitable, which will seriously deteriorate the receiving and transmitting signals characteristics of the antenna array [5-6]. In addition, the strong coupling will lead to the signal disturbing from each other antenna element and degrades the maximum achievable performance of the system. Thereby, the mutual decoupling design techniques are required in the practical MIMO or massive MIMO antenna arrays to reject the mutual effects from the neighboring elements.

Until now, there are many existing mutual decoupling techniques used in the MIMO antenna array, including mutual decoupling networking [7-9], defected ground structure (DGS) [10-12], electromagnetic band gap (EBG) [13-15], and metamaterial [16-20], and so on. In [7], mutual decoupling network techniques are adopted and placed between the two neighboring elements in the antenna array, which can reduce the direct coupling but it cannot eliminate the indirect coupling between the elements in the antenna array. In addition, the mutual decoupling networks proposed in [8] are loaded between two-element antenna array, which is difficult to be expanded in massive MIMO antenna array. The DGS reported in [10-12] changes the electric current path in the public metaled ground plane, which can effectively reduce the mutual coupling between the antenna array elements, while it may increase the back radiation and electromagnetic leak. For the EBGs studied in [13-15], they are installed between the antenna array elements, which can provide

a high impedance characteristic to reject the electromagnetic wave propagation from adjacent antenna array elements. However, this method placed the EBG and the antenna elements on the same substrate to suppress the propagation of the surface waves, resulting in large edge-to-edge distance. Recently, the metamaterial has attracted more attention owing to its unique characteristics like the high impedance within the operation band [16-20]. Then, the metamaterial has been widely studied to create meta-surface to implement the mutual coupling reduction in the MIMO antenna array [21-22]. However, they cannot get ideal matching to the original antenna array. On the other hand, the metamaterial can be regarded as an EBG structure by using its high impedance characteristic in the operating band [22]. The metamaterial can also be used to enhance the antenna gain [23].

In order to expand the meta-surface to mutual decoupling in the massive MIMO antenna array and to further reach the great matching to original antenna array, the periodic metamaterial is designed as a frequency selective surface by integrating the modified split-ring resonators (SRRs) and metal grid [24]. However, it has a complex structure because the frequency selective characteristics obtaining from the resonant between the modified SRRs which are placed on different layers.

In this paper, the modified SRRs and SRRs are used to construct a meta-surface to reduce the mutual coupling between a two-element MIMO antenna array, which is modeled and optimized in the HFSS based on the finite element method (FEM). Comparing with the traditional one, the proposed meta-surface decoupling is covering to the top of the MIMO antenna array with a distance of 2 mm to make the antenna array much more compact. The proposed antenna array is operated at 5.5-5.75 GHz for small medical radar and WiMAX applications. In this design, the edge-to-edge distance between two patch elements is set to be 2mm, which is closely installed and uses the same ground plane. To further investigate the decoupling function of the proposed meta-material structure in the MIMO antenna array design, a meta-surface (with 4×6 cells) is designed with the same size of the antenna array and is used to realize the coupling reduction. In comparison with the traditional mutual decoupling techniques, this work has follow features:

(1) The proposed meta-material structure is realized based on modified SRRs, making them easy to design.

(2) The proposed meta-material structure has a great impedance matching to the MIMO antenna array, resulting in very small edge-to-edge distance between two patch elements.

(3) The proposed meta-material structure is

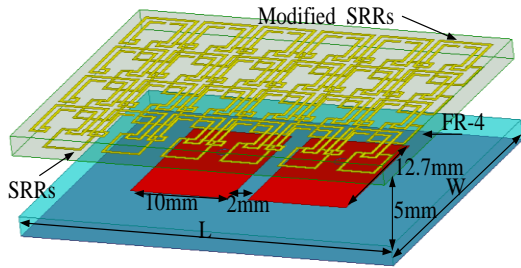
designed on the same substrate with two different SRR layers to provide a stable bandwidth of the meta-material.

(4) Since the edge-to-edge distance between the neighboring elements of the antenna array is set to be 2mm, the proposed mutual coupling reduction scheme can be easily integrated in the massive MIMO antenna arrays.

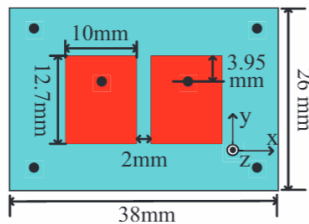
II. THE GEOMETRY OF THE PROPOSED MIMO ANTENNA ARRAY

The proposed MIMO antenna array is presented in Fig. 1. We can see that the two patch antenna elements are printed on a FR-4 substrate with a thickness of 1.6mm, a relative permittivity of 4.4 and a loss tangent of 0.02, while there is a ground plane on the other side of the MIMO antenna. A meta-material structure is realized by printing the modified SRRs on the top of the second FR-4 substrate, while the SRRs are designed on the bottom of the second substrate to help to expand the operating bandwidth of the meta-material. Then, the developed meta-material structure is installed above the designed MIMO antenna array with a gap of 5 mm between the bottom of meta-material structure and the top of the MIMO antenna array. In this design, the meta-material structure aims to block the space-wave propagation and reduces the mutual coupling of the antenna array. The proposed MIMO antenna is fed by probes, which is connected by using the SMA connectors.

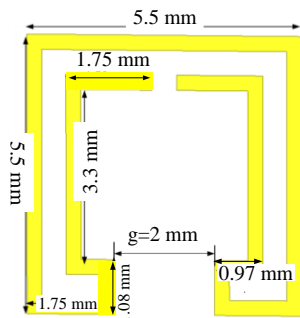
From Fig. 1, we can see that the proposed meta-material structure is realized by a 6×4 meta-material cell matrix, which can cover the entire area of the MIMO antenna array. The principle of the proposed MIMO antenna array scheme is listed in Fig. 2. If one of the antenna is used as the source of the MIMO antenna, there will be induction currents distributed on the near-by antenna element since the distance of these antenna elements are short. Then, the mutual coupling will be happened between the antenna elements. The proposed 6×4 meta-material matrix loading on the top of the MIMO antenna array proposed a high impedance band to suppress the interferences from the near-by antenna elements. To better understand the performance of the meta-material structure and the mutual coupling reduction results, the simulated surface current distribution without and with proposed 6×4 meta-material matrix loading are presented in Fig. 3. Without the proposed 6×4 meta-material matrix, one can see that a strong induction current appears on the right patch antenna when the left patch antenna is excited. In contrast, with the proposed 6×4 meta-material matrix loading, the current on the right patch antenna is very weak. Thus, it is concluded that the suspended 6×4 meta-material matrix can effectively reduce the mutual coupling between antenna array elements.



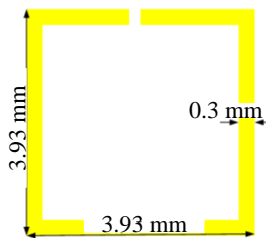
(a) 3-D view



(b) MIMO antenna array without the meta-material loading



(c) Modified SRR cell



(d) SRR cell

Fig. 1. Geometry of the proposed MIMO antenna array.

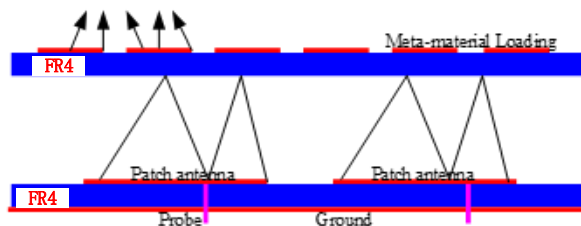


Fig. 2. Radiation principle of the proposed MIM (the block lines are the wave propagation path and the arrows are the directions of the radiation).

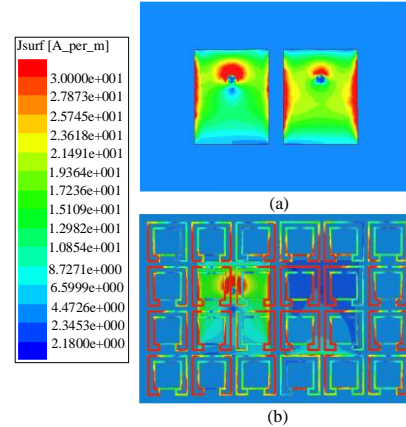


Fig. 3. Surface current distribution of the proposed MIMO antenna array for 5.5 GHz at time of 0: (a) without metamaterial matrix loading, and (b) with metamaterial matrix loading.

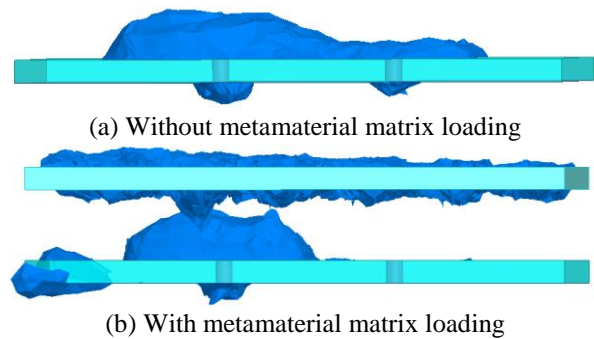


Fig. 4. Calculated electric field distributions of the MIMO antenna array.

To further discuss the above phenomena, the electric field distributions of the proposed MIMO antenna array without and with the proposed 6×4 meta-material matrix loading are shown in Fig. 4. Herein, two antennas in the array are fed together and the results are obtained using the HFSS. We can see that without the 6×4 meta-material matrix loading, a large amount of electric field is coupled to the right patch antenna from the space propagation. Conversely, the electric field is directed toward the broadside direction when the proposed 6×4 meta-material matrix loading is used as a cover.

III. RESULTS AND DISCUSSIONS

From the optimization of the MIMO antenna array based on the HFSS, the finalized MIMO antenna array has been fabricated and measured in a chamber. Figure 5 shows the fabricated MIMO antenna for top and side view. Also, the measurement setup of the MIMO antenna array in the chamber is also given and presented in Fig. 6.

The measured S-parameters, including the reflection coefficient (S11) and isolation (S12) are presented in Fig. 7. We can see that the proposed MIMO antenna integrated with the proposed 6×4 meta-material matrix loading has almost the same impedance bandwidth, meaning that the proposed 6×4 meta-material matrix loading scheme does not affect the performance of the MIMO antenna. However, we can see that the isolation has been improved by more than 20dB via the 6×4 meta-material matrix loading. Thus, the mutual coupling of the MIMO antenna array has been reduced to be less than -20dB. This is because that the proposed 6×4 meta-material matrix loading can block the space-wave propagation. There are some differences in between the measured and simulated results, which is caused by the instable of the FR-4 substrate, fabrication tolerance error and measurement errors. Herein, the fabrication tolerance error might be the main effects on the measured results.

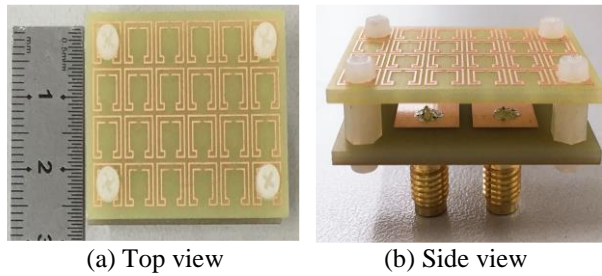


Fig. 5. Photograph of the fabricated prototype.

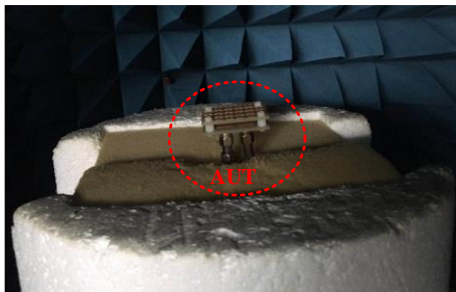


Fig. 6. The measurement setup of the MIMO antenna array in the chamber (AUT: Antenna under test).

Figure 8 shows the radiation patterns of the proposed MIMO antenna array. The radiation patterns at E-plane and H-plane have some difference, which might be caused by the asymmetry of the meta-material array effects. The simulated 3D radiation patterns of the proposed antenna array is presented in Fig. 9. The obtained radiation patterns show that the proposed antenna has directional-like radiation patterns owing to the effects of the meta-material loading. However, its radiation patterns are similar to that of the directional patch antenna. Thus, the loaded 6×4 meta-material

matrix loading can also enhance the gain of the MIMO antenna because the meta-material matrix aided in concentrating more energy into the band-pass frequency band. The measured radiation efficiency is 66%, the measured gain is 4.65 dBi and the measured ECC is less than 0.015.

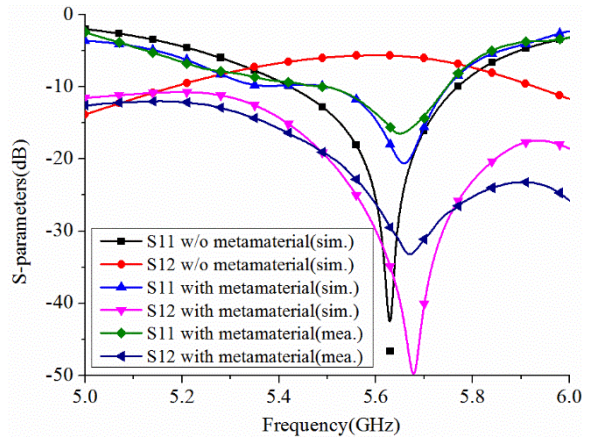


Fig. 7. The simulated and measured S-parameters.

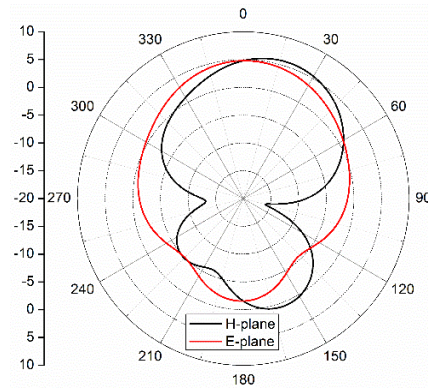


Fig. 8. The radiation patterns of the MIMO antenna array at 5.5 GHz.

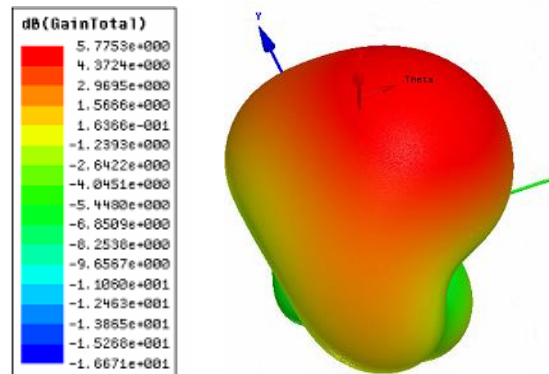


Fig. 9. The simulated 3D radiation patterns of the proposed antenna array at 5.5 GHz.

To prove the advantage of the designed MIMO antenna array, the performance of the proposed MIMO antenna array is compared with the state-of-the-art in Table 1. From the Table 1, it can be found that the proposed MIMO antenna has the small size, high gain and efficiency.

Table 1 Comparison of the proposed MIMO antenna array

Ref.	10-dB BW	Size (mm ²)	Iso. Enhance (dB)	Peak ECC/Gain	Eff. (%)
[7]	9.5%	40×40.4	33	NA/6.55	NA
[11]	1.9%	36×36	12	NA/NA	NA
[17]	1%	70×30	11	NA/4.37	NA
PW	4.4%	38×26	25	0.015/4.65	66

Notes: PW: Proposed work; Iso.: Isolation; ECC: envelope correlation coefficient.

IV. CONCLUSION

A high isolation two-element MIMO antenna array has been proposed by using a 6×4 meta-material matrix loading technique and its performance has been investigated and discussed numerically and experimentally. The proposed MIMO antenna array is optimized, fabricated and measured to verify its performance, while the results demonstrate that the isolation of the proposed MIMO antenna array is less than -20 dB within the operating band. In the future, the proposed technique can be used for developing the dual-band or dual-polarization low mutual coupling MIMO arrays [25-26], beamforming [27], direction of arrival (DOA) [28-29] using adaptive methods [30-36].

ACKNOWLEDGMENT

This work was supported in part by the Fundamental Research Funds for the Central Universities HEUCFG201829 and 3072019CFG0801, China Postdoctoral Science Foundation (2017M620918, 2019T120134), and the National Key Research and Development Program of China under Grant 2016YFE0111100.

REFERENCES

- [1] H. Zhang, Z. Wang, J. Yu, and J. Huang, "A compact MIMO antenna for wireless communication," *IEEE Antennas and Propagation Magazine*, vol.50, pp. 104-107, 2008.
- [2] Y. Li, W. Li, and W. Yu, "A multi-band/UWB MIMO/diversity antenna with an enhance isolation using radial stub loaded resonator," *Applied Computational Electromagnetics Society Journal*, vol. 28, no. 1, pp. 8-20, 2013.
- [3] M. Jensen and J. Wallace, "A review of antennas and propagation for MIMO wireless communications," *IEEE Trans. Antennas Propag.*, vol. 52, no. 11, pp. 2810-2824, Nov. 2004.
- [4] M. Wang, Y. Li, H. Zou, et al., "Compact MIMO antenna for 5G portable device using simple neutralization line structures," *2018 IEEE International Symposium on Antennas and Propagation & USNC/URSI National Radio Science Meeting*, Boston, MA, USA, July 8-13, 2018.
- [5] E. G. Larsson, O. Edfors, F. Tufvesson, and T. L. Marzetta, "Massive MIMO for next generation wireless systems," *IEEE Commun. Mag.*, vol. 52, no. 2, pp. 186-195, Feb. 2014.
- [6] L. Lu, G. Li, A. Swindlehurst, A. Ashikhmin, and R. Zhang, "An overview of massive MIMO: Benefits and challenges," *IEEE J. Sel. Topics Signal Process.*, vol. 8, no. 5, pp. 742-758, Oct. 2014.
- [7] R. Xia, S. Qu, P. Li, Q. Jiang, and Z. Nie, "An efficient decoupling feeding network for microstrip antenna array," *IEEE Antennas Wireless Propag. Letts.*, vol. 14, pp. 871-874, 2015.
- [8] L. Zhao and K. Wu, "A dual-band coupled resonator decoupling network for two coupled antennas," *IEEE Trans. Antennas Propag.*, vol. 63, no. 7, pp. 2843-2850, July 2015.
- [9] L. Zhao, F. Liu, X. Shen, G. Jing, Y. Cai, and Y. Li, "A high-pass antenna interference cancellation chip for mutual coupling reduction of antennas in contiguous frequency bands," *IEEE Access*, vol. 6, pp. 38097-38105, 2018.
- [10] D. Hou, S. Xiao, B. Wang, L. Jiang, J. Wang, and W. Hong, "Elimination of scan blindness with compact defected ground structures in microstrip phased array," *IET Microw. Antennas Propag.*, vol. 3, no. 2, pp. 269-275, 2009.
- [11] F. Zhu, J. Xu, and Q. Xu, "Reduction of mutual coupling between closely-packed antenna elements using defected ground structure," *IEEE Trans. Antennas Propag.*, vol. 55, no. 6, pp. 1732-1738, 2007.
- [12] K. Wei, J. Li, L. Wang, Z. Xing, and R. Xu, "Mutual coupling reduction by novel fractal defected ground structure bandgap filter," *IEEE Trans. Antennas Propag.*, vol. 64, no. 10, pp. 4328-4335, 2006.
- [13] F. Yang and Y. Rahmat-Samii, "Microstrip antennas integrated with electromagnetic band-gap (EBG) structures: A low mutual coupling design for array applications," *IEEE Transactions on Antennas and Propagation*, vol. 51, no. 10, pp. 2936-2946, 2003.
- [14] T. Jiang, T. Jiao, and Y. Li, "Array mutual coupling reduction using L-loading E-shaped electromagnetic band gap structures," *Int. J. Antennas Propag.*, vol. 2016, Article ID: 6731014, 9 pages, 2016.

- [15] T. Jiang, T. Jiao, and Y. Li, "A low mutual coupling MIMO antenna using periodic multi-layered electromagnetic band gap structures," *Appl. Comput. Electromagn. Soc. J.*, vol. 33, no. 3, pp. 758-763, 2018.
- [16] R. Hafezifard, M. Moghadasi, J. Mohassel, and R. Sadeghzadeh, "Mutual coupling reduction for two closely spaced meander line antennas using metamaterial substrate," *IEEE Antennas Wireless Propag. Letts.*, vol. 15, pp. 40-43, 2016.
- [17] Z. Qamar, U. Naeem, S. Khan, M. Chongcheawchamnan, and M. Shafique, "Mutual coupling reduction for high-performance densely packed patch antenna arrays on finite substrate," *IEEE Trans. Antennas Propag.*, vol. 64, no. 5, pp. 1653-1660, May 2016.
- [18] K. Yu, Y. Li, and X. Liu, "Mutual coupling reduction of a MIMO antenna array using 3-D novel meta-material structures," *Appl. Comput. Electromagn. Soc. J.*, vol. 33, no. 7, pp. 758-763, 2018.
- [19] S. Luo, Y. Li, Y. Xia, G. Yang, L. Sun, and L. Zhao, "Mutual coupling reduction of a dual-band antenna array using dual-frequency metamaterial structure," *Applied Computational Electromagnetics Society Journal*, vol. 34, no. 3, pp. 403-410, 2019.
- [20] S. Luo, Y. Li, Y. Xia, and L. Zhang, "A low mutual coupling antenna array with gain enhancement using metamaterial loading and neutralization line structure," *Applied Computational Electromagnetics Society Journal*, vol. 34, no. 3, pp. 411-418, 2019.
- [21] M. Farahani, J. Pourahmadazar, M. Akbari, et al., "Mutual coupling reduction in millimeter-wave MIMO antenna array using a metamaterial polarization-rotator wall," *IEEE Antennas and Wireless Propagation Letters*, vol. 16, pp. 2324, 2327, 2017.
- [22] S. N. Boyko, A. S. Kukharenko, and Y. S. Yaskin, "EBG metamaterial ground plane application for GNSS antenna multipath mitigating," *International Workshop on Antenna Technology (iWAT)*, Seoul, South Korea, 2015.
- [23] D. Binion, P. L. Werner, and D. H. Werner, "Metamaterial enhanced antenna systems: A review," *2018 International Applied Computational Electromagnetics Society Symposium (ACES)*, Denver, CO, USA, March 25-29, 2018.
- [24] S. Luo, Y. Li, C. Y. D. Sim, Y. Xia, and X. Liu, "MIMO antenna array based on metamaterial frequency elective surface," *International Journal of RF and Microwave Computer-Aided Engineering*, Submitted.
- [25] F. Liu, H. Guo, L. Zhao, et al., "Dual-band metasurface-based decoupling method for two closely packed dual-band antennas," *IEEE Transactions on Antennas and Propagation*, 10.1109/TAP.2019.2940316.
- [26] J. Guo, F. Liu, L. Zhao, Y. Yin, G. L. Huang, and Y. Li, "Meta-surface antenna array decoupling designs for two linear polarized antennas coupled in H-plane and E-plane," *IEEE Access*, vol. 7, pp. 100442-100452, 2019.
- [27] W. Shi, Y. Li, L. Zhao, and X. Liu, "Controllable sparse antenna array for adaptive beamforming," *IEEE Access*, vol. 7, pp. 6412-6423, 2019.
- [28] X. Zhang, T. Jiang, Y. Li, and X. Liu, "An off-grid DOA estimation method using proximal splitting and successive nonconvex sparsity approximation," *IEEE Access*, vol. 7, pp. 66764-66773, 2019.
- [29] X. Zhang, T. Jiang, Y. Li, and Y. Zakharov, "A novel block sparse reconstruction method for DOA estimation with unknown mutual coupling," *IEEE Communications Letters*, vol. 23, no. 10, pp. 1845-1848, 2019.
- [30] W. Shi, Y. Li, and Y. Wang, "Noise-free maximum correntropy criterion algorithm in non-Gaussian environment," *IEEE Transactions on Circuits and Systems II: Express Briefs*, 10.1109/TCSII.2019.2914511.
- [31] Y. Li, Z. Jiang, W. Shi, X. Han, and B. Chen, "Blocked maximum correntropy criterion algorithm for cluster-sparse system identifications," *IEEE Transactions on Circuits and Systems II: Express Briefs*, 10.1109/TCSII.2019.2891654.
- [32] Y. Li, Z. Jiang, O. M. O. Osman, X. Han, and J. Yin, "Mixed norm constrained sparse APA algorithm for satellite and network echo channel estimation," *IEEE Access*, vol. 6, pp. 65901-65908, 2018.
- [33] Y. Li, Y. Wang, and T. Jiang, "Norm-adaption penalized least mean square/fourth algorithm for sparse channel estimation," *Signal Processing*, vol. 28, pp. 243-251, 2016.
- [34] Y. Li, Y. Wang, and T. Jiang, "Sparse-aware set-membership NLMS algorithms and their application for sparse channel estimation and echo cancelation," *AEU-International Journal of Electronics and Communications*, vol. 70, no. 7, pp. 895-902, 2016.
- [35] Y. Li, Z. Jiang, Z. Jin, X. Han, and J. Yin, "Cluster-sparse proportionate NLMS algorithm with the hybrid norm constraint," *IEEE Access*, vol. 6, pp. 47794-47803, 2018.
- [36] Q. Wu, Y. Li, Y. Zakharov, W. Xue, and W. Shi, "A kernel affine projection-like algorithm in reproducing kernel hilbert space," *IEEE Transactions on Circuits and Systems II: Express Briefs*, 10.1109/TCSII.2019.2947317.

Four-Element Planar MIMO Antenna for Indoor Communications with High Isolation

Mohamed M. Morsy

Department of Electrical Engineering
Texas A&M University-Texarkana, Texarkana, TX 75503, USA
mmorsy@tamut.edu

Abstract — A low-profile monopole microstrip antennas with multiple-input-multiple-output (MIMO) configuration for a 4G/5G communication terminal is presented. The MIMO antenna system consists of four elements that operate in the LTE1800/2600 and GSM1800 bands. The antenna elements are mounted along the four sides of a rectangular ground plane of size $120 \times 100 \text{ mm}^2$. Spatial diversity technique and a modified ground plane are used to enhance isolation between elements. To mitigate the mutual coupling effect, the lower corners of the ground plane have been truncated. The measured isolation is lower than -17 dB between any two elements over the operating frequency bands. The total efficiency ranges from 69% to 83% and from 73% to 86% over LTE1800 and LTE2600 bands, respectively. The diversity performance of the measured envelope correlation coefficient (ECC) and radiation patterns meet the diversity criteria for 4/5G networks.

Index Terms — LTE antenna, Microstrip antenna, MIMO antenna, Monopole antennas, Planar antenna

I. INTRODUCTION

The development of the long-term-evolution (LTE) technology has been an on-going process in the last decade. LTE satisfies the demand of the 4/5G networks that require high data capacity and speed. Because of the various band allocations of LTE in different countries, the design of LTE antennas mandates multiple frequency bands operation. Furthermore, MIMO is another major technology used to enhance the performance of LTE networks. Although MIMO technology adds to the complexity of LTE antenna design in terms of number of antennas, it provides high data rates and improved spectral efficiency. In order to have an efficient MIMO antenna system for user's devices, there are many challenges that have to be addressed. Among them is to design uncorrelated MIMO antenna elements in a confined space. Many techniques have been used to increase the isolation of MIMO elements while maintaining a compact design. The most common technique is to use the spatial diversity technique by

separating antenna elements by 0.5λ . However, this technique may not be suitable for most user devices, since it requires a relatively large space to place the antenna system. Thus, several isolation techniques have been used to mitigate the mutual coupling effect of MIMO elements in a confined space. Among them are the use of parasitic structures [1], modified ground planes [2], orthogonally-oriented elements [3, 4], metamaterial structures [5, 6]. Radiation diversity has also proved to be an effective isolation technique [7-9]. As shown in [4], placing elements in orthogonal position help mitigate mutual coupling. In [10], a slotted wideband 4-element MIMO antenna is presented. The mutual coupling is only -14 dB between elements. Electromagnetic Band Gap (EBG) structure has proven to be successful in reducing the mutual coupling between MIMO elements [11, 12]. Moreover, planar and low-profile MIMO structures have proved to be successful candidates for wireless devices [13].

This letter presents a low-profile dual-band MIMO antenna for LTE1800 and LTE2600 bands for indoor applications such as LTE routers or repeaters. The design consists of four elements that are placed at the four sides of the ground plane. To enhance the isolation between these closely spaced elements, the ground plane is truncated at its lower corners. The coupling level is below -17 dB in the operating bands.

II. ANTENNA CONFIGURATION AND DESIGN

The geometry of the proposed MIMO antenna is given in Fig. 1 (a), while a photograph of the antenna prototype is shown in Fig. 1 (b). The antenna is printed on a single-sided FR4 substrate with a thickness of 0.8 mm and a dielectric constant of 4.4. The overall size of the printed MIMO antenna is $128 \times 148 \text{ mm}^2$. The large size of the ground plane help improve isolation between elements and free up more space for other circuit components. Table 1 lists the dimensions of the proposed MIMO antenna. Antennas 1 and 3 are designed to operate over the LTE1800 bands, while antennas 2 and 4 operate over LTE2600 bands. The resonance of each element is

determined by its total path length. The path length of each of antennas 1 and 3 is 105 mm, while the path length of each of antennas 2 and 4 is 75 mm. The width of each trace of radiation elements is determined by rigorous parametric analysis in order to achieve good matching over the operating frequency bands. The full-wave simulation software CST Microwave Studio is used to analyze the design parameters of the proposed antenna [14].

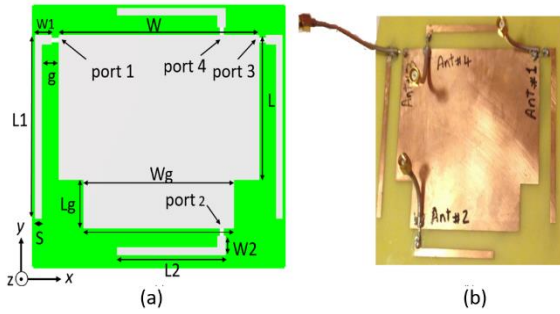


Fig. 1. (a) Geometry of the proposed MIMO antenna, and (b) photograph of the fabricated MIMO antenna.

Table 1: Dimensions of the proposed MIMO antenna

Parameter	W	L	L1	L2	W_g
Value (mm)	120	75	95	65	90
Parameter	L_g	W1	W2	g	S
Value (mm)	25	10	10	10	4

The simulated and measured reflection coefficients of antenna elements are plotted in Figs. 2 and 3. It is seen that the measured and simulated reflection coefficients (S_{ii} , $i=1,2,3,4$) are in agreement with the measured data. The simulated and measured mutual couplings are shown in Fig. 4. It is seen that the measured mutual couplings (S_{13} , S_{24}) are all below -17 dB across LTE1800, and LTE2600 bands as shown in Figs. 4 (a) and 4 (b), respectively.

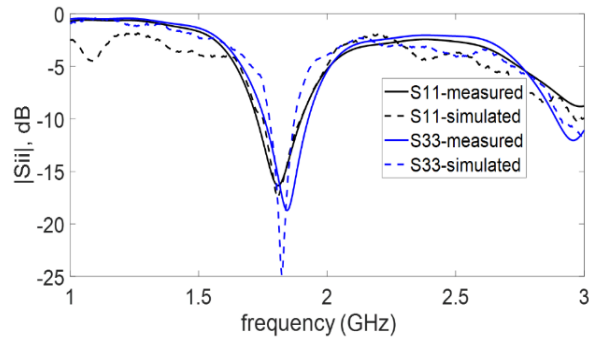


Fig. 2. Measured and simulated reflection coefficients of antennas 1 and 3.

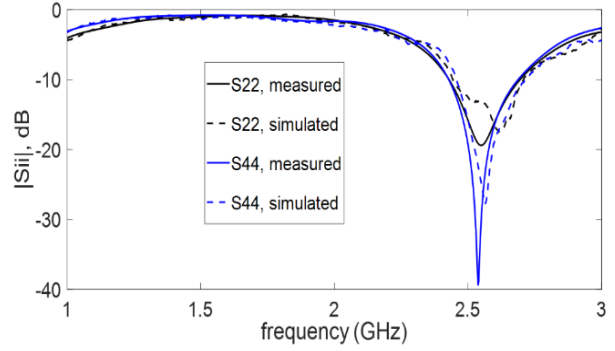
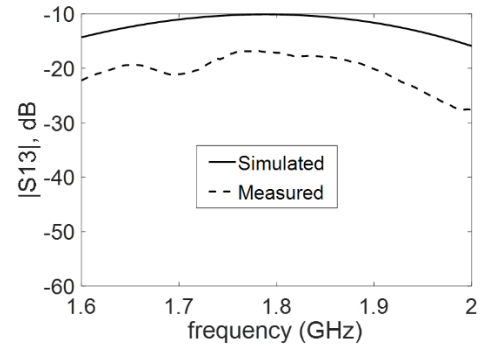
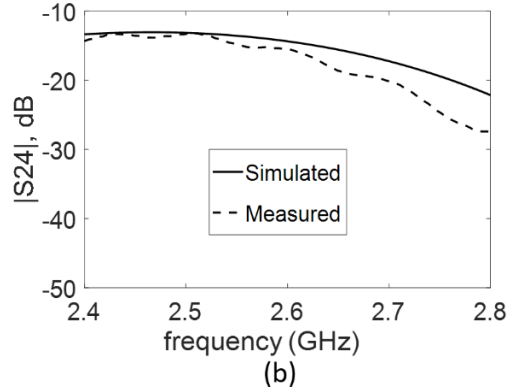


Fig. 3. Measured and simulated reflection coefficients of antennas 2 and 4.



(a)



(b)

Fig. 4. Measured and simulated mutual couplings: (a) measured and simulated S_{13} , and (b) measured and simulated S_{24} .

The isolation behavior can be studied by comparing the current distributions of the optimized design (with trimmed lower corners of the ground plane), as shown in Figs. 5 (b) and 5 (d) with the corresponding current distributions of the proposed antenna without trimming the lower corners of the ground plane as displayed in Figs. 5 (a), and 5 (c). In Figs. 5 (a) and 5 (b), antenna 1 is excited at 1.8 GHz, while other elements are terminated by a 50- Ω port. Similarly, antenna 2 is excited at 2.6 GHz as shown in Figs. 5 (c) and 5 (d). After trimming the

lower corners of the ground plane, the surface current, flowing between antennas 1 and 3, is substantially small, and hence the mutual coupling is reduced. Similarly, the trimmed lower corners have disturbed the current distribution between antennas 2 and 4, and hence an improved isolation is achieved. Although no complicated isolation structures are used, isolation is further enhanced by placing elements of same operation frequency on opposite sides of the trimmed ground plane. The separation distance between antennas 1 and 3 is 0.7λ ($f=1.6$ GHz), while the separation distance between antennas 2 and 4 is 0.87λ ($f=2.6$ GHz). That configuration has resulted in substantially reduced isolation of less than -18 dB between antennas 1 and 3 over LTE1800 bands, while the measured isolation is less than -17 dB between antennas 2 and 4 over LTE2600 bands.

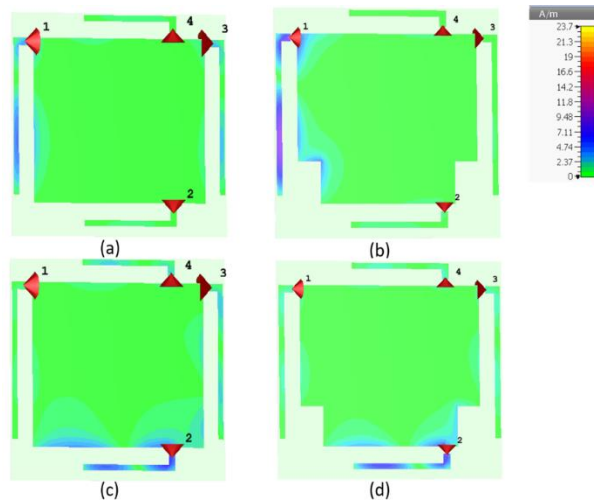


Fig. 5. Surface current distribution in A/m: (a) Antenna 1 is excited without the isolation structure, (b) Antenna 1 is excited with the isolation structure, (c) Antenna 2 is excited without the isolation structure, and (d) Antenna 2 is excited with the isolation structure.

III. RADIATION PATTERN AND DIVERSITY PERFORMANCE

The measured gain patterns of antenna elements 1 and 2 are presented in Fig. 6. The radiation patterns of antennas 3 and 4 are similar to those of antennas 1 and 2; respectively. Figures 6 (a) and 6 (b) exhibit the total gain at 1.8 GHz and 2.6 GHz in the x-z, and y-z planes; respectively. It is seen that the antenna exhibits omnidirectional patterns in the x-z plane at 1.8 and 2.6 GHz, as shown in Fig. 6 (a). However, Fig. 6 (b) shows only omnidirectional pattern at 2.6 GHz in the y-z plane. Figure 7 shows the total antenna efficiency and realized gain of the 4-element MIMO antenna. It is seen that efficiency of antennas 1 and 3 ranges from 69% to 85% over LTE1800 bands. And the efficiency of antennas 2

and 4 ranges from 73% to 86% over LTE2600 bands. The peak realized gain ranges from 3 to 4 dBi over LTE1800 bands, and from 2.6 to 3 dBi over LTE2600 bands. The envelope correlation coefficient (ECC) is used to evaluate the diversity performance of MIMO antenna system. In this Letter, the ECC is calculated by using measured far-field radiation patterns, as shown in Eq. (1) [15]:

$$\rho_e = \frac{\oint \{XPR \cdot E_{\theta 1}(\Omega)E_{\theta 2}^*(\Omega)P_{\theta}(\Omega) + E_{\phi 1}(\Omega)E_{\phi 2}^*(\Omega)P_{\phi}(\Omega)\}d\Omega}{B1 B2},$$

$$B1 = \sqrt{\oint \{XPR \cdot E_{\theta 1}(\Omega)E_{\theta 1}^*(\Omega)P_{\theta}(\Omega) + E_{\phi 1}(\Omega)E_{\phi 1}^*(\Omega)P_{\phi}(\Omega)\}d\Omega},$$

$$B2 = \sqrt{\oint \{XPR \cdot E_{\theta 2}(\Omega)E_{\theta 2}^*(\Omega)P_{\theta}(\Omega) + E_{\phi 2}(\Omega)E_{\phi 2}^*(\Omega)P_{\phi}(\Omega)\}d\Omega}.$$
(1)

where XPR is the cross-polarization radiation. For an isotropic environment, XPR=1. $E_{\theta}(\Omega)$ and $E_{\phi}(\Omega)$ are the orthogonal θ - and ϕ -components of the antenna radiation pattern. $P_{\theta}(\Omega)$ and $P_{\phi}(\Omega)$ are the angular power density functions of the incident wave. As shown in Fig. 7, the computed ECC is less than 0.05 and 0.03 over LTE1800 and LTE2600 bands, respectively.

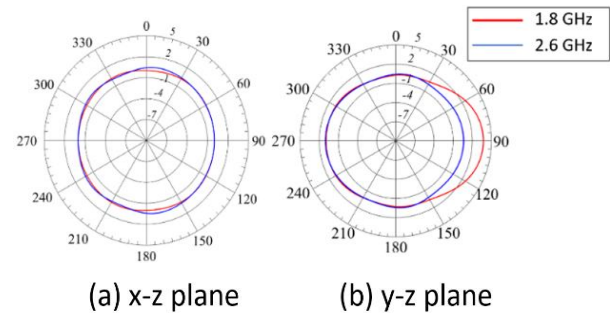


Fig. 6. Measured radiation patterns (gain in dBi) of the proposed antenna at 1.8 and 2.6 GHz: (a) x-z plane and (b) y-z plane.

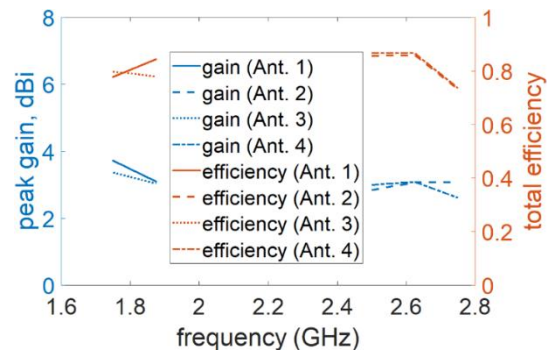


Fig. 7. Peak gain and total efficiency of MIMO antennas system over LTE1800 and LTE2600 bands.

Table 2 compares the total size (including the ground plane), covered LTE bands, efficiency, and ECC of the proposed design with some recently published results of 4-element LTE MIMO antennas. Considering

the covered LTE bands, it is seen that the proposed antenna has better performance in terms of isolation and ECC compared with others listed in Table 2.

Table 2: Performance comparison between the proposed antenna and other 4-element MIMO antennas in the LTE band

Ref.	Size (mm ²)	LTE Bands (MHz)	Isolation dB	Total Efficiency %	ECC
[16]	115×83	LTE3500	< -16 dB	-	<0.03
[17]	136×68.8	LTE2300 LTE2600	<-11 dB	85-95	<0.3
[18]	108×108	LTE2100 LTE2300 LTE2600	<-12 dB	82-88	<0.2
[10]	120×140	LTE2100 LTE2300	<-14 dB	60-80	<0.25
This work	128×148	LTE1800 LTE2600	<-17 dB	69-86	<0.05

IV. CONCLUSION

A novel four-element MIMO antenna system which covers LTE1800 (1750–1880 MHz), and LTE2600 (2500–2690 MHz) as well as GSM1800 bands is proposed. The antenna elements are printed monopoles deployed on a low-profile PCB dimensions of 128×148 mm² and an element size of 95×5 mm². By utilizing spatial diversity technique and appropriately trimming the lower corners of the ground plane, the mutual couplings among the elements are all below -17 dB without using any additional decoupling structures or circuitry. The designed antennas feature very low envelope correlation coefficients, near-omnidirectional gain patterns, and reasonable total antenna efficiency values in operating bands. The measured and simulated results are in good agreement. Based on the diversity performance, radiation patterns, and s-parameters results, the antenna is a good candidate for indoor applications such as LTE routers and repeaters.

REFERENCES

- [1] A. Toktas and A. Akdagli, "Wideband MIMO antenna with enhanced isolation for LTE, WiMAX and WLAN mobile handsets," *Electron. Lett.*, vol. 50, no. 10, pp. 723-724, May 2014.
- [2] K. Kim and K. Ahn, "The high isolation dual-band inverted F antenna diversity system with the small N-section resonators on the ground plane," *Microw. Opt. Technol. Lett.*, vol. 49, pp. 731-734, Jan. 2007.
- [3] J. Malik, D. Nagpal, and M. V. Kartikeyan, "MIMO antenna with omnidirectional pattern diversity," *Electron. Lett.*, vol. 52, no. 2, pp. 102-104, Jan. 2016.
- [4] R. R. Ramirez and F. De Flaviis, "A mutual coupling study of linear and circular polarized microstrip antennas for diversity wireless systems," *IEEE Trans. Antennas Propag.*, vol. 51, no. 2, pp. 238-248, Feb. 2003.
- [5] D. A. Ketzaki and T. V. Yioultsis, "Metamaterial-based design of planar compact MIMO monopoles," *IEEE Trans. Antennas Propag.*, vol. 61, no. 5, pp. 2758-2766, May 2013.
- [6] K. Yu, Y. Li, and X. Liu, "Mutual coupling reduction of a MIMO antenna array using 3-D novel meta-material structures," *Applied Computational Electromagnetic Society (ACES) Journal*, vol. 33, no. 7, pp. 758-763, Mar. 2019.
- [7] K. Wei, Z. Zhang, W. Chen, and Z. Feng, "A novel hybrid-fed patch antenna with pattern diversity," *IEEE Antennas Wirel. Propag. Lett.*, vol. 9, pp. 562-565, May 2010.
- [8] S. Karamzadeh, "A novel compact polarization diversity ultra-wideband MIMO antenna," *Applied Computational Electromagnetic Society (ACES) Journal*, vol. 32, no. 1, pp. 74-80, Jan. 2017.
- [9] H. Li, L. Kang, Y. Xu, and Y.-Z. Yin, "Planar dual-band WLAN MIMO antenna with high isolation," *Applied Computational Electromagnetic Society (ACES) Journal*, vol. 31, no. 12, pp. 1410-1415, Dec. 2016.
- [10] R. Anitha, P. V. Vinesh, K. C. Prakash, P. Mohanan, and K. Vasudevan, "A compact quad element slotted ground wideband antenna for MIMO applications," *IEEE Trans. Antennas Propag.*, vol. 64, no. 10, pp. 4550-4553, Oct. 2016.
- [11] H. Sajjad, S. Khan, and E. Arvas, "Mutual coupling reduction in array elements using EBG structures," in *Proc. International Applied Computational Electromagnetics Society Symposium*, Florence,

- Italy, pp. 1-2, 2017.
- [12] J. Kumar, "Compact MIMO antenna," *Microw. Opt Technol Lett.*, vol. 58, pp. 1294-1298, Mar. 2016.
- [13] F. Ahmed, R. Li, and Y. Feng, "Development of a compact planar multiband MIMO antenna for 4G/LTE/WLAN mobile phone standards," *2013 Proceedings of the International Symposium on Antennas & Propagation*, Nanjing, pp. 539-542. 2013.
- [14] CST Microwave Studio, ver. 2019, Computer Simulation Technology, Framingham, MA, 2019.
- [15] S. Stein, "On cross coupling in multiple-beam antennas," *IRE Trans. on Ant. and Prop.*, vol. 10, no. 5, pp. 548-557, Sep. 1962.
- [16] W.-W. Lee and B. Jang, "A smart 4 by 4 MIMO antenna systems for LTE smartphones," *Microw. Opt. Tech. Lett.*, vol. 58, pp. 2668-2672, Aug. 2016.
- [17] Yang and T. Li, "Box-folded four-element MIMO antenna system for LTE handsets," *Electron. Lett.*, vol. 51, no. 6, pp. 440-441, Mar. 2015.
- [18] A. A. Yussuf and S. Paker, "Design of wideband MIMO antenna for wireless applications," in *Proc. Signal Processing and Communications Applications*

Conference (SIU), Antalya, Turkey, pp. 1-14, 2017.



Mohamed Morsy received the B.S. degree in Electrical Engineering from Alexandria University, Egypt in 2004 and the M.S. and Ph.D. degrees in Electrical and Computer Engineering from Southern Illinois University, Carbondale, IL, in 2006 and 2010; respectively.

Since 2018, he has been an Associate Professor with the Electrical Engineering Department, Texas A&M University-Texarkana, Texarkana, TX. He is the author of more than 20 peer-review articles. His research interests include electromagnetic devices, antennas, RF filters, and dielectric resonators (DR). Other subjects of research are on designing antennas for the 4/5G- mobile terminals, and phased array antennas.

Morsy is an IEEE senior member and an IDEAL (Institute for the Development of Excellence in Assessment Leadership) scholar.

Optimization of a Dual-Band, Printed Octafilar Antenna

Joseph D. Majkowski

L3Harris Communication Systems
Rochester NY, 14610, United States
Joe.Majkowski@L3Harris.com

Abstract — This paper presents several innovative techniques for the design and optimization of a dual band, octafilar helix antenna. The technical challenge of this design is how close the two bands of operation are, as well as the requirement to fit inside a radome with $.07\lambda$ diameter and $.33\lambda$ length. This was achieved through a novel technique of applying differing pitches and terminations to the upper and lower frequency antenna filars and then feeding them from a similar location at the base. This allowed for optimal current distribution on each of the two antenna filars. The final design produced gain greater than 0dBic at zenith across both bands of operation. The techniques discussed in this paper were seen to grow low frequency performance by as much as 2.5dBic over a typical octafilar design of the same size.

Index Terms — Dualband, octafilar, QHA.

I. INTRODUCTION

Satellite communications have seen continuous growth in the past few decades as we continue to develop and place new constellations in space. These constellations can vary in operational frequencies, type of orbit, and years of service. As the frequency spectrum becomes ever more crowded, the need for close frequency, dual banded structures continue to rise. These antennas must meet strict performance standards to close communication links with geostationary earth orbit or geosynchronous equatorial orbit (GEO) satellite constellations. These constellations are located at altitudes of approximately 35786 kilometers, (22236 miles), above mean sea level. Given the large propagation distance, path loss is very high, which gives rise to the need for high-performance antennas to close the links.

The quadrafilar helix antenna, (QHA), is a prime candidate for utilization in such communication links. The advantages of these antennas lie in their cardioid shaped pattern, low axial ratio, and high right-hand circular polarization (RHCP) gain [1]. Another main advantage of QHA antennas is ability to produce a forward firing antenna which is independent of the ground plane presented. This gives the antenna significantly

better performance over circularly polarized microstrip patch antennas which quickly lose desired performance without an electrically large ground plane [2] The QHA also exhibits an advantage in terms of low angle elevation performance. Typically, the wrapping of the elements can be reduced to increase low angle elevation performance at the cost of gain at zenith.

As satellite communications grew so too did the need for wide bandwidth, increased performance, multiple bands of operation and small form factor antennas. This led to the evolution of antennas such as the QHA by adding multiple filars [3,4]. This configuration can extend or add bandwidth and even enhance performance but does little to affect size.

Multiple techniques were explored to help decrease the size of these antennas. These techniques were the DMFA (Dielectric Multi-filar helical antenna) and the PMFA (Printed Multi-filar helical antenna). The DMFA utilizes high ϵ_R to shrink the overall package size [3,4]. While effective, this typically will result in a decrease in bandwidth as well as decreased efficiency. The PMFA allows for a broad scope of artwork to be employed for the filars. This has led to utilization of differing meandering techniques such as fractals and folded arms [5,6]. Printing has also allowed for the use of rigid boards to make shapes outside of a cylinder, such as the square shaped QHA [7].

The more traditional wire-based elements explore other techniques to improve performance. Such techniques include small matching networks both at the element feeds and at the top of the elements [8,9]. These methods help to add more bandwidth to the antenna, but are limited due to the poor radiation resistance of the structure. To achieve a second band of operation two separate quadrifilars, with differing lengths and circumferences, were nested inside one another to reduce size [10]. Another design provided a switching diode to change electrical length of the element and switch between two modes of operation [11].

In this paper, a novel, dual quadrifilar or octafilar is designed, fabricated and measured. The two filar structures, which occupy the same circumference, have separate termination points which allows for proper

resonant length to be set individually for each loop. The high frequency and low frequency filar structures are also set at differing pitch angles to maximize isolation of the two nested QHA while maintaining a low frequency coupling factor to improve low frequency impedance. The high frequency band structure's orthogonal elements also needed to be electrically isolated from one another to prevent improper current distribution from occurring. The antenna structure itself was fed with a 90-degree hybrid and two phase matched baluns. Finally, a fiberglass radome was custom designed and utilized to house the final antenna. Details of the final antenna are shown and described along with both experimental and numerical results.

II. QHA ANTENNA BACKGROUND

The QHA, in one form or another, has been around for decades in the satellite communication world. It is utilized primarily for its ease of implementation, high gain, and ability to customize both pattern width and polarization.

The QHA can be approximated as two orthogonal loops. Like a loop, these structures have low radiation resistance which makes them very hard to match and thus even more challenging to achieve wide bandwidths. The overall antenna efficiency and radiation performance is closely tied to overall antenna size characteristics. The general trend is the wider the diameter of the QHA, the wider the bandwidth, the higher the radiation resistance, and ultimately the more efficient the antenna is. This will be the trend until the diameter QHA approaches $\lambda/4$ of the intended frequency. These trends are explained graphically for helical antennas in Fig. 1 as well as empirically through equations (1-3). Equations (1-3) show that the circumference of helical antennas is the largest contributing factor to antenna performance. The Red dot on Fig. 1 shows where the antenna in this paper lies upon the chart. From Fig. 1 it is seen that the designed antenna is roughly one-third the size of a typically designed octafilar antenna:

$$Z_{in} \approx 140 * \frac{c}{\lambda}, \tag{1}$$

$$G \approx \frac{6.2 * C^2 * N * S * f^3}{c^3} - (-10 * \log(1 - \Gamma^2)), \tag{2}$$

$$HPBW \approx \frac{65\lambda}{c \sqrt{\frac{NS}{\lambda}}} \tag{3}$$

Upon further inspection of Fig. 1, the ideal circumference for QHA and octafilar designs is seen to be between $.8\lambda$ and 1.2λ with a spacing of $1\lambda - 1.6\lambda$ and a pitch angle between 45 and 60 degrees. The optimal width/length design for helical antennas sits around 1/2. These parameters allow for excellent input impedance, gain, and HPBW. However, once the size of the antenna starts to shrink, especially the circumference, the input impedance will drop significantly. This can be seen in Fig. 2 with the red dot marking the size of the

antenna in this paper. The input impedance of the lower frequency loop is seen to be very low, sitting at about 6 ohms.

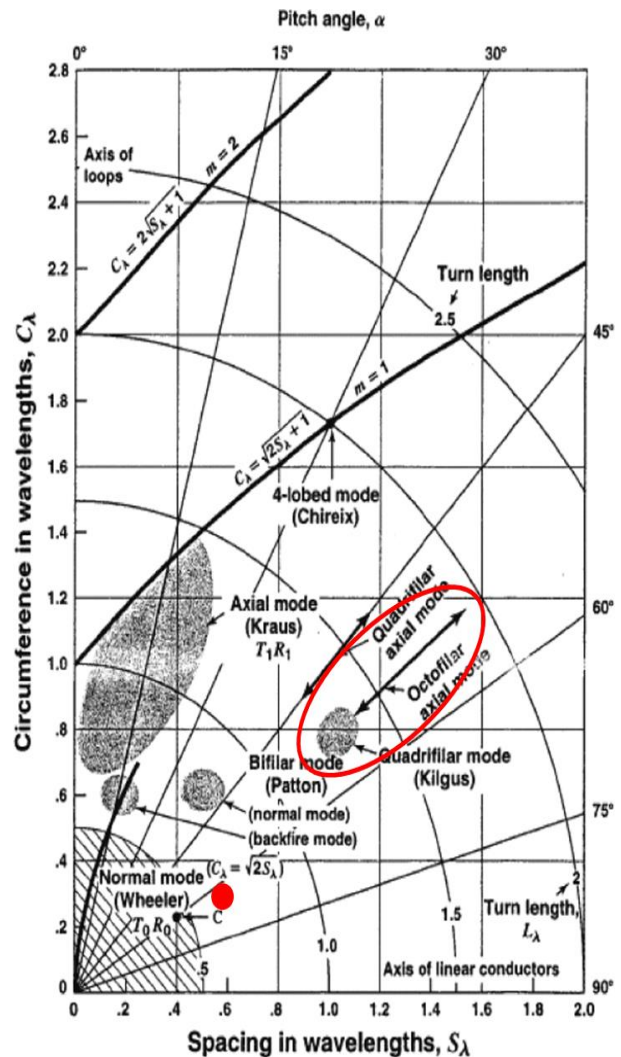


Fig. 1. Helical Mode Chart (reproduced from [12]).

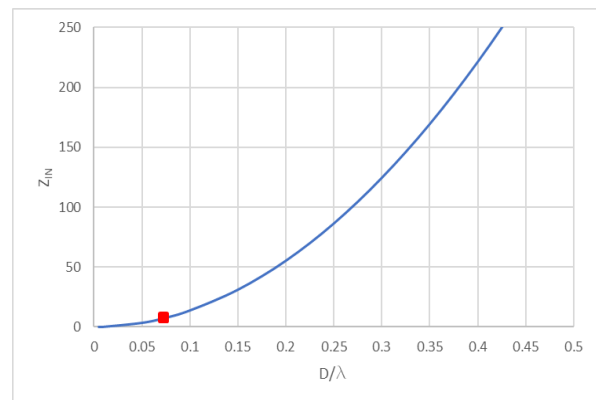


Fig. 2. Input impedance as a function of helix diameter.

To achieve maximum radiation with a QHA structure the elements need to be balanced and fed 90 degrees out of phase. The elements are designed such that RF current peaks occur at the far ends of the cylindrical structure. Following this the voltage should be inverted of the current and produce a peak halfway along the structure. This distribution allows for the cardioid shape pattern and high peak gain values. An HFSS simulation was performed on an ideal QHA to demonstrate the current and voltage distribution [13]. The results can be seen in Fig. 3.

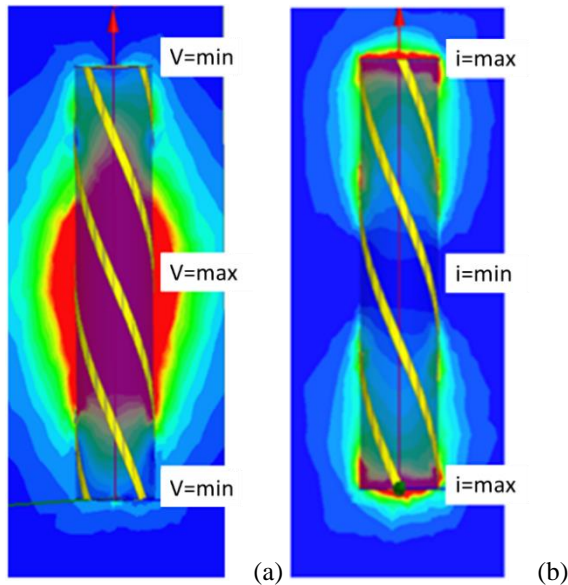


Fig. 3. Colored contour plots showing proper radiation for a QHA at resonance for: (a) voltage (V/m) and (b) current (A/m).

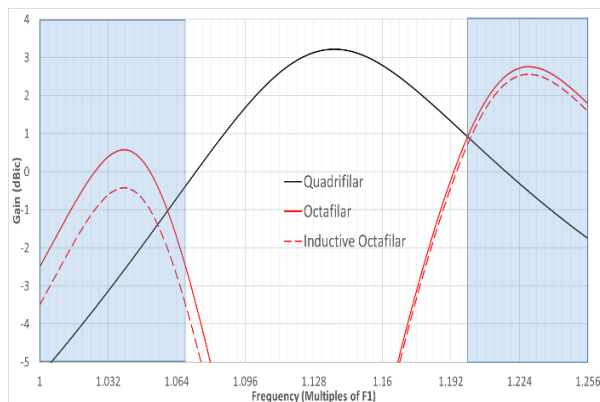


Fig. 4. Simulation results comparing standard quadrifilar, octafilar, and inductively loaded octafilar design gains with a $.07\lambda$ diameter.

Due to the size restriction of the proposed antenna, an HFSS simulation was performed on an ideal QHA, octafilar, and inductively loaded octafilar design in

HFSS at the necessary $.07\lambda$ diameter. The peak gain results at zenith of these three simulations are compared in Fig. 4. The graph expresses the frequency in terms of multiples of the lowest operating frequency, F1.

The octafilars were simulated with an ideal 45 degree spacing between all elements. The octafilar had a separation in heights of the high and low frequency elements whereas the loaded octafilar had the same termination point for the low and high frequency elements. The quadrifilar is seen to have a narrow bandwidth and fall well below the necessary 0dBic gain performance. In fact, the QHA is seen to only rise above the 0 dBic threshold in the area of band separation. Thus, the QHA would be a poor choice for this application due to its bandwidth limitation.

The octafilar produces better performance in the two separated bands of operation but will need modifications in order to improve performance above the necessary 0dBic threshold. The inductively loaded octafilar is slightly shorter and is forced to go resonant at the high frequencies via inductive loading. This causes even more degradation in the low frequency band of operation due to the smaller overall size of the antenna. Thus the inductively loaded octafilar is a poor choice for this application as it only reduces the height of the antenna and produces even lower efficiency in the low frequency band.

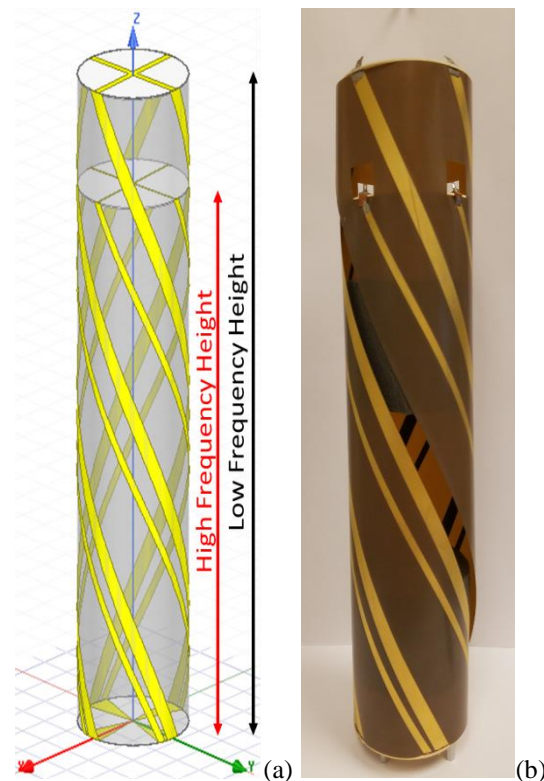


Fig. 5. Image of antenna for: (a) HFSS model and (b) as built.

The designed octafilar can be seen in Fig. 5 and Fig. 6 with dimensions. The antenna has two differing lengths of filars, each fed from a singular point at the base. The low frequency total height is $.33\lambda$ while the high frequency height is $.275\lambda$. The low and high frequency elements each have their own pitch angle set at 63° and 60° respectively which causes them to complete roughly $.75$ of a complete revolution. Finally, the higher frequency structure has the perpendicular arms DC isolated from each other with a small via connected trace to the back of the rigid PWB.

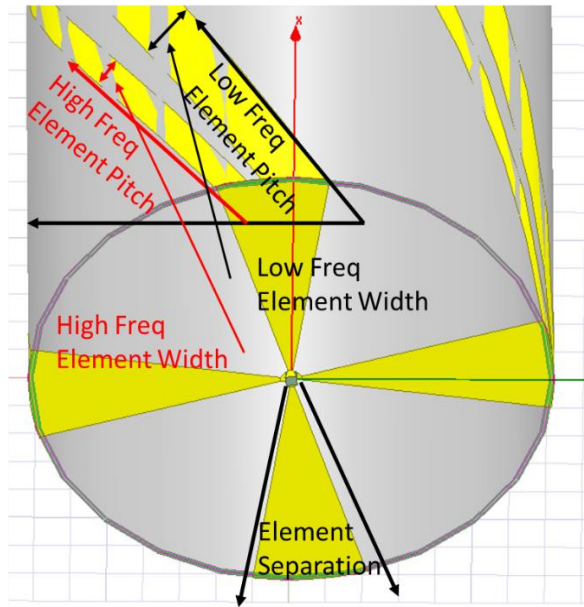


Fig. 6. HFSS image of feed of antenna with dimensions.

III. SEPERATED LOOP HEIGHTS

An HFSS simulation was performed comparing the relative gain performance of a quadrifilar, an octafilar, and an inductively loaded octafilar. This comparison is seen in the plot in Fig. 4. By forcing the antenna to become resonant with methods such as inductors or meandering, the overall performance of the low frequency element is degraded.

To setup proper voltage and current distribution, the high and low frequency elements were each set to differing heights. This height difference allowed for each element to naturally reach its proper electrical length. Naturally reaching proper electrical length enables the structure to radiate properly in each band, producing the cardioid shaped pattern. Completing the loops at differing heights also allowed for each element thickness, height, and crossing structure to be fine-tuned which allow for the performance of each structure to be finely controlled.

As seen in Fig. 5 the structure was constructed utilizing rigid PWBs (Printed Wiring Board) that soldered directly onto the FWB (Flexible Wiring Board) on which the main filars were printed. The PWB/FWB method allows for the dimensions of each structure to be finely controlled while maintaining a quick, easy, and controllable production method.

During the design process it was discovered that the high and low frequency termination points have a coupling correlation. It was found through parametric study that the optimum delta between the completion of the loops was set at a $.05\lambda$ spacing. As the spacing began to grow or shrink outside of that distance the gain of the structure was adversely affected.

IV. DIFFERING PITCHED ELEMENTS

Upon inspection of the numerical results it is found that an octafilar with a small diameter still has ideal gain. However, the end performance lacks due to the mismatch loss that is presented by the low impedance structure of the antenna. The initial untuned antenna was seen to have low frequency impedance of 6 ohms.

The model was constructed in HFSS utilizing perfect E sheets wrapped around a cylinder. Modeling the structure in this method helped to speed up computational time as well as prevent non-manifold edges from occurring in the model. The model was found to be very close to a thickened sheet version of the model.

Parametric sweeps were run with this model to look at the impedance of the structure as the angle of separation between the high and low frequency structure was varied. This was further elaborated by also varying the angle at which the low frequency element was wrapped. This was characterized in Fig. 7 as ext pitch to signify that the low frequency element pitch is X degrees more than the high frequency element pitch. Changing the pitch of the low frequency element with respect to the high frequency element allows for the separation between the two elements to grow as the antenna element length is traversed. This will present more coupling toward the feed of the antenna while reducing coupling further away from the feed of the elements.

Figure 7 (a) shows that the closer the elements become, or the lower their separation, the higher the impedance gets for the low frequency structure. The low frequency structure gets to 22 ohms with a separation of 25 degrees. This phenomenon is also followed by an inductive detuning that causes the structure to resonate a little lower in frequency. Figure 7 (b) shows a slightly less dramatic but opposite effect in impedance, dropping down from 13 ohms to 11 ohms at 25 degrees of separation. This is also accompanied by an inductive detuning of the antenna.

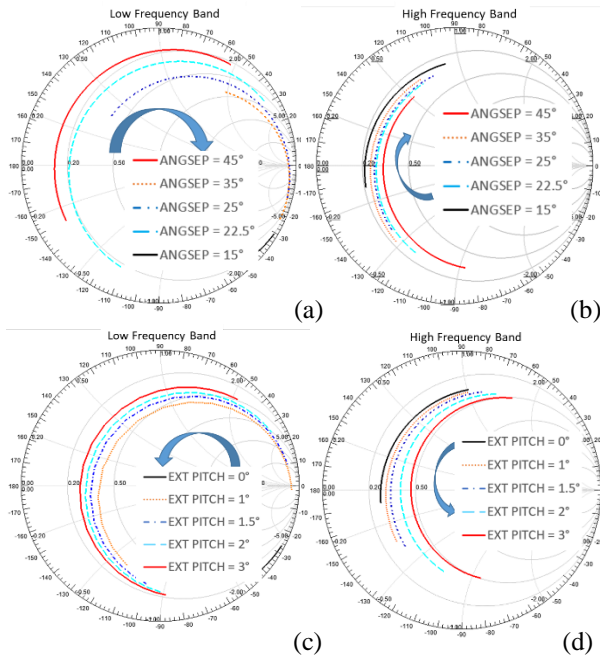


Fig. 7. Impedance charts for varying: (a) angle of separation at base of element in low frequency band, (b) angle of separation at base of element in high frequency band, (c) extra pitch angle applied to high frequency element in low frequency band, and (d) extra pitch angle applied to high frequency element in high frequency band.

The low frequency structure pitch angle was then varied while keeping the high frequency structure pitch angle constant. Figure 7 (c) shows the impedance of the low frequency structure decreasing from 22 ohms to 17 ohms while losing a large amount of the inductance introduced by decreasing the element separation. Figure 7 (d) shows the high frequency structure impedance doing the opposite and increasing in resistance by about 10 ohms while also losing the inductive loading introduced by bringing the elements closer together.

Thus, a balance of the two techniques allows for an increase in Low band impedance by about 15 ohms while only negatively affecting the high frequency band by 2 ohms. This translates to about a 2.5dB improvement in low frequency band performance while only adversely affecting the high frequency band by about .5dB.

V. UNEVEN CURRENT DISTRIBUTIONS

Due to the proximity of both the high frequency and low frequency crossing points a coupling issue is introduced onto the high frequency structure. This coupling causes a current imbalance to occur, forcing most of the current at high frequency onto a single filar. This uneven current distribution phenomenon can be

seen in Fig. 8. Current from 3 of the copper traces all combine to go down the farthest right copper trace. The distribution causes a 1-2 dB drop in performance to occur over 30% of the high frequency band as seen in Fig. 9.

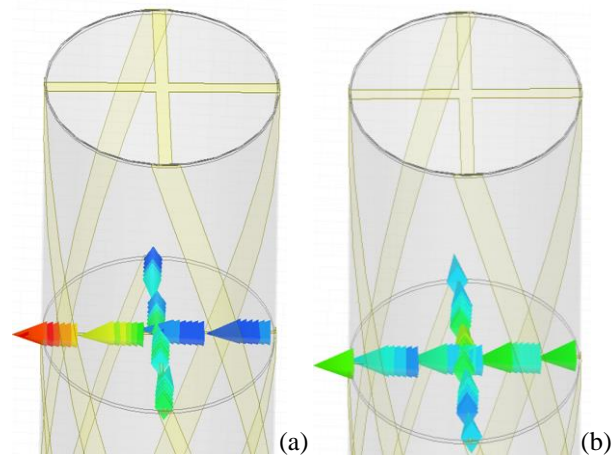


Fig. 8. Image of current distribution on high frequency element termination: (a) DC connected and (b) DC isolated.

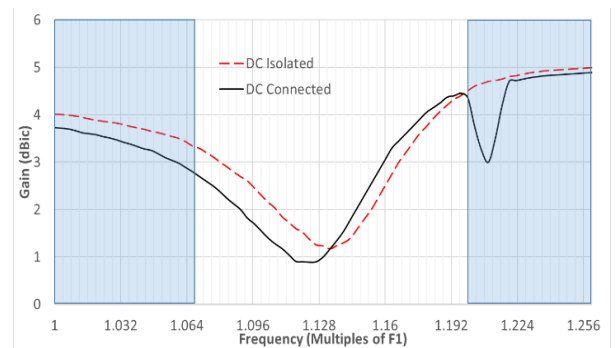


Fig. 9. Simulation of gain at zenith of antenna with high frequency 0° and 90° elements DC connected and DC isolated.

To prevent the unwanted combination of currents on the traces, the crossing point of the high frequency structure was DC isolated from one another as seen in Fig. 10. This was realized by taking the horizontal trace and creating two via points to bring the trace to the back of the rigid PWB and run underneath the vertical element.

DC isolation is a bit counterintuitive to solve the problem. Typically, the traces are combined to force equal current distributions to occur on the filars. However, in this configuration this special technique is necessary to reduce the coupling between high and low frequency elements and thus retain performance.

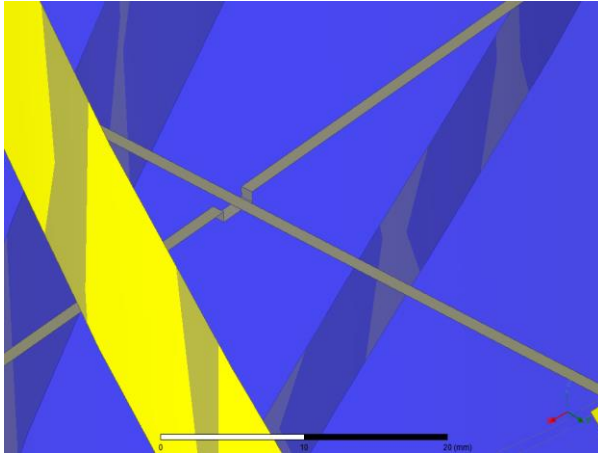


Fig. 10. Close up HFSS image of high frequency crossover point with DC Isolation.

VI. FEEDING STRUCTURE AND RADOME

The antenna structure was fabricated on a 4-mil thick piece of Dupont® Pyralux AP 9141R with a dielectric constant of 3.3. Tabs were created to be able to insert directly into the rigid PWBs that controlled the crossing points of the loops. The boards were then simply soldered into place with the excess tab being clipped off. The FWB not only allowed for ease of manufacturing but also allowed for accurate dimensions to be rendered on the final antenna. This whole assembly was then inserted into a radome which could withstand the rigors of MIL STD 810-G testing.

A 1/32" wall thickness cylinder of fiberglass was chosen as a radome due to its structural integrity, good electrical properties and customizable size. However, once the radome was affixed to the antenna structure, significant dielectric loading was seen. This loading also seemed to vary proto-type to proto-type and test to test. The main source of variance was due to irregularities in how the antenna cylinder was formed, thus leading to varying dielectric loading unit to unit. To get maximum consistency, as well as mechanical integrity, an oversized section of polyurethane foam was inserted as the core of the antenna element. The dielectric associated with such a material is typically around 1.02-1.05 depending upon material density and manufacturing techniques of the foam. Thus, it had minimal effects upon the overall antenna performance but helped to increase maximum contact to the radome structure creating a consistent dielectric loading unit to unit. The shift in frequency due to dielectric loading of the fiberglass was $.05\lambda$. A small portion of this radome can be seen in Fig. 11.

The antenna was fed with an Anaren® Xinger 90-degree hybrid coupler. The hybrid was outfitted with a 20-watt resistor to handle maximum transmitter power. This hybrid not only feeds the two antenna elements 90 degrees out of phase but also will provide a VSWR of

under 1.5:1 across the band. The hybrid and 50-ohm load were mounted to a PCB as seen in right side of Fig. 10. The PCB was then attached to a large aluminum radome adaptor that also acts as a heat sink for any heat generated in the 50-ohm load.

A pair of phase matched Baluns are then utilized to feed the antenna to the 90 degree hybrid. This will serve the purpose of helping to isolate the antenna while also maintaining the necessary phase offset when feeding.

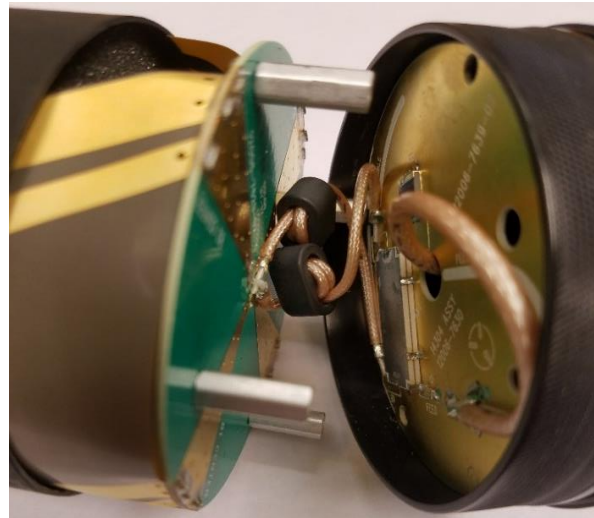


Fig. 11. Image of the feed structure and radome of prototype antenna.

VII. RESULTS

The antennas were measured in a 5-meter by 3-meter anechoic chamber. All measurements were taken utilizing an Agilent E5017B network analyzer. The turntable utilized for patterns is an ETS Lindgren 2188, 1.2-meter diameter turntable with ETS 2090 controller. Finally, all gain measurements were taken utilizing the 3-antenna technique with antennas from the A.H. Systems AK-4G calibrated antenna kit and TDS-535-2 calibrated dipole kit.

The smith chart can be seen in Fig. 12. The return loss can be seen in Fig. 13. Overall the performance of the antenna matches shape closely with simulation but has a higher resistance. This discrepancy can be accounted for by the addition of the baluns for measurement as well as the losses associated with the radome. The contact with the radome is nonideal and creates small air gaps that do not exist in the model. The model was also constructed using Perfect E sheets, to speed up the simulation, which do not properly reflect the losses associated with copper on an FWB. However, the simulation and measurement both agree that the antenna is resonant slightly above and below the center frequency of the lower and upper frequency bands respectively. This is necessary to achieve peak gain at

the center of each frequency band.

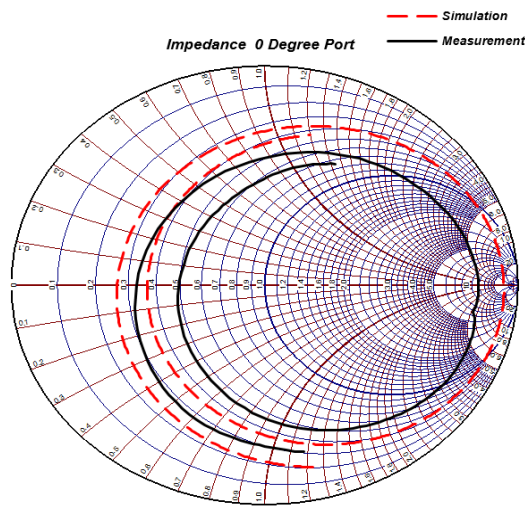


Fig. 12. Smith chart of 0 degree port of antenna elements.

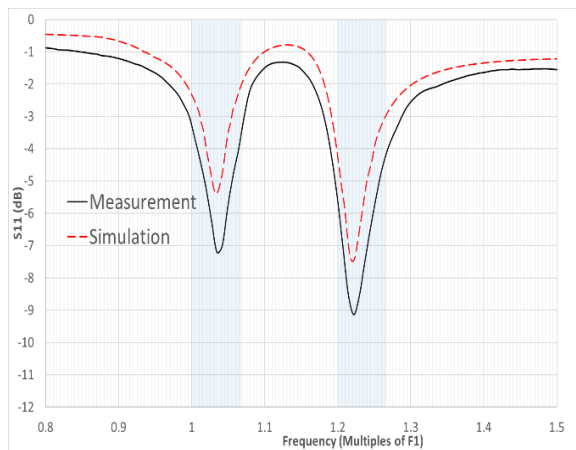


Fig. 13. Return loss of 0 degree port of antenna elements.

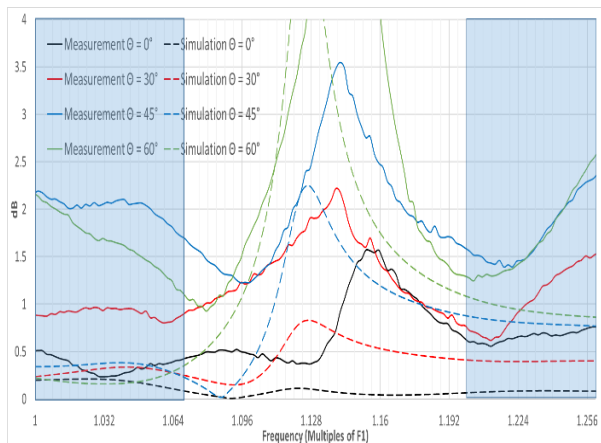


Fig. 14. Axial ratio of antenna at varying elevation angles.

The axial ratio of the antenna at varying elevation angles can be seen in Fig. 14. Both the model and the simulation show acceptable axial ratio at low elevation angles in the bands of operation. However, the measurement shows a steeper increase in axial ratio as elevation angle decreases than that of the model. This difference in measurement result can be attributed to the imperfect construction of the antenna versus a perfectly constructed and balanced numerical model. The 90-degree hybrid utilized for measurements versus the ideal phase shifter utilized in the model will also cause shifts in the axial ratio. These differences will be most prominent at the antenna and device band edges where phase imbalance is typically at the highest acceptable level for the device. This is especially true at the highest frequency where phase imbalance will of course be the highest.

Gain patterns at the middle of each band of the antenna can be seen in Fig. 15 and Fig. 16 with a comparison of peak gains seen in Table 1. Simulation and measurement are very comparable across both bands of operation. The peak delta is about 1 dB and can be accounted for by the addition of the real world hybrid in the antenna to achieve circular polarization as well as the outside elements such as the baluns, heatsink, and gooseneck.

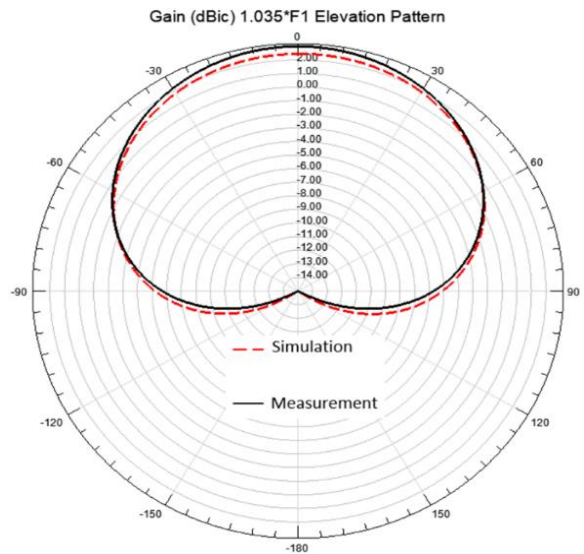


Fig. 15. Radiation pattern comparison of low frequency band for 1.035*F1.

The maximum gain of the antenna is perfectly centered at Zenith and realizes the goal of greater than 0 dBic across the lower frequency band, peaking out at 3dBic. The same can be said of the upper frequency band where the goal of greater than 2dBic is met across the upper frequency band with a peak of 3.5dBic.

The patterns are incredibly wide and exhibit a

excellent HPBW of $\pm 60^\circ$ off of zenith. This good low elevation angle gain is beneficial to forming terrestrial links. Overall the patterns agree numerical to measurement very well across both bands of operation from both a shape, gain and HPBW perspective. It is seen in Table 1 that the majority of the the optimized octafilar benefit occurs at the low frequency band where impedance was optimized. This translated to at least a 2.5 dBic improvement over the other techniques.

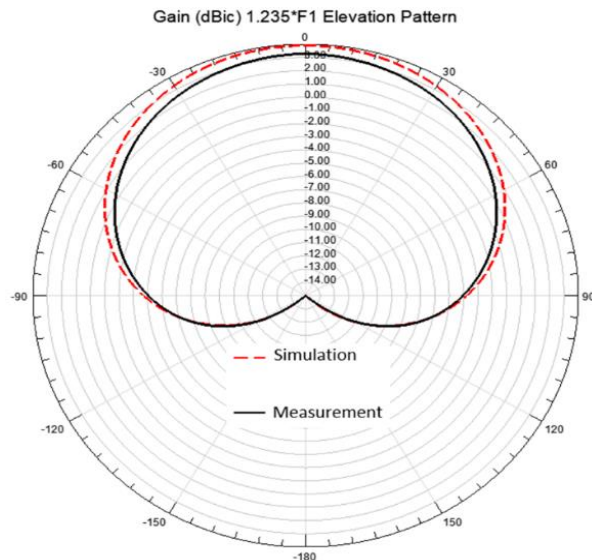


Fig. 16. Radation patten comparison of high frequency band for 1.235*F1.

Table 1: Comparison of peak gain at zenith of various QHA designs

Frequency (λ) \ Gain(dBic)	1	1.035	1.07	1.2	1.235	1.27
Quadrifilar (Numerical)	-5.37	-2.73	-0.48	0.91	-0.76	-2.18
Octafilar (Numerical)	-2.503	0.45	-2.22	0.94	2.71	1.17
Inductive Octafilar (Numerical)	-3.5	-0.55	-3.22	0.74	2.51	0.97
Optimized Octafilar (Numerical)	-0.05	2.45	0.65	2.31	3.89	2.51
Optimized Octafilar (Measurement)	0.34	3	0.22	2.07	3.27	2.49

VIII. CONCLUSION

A small diameter, light weight, dual-band octafilar antenna was designed and fabricated for operation over two $.07\lambda$ bands of operation. The two sets of filars ended up with differing heights of termination to allow for

optimal current distributions and peak gain. The two sets of filars also had differing pitches and separation which allowed for improved performance in the low frequency band with minimal degradation on the performance of the high frequency band. The High frequency 0° and 90° crossing point needed to be DC isolated from one another to prevent improper current distribution and hence a decrease in performance.

These novel techniques allowed for equal wraps around the circumference of the tube which created equal shaped cardioid patterns with good low elevation performance. The end antenna was then fed with a 90-degree hybrid and isolated from the mounting structure with phase matched baluns. The resulting antenna was able to provide the necessary high performance in a significantly smaller and lighter weight package size which was acceptable to the end user.

ACKNOWLEDGEMENTS

The author would like to acknowledge Malcolm Packer of L3Harris Communication Systems of Rochester, NY for his help in editing this paper and his constant guidance and support.

REFERENCES

- [1] C. A. Balanis, *Antenna Theory*. 3rd Ed., New York: Wiley, pp. 549-600, 2005.
- [2] N. M. Tuan, K. Byoungchul, C. Hosung, and P. Ikmo, "Effects of ground plane size on a square microstrip patch antenna designed on a low-permittivity substrate with an air gap," *Antenna Technology (iWAT) 2010 International Workshop on*, pp. 1-4, 2010.
- [3] O. P. Leisten, J. C. Vardaxoglou, P. McEvoy, R. Seager, and A. Wingfield, "Miniature dielectrically-loaded quadrifilar antenna for global positioning system (GPS)," *Electronics Letters*, vol. 37, pp. 1321-1322, 2001.
- [4] S. Liu and Q.-X. Chi, "A novel dielectrically-loaded antenna for tri-band GPS applications," *38th European Microwave Conference*, 2008.
- [5] A. Takacs, H. Aubert, D. Belot, and H. Diez, "Miniaturization of compact quadrifilar helix antennas for telemetry, tracking and command applications," *Progress In Electromagnetics Research C*, vol. 60, pp. 125-136, 2015.
- [6] A. Petros and S. Licul, "Folded quadrifilar helix antenna," in *IEEE Antennas and Propagation Symposium*, v. 4, pp. 569-572, 2001.
- [7] W. I. Son, H. Tae, and J. Yu, "Compact square quadrifilar helix antenna for SDARS application in portable terminals," *Electronics Letters*, vol. 47, no. 4, pp. 232-233, 2011.
- [8] M. Hosseini, M. Hakkak, and P. Rezaei, "Design of a dual-band quadrifilar helix antenna", *IEEE Antennas Wireless. Propagation. Lett.*, vol. 4, pp.

- 39-42, 2005.
- [9] D. Lamensdorf and M. A. Smolinski, "Dual band quadrifilar helix antenna," *Proc. IEEE Int. Symp. Antennas and Propagation*, vol. 3, pp. 488-491, 2002.
 - [10] J. Lowdell, G. Cox, M. Notter, and K. Keen, "Dual band quadrifilar helix antennas for UHF/VHF band operation," presented at the *ICAP*, Exeter, 2003.
 - [11] A. Sainati, A. Robert, J. J. Groppelli, R. C. Olesen, and A. J. Stanland, "A band-switched resonant quadrifilar helix," *IEEE Trans. Antennas Propag.*, vol. AP-30, no. 5, pp. 1010-1013, Sep. 1982.
 - [12] J. D. Kraus, *Antennas*. McGraw-Hill, 1988.
 - [13] Ansoft High Frequency Structure Simulator (HFSS), ver. 17, Ansoft Corporation, Pittsburgh, PA, 2017.



Joseph Daniel Majkowski received his B.S. and M.S. degrees in Electrical Engineering from the Rochester Institute of Technology in 2012.

He joined Harris Communications in 2012 where he began as a System Engineer. In 2013 he changed roles within the company to an Electromagnetic Engineer position. He has since won corporate wide technological innovation awards in 2017 and 2018 for his work in matching circuits and antenna design. This work has led to four patent filings to date. He was also the chair of the IEEE Rochester section MTT17/AP03 society in 2018.

Study of Bandwidth and Resonant Frequency of a Rectangular Superconducting Thin Film Patch Antenna at Temperatures near T_c

Abdelkrim Belhedri¹, Abderraouf Messai¹, Tayeb A. Denidni², and Boualem Mekimah¹

¹Electronics Department, Frères Mentouri University, 25000, Constantine, Algeria
belhedri.abdelkrim@umc.edu.dz, r_messai@yahoo.fr, b_mekimah@umc.edu.dz

²EMT INRS Montreal Canada
denidni@emt.inrs.ca

Abstract — Our work presents a study of High Temperature Superconductor (HTS) Yttrium Barium Copper Oxide YBaCuO rectangular thin film. It is considered to be etched on lanthanum aluminate (LaAlO₃) substrate. Results are exhibited for different values of temperature and patch thickness. Validated and compared to those in literature, these results show direct proportionality between patch thickness and both of resonant frequency and bandwidth for temperatures relatively far from the critical temperature T_c . When temperature becomes very close to T_c , proportionality between resonant frequency and patch thickness is maintained; but it is inverted between bandwidth and patch thickness. Bandwidth is broadened at low values of thickness, but it decreases considerably when thickness increases.

Index Terms — Bandwidth, critical temperature, film thickness, high temperature superconductor, patch thickness, resonant frequency, superconductor antennas.

I. INTRODUCTION

HTS antennas show considerable improvement over identical antennas made with their normal metal counterparts [1-3]. A 4-element array in [1] presents a gain 0.9 dB for a direct-coupled feed and 1.7 dB for a gap coupled one. A 100-element array in [4] shows an improvement of 8 to 10 dB. Superconductor antennas have shown certain superiority against conductor antennas, because of their small losses, reduced time of propagation, and large scale of integration [3], [5-6]. Despite having higher gain compared to conductor antennas, their narrow bandwidth severely limits their application [2]. They could be used for RF applications in deep-space, where temperatures are very low [7-8] and do not need to have cooling systems.

Working at temperatures very close to high temperature of transition, using superconductor thin films, allow a big scale of integration relatively to conductors [9]. Bandwidth enhancement has been shown

when working with thin films at temperatures near to the critical temperature T_c [10].

Some planar microwave circuits, such as patch antennas [1] and resonators [11-12], fabricated on lanthanum aluminate substrates have shown substantial improvement over identical circuits fabricated with gold, silver, or copper metallization.

Our work is a study of a rectangular YBaCuO thin film supposed to be etched on a LaAlO₃ substrate. As mentioned by [1], the LaAlO₃ is used in the experiment because of its good lattice match with HTS like YBCO films having low surface impedance and $T_c = 90\text{K}$.

First, a mathematical formulation of the problem, based on the Method of Moments (MoMs) is realized. A system of linear equations that leads to an impedance matrix is used to determine the resonant frequency (f_r) and the bandwidth (BW), where a non-trivial solution to the impedance matrix is imposed. The obtained results show a big agreement between our results and the experimental results in [1].

Second, a focus on the variations of f_r and BW in function of the patch thickness is done. These variations are very important when the temperature moves towards T_c . Temperature must be maintained constant in order to keep both of resonant frequency and bandwidth constant; because at this region, near to the critical temperature, the variations of f_r and BW are very important. In other words, any small shift in temperature will induce a significant shift of f_r and BW .

II. MATHEMATICAL FORMULATION

The studied structure is shown in Fig. 1. It consists of a rectangular high Temperature Superconductor (HTS) YBaCuO thin film, of dimensions L and W . It has a thickness t and it is supposed to be etched on lanthanum aluminate (LaAlO₃) of thickness h . The full-wave method of Moments is used to analyze this structure.

In spectral domain, transverse electric field \vec{E} on the patch is function of Green tensor $\vec{\vec{G}}$, and current density

\tilde{J} on the patch [3]:

$$\tilde{\tilde{E}} = \begin{bmatrix} \tilde{\tilde{E}}_x \\ \tilde{\tilde{E}}_y \end{bmatrix} = \begin{bmatrix} G_{xx} & G_{xy} \\ G_{yx} & G_{yy} \end{bmatrix} \cdot \begin{bmatrix} \tilde{J}_x \\ \tilde{J}_y \end{bmatrix}. \quad (1)$$

In free space, electric field is obtained by using the inverse Fourier transform of $\tilde{\tilde{E}}$ as follows:

$$E_x(x, y) = \frac{1}{4\pi^2} \iint_{-\infty-\infty}^{+\infty+\infty} [G_{xx} \tilde{J}_x + G_{xy} \tilde{J}_y] e^{+i(k_x x + k_y y)} dk_x dk_y, \quad (2a)$$

$$E_y(x, y) = \frac{1}{4\pi^2} \iint_{-\infty-\infty}^{+\infty+\infty} [G_{yx} \tilde{J}_x + G_{yy} \tilde{J}_y] e^{+i(k_x x + k_y y)} dk_x dk_y. \quad (2b)$$

Using the method of moments - Galekin - procedure - current distribution on the patch is developed into series of known base functions; J_{xn}, J_{ym} ; with unknown coefficients, a_n and b_m [13],

$$J_x(x, y) = \sum_{n=1}^N a_n J_{xn}(x, y),$$

and

$$J_y(x, y) = \sum_{m=1}^M b_m J_{ym}(x, y).$$

The following impedance matrix is obtained after mathematical manipulations in the previous relations:

$$\begin{bmatrix} (Z_{kn}^1)_{N \times N} & (Z_{km}^2)_{N \times M} \\ (Z_{ln}^3)_{M \times N} & (Z_{lm}^4)_{M \times M} \end{bmatrix} \begin{bmatrix} (a_n)_{N \times 1} \\ (b_m)_{M \times 1} \end{bmatrix} = \begin{bmatrix} 0 \\ 0 \end{bmatrix}, \quad (3)$$

with: $k, n = \overline{1, N}$; $l, m = \overline{1, M}$ and,

$$Z_{kn}^1 = \iint_{-\infty-\infty}^{+\infty+\infty} \tilde{J}_{xk}(-k_x, -k_y) \cdot G_{xx} \cdot \tilde{J}_{xn}(k_x, k_y) dk_x dk_y,$$

$$Z_{km}^2 = \iint_{-\infty-\infty}^{+\infty+\infty} \tilde{J}_{xk}(-k_x, -k_y) \cdot G_{xy} \cdot \tilde{J}_{ym}(k_x, k_y) dk_x dk_y,$$

$$Z_{ln}^3 = \iint_{-\infty-\infty}^{+\infty+\infty} \tilde{J}_{yl}(-k_x, -k_y) \cdot G_{yx} \cdot \tilde{J}_{xn}(k_x, k_y) dk_x dk_y,$$

$$Z_{lm}^4 = \iint_{-\infty-\infty}^{+\infty+\infty} \tilde{J}_{yl}(-k_x, -k_y) \cdot G_{yy} \cdot \tilde{J}_{ym}(k_x, k_y) dk_x dk_y.$$

A rectangular cavity, with lateral magnetic walls and TM_{01} mode, are considered [13]:

$$J_{xn}(x, y) = \sin\left[\frac{n_1\pi}{L}\left(x + \frac{L}{2}\right)\right] \cos\left[\frac{n_2\pi}{W}\left(y + \frac{W}{2}\right)\right], \quad (4a)$$

$$J_{ym}(x, y) = \sin\left[\frac{m_2\pi}{W}\left(y + \frac{W}{2}\right)\right] \cos\left[\frac{m_1\pi}{L}\left(x + \frac{L}{2}\right)\right]. \quad (4b)$$

In case of superconductivity, tangential components of the electric field on the patch are [3]:

$$\begin{cases} E_x^o(x, y, z) = Z_s \cdot J_x(x, y) \\ E_y^o(x, y, z) = Z_s \cdot J_y(x, y) \end{cases} \quad (5)$$

where, "o" indicates the outside of the patch, J the surface current density, and Z_s the patch surface impedance. According to Gorter and Casimir, Z_s can be

expressed as [14]:

$$Z_s = \frac{1}{t \cdot \sigma_n}, \quad \text{and} \quad \lambda = \lambda_0 \left[1 - \left(\frac{T}{T_c}\right)^4\right]^{-\frac{1}{2}}, \quad (6)$$

λ_0 is the penetration depth at 0 K, and σ_n the normal state conductivity. After manipulations we obtain:

$$\begin{bmatrix} \tilde{\tilde{E}}_x(k_x, k_y) \\ \tilde{\tilde{E}}_y(k_x, k_y) \end{bmatrix} = \begin{bmatrix} (G_{xx} - Z_s) & G_{xy} \\ G_{yx} & (G_{yy} - Z_s) \end{bmatrix} \cdot \begin{bmatrix} \tilde{J}_x(k_x, k_y) \\ \tilde{J}_y(k_x, k_y) \end{bmatrix}. \quad (7)$$

A non-trivial solution of (3), when G_{xx} and G_{yy} are respectively replaced by $G_{xx} - Z_s$ and $G_{yy} - Z_s$ of equation (7), implies that [13-14]:

$$\det[Z(f)] = 0. \quad (8)$$

The complex resonant frequency is,

$$f = f_r + if_i, \quad (9)$$

where, f_i and f_r are respectively imaginary part and real part of resonant the frequency. The bandwidth is:

$$BW = \frac{2f_i}{f_r}. \quad (10)$$

III. RESULTS

Dimensions and characteristics of the patch antenna, in Fig. 1 are: $L = 1.63 \text{ mm}$, $W = 0.935 \text{ mm}$, film critical temperature $T_c = 89 \text{ K}$, and LaAlO₃ thickness $h = 0.254 \text{ mm}$. The film thickness t is supposed to vary from 10 nm up to 350 nm, $\lambda_0 = 140 \text{ nm}$, and $\sigma_n = 10^6 \text{ Sm}^{-1}$. The relative permittivity value $\epsilon_r = 23.3459$ is taken from the curve in Fig. 2 at $T = 50 \text{ K}$.

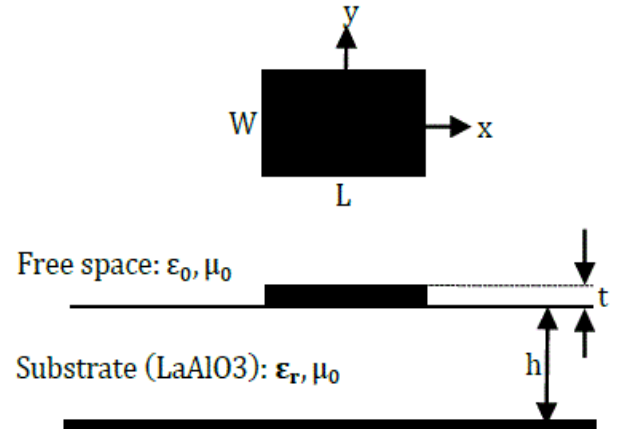


Fig. 1. Structure geometry of the studied antenna.

Based on the theoretical formulation in Section II, our problem is modeled and computed results; according to (8), (9), and (10); are compared to those measured in [1]. They are found to be in good agreement as it is mentioned in Table 1. It is clear that, at $T = 50 \text{ K}$, there is an error of 0.84 % between our computed gold and that measured in [1]. Similarly, there is 1.3 % of error between our computed HTS and the measured in [1].

Table 1: Our results compared to [1]

Our Results					[1]							
Resonant Frequency (GHz)		Modeled			Measured			Resonant Frequency (GHz)		Modeled		
Gold	HTS	HTS		Gold	HTS		Gold	HTS				
29.043	29.039	28.912		29.290	28.667							

Measured values of resonant frequencies for either gold and HTS and the relative permittivity of LaAlO₃ variations are represented in Fig. 2. They are extracted from direct coupled curves of [1].

Our computed results are represented in Fig. 2 in order to compare them with the measured values. Both of gold electrical conductivity and LaAlO₃ relative permittivity variations in function of temperature variations are taken into consideration. It is clear that the relative permittivity of LaAlO₃ is proportional to temperature. The computed values of resonant frequency of Gold decrease slowly in the same manner as the measured ones with a slight down shift of about less than 0.25 GHz as the temperature increases. This decrease is because of the slow increase of the relative permittivity with temperature. As for Gold, the HTS computed values vary in the same manner as the measured ones with a shift up of about 0.372 GHz. In Fig. 3, temperature is first, maintained at 40 K then at 70 K. The thickness is varied from 10 nm up to 350 nm. It can be seen that both of resonant frequencies and bandwidths, for the above temperatures, present a small increase as patch thickness increases. This increase is relatively rapid around 10 nm thickness.

For temperatures very close to T_C , the resonant frequency continues to increase when thickness increases. A rapid increase is visible in Fig. 4 when thickness is less than 50 nm. On the other hand, the bandwidth decreases rapidly when the film thickness increases. This decrease is accentuated for values of thickness less than 100 nm at $T = 88.9$ K. This accentuation decreases as the temperature shifts down T_C . Taking into consideration the relative permittivity value for each value of temperature, typical values of temperature and the corresponding values of resonant frequency and bandwidth are summarized in Table 2.

We notice, for a 10 nm, that the bandwidth increases from 5.05% to 41.085%, while the resonant frequency decreases from 24.569 GHz to 16.567 GHz when the temperature increases from 88.5 K to 88.9 K.

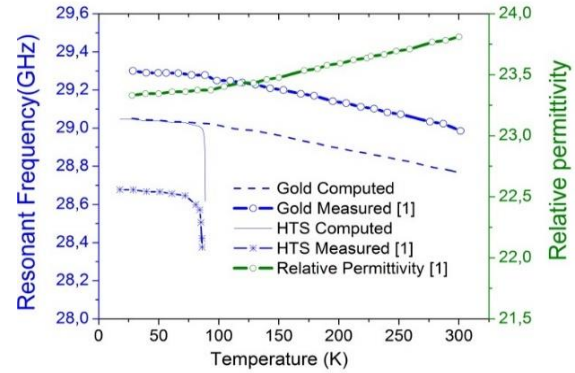


Fig. 2. LaAlO₃ relative permittivity, resonant frequency in GHz for Gold and HTS in function of temperature $T_c = 89$ K, $\lambda_0 = 140$ nm, $t = 350$ nm, $\sigma_n = 10^6$ Sm⁻¹, and $\sigma_{gold} = 44.2 \times 10^6$ Sm⁻¹.

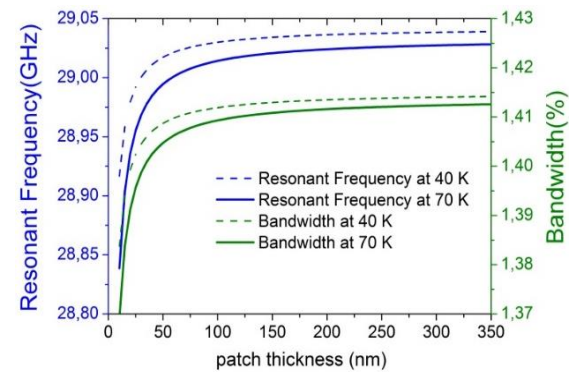


Fig. 3. Resonant frequency, bandwidth variations in function of patch thickness at 40 K and 70 K, $T_c = 89$ K, $\lambda_0 = 140$ nm, and $\sigma_n = 10^6$ Sm⁻¹.

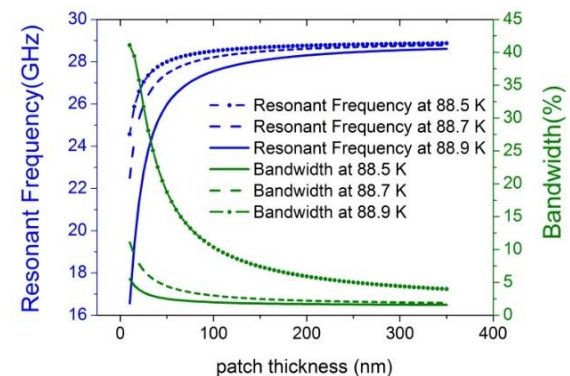


Fig. 4. Resonant frequency, bandwidth variations versus patch thickness at 88.5 K, 88.7 K, and 88.9 K, $T_c = 89$ K, $\lambda_0 = 140$ nm, and $\sigma_n = 10^6$ Sm⁻¹.

The bandwidth drops drastically when the temperature shifts down the high temperature of transition.

Table 2: Resonant frequency and bandwidth typical values at different values of temperature and relative permittivity

$T_c = 89\text{ K}$, $t = 10\text{ nm}$ $\lambda_0 = 140\text{ nm}$, and $\sigma_n = 10^6\text{ Sm}^{-1}$			
T (K)	ϵ_r	Resonant Frequency (GHz)	BW (%)
88.9	23.375	16.567	41.085
88.7	23.375	22.509	11.082
88.5	23.375	24.569	5.505
70	23.3605	28.839	1.369
40	23.3459	28.917	1.384

IV. CONCLUSION

Our results show that there is a direct proportionality between patch thickness and both of resonant frequency and bandwidth at temperatures relatively far from T_c . Contrarily to temperatures near to T_c , this proportionality is inverted between bandwidth and patch thickness. This inversion occurs when temperature moves towards the critical temperature T_c , depending on both of temperature and patch thickness. In perspective, research works are in progress to determine the relationship between temperature, patch thickness, and the inversion of proportionality.

REFERENCES

- [1] M. A. Richard, K. B. Bhasin, and P. C. Clasp, "Superconducting microstrip antennas: An experimental comparison of two feeding methods," *IEEE Transactions on Antennas and Propagation*, vol. 41, no. 7, July 1993.
- [2] S. Liu and B. Guan, "Wideband high-temperature superconducting microstrip antenna," *Electronics Letters*, vol. 41, no. 17, Aug. 2005.
- [3] T. Fortaki, M. Amir, S. Benkouda, and A. Benghalia, "Study of high T_c superconducting microstrip antenna," *Piers Online*, vol. 5, no. 4, 2009.
- [4] R. J. Dinger, "Some potential antenna applications of high temperature superconductors," *J. Superconductivity*, vol. 3, no. 3, pp. 287-296, Sept. 1990.
- [5] S. Bedra, T. Fortaki, A. Messai, and R. Bedra, "Spectral domain analysis of resonant characteristics of high T_c superconducting rectangular microstrip patch printed on isotropic or uniaxial anisotropic substrates," *Wireless Personal Communications*, Springer, July 2015.
- [6] A. Messai, S. Benkouda, M. Amir, S. Bedra, and T. Fortaki, "Analysis of high T_c superconducting rectangular microstrip patches over ground planes with rectangular apertures in substrates containing anisotropic materials," *International Journal of Antennas and Propagation*, 2013.
- [7] N. Chahat, J. Sauder, R. E. Hodges, M. Thomson, and Y. Rahmat-Samii, "The deep-space network telecommunication CubeSat antenna using the deployable Ka-band mesh reflector antenna," *IEEE Antennas and Propagation Magazine*, vol. 59, no. 4, Apr. 2017.
- [8] S.-H. Hong, G.-B. Choi, R.-H. Baek, H.-S. Kang, S.-W. Jung, and Y.-H. Jeong, "Low-temperature performance of nanoscale MOSFET for deep-space RF applications," *IEEE Electron Device Letters*, vol. 29, no. 7, July 2008.
- [9] A. Belhedri, A. Messai, and B. Mekimah, "Miniaturization of microstrip patch antennas using superconducting thin films at the high temperature of transition," *5th International Conference on Information and Communication Systems (ICICS)*, 2014.
- [10] A. Belhedri, A. Messai, and B. Mekimah, "Performance amelioration of microstrip patch antennas using thin films at the high temperature of transition," *Science and Information Conference*, London, UK, Aug. 2014.
- [11] C. M. Chorey, K. Kong, K. B. Bhasin, J. D. Warner, and T. Itoh, "YBCO superconducting ring resonator at millimeter-wave frequencies," *IEEE Trans. Microwave Theory Tech.*, vol. 39, pp. 1480-1487, Sept. 1991.
- [12] J. H. Takemoto, F. K. Oshita, H. R. Fetterman, P. Korbin, and E. Sovoro, "Microstrip ring resonator technique for measuring microwave attenuation in high- T_c superconducting thin films," *IEEE Trans. Microwave Theory Tech.*, vol. 37, pp. 1650-1652, 1989.
- [13] T. Fortaki, D. Khedrouche, F. Bouttout, and A. Benghalia, "Anumerically efficient full-wave analysis of a tunable rectangular microstrip patch," *Int. J. Electronics*, vol. 91, no. 1, Jan. 2004.
- [14] T. Fortaki, S. Benkouda, M. Mounir, and A. Benghalia, "Air gap tuning effect on the resonant frequency and half-power bandwidth of superconducting microstrip patch," *Piers Online*, vol. 5, no. 4, 2009.

Autoencoder Based Optimization for Electromagnetics Problems

S. Barmada, N. Fontana, D. Thomopoulos, and M. Tucci

DESTEC, University of Pisa
56122, Pisa, Italy

sami.barmada@unipi.it, nunzia.fontana@unipi.it, dimitri.thomopoulos@unipi.it, mauro.tucci@unipi.it

Abstract — In this work a novel approach is presented for topology optimization of electromagnetic devices. In particular a surrogate model based on Deep Neural Networks with encoder-decoder architecture is introduced. A first autoencoder learns to represent the input images that describe the topology, i.e., geometry and materials. The novel idea is to use the low dimensional latent space (i.e., the output space of the encoder) as the search space of the optimization algorithm, instead of using the higher dimensional space represented by the input images. A second neural network learns the relationship between the encoder outputs and the objective function (i.e., an electromagnetic quantity that is crucial for the design of the device) which is calculated by means of a numerical analysis. The calculation time for the optimization is greatly improved by reducing the dimensionality of the search space, and by introducing the surrogate model, whereas the quality of the result is slightly affected.

Index Terms — Deep neural networks, surrogate model, topology optimization.

I. INTRODUCTION

Design optimization of electromagnetic (EM) devices based on field computation is nowadays of interest both for research and industries. The conventional approach usually faces the following main challenges:

- It is often difficult to set an adequate design space that includes a solution with satisfactory performance, as the design variables introduced by the user restrict the ability of the optimization models to deal with any arbitrary change in the design of a machine;
- when numerical models are used to calculate the EM fields (i.e., in the majority of the cases since an analytical solution is rarely available), the computational burden resulting from repeated simulations is often excessive.

In some specific cases, when the optimization is not limited to a reduced set of parameters, the first problem can be overcome by topology optimization [1], which does not require the definition of the design variables. In fact, geometries and materials are flexibly represented

using a bitmap approach, which describes the device (or the part of the device that needs to be optimized) as a set of pixels. In addition, different materials could be represented by different colors (or grayscale levels). This allows free modification of material boundaries, that could be characterized also by the appearance of holes in the design region, resulting in new shapes which may outperform conventional design. The remarkable drawback is the increased dimensionality of the optimization search space, related to the bitmap resolution and color space.

The second problem has led to the development of several surrogate models to aid the optimization process [2], [3]. Extensive research has been carried out in the field of magnetic equivalent circuits and neural networks, based on curve fitting, to partially or completely bypass computing the field solution using numerical techniques (often Finite Element Analysis, FEA). Most of these methods are usually suitable for specific types of problems and describe systems with very few parameters, i.e., they suffer of the first issue.

Some preliminary studies used deep learning Convolutional Neural Networks (CNNs) as surrogate models for the computation of EM quantities [4]. In fact, CNNs have excellent capability in extracting relevant features from the input image and relating them to a desired output EM quantity. However, evolutionary optimization algorithms are not as well suited as deep neural networks to deal with high dimensional bitmaps as search space.

The motivation of this work is the need to reduce the dimensionality of the search space for topology optimization. In particular, we exploit the feature extraction capabilities of a CNN based autoencoder that learns from the space of input bitmaps, and the encoded space (also called latent space) is used as the search space for the optimization.

The main contributions of this paper are summarized as follows:

- The evolutionary optimization algorithm works in the latent space that represents the original high dimensional bitmap space almost perfectly;
- A new neural network surrogate model approach

is proposed and applied during optimization, reducing the time cost for calculating the numerical solution;

- The constraints are defined both in the encoded space and in the decoded (original) space.

The proposed method is applied here to a 2D test case, similar to the one shown in [5]: the shape of a “magnetic channel” is optimized, with the aim of maximizing the magnetic energy on a target zone. The 2D simulations are performed with a commercial code, and the results show that the proposed procedure can speed up optimization procedures.

II. AUTOENCODER FOR DIMENSIONALITY REDUCTION AND SURROGATE MODEL

A. Autoencoder for dimensionality reduction

The term autoencoder [6], shown in Fig. 1, is usually referred to an unsupervised neural network composed by an encoder, that maps the input space (usually of large dimension, for instance an image) to a reduced number of features, denoted as code or latent space, and a decoder that maps the latent variables back to the original data.

The dimensionality reduction (i.e., compression) made by the encoder is learned in order to minimize the error between the decoder output and original input, i.e., the reconstruction error. Then, the latent representation can be considered as a reduced feature space that fully describes the original high dimensional input space.

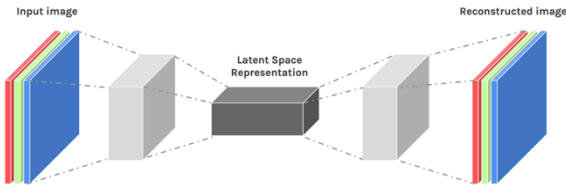


Fig. 1. Typical structure of an autoencoder.

The main idea of this proposal is to train the autoencoder with a proper set of bitmaps describing different geometries of the system to be optimized (i.e., different design solutions). At the end of the training period, the autoencoder has created a consistent representation in the latent space of the different geometries.

For the readers that might not be familiar with the structure of an autoencoder, it can be described, in its simplest form, by a set of equations; given one hidden layer, the encoder stage takes the input $\mathbf{x} \in \mathbb{R}^n$ and maps it to $\mathbf{h} \in \mathbb{R}^p$ according to:

$$\mathbf{h} = \sigma(\mathbf{W}\mathbf{x} + \mathbf{b}), \quad (1)$$

where the image \mathbf{h} is usually referred to as code, and the space of \mathbf{h} is the latent space. With the same terminology usually used for neural networks, σ , \mathbf{W} , \mathbf{b} respectively are

the sigmoidal activation function, the weight matrix and a bias vector that will be learned during the training process.

The decode stage of the autoencoder maps \mathbf{h} to the reconstruction \mathbf{x}' :

$$\mathbf{x}' = \sigma'(\mathbf{W}'\mathbf{h} + \mathbf{b}'), \quad (2)$$

in which σ' , \mathbf{W}' , \mathbf{b}' are not necessarily related to the corresponding quantities of equation (2).

During the training phase, the autoencoder is trained to minimise the reconstruction error, explained as follows:

$$\begin{aligned} \mathcal{L}(\mathbf{x}, \mathbf{x}') &= \|\mathbf{x} - \mathbf{x}'\|^2 = \\ &= \|\mathbf{x} - \sigma'(\mathbf{W}'(\sigma(\mathbf{W}\mathbf{x} + \mathbf{b})) + \mathbf{b}')\|^2. \end{aligned} \quad (3)$$

Once this is done, the optimization is performed in the latent space, hence working with a lower number of parameters to be optimized.

The main issue here is the lack of physical meaning of the latent space entries. For this reason, an additional surrogate neural network model is needed.

In order to well represent the input space the autoencoder needs to be trained with a large variety of geometries, including shapes that correspond to low performance designs. The latent space corresponding to the training data is then analyzed by means of determining the upper and lower bounds of each latent variable. These bounds are used in the following as constraints for the optimization, which will be performed in the space of the latent variables. It is important to note that decoder and encoder networks are tightly interconnected, and cannot be adopted separately, and that a properly trained autoencoder ensures univocity of mapping of training data.

B. Surrogate neural network model

For each image (design solution) of the training set we pre-calculated the corresponding EM quantity to be optimized by means of a FEA (but any other computational technique could be used). A second neural network based surrogate model is also trained using the latent representation of the corresponding geometry as input, and the desired quantity as output. This approach allows the surrogate model to benefit from the dimensionality reduction provided by the autoencoder.

The role of the surrogate model is to provide a fast prediction of the objective function, bypassing the expensive numerical computation. The surrogate model is trained offline before optimization, and it is also updated online using the new input-output pairs generated during the optimization process.

Figure 2 shows two neural networks architectures, in the typical graphical representation showing the inputs, the weights and the activation functions. In particular, the top part of Fig. 2 shows the autoencoder having dimensionality from 100 to 20 (these numbers are the ones used in the test case), while the bottom of Fig. 2 shows the surrogate model having as input the

20 variables of the decoder's latent space and as output the desired EM quantity T_{em} (a standard feed forward NN with one hidden layer, [7]). The whole structure represented in Fig. 2, is a Deep Neural Network architecture.

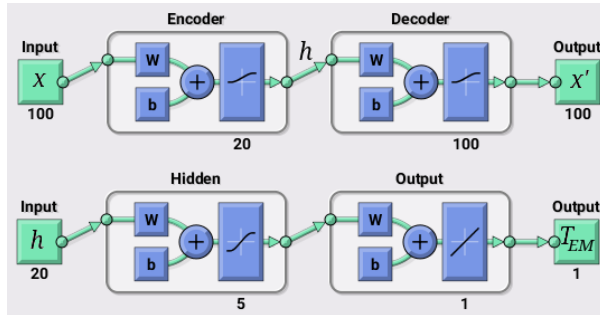


Fig. 2. Top: autoencoder; bottom: surrogate model structure.

III. OPTIMIZATION

As explained before, the optimization is carried out in the latent space, working on the reduced set of parameters. As in any optimization process, a fitness function has to be calculated at each step. The main advantage in using the proposed approach, is that at each iteration the calculation of the fitness function is not performed through a time-consuming numerical solution, but by the surrogate neural network model. This procedure might lead, though, to meaningless solution, because working in the latent space of the autoencoder does not allow the imposition of constraints to the physical variables.

For this reason, the authors propose an approach that will be explained later in this section.

In the literature, when dealing with topology optimization, Genetic Algorithms (GA) are often used; in this formulation, an evolutionary optimization algorithm, previously proposed by the authors is used [8], which is based on self-organizing maps, SOM, and denoted as self-organizing centroids optimization, SOC-opt. It was shown that SOC-opt outperforms many standard evolutionary optimization algorithms in a number of benchmarks. The algorithm uses a population of fixed size, and implements selection and mutation operators.

In the following descriptions, we will refer to a FEA, since this is the numerical method used in our test case; the set of the pre-calculated FEA solutions (that are used to train the autoencoder), are included in a set that we call *FEAdata*.

The optimization is carried out as follows:

1. Initialize the population in the latent space randomly within the bounds of the latent variables;

2. Provide each solution to the surrogate model in order to calculate the corresponding torque;
3. Calculate the new population of feasible solutions;
4. Divide the population in two subsets: *subset1* (eventually empty) contains individuals to be simulated with FEA, *subset2* the remaining population;
5. Decompress each individual of *subset1* to the corresponding bitmap using the decoder section of the autoencoder, provide the bitmap to the FEA software to calculate the fitness function, update the surrogate model with such solutions, add the solutions to *FEAdata*;
6. Provide each individual of *subset2* to the surrogate model in order to calculate the corresponding fitness function;
7. Iterate steps 3 to 6 until a stop criterion is verified.

The classifications of the individuals either in *subset1* or in *subset2* is carried out by means of the following heuristic strategy: a point is included in *subset2* if it is located in the *FEAdata* convex hull; on the contrary, if the individual is outside the convex hull then the fitness function is evaluated through a regular FEA analysis (*subset1*). The criterion is graphically shown in Fig. 3.

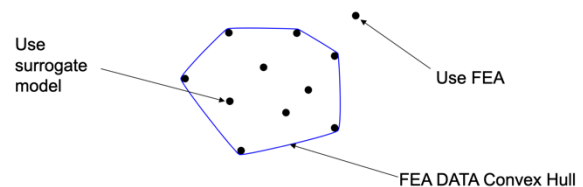


Fig. 3. Fitness function calculation criterion.

IV. TEST CASE

A. Description of the magnetostatics problem

The performance of the method has been tested on a simple magnetostatics test case, very similar to the test case shown in [5].

In particular, we perform the optimization of the distribution of the magnetic material $\mu_r = 1000$ in the design domain: practically speaking the objective of this optimization is maximizing the energy in the target domain finding the best feasible shape for the magnetic circuits. The source of the magnetic field is a permanent magnet characterized by a remnant flux density $B_r = 1T$, while the target domain is characterized by a rectangular shape of $\mu_r = 1$ above a rectangle of ferromagnetic material $\mu_r = 5000$. At first sight it is evident that the solution has to be in the form of a ferromagnetic channel connecting the permanent magnet and the target region. The presence of the iron below the

target and the presence of the airgap between the design domain and the target make the problem non-trivial. Figure 4 shows a simple outline of the problem.

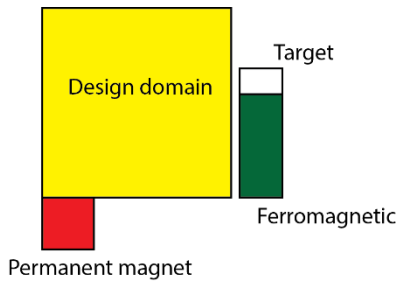


Fig. 4. Description of the test case.

B. Autoencoder training

The proper training set has been obtained by randomly generate 10^4 geometries, represented by 10×10 matrices in which each single entry can be either 1 or 0 (ferromagnetic material or vacuum). In order to have physically reasonable geometries, the following constraints have been imposed: a) the ferromagnetic material be characterized by a connected shape, b) 40% of the design space must be filled by the ferromagnetic material.

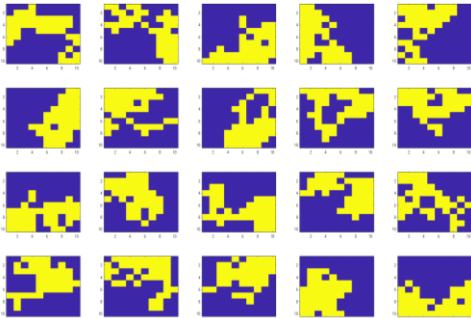


Fig. 5. Example of randomly generated geometries with the above mentioned constraints.

Starting from a dimension of 100 inputs (the number of “pixels” of each image), the latent space is characterized by a dimension of 20 variables and a 5-fold cross validation on the reconstruction error has been evaluated. Figure 5 shows few of the randomly generated geometries, while Fig. 6 shows the relative reconstructed images. In particular Fig. 6 is related to a continuous output (between 0 and 1): a proper threshold is then needed to move back to the materials discrete space (1 or 0). In this case the chosen threshold value is 0.5 and used in Figs. 8 and 9.

The ability of the autoencoder to well represent the original information can be easily verified.

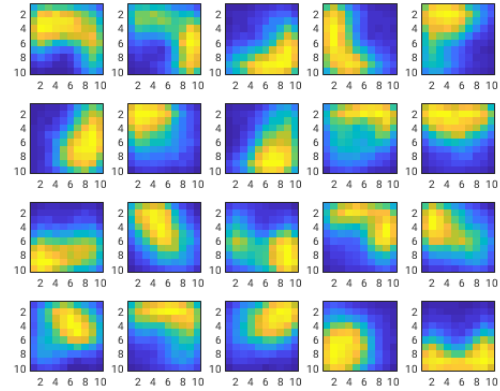


Fig. 6. Reconstructed geometries.

C. Neural network surrogate model training

The neural network surrogate model should be able to estimate the energy in the target zone from the geometry as represented in the latent space: for this reason, the input to the neural network has dimension 20 (latent space variables), while the output has dimension 1 (energy in the target area).

The same randomly generated 10^4 geometries have been simulated with Comsol, a commercial FEM software: each simulation (that includes magnetic field calculation and the evaluation of the magnetic energy in the target area) takes about 2s on an Intel I7 – 6 cores 4.0 GHz CPU.

Figure 7 shows the accuracy of the surrogate model with respect to the results obtained by the FEM model for 1100 geometries that have not been used for the neural network training: it is evident that the output of the surrogate model is accurate, and it can be used in the optimization algorithm.

Each evaluation of the target energy by the use of the surrogate model costs about $40\mu\text{s}$, $5 \cdot 10^5$ times faster than the corresponding FEM solution.

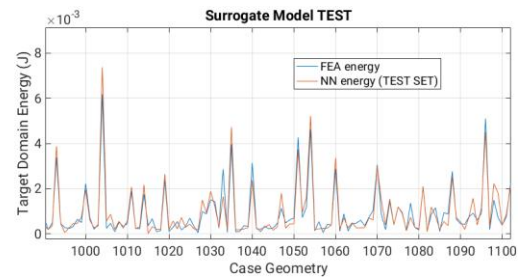


Fig. 7. Comparison between target energy calculated by FEM and by neural network model.

D. Optimization procedure results

The SOC-Opt optimization algorithm explained in

Section III has been implemented. The results relative to one optimization procedure (considering a stopping criteria of 10^5 global evaluations) are shown in Figs. 8 and 9. Figure 8 shows the field map and flux lines relative to the best solution among the original random geometries (target energy 0.0116 J), while Fig. 9 shows the same quantities relative the optimization procedure (target energy 0.01306J).

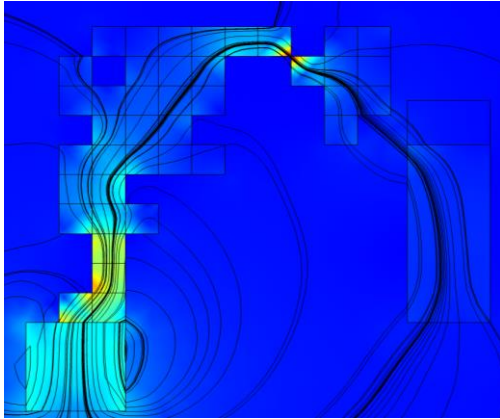


Fig. 8. Field map (B) and flux lines relative to the best solution among the initial pre-calculated random geometries.

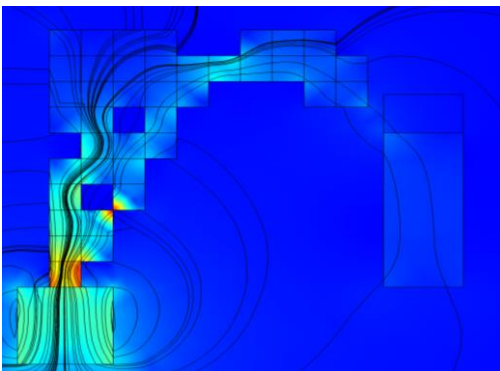


Fig. 9. Field map (B) and flux lines relative to the best solution after the optimization procedure.

The increase of the energy in the target region shows that the optimization procedure has reached its goal. There is no analytical solution to the problem, so we have no guarantee that the reached solution is a local or a global optimal (even though the SOC-Opt algorithm is robust in this point of view), and there might be different geometries giving practically coincident target energies. However, after numerous optimization procedures, the one shown in Fig. 9 is the best result obtained in terms of final energy.

Table 1 shows the CPU time required for training and for optimization, in which only 500 cases over 10^5

were outside the convex hull of the autoencoder (hence needed a FEA evaluation).

It is evident that the cost of the initial pre-calculated solutions is not negligible and it is a price to pay whenever neural networks to be trained are present. In this case, given the specific problem (basically no geometrical shape constraint) the number of iterations of the optimization procedure is one order of magnitude higher than the pre-calculated FEA solution, hence the final CPU time effort is positively affected by the use of proposed technique

Table 1: CPU time for training and optimization

Evaluations	Time
10^4 FEA Solutions (pre-calculated)	$2 \cdot 10^4$ s
99500 surrogate model (optimization)	4s
500 FEA solutions (optimization)	1000s

V. CONCLUSION

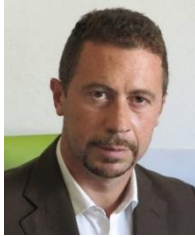
Optimizing an EM device in the latent representation space of an autoencoder has shown to be a promising approach, allowing the flexibility of topology optimization and reducing the dimensionality of both the search space and the surrogate model. Through the decoder it is possible to observe the solutions, and the introduction of a surrogate model approach, which also works in the latent space, reduces the number of required FEA simulations. Further work will be devoted to study the potential application in the case of multiobjective optimization.

REFERENCES

- [1] T. Sato, K. Watanabe, and H. Igarashi, "Multimaterial topology optimization of electric machines based on normalized Gaussian network," *IEEE Transactions on Magnetics*, vol. 51, no. 3, pp. 1-4, Mar. 2015.
- [2] B. Xia, Z. Ren, and C. Koh, "Utilizing Kriging surrogate models for multi-objective robust optimization of electromagnetic devices," in *IEEE Transactions on Magnetics*, vol. 50, no. 2, pp. 693-696, Feb. 2014.
- [3] A. Khan, V. Ghorbanian, and D. A. Lowther, "Deep Learning for magnetic field estimation," *Proceedings of 2018 IEEE Conference on Electromagnetic Field Computation (CEFC)*, Hangzhou, China, 2018.
- [4] H. Igarashi and H. Sasaki, "Topology Optimization Accelerated by Deep Learning," *Proceedings of 2018 IEEE Conference on Electromagnetic Field Computation (CEFC)*, Hangzhou, China, 2018.
- [5] R. Kawamata, S. Wakao, N. Murata, and Y.

Okamoto, "Development of Encoder-Decoder Predicting Search Process of Level-set Method in Magnetic Circuit Design," *Proceedings of Compumag. 2019*, Paris, France, July 16-19, 2019.

- [6] I. Goodfellow, Y. Bengio, and A. Courville, *Deep Learning*, vol. 1, Cambridge: MIT Press, 2016.
- [7] S. Haykin, *Neural Networks, A Comprehensive Foundation*, Prentice Hall, 1998
- [8] S. Barmada, M. Raugi, and M. Tucci, "An evolutionary algorithm for global optimization based on self-organizing maps," *Engineering Optimization*, vol. 48, no. 10, pp. 1740-1758, Jan. 2016.



Sami Barmada received the M.S. and Ph.D. degrees in Electrical Engineering from the University of Pisa, Italy, in 1995 and 2001, respectively. He currently is Full Professor with the Department of Energy and System Engineering (DESTEC), University of Pisa. His teaching activity is related to circuit theory and electromagnetics. His research activity is mainly dedicated to applied electromagnetics, EM fields calculation, power line communications and wireless power transfer devices, non destructive testing. He is author and coauthor of approximately 100 papers in international journals and refereed conferences. Prof. Barmada was the recipient of the 2003 J. F. Alcock Memorial Prize, presented by the Institution of Mechanical Engineering, Railway Division, for the Best Paper in Technical Innovation, he is IEEE Senior Member and ACES Fellow. He served as ACES President from 2015 to 2017, he is a member of the International Steering Committee of the CEFC Conference and he has been general chairman and technical program chairman of international conferences.



Nunzia Fontana was born in Agrigento, Italy, in 1984. She received the M.Sc. degree (summa cum laude) in Telecommunications Engineering and the Ph.D. in Remote Sensing from the University of Pisa, Pisa, Italy, in 2008 and in 2012, respectively. In 2011, she carried

out an internship with Queen Mary University of London, London, U.K. From 2012 to 2016, she was a Post-Doctoral Researcher with University of Pisa. From 2016 to 2019, she was a Researcher with the Italian Inter-University Consortium for Telecommunications and she was External Lecturer in biomedical engineering at University of Pisa. She is currently an Assistant Professor with the University of Pisa. Her current research interests include: Wireless Power Transfer; antennas, impedance matching networks design, prototyping and RF testing; radio frequency coils design for magnetic resonance and RF testing and bioelectromagnetics. Her research activity has been published in several international scientific journals and in a number of international conference proceedings.



Dimitri Thomopoulos was born in Bologna, Italy, in 1987. He received the M.Sc. degree in Business and Industrial Engineering and Ph.D. in Automatic Control Systems and Operational Research from the University of Bologna, Bologna, Italy in 2012 and in 2016, respectively. From 2017 to 2018, he was a Post-Doctoral Researcher at LIX CNRS - École Polytechnique, Palaiseau, France. He is currently Research Fellow at the University of Pisa. His current research interests include: combinatorial optimization, non-linear optimization, mostly applied to energy problems; power-systems, micro-grids, hydro unit commitment, and wind farm optimization; computational intelligence and big data analysis, with applications in electromagnetism.



Mauro Tucci received the Ph.D. degree in Applied Electromagnetism from the University of Pisa, Italy, in 2008. Currently, he is an Associate Professor with the Department of Energy, Systems, Territory and Constructions Engineering, University of Pisa. His research interests include computational intelligence and big data analysis, with applications in electromagnetism, non destructive testing, powerline communications, forecasting and smart grids. He is author and coauthor of approximately 80 papers in international journals and refereed conferences, he is IEEE Senior Member and he served as Technical Program Chair of ACES 2017 conference.

Characterization of Atmospheric Absorption in the 60 GHz Frequency Band Using a Multi-Pole Material Model

Müberra Arvas¹, Ercumend Arvas¹, and Mohammad A. Alsunaidi²

¹Department of Electrical Engineering
Istanbul Medipol University, Istanbul, Turkey
marvas@st.medipol.edu.tr, earvas@medipol.edu.tr

²Electrical and Electronics Engineering Department
Marmara University, Istanbul, Turkey
mohammad.alsunaidi@marmara.edu.tr

Abstract — Atmospheric attenuation of electromagnetic signals at the 60 GHz frequency band is dominated by oxygen absorption which represents a major obstacle to 5G communications using this band. So far, only empirical equations that fit the experimental absorption data have been reported. These empirical models are not suitable to employ in standard full-wave electromagnetic simulators based on the numerical solution of Maxwell's equations. In this paper, a frequency-dependent material model for atmospheric absorption at the 60 GHz band is presented. Further, a numerical simulator that incorporates this multi-pole material dispersion model and uses the rotating boundary conditions to allow for long propagation distances is developed. The simulation algorithm is based on the auxiliary differential equation finite-difference time-domain (ADE-FDTD) technique which implements the general electric polarization formulation. The results are useful in the prediction of propagation power loss between line-of-sight communication links and in the planning and positioning of ground and air-borne facilities.

Index Terms — 5G communications, 60GHz frequency band, atmospheric attenuation, FDTD method, lorentz model, oxygen absorption.

I. INTRODUCTION

The demand for fast data transfer and large bandwidth is expected to grow further and further over the coming decades. This is in part due to the large number of multi-media applications that require real-time communications and processing, and in part due to the growing consumer expectations and demands. The fact that the unlicensed 60 GHz frequency band is a strong contender to satisfy such demands requires addressing important issues and challenges pertinent to this band. The sea level atmosphere is known for its significant attenuation of frequencies around 60 GHz

due to high oxygen absorption. Oxygen absorption constitutes over 95% of this atmospheric attenuation which peaks around 60 GHz, with a value of over 15 dB/km. The successful adoption of 5G communications using the 60 GHz frequency band for wireless and radio communications relies on the introduction of novel antenna designs and communication strategies to overcome the channel loss. There has been a lot of emphasis on measurement [1,2] and modeling [3-6] techniques of atmospheric attenuation. The modeling effort focuses on the precise representation of the physical phenomena involving oxygen absorption lines at different atmospheric conditions. The final product of these models is customarily represented by a large verity of functions and polynomials (empirical fitting) with several physical parameters and mixing coefficients. The resulting empirical models are useful and can be utilized to approximate attenuation levels as a function of frequency and elevation. On the other hand, work has been done on the utilization of these models in solving real-life propagation problems. Grishin et al. used experimental data for atmospheric signal attenuation in an analytical model based on solving an inverse problem to simulate satellite signal propagation [7]. The work done in [8,9] simulated the signal absorption and dispersion due to the atmosphere by embedding the empirical relations into a transfer function and placed it in the channel part of the communication system. Other methods based on analytical solutions can in fact utilize these empirical functions but only for the treatment of simple propagation situations. Calculations based on the ray tracing method and the parabolic wave approximation have been proposed [10-13]. The ray tracing method is more suited for propagation problems with large-size features over a smooth ground in a homogeneous atmosphere. For complex environments, the computational time drastically increases and the accuracy deteriorates as the number of required rays

significantly increases. Also, the method fails for gazing angles. On the other hand, although the methods based on parabolic approximation are good for large distance propagation, they become less effective in solving problems involving complex terrain and strong atmospheric dispersion. Obviously, because empirical models representing the atmosphere involve complicated expressions and functions, analytical methods become limited in application. Instead, the empirical models need to be incorporated into standard full-wave electromagnetic simulators using, for example, the finite-difference time-domain method (FDTD) and the finite-element method (FEM).

The objective of this work is three-fold. First, a material model of atmospheric attenuation is developed by fitting measurement data to standard Lorentz poles. The reason behind this choice is that Lorentz functions represent the most general matter-wave interaction forms. Second, the material model is incorporated in the time-domain simulations of Maxwell's equations and specifically in a FDTD algorithm. This objective is achieved through the general polarization formulation and the auxiliary differential equation (ADE) technique [14,17]. Finally, simulations of long-distance propagations in the 60 GHz frequency band are carried out. To the best of our knowledge, this is the first report of incorporating atmospheric attenuation in a FDTD algorithm using the Lorentz model. This model should find applications in many disciplines, including remote sensing, geophysical mapping and in point-to-point communications, where it can help in planning the positions of ground and air-borne facilities.

II. ATMOSPHERIC MATERIAL MODEL

The frequency-dependent behavior of dispersive materials can be described by the constituent relations. For non-magnetic materials, the electric polarization is used to represent the dielectric effects inside the material. Assuming a linear material response, the frequency-dependent electric flux density can be written as:

$$\vec{D}(\omega) = \epsilon_0 \epsilon_\infty \vec{E}(\omega) + \vec{P}(\omega), \quad (1)$$

where ϵ_0 is the free space permittivity, ϵ_∞ is the high frequency dielectric constant and ω is the frequency. The first order linear polarization $\vec{P}(\omega)$ is related to the electric field intensity, $\vec{E}(\omega)$, in the frequency domain by the electric susceptibility as:

$$\vec{P}(\omega) = \epsilon_0 \chi(\omega) \vec{E}(\omega). \quad (2)$$

Combining equation (1) and equation (2), one can write:

$$\epsilon_r(\omega) = \epsilon_\infty + \chi(\omega), \quad (3)$$

where $\epsilon_r(\omega)$ is the frequency-dependent complex relative permittivity of the dispersive material. The dispersion relation for the electric susceptibility $\chi(\omega)$ that represents the material-wave interaction can be

represented by a general Lorentz model function of the form:

$$\chi(\omega) = \frac{\mathbf{a}}{\mathbf{b} + jc\omega - d\omega^2}, \quad (4)$$

where \mathbf{a} , \mathbf{b} , \mathbf{c} and \mathbf{d} are model parameters that can be obtained from material properties or by fitting to experimental data. The atmospheric material model developed in this work is based on a recent report by the International Telecommunication Union [2]. The report provides empirical methods to estimate the attenuation of atmospheric gases on terrestrial and slant paths using experimental data. In the report, an estimate of gaseous attenuation computed by summation of individual absorption lines for the frequency range 1 GHz to 1 THz is given. Figure 1 is a reproduction of the atmospheric specific attenuation using several empirical formulae given in [2] for frequencies between 40 and 80 GHz. The curve in Fig. 1 is based on atmospheric conditions of dry air with total air pressure of 1033.6 hPa and average temperature of 15 °C.

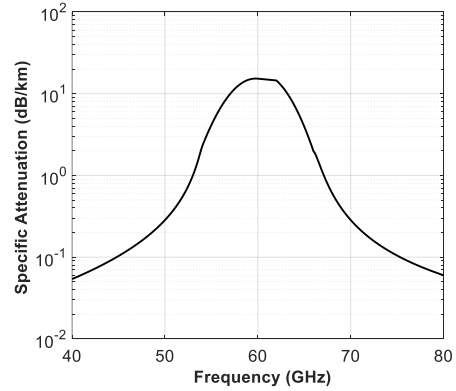


Fig. 1. Atmospheric specific attenuation for the 40-80 GHz frequency range at sea level, as given by the empirical formulae in [2].

In this work, a fitting to the general Lorentz poles is performed. The strategy for using the experimental data is as follows. For any given frequency range and elevation, frequency-dependent complex permittivity values are obtained from attenuation readings using the following relations:

$$\epsilon_r' = (n')^2 + (n'')^2, \quad (5-1)$$

$$\epsilon_r'' = -\alpha n' v / \omega, \quad (5-2)$$

where n' and n'' are the real and imaginary parts of the complex refractive index, respectively, α is the attenuation coefficient and v is the speed of light. Those complex permittivity data are fitted to standard material models with as many poles as necessary. Out of the fitting process, the required parameters for the time-domain simulator are obtained. Here, a Lorentzian dielectric function of the form:

$$\varepsilon_r(\omega) = \varepsilon_\infty + (\varepsilon_s - \varepsilon_\infty) \sum_{i=1}^M \frac{A_i \omega_i^2}{\omega_i^2 + j2\delta_i \omega - \omega^2}, \quad (6)$$

is used, with $\mathbf{a}_i = (\varepsilon_s - \varepsilon_\infty) A_i \omega_i^2$, $\mathbf{b}_i = \omega_i^2$, $\mathbf{c}_i = 2\delta_i$ and $\mathbf{d}_i = 1$ being the parameters in equation (4). In equation (6), ε_s is the effective static dielectric constant, A_i is the pole strength, ω_i is the resonance frequency and δ_i is the damping parameter for i^{th} pole. M represents the total number of poles of the material dispersion relation.

The fitting process to Lorentzian poles goes as follows. One can start with a Lorentzian pole that has a peak around the center of the curve in Fig. 1 (i.e., around 60 GHz). This step yields the value of the resonance frequency of the first pole. Next, to accommodate for the width of the spectrum of the measurement data, other poles at above and below the first resonance frequency are added. Finally, the values of the pole strength and damping parameter for each pole are adjusted such that a reasonable fit is obtained. Table 1 shows the a , b , c and d parameters for the three Lorentz poles used for atmospheric attenuation modeling. These parameters are related to the pole parameters using equation (6). The resulting dielectric function (real and imaginary parts) is shown in Fig. 2, together with the reference measurement data. The fitting is good in general, and focus has been made on the frequency range around 60 GHz where the expected bandwidth of the transmitting antenna is located. The obtained poles form the basis for the relation between the electric polarization and the electric field.

Next, the frequency-domain dielectric function is incorporated in a time-domain simulator using the ADE-FDTD method. Equation (2) can be expressed in the time domain using the Fourier transform, as reported in [16]. The procedure results in a second order differential equation for the electric polarization vector given by:

$$\mathbf{b}P + \mathbf{c} \frac{d}{dt} P + \mathbf{d} \frac{d^2}{dt^2} P = \mathbf{a} \varepsilon_0 E. \quad (7)$$

Using finite-difference approximations, the time domain update equation for the linear polarization in equation (7) becomes:

$$P^{n+1} = C_1 P^n + C_2 P^{n-1} + C_3 E^n. \quad (8)$$

The constants in equation (8) are given by:

$$C_1 = \frac{4\mathbf{d}}{2\mathbf{d} + \mathbf{c}\Delta t + \mathbf{b}\Delta t^2}, \quad (9-1)$$

$$C_2 = \frac{-2\mathbf{d} + \mathbf{c}\Delta t - \mathbf{b}\Delta t^2}{2\mathbf{d} + \mathbf{c}\Delta t + \mathbf{b}\Delta t^2}, \quad (9-2)$$

$$C_3 = \frac{2\mathbf{a}\varepsilon_0 \Delta t^2}{2\mathbf{d} + \mathbf{c}\Delta t + \mathbf{b}\Delta t^2}, \quad (9-3)$$

where n is the time index and Δt is the time step. It should be noted that in deriving the expressions in equation (9), semi-implicit finite-differencing has been used. In this case, the first term on the right-hand side of equation (7) was approximated using the average of P^{n-1} and P^{n+1} time instances. This scheme is known to improve the stability of the overall algorithm, even with strong dispersion. All field components and parameters

are arranged on the FDTD computational grid using the standard Yee's cell. The time-domain algorithm proceeds as follows. First, the electric flux densities are evaluated using Maxwell's curl equation with available magnetic field samples. Next, the linear polarization vector is updated using equation (8). Third, the electric field intensity components are updated using the time-domain version of equation (1) as:

$$E^{n+1} = \frac{D^{n+1} - \sum_{i=1}^M P_i^{n+1}}{\varepsilon_0 \varepsilon_\infty}. \quad (10)$$

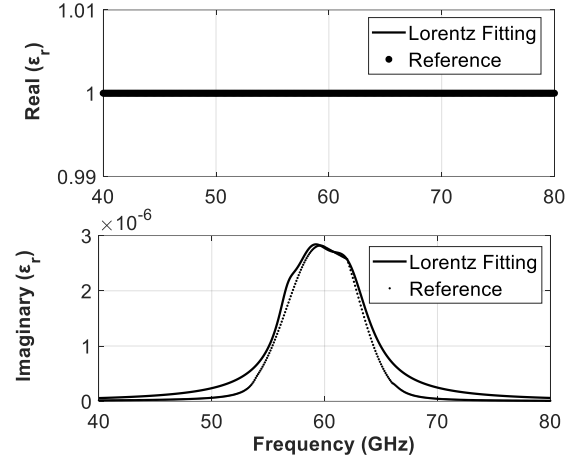


Fig. 2. Real and imaginary dielectric constant curves as obtained from the empirical attenuation function (Ref 2, dashed line) and the corresponding 3-pole Lorentz fit (solid line) for sea level atmospheric conditions.

Table 1: Lorentz pole parameters for atmospheric attenuation at sea level

Pole i	\mathbf{a}_i (rad/s) ²	\mathbf{b}_i (rad/s) ²	\mathbf{c}_i (rad/s)	\mathbf{d}_i
1	2.0245×10^{16}	1.5210×10^{23}	3.0×10^{10}	1
2	2.4546×10^{16}	1.3690×10^{23}	3.2×10^{10}	1
3	2.7960×10^{15}	1.2709×10^{23}	1.2×10^{10}	1

Finally, the second Maxwell's curl equation is used to calculate the magnetic field components. The flowchart in Fig. 3 describes the sequence of calculations in the resulting algorithm. It is important to mention here that solving this problem using the classical ADE algorithm [18] would introduce higher order time derivatives, the solution of which would require matrix inversion. When applied to the problem presented in this work with three Lorentzian poles, derivatives of the sixth order result. It would be necessary to save a large number of time samples and hence, using a mixed explicit-implicit scheme, matrix inversion is needed. The FDTD algorithm used here is significantly more efficient and robust. Other ADE algorithms reported in literature

require complex-domain operations (for example [19]). In general, complex-domain operations require twice as much computation time and memory storage as normal real operations. The computational requirements are clearly a function of the number of poles of the dispersion model. For multi-pole dispersion problems, these FDTD algorithms would require more constants to be evaluated and stored in memory.

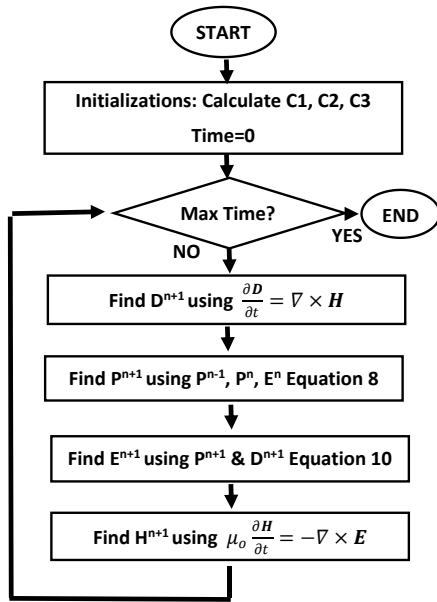


Fig. 3. Flowchart of the calculation sequence in the time-domain algorithm.

III. SIMULATION RESULTS

To test wave propagation using the proposed atmosphere model, the FDTD simulation algorithm presented in section II is implemented. A time-limited pulse of a Gaussian form given by:

$$A(t) = A_o \exp \left[-\left(\frac{t-t_o}{t_p} \right)^2 \right] \cos[\omega_c(t - t_o)], \quad (11)$$

is used as a point-source excitation, where A_o is the initial pulse amplitude, t is time variable, t_o is the offset time, t_p is the pulse waist and ω_c is the central frequency. The parameter t_p is used to steer the frequency contents of the pulse. In this work, a pulse waist of 20 picoseconds is used such that it covers a large frequency band around 60 GHz, which is taken as the central frequency ω_c . A plane wave propagation in a one-dimensional sea-level atmosphere is considered. The value of the spatial step is set to a very small fraction of the smallest wavelength involved in propagation. This is required to ensure that numerical dispersion is significantly minimized, and that channel dispersion is correctly represented. Accordingly, a spatial step size of 0.01 mm is used. The stability of the algorithm is determined by the standard Courant-Friedrichs-Lewy (CFL) condition for the FDTD method,

which is given by [15]:

$$\Delta t \leq \frac{1}{v_{\max} \sqrt{\frac{1}{\Delta x^2} + \frac{1}{\Delta y^2} + \frac{1}{\Delta z^2}}}. \quad (12)$$

A time step of 0.03 picoseconds satisfies this condition. Numerical dispersion is an artifact of the approximation of the spatial derivatives in finite differences. Because the spatial step is finite, errors in data transmission throughout the computational grid propagate and accumulate. The general guideline is to make the spatial step a very small fraction of the smallest wavelength involved in the propagation. This problem becomes more serious if the medium of propagation is itself dispersive. Consequently, with high levels of space resolution, the memory requirement for the simulation of hundreds of meters of propagation distance becomes unaffordable. To solve this problem, the rotating boundary conditions have been used. In this case, as shown in Fig. 4, the pulse propagates across the whole domain, exits the computational window from one boundary and re-enters from the other boundary to start propagating the domain again.

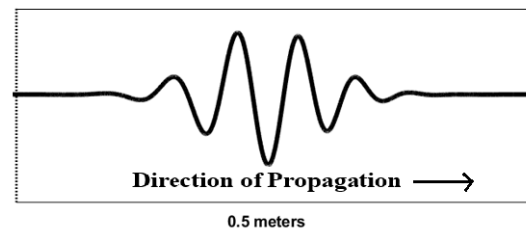


Fig. 4. Pulse propagation in rotating boundary conditions. The total length of the computational window is half a meter.

The rotating boundary conditions are thus defined as follows. For the first Maxwell's equation, the curl is evaluated in one-dimensional case using:

$$\left. \frac{\partial D}{\partial t} \right|_{i=i_1} = \frac{H(i_1) - H(i_{\max-1})}{\Delta x}, \quad (13)$$

and

$$\left. \frac{\partial D}{\partial t} \right|_{i=i_{\max}} = \frac{H(i_{\max-1}) - H(i_1)}{\Delta x}. \quad (14)$$

In equations (12) and (13), i_1 and i_{\max} are the first and last points in the computational domain, and Δx is the spatial step. The curl in the second Maxwell's equation is treated similarly. The initial size of the computational domain is set to half a meter. The choice of this initial domain size ensures that it is wide enough to comfortably accommodate the pulse at any time throughout the simulation, even with the resulting dispersion due to the channel. The pulse transpasses the computational domain for multiples of times to achieve a certain propagation distance. In this study, the pulse is propagated well over one kilometer. Also, a reference simulation in a lossless atmosphere was carried out such

that comparisons are possible. Figure 5 shows the time-domain electric field waveform for the propagating pulse at 1000 meters. The reference waveform for a lossless atmosphere is also shown in the figure. The attenuation and dispersion of the pulse is evident. Power calculations have been performed to validate the numerical model. The spectrum of the received signal power has been produced after propagation of 1000 m. At any given location, the power density is given by:

$$\vec{S} = \frac{1}{2} \vec{E} \times \vec{H}^* \tag{15}$$

For a wave propagating along the x direction, the spectrum of the real power density is given by:

$$S(f)_{x,r} = \frac{1}{2} [E(f)_{y,r} H(f)_{z,r} + E(f)_{y,i} H(f)_{z,i}] \tag{16}$$

where the subscripts r and i denote the real and imaginary parts, respectively. The amount of received power at several distances are shown in Fig. 6. It is clearly seen from the figure that a signal at 60 GHz loses more than 97% of its initial power within the first kilometer. The propagation of the 50, 60 and 70 GHz frequency components are shown separately in Fig. 7, where normalization has been made to the input value for each frequency component. Table 2 and Fig. 8 show the comparison between the amount of loss per kilometer, as given by the reference attenuation curve (Fig. 1) and by the FDTD simulation, for selected frequencies. The slight discrepancies in the power loss are attributed to the imperfections in the fitting process.

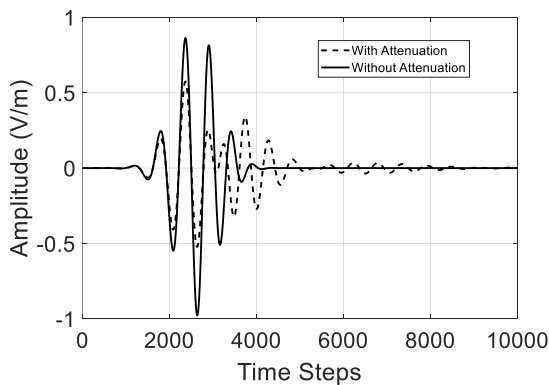


Fig. 5. Time profile of the received electric field at a distance of 1000 meters, with and without attenuation.

Table 2: Loss comparison between simulation results and reference data

Frequency (GHz)	Loss (dB/km)	
	Reference	Simulation
57	8.78	9.00
58	11.43	11.42
59	15.23	14.26
60	15.26	16.04
61	14.89	14.61
62	14.51	11.93
63	10.75	9.61

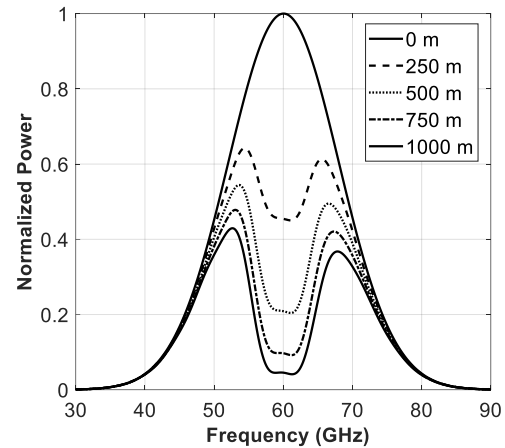


Fig. 6. Normalized signal power at different propagation distances versus frequency.

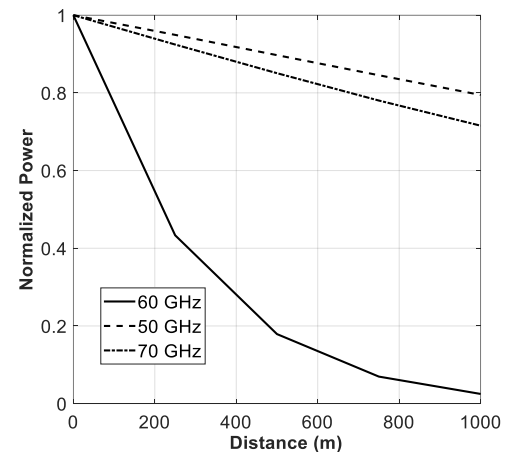


Fig. 7. Normalized received power for the 50, 60 and 70 GHz frequency components versus distance.

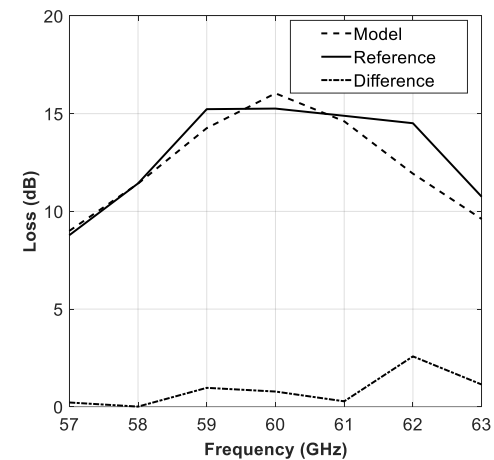


Fig. 8. Estimated loss after propagation of 1000 meters, as given by the simulation model. The reference values and the difference are shown for comparison.

IV. CONCLUSION

A propagation model for atmospheric absorption of 60 GHz band signals has been presented. The model is incorporated in an FDTD numerical simulator as a multi-pole material dispersion term using the ADE technique. The rotating boundary conditions have been used to allow for long propagation distances. Also, the validity of the model has been demonstrated. This model is very useful in the study of many situations involving free space communications with the possibility of incorporating different scenarios, such as reflections from buildings, presence of ground, terrain and water bodies and interference. It can be added to commercial electromagnetic software packages as a separate material module. The results are also useful in the prediction of propagation power loss such that methods for loss compensation can be devised. Work is underway to model atmospheric attenuation at different elevations and different weather conditions.

REFERENCES

- [1] D. S. Makarov, M. Y. Tretyakov, and P. W. Rosenkranz, "60-GHz oxygen band: Precise experimental profiles and extended absorption modeling in a wide temperature range," *Journal of Quantitative Spectroscopy & Radiative Transfer*, 112, pp. 1420-1428, 2011.
- [2] International Telecommunication Union, *Attenuation by atmospheric gases*, Recommendation ITU-R P.676-9, 02/2012.
- [3] H. J. Liebe, "MPM: An atmospheric millimeter-wave propagation model," *International Journal of Infrared and Millimeter Waves*, 10.6, pp. 631-650, 1989.
- [4] M. Y. Tretyakov, M. Koshelev, V. Dorovskikh, D. S. Makarov, and P. W. Rosenkranz, "60-GHz oxygen band: Precise broadening and central frequencies of fine-structure lines, absolute absorption profile at atmospheric pressure, and revision of mixing coefficients," *Journal of Molecular Spectroscopy*, 231, 1-14, 2005.
- [5] G. Frank, J. Wentz, and T. Meissner, "Atmospheric absorption model for dry air and water vapor at microwave frequencies below 100 GHz derived from spaceborne radiometer observations," *Radio Sci.*, 51, 2016.
- [6] B. T. Nguyen, A. Samimi, and J. J. Simpson, "Recent advances in FDTD modeling of electromagnetic wave propagation in the ionosphere," *ACES Journal*, vol. 29, no. 12, pp. 1003-1012, Dec. 2014.
- [7] D. V. Grishin, D. Y. Danilov, and L. Kurakhtenkov, "Use of ITU-R recommendations in calculating tropospheric signal attenuation in the simulation modeling problems of satellite systems," *Systems of Signal Synchn. Generating and Processing in Telecomm.*, pp. 1-4, 2017.
- [8] A. C. Valdez, "Analysis of Atmospheric Effects due to Atmospheric Oxygen on a Wideband Digital Signal in the 60 GHz Band," *Master's thesis, Virginia Polytechnic Institute*, 2001.
- [9] A. Chinmayi, M. Vasanthi, and T. Rama Rao, "Performance evaluation of RF based Inter satellite communication link at 60 GHz," *International Conference on Wireless Communications, Signal Processing and Networking*, India, Mar. 2016.
- [10] J. G. Powers, J. B. Klemp, W. C. Skamarock, C. A. Davis, J. Dudhia, D. O. Gill, J. L. Coen, and D. J. Gochis, "The weather research and forecasting model: Overview, system efforts, and future directions," *American Meteorological Society*, vol. 98, no. 8, pp. 1717-1737, 2017.
- [11] A. E. Barrios, "A terrain parabolic equation model for propagation in the troposphere," *IEEE Transactions on Antennas and Propagation*, vol. 42, no. 1, pp. 90-98, 1994.
- [12] J. Kuttler and G. D. Dockery, "Theoretical description of the parabolic approximation/Fourier split-step method of representing electromagnetic propagation in the troposphere," *Radio Science*, vol. 26, no. 02, pp. 381-393, 1991.
- [13] H. Zhou, A. Chabory, and R. Douvenot, "A 3-D split-step Fourier algorithm based on a discrete spectral representation of the propagation equation," *IEEE Transactions on Antennas and Propagation*, vol. 65, no. 4, pp. 1988, 1995, 2017.
- [14] M. A. Eleiwa and A. Z. Elsherbeni, "Debye constants for biological tissues from 30 Hz to 20 GHz," *ACES Journal*, vol. 16, no. 3, Nov. 2001.
- [15] Atef Elsherbeni and Veysel Demir, *The Finite Difference Time Domain Method for Electromagnetics with MATLAB Simulations*, Second Edition, Edison, NJ, 2015.
- [16] M. A. Alsunaidi and A. Al-Jabr, "A general ADE-FDTD algorithm for the simulation of dispersive structures," *IEEE Photonics Tech. Lett.*, vol. 21, no. 12, pp. 817-819, June 2000.
- [17] M. Arvas and M. A. Alsunaidi, "A multi-pole model for oxygen absorption of 60 GHz frequency band communication signals," *The Computational Methods and Telecommunication in Electrical Engineering and Finance, Sarajevo*, pp. 92-94, May 6-9, 2018.
- [18] A. Taflove, *Computational Electrodynamics: The Finite-Difference Time-Domain Method*, Artech House, Norwood, MA, 1995.
- [19] M. Han, R. Dutton, and S. Fan, "Model dispersive media in finite-difference time-domain method with complex-conjugate pole-residue pairs," *IEEE Microw. Wireless Compon. Lett.*, 16, pp. 119-121, 2006.



Ercumend Arvas received the B.S. and M.S. degrees from the Middle East Technical University, Ankara, Turkey in 1976 and 1979, respectively, and the Ph.D. degree from Syracuse University, Syracuse, NY in 1983, all in Electrical Engineering. From 1984 to 1987, he was with the

Electrical Engineering Department, Rochester Institute of Technology, Rochester, NY. He was with the EE Department of Syracuse University between 1987 and 2014. He is currently a Professor in the EE Department of Istanbul Medipol University. His research and teaching interests are in electromagnetic scattering and microwave devices. Arvas is a Member of the Applied Computational Electromagnetics Society (ACES), and Fellow of IEEE and Electromagnetics Academy.



M. A. Alsunaidi is currently a Visiting Professor at the Electrical and Electronics Engineering Department of Marmara University, Istanbul, Turkey. His main areas of reaserch are optoelectronics and computational electromagnetics. His fields of interest include antenna

design, solid-state lighting and plasmonics.



Muberra Arvas has joined Prof. Ercumend Arvas' project group in 2015. She is currently doing her M.S.E.E under the supervision of Prof. Ercumend Arvas, in Istanbul Medipol University, Turkey. Her current research areas are antennas and numerical electromagnetics.

A Tunable Trisection Bandpass Filter with Constant Fractional Bandwidth Based on Magnetic Coupling

Mingye Fu, Qianyin Xiang, and Quanyuan Feng

School of Information Science and Technology
Southwest Jiaotong University, Chengdu, Sichuan, 610031, China
qyxiang@swjtu.edu.cn

Abstract — A tunable microstrip trisection bandpass filter with source-load coupling is proposed in this paper. Magnetic cross coupling structure based on varactor loaded open ring resonators is employed. No extra capacitor is used to adjust the coupling coefficients directly. Normalized coupling matrix M is used to calculate the frequency response, and formulas for computing the S parameters based on the resonator with unconventional phase performance are given. Coupling coefficients are investigated by computing the integral of the distributed voltage/current and it is proved that the coupling coefficients can meet the requirements of constant fractional bandwidth (CFBW). Due to the magnetic cross coupled trisection structure and the electrical source-load coupling, this tunable filter has three transmission zeros at finite frequency which can effectively improve the frequency selectivity. The measurement agrees well with the simulation. The center frequency can be tuned from 1097 MHz to 1936 MHz. In this tuning range, the insertion loss varies from 7.8 dB to 4 dB. A constant fractional bandwidth of about 5% is achieved.

Index Terms — cross-coupling, trisection filter, tunable bandpass filter.

I. INTRODUCTION

With the fast development of wireless communications, reconfigurable RF/microwave systems, which can be used in electronic countermeasures, software defined radio and so on, are highly demanded. The tunable filter, which dynamically receives the wanted signals or rejects the interferences, is regarded as a core component in reconfigurable RF/microwave systems. For tunable bandpass filters, high frequency selectivity is vital since it can effectively restrain the near-passband interference. One approach to improve frequency selectivity is utilizing high resonators with high unloaded quality factor (Q_u) such as cavity resonators [1, 2] or SIW filters [3, 4]. For varactor-tuning microstrip bandpass filters, the resonator quality factor is relatively lower. Transmission zeros can be used for improving the frequency selectivity, and

crossed coupling can bring transmission zeros by making signals transmit through different paths and cancel each other at a specified frequency [5-7].

Crossed coupling has already been widely used in fixed filters [8-12]. By applying source-load coupling, N th order canonical filters with N finite transmission zeros can be achieved [10]. Recently, tunable cross-coupled tunable filters have been reported. The roll-off rate of second order tunable cross-coupled filter based on source-load cross coupling [13, 14] is limited, and several fourth order cross-coupled filters with higher frequency selectivity have been reported [6, 7, 15, 16]. In [6, 7, 15-17], tunable capacitors are placed in the coupling region for tuning the electric coupling coefficient directly, and bandwidth becomes tunable since coupling coefficients can be tuned. However, this method requires more capacitors, which may lead to higher insertion loss and increase the difficulty of practical layout design. Meanwhile, tunable capacitors which are now available on the market are relatively large as coupling capacitor. Therefore, the capacitance in resonators should be very large to maintain a relatively small coupling coefficient [6]. Tunable third order filter is a useful topology to reduce the designing difficulty and maintain the roll-off rate [18-20]. A typical third order filter is trisection filter which is desirable for some applications requiring only a higher selectivity on one side of the passband due to the advantage of its asymmetrical frequency response. [18-20] reported several third order tunable filters but they only have one or two transmission zeros. Combining cross coupled trisection structure with source-load cross coupling can bring three transmission zeros.

Open ring resonators (ORRs) are common used in microstrip filters [8, 21-23]. It can be utilized for designing tunable filters by adding a tunable capacitor at the open ends of the microstrip line. At the resonant frequency, the magnetic energy is mainly stored in the middle of the microstrip line while the majority of electrical energy is stored at the terminal region of the microstrip line and the capacitor. The larger the capacitance, the less electrical energy there is in the microstrip line, therefore, the electrical coupling can

not make the fractional bandwidth of tunable filter keep in constant.

In this paper, magnetic coupling structure based on varactor loaded ORRs are utilized to design tunable trisection filter with constant fractional bandwidth. Formulas for computing the S parameters based on the resonator with unconventional phase performance are given. Coupling coefficients are investigated by computing the integral of the distributed voltage/current. All-magnetic cross coupled resonators and source to load electric coupling are designed to generate three transmission zeros for improving the frequency selectivity.

II. FILTER SYNTHESIS

The most important parameters that influence filter bandwidth are coupling coefficient k and external quality factor Q_{ext} . In order to attain the desired k and Q_{ext} for constant fractional bandwidth, filter synthesis can be applied based on normalized coupling matrix M [8, 24-26]. The formulas for calculating the lowpass S parameters based on M matrix can be written as [8]:

$$\begin{cases} S_{21} = -2jA_{n+2,1}^{-1} \\ S_{11} = 1 + 2jA_{1,1}^{-1} \end{cases}, \quad (1)$$

where n is the order of the filter, $A_{i,j}^{-1}$ denotes the i^{th} row and j^{th} column element of A^{-1} , which is given by:

$$A = M + \Omega \cdot U - j \cdot q, \quad (2)$$

in which U is the $(n+2) \times (n+2)$ identity matrix except $U_{1,1} = U_{n+2,n+2} = 0$; q is a $(n+2) \times (n+2)$ matrix with all zeros except $q_{1,1} = q_{n+2,n+2} = 1$, and Ω is angular frequency. To get bandpass response, a lowpass-to-bandpass transformation can be written as:

$$\Omega = \frac{1}{FBW} \left(\frac{\omega}{\omega_0} - \frac{\omega_0}{\omega} \right), \quad (3)$$

where ω_0 is center angular frequency of the transformed bandpass filters, ω denotes angular frequency and FBW is the fractional bandwidth. The desired coupling coefficient between i^{th} and j^{th} resonators k_{ij} , and external quality factor Q_{ext} , which can determine the frequency response of the bandpass filter, can be obtained as:

$$k_{ij} = M_{ij} \cdot FBW = M_{ij} \frac{ABW}{f_0}, \quad (4)$$

$$Q_{ext} = \frac{1}{M_{S1}^2 FBW} = \frac{f_0}{M_{S1}^2 ABW}, \quad (5)$$

where M_{ij} denotes the entries in M matrix ($i, j = S, 1, 2, \dots, N, L, S$ stands for the input source and L for the output load. The filter is N th order), f_0 is the center frequency and ABW is the absolute bandwidth.

Figure 1 is the topology used for designing the tunable filter in this paper, where, E stands for electrical coupling and M is magnetic coupling. 1~3 denote resonator 1 to resonator 3. There are three paths from source to load, and the M matrix in (6) is used for

computing the frequency response, as in Fig. 2. This topology can generate three transmission zeros at finite frequency,

$$M = \begin{pmatrix} 0 & 1.3 & 0 & 0 & -0.005 \\ 1.3 & 0 & 0.78 & 0.58 & 0 \\ 0 & 0.78 & 0 & 0.78 & 0 \\ 0 & 0.58 & 0.78 & 0 & 1.3 \\ -0.005 & 0 & 0 & 1.3 & 0 \end{pmatrix}. \quad (6)$$

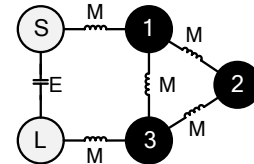


Fig. 1. The topology of the trisection bandpass filter.

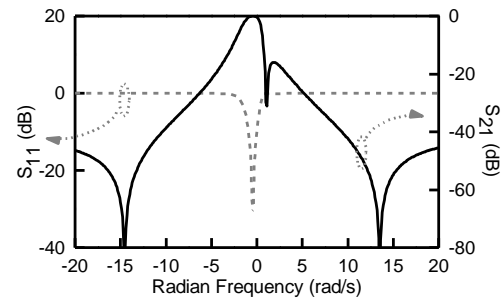


Fig. 2. The frequency response of the M matrix.

In the traditional synthesis method, the resonators have a phase shift of $\pi/2$ at low frequency and $-\pi/2$ at high frequency [26]. Figure 3 shows that the phase shift of varactor loaded ORR is opposite. Hence the U in (2) should be changed to:

$$U = \text{diag}[0, -1, -1, -1, 0]. \quad (7)$$

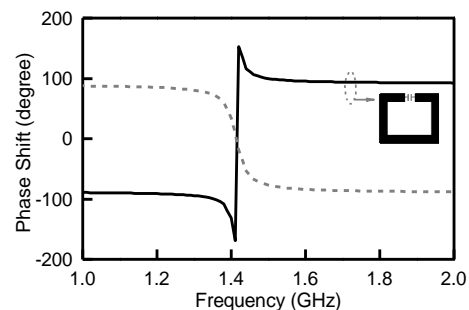


Fig. 3. The phase response of varactor loaded ORR (black solid line), and the resonators in traditional synthesis method (gray dashed line).

Figure 4 shows the response based on the topology shown in Fig. 1 based on the varactor loaded ORR, with

$FBW = 0.05$ under center frequency of 1.3 GHz, 1.5 GHz, and 1.7 GHz, respectively. The desired coupling coefficients and external quality factor versus center frequency can be calculated using (4) and (5), as shown in Fig. 2.

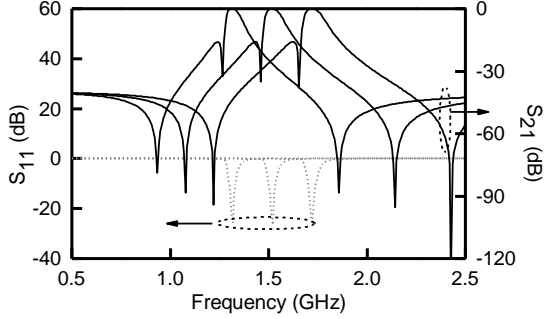


Fig. 1. Bandpass response of the M matrix. This calculation uses the modified U .

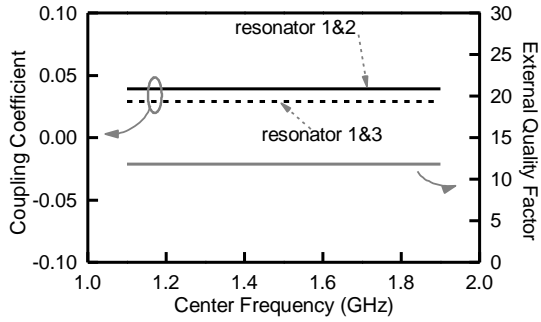


Fig. 2. The desired coupling coefficients and external quality factor extracted from M matrix.

III. FILTER DESIGN

Figure 6 shows the tunable cross coupled trisection bandpass filter based on the magnetic coupled varactor loaded ORR. $D_1 \sim D_6$ are the varactors and $R_1 \sim R_6$ are 5.1 k Ω resistors used as RF chokes. Feedlines utilize magnetic coupling to achieve matching and electrical source-load coupling is implemented through feedlines. Table 1 lists their physical parameters in Fig. 6. Three types of geometry parameters are used for studying the coupling structure.

A. Coupling coefficients

The relationship between center angular frequency ω_0 and the equivalent capacitance of varactors can be analyzed by half circuit of the resonators. For resonator 1 and resonator 3 in Fig. 6, their half circuit is shown in Fig. 7 (a). It is made up with two short ended microstrip lines and two capacitors named C_L . Y_0 is the characteristic admittance of the microstrip lines, θ_1 is

the electrical length of the coupling region and θ_2 is the electrical length of each microstrip line.

At resonating frequency ω_0 , the tunable capacitance C_L can be written as:

$$j\omega C_L - jY_0 \cot \theta_2 = 0, \quad (8)$$

$$C_L = \frac{Y_0 \cot \theta_2 |_{\omega=\omega_0}}{\omega_0}. \quad (9)$$

The calculated curves of the tunable capacitor C_L versus center frequency based on the three geometries in Table 1 are shown in Fig. 8. Since L_2 , L_3 and W_2 of the three geometries are same, the calculated curves coincide.

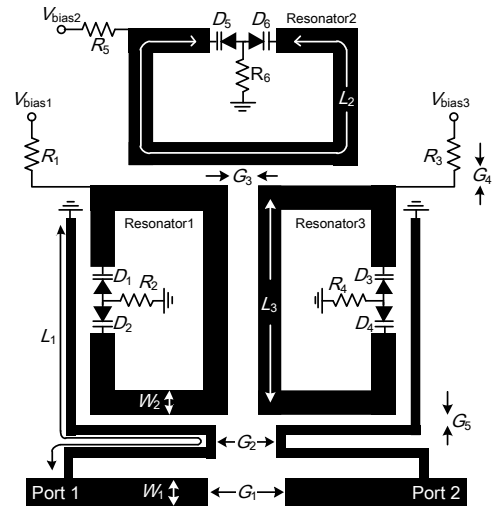


Fig. 6. The electrical circuit model of this filter.

Table 1: Physical parameters of 3rd tunable filters

Parameters (unit: mm)	Dimensio n 1	Dimension 2	Dimensio n 3
L_2	26.9	26.9	26.9
L_3	11.1	11.1	11.1
W_2	0.7	0.7	0.7
G_3	1.8	2	2.2
G_4	0.4	0.6	0.8

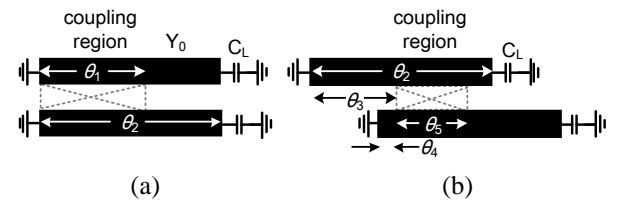


Fig. 7. The equivalent model of half circuit of coupled resonators: (a) resonator 1 and 3, and (b) resonator 1 and 2.

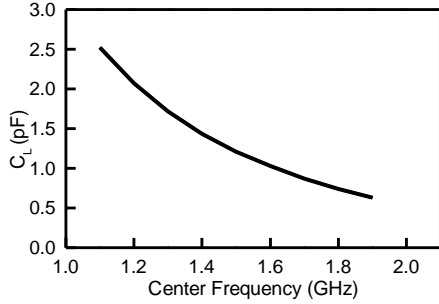


Fig. 8. The calculated C_L versus center frequency.

Coupling coefficients can be analyzed by energy method used in [18, 27]. In the half circuit of resonator 1 and 3 shown in Fig. 7 (a), the electrical energy and magnetic energy stored in each resonator at center frequency can be written as:

$$W_{C_1} = W_{L_1} = W_{C_3} = W_{L_3} = \frac{1}{2}LY_0^2 \int_0^{\theta_1} \cos^2 \theta d\theta, \quad (10)$$

where W_{L_i} ($i = 1, 3$) denotes magnetic energy in i^{th} resonator, W_{C_i} ($i = 1, 3$) denotes electric energy in i^{th} resonator, L is the self-inductance of the microstrip lines. Meanwhile, the magnetic energy stored in the coupling region, W_{L_m} , is expressed as:

$$W_{L_m} = L_m Y_0^2 \int_0^{\theta_1} \cos^2 \theta d\theta. \quad (11)$$

L_m is the mutual inductance between the two lines. Therefore, the magnetic coupling coefficient of this half circuit is obtained by the energy relationship:

$$k_L = \frac{W_{L_m}}{2\sqrt{W_{L_1}W_{L_3}}}. \quad (12)$$

The electrical energy stored in coupling region is,

$$W_{C_m} = -C_m \int_0^{\theta_1} \sin^2 \theta d\theta. \quad (13)$$

C_m is the mutual capacitance between the two lines. So electrical coupling coefficient can be calculated:

$$k_C = \frac{W_{C_m}}{2\sqrt{W_{C_1}W_{C_3}}}. \quad (14)$$

The total coupling coefficient of this half circuit is the sum of k_C and k_L , which is,

$$k = k_L + k_C. \quad (15)$$

As for resonator 1 and resonator 2, the half circuit is shown in Fig. 7 (b). Energy stored in each resonator can be calculated using (10). However, the formula to get energy stored in coupling region should be modified:

$$W_{L_m} = L_m Y_0^2 \int_{\theta_3}^{\theta_2} \cos \theta \cos(\theta - (\theta_3 - \theta_4)) d\theta, \quad (16)$$

$$W_{C_m} = -C_m \int_{\theta_3}^{\theta_2} \sin \theta \sin(\theta - (\theta_3 - \theta_4)) d\theta. \quad (17)$$

Rewrite (12) and (14) as:

$$k_L = \frac{W_{L_m}}{2\sqrt{W_{L_1}W_{L_2}}}, \quad (18)$$

$$k_C = \frac{W_{C_m}}{2\sqrt{W_{C_1}W_{C_2}}}. \quad (19)$$

For the entire resonators, the energy stored in each resonator is doubled, yet the energy stored in the coupling region does not change. As a result, the coupling coefficient between resonator 1 and 2 is equal to $k/2$. The coupling coefficients versus center frequency can be calculated by using (9) ~ (19), as shown in Fig. 9 (a) and Fig. 9 (b). It shows that, the strength of coupling can be controlled by adjusting its physical parameters, and the geometry parameters of Dimension 2 in Table 1 will be implemented in the design so that a 5% constant FBW (CFBW) can be achieved.

Simulation is carried out to verify the above calculation. f_1 and f_2 are the splitting resonant frequencies in the simulation, and the coupling coefficient k can be calculated as:

$$k = \frac{f_1^2 - f_2^2}{f_1^2 + f_2^2}. \quad (20)$$

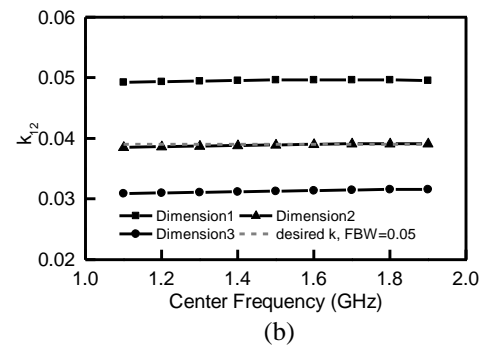
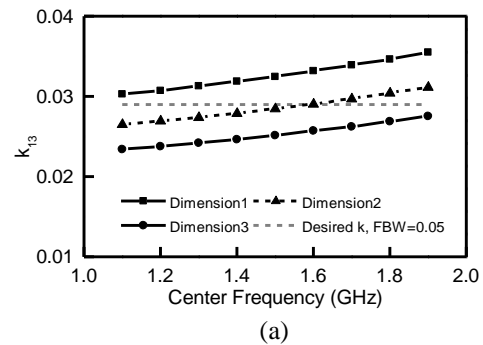


Fig. 9. The calculated results versus center frequency: (a) coupling coefficient k_{12} , and (b) coupling coefficient k_{13} .

Figure 10 shows the simulated loaded capacitance versus center frequency compared with calculated results. It shows that the center frequency can be tuned from 1.1 GHz to almost 2 GHz when C_L is tuned from 0.6 pF to 2.4 pF, and the calculation matches the simulation very well. The slope of coupling coefficient curves is very small, which meets the requirement of

CFBW response.

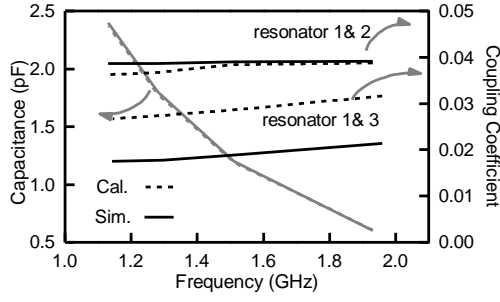


Fig. 10. The tunable capacitance and coupling coefficients versus center frequency of calculation and simulation.

B. External quality factor

External quality factor Q_{ext} mainly influences the bandwidth, roll-off, inband ripple. For tunable filters with CFBW, Q_{ext} needs to be constant. It can be gotten by simulating single loaded circuits shown in Fig. 11 (a) [8], and Q_{ext} can be calculated as:

$$Q_{ext} = \frac{2\pi f_0 \tau_{S_{11}}}{4}, \quad (21)$$

or,

$$Q_{ext} = \frac{f_0}{\Delta f_{\pm\pi/20}} = \frac{f_0}{f_{-\pi/2} - f_{+\pi/2}}, \quad (22)$$

where $\tau_{S_{11}}$ is group delay of S_{11} , $f_{\pi/2}$ and $f_{-\pi/2}$ are frequency point at which the phase of S_{11} of the one-terminal network in Fig. 11 (a) is $\pm\pi/2$, respectively.

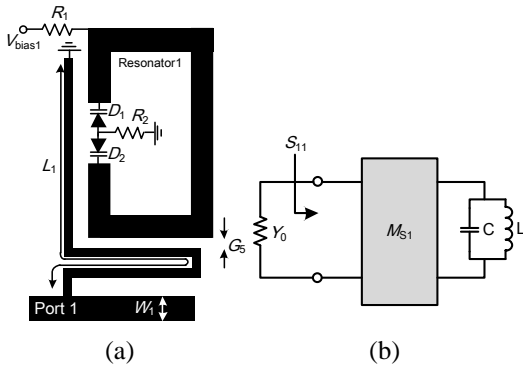


Fig. 11. The simulation circuit and its equivalent model.

$L_1=25$ mm, $W_1=2.2$ mm and other parameters except G_5 are kept as in dimension 2 mentioned earlier. The gap between feedline and resonator can influence Q_{ext} . We simulated four conditions that G_5 in Fig. 11 (a) is 0.05 mm, 0.1 mm, 0.2 mm and 0.3 mm, respectively. The simulated external quality factors are shown in Fig. 12. When G_5 increases, Q_{ext} decreases. This can be explained by the equivalent model in Fig. 11 (b). At $f_{-\pi/2}$ or $f_{\pi/2}$, we have:

$$Y_0 = \left| j \frac{2\pi f_{\pm\pi/2} L M_{S_{11}}^2}{1 - (2\pi f_{\pm\pi/2})^2 L C} \right|, \quad (23)$$

because,

$$S_{11} = \frac{Y_0 - j \frac{\omega L M_{S_{11}}^2}{1 - \omega^2 L C}}{Y_0 + j \frac{\omega L M_{S_{11}}^2}{1 - \omega^2 L C}} \quad (24)$$

By solving equation (23), the denominator of equation (22) is attained:

$$f_{-\pi/2} - f_{+\pi/2} = \frac{M_{S_{11}}^2}{2\pi C Y_0}. \quad (25)$$

Substituting (25) into (22), the external quality of the circuits in Fig. 11 (b) is:

$$Q_{ext} = \frac{C Y_0}{M_{S_{11}}^2 \sqrt{L C}}. \quad (26)$$

when the gap becomes narrower, the coupling is enhanced so $|M_{S_{11}}|$ increases. Equation (26) implies that the external quality factor will decrease if C and L are constant (i.e., f_0 is fixed). When G_5 equals to 0.1 mm, the external quality factor is the closest to the desired value. Q_{ext} is also required to be unchangeable for CFBW filters and the simulated results satisfy this requirement.

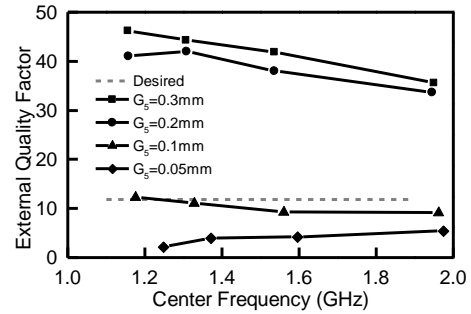


Fig. 12. Simulated external quality factor versus center frequency.

C. Source-load coupling

S_{21} of lowpass prototype filter at $\Omega = \infty$ can be written as [26]:

$$S_{21\infty} = \frac{2|M_{SL}|}{1 + M_{SL}^2}. \quad (27)$$

If the coupling of source-load is enhanced, $|M_{SL}|$ will increase, and $S_{21\infty}$ increases when $|M_{SL}| < 1$. The electric type M_{SL} of this filter is desired to be -0.005 for a 40-dB rejection level. M_{SL} can be simulated by removing all resonators. A two-port network consisting of only two feed lines is obtained as shown in Fig. 13. The image part of Y_{12} of the network is used to extract M_{SL} [28] since Y_{12} denotes a J inverter with $J = \text{Im}(Y_{12})$:

$$M_{SL} = \text{Im}(Y_{12}) \times 50. \quad (28)$$

The simulation is carried out when G_1 (other parameters in Fig. 6 are fixed, $G_2=2.4$ mm) is varying. Figure 14 shows the different $\text{Im}(Y_{12})$. It is obvious that $|\text{Im}(Y_{12})|$ is negatively relative to G_1 . $|\text{Im}(Y_{12})|$ is controllable so it is possible to meet desired $|M_{SL}|$ by adjusting the gap. Finally, G_1 is chosen to be 3.4 mm.

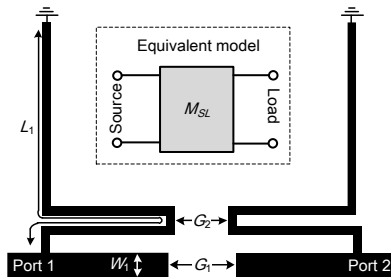


Fig. 13. The simulation circuit of M_{SL} .

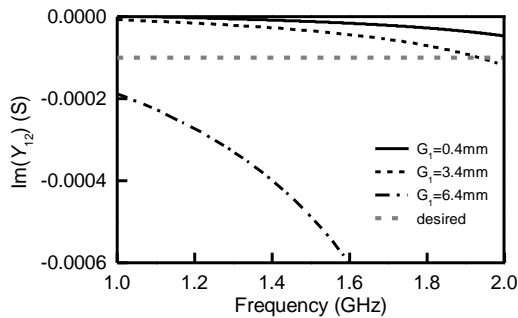


Fig. 14. The simulated imaginary of Y_{12} .

IV. FILTER SIMULATION

A layout of the filter is designed and simulated. The substrate with $h = 0.8$ mm, $\epsilon_r = 2.65$, $\tan\delta = 0.001$, and SMV1405 varactor diode are utilized. Figure 15 shows the S parameters under 0V, 1V, 3V, 7V, 14V and 30V bias voltages.

The center frequency varies from 1086MHz to 1941 MHz which means a 179% tuning range is achieved. As shown in Fig. 16, in the tuning range, fractional bandwidth of this filter keeps almost unchangeable (4.25% ~4.73%) and the insertion loss is less than 6.2 dB. Additionally, there are three transmission zeros besides the passband. One is generated by the utilized trisection structure and is located at lower edge of the passband. The other two transmission zeros exist at each edge of the passband due to the source-load coupling. These zeros can improve the selectivity of this filter. The rejection is approximately 40 dB (higher frequency, estimated by the frequency response's asymptote in Fig. 15) or higher than 50 dB (lower frequency, estimated by the frequency response's stationary point in Fig. 15).

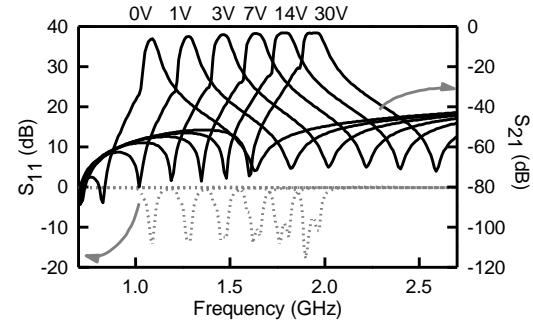


Fig. 15. Simulated S parameters under typical tuning states.

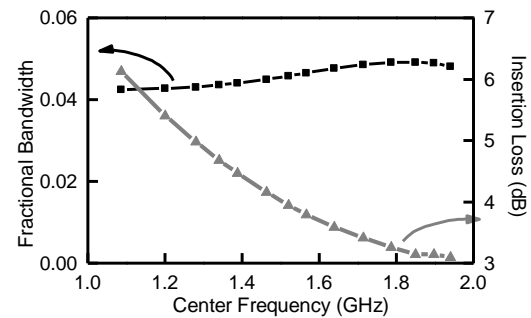


Fig. 16. Simulated insertion loss and fractional bandwidth (FBW).

V. FABRICATION AND MEASUREMENT

The filter is fabricated with an overall size of 36 mm \times 40 mm, as shown in Fig. 17. Three lines on the sectorial pads are connected to the DC supply to bias the varactors. The frequency response of the filter is measured by Agilent E5071C vector network analyzer.

The bias voltage is swept from 0 V to 30 V and $V_{\text{bias1}} = V_{\text{bias2}} = V_{\text{bias3}}$. Figure 18 shows the measured S parameters with 0V, 1V, 3V, 7V, 14V, and 30V bias voltages. The measured frequency responses agree well with the simulation. The tuning ratio of center frequency is approximately 176% (1097 MHz ~ 1936 MHz). Three transmission zeros are generated, and the selectivity of this filter is improved by the transmission zeros. The rejection level is about 40 dB (higher frequency) or higher than 50 dB (lower frequency).

Figure 19 shows the measured insertion loss and fractional bandwidth. The fractional bandwidth maintains 4.1% ~5.3%. It is very narrow, which is useful for channelization. The insertion loss changes from 7.8 dB to 4 dB, which is approximately 1 dB higher than simulation. Besides the inaccuracy in PCB fabrication and the practical discrepancy between varactors, this is mainly due to the errors in welding. The PCB is relatively small in size and the gap between feedlines and resonators is very narrow. So, the solder joint,

which is not small enough to be ignored or to be regarded as ideal connection point, has a great effect on the performance. A similar situation can be seen in [29]. This is not simulated in software and can be solved by precise fabrication or lower frequency application with larger board area. Nonlinear characteristics is usually represented by IIP3 (input 3rd order intercept point), for example [29]. It can be obtained by feeding dual tone signals and measuring the output frequency spectrum. The frequencies of the input signals are set to be $f_0 \pm 1$ MHz. The tested IIP 3 is shown in Fig. 20. Table 2 shows the comparison with several recent cross-coupled tunable filters.

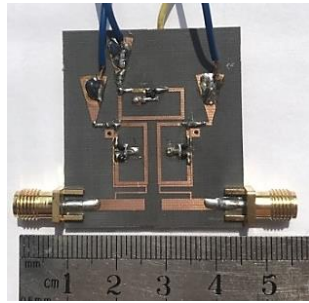


Fig. 17. The photograph of the fabricated filter.

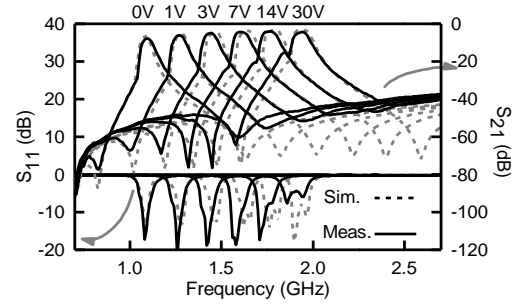


Fig. 18. The measured S parameters.

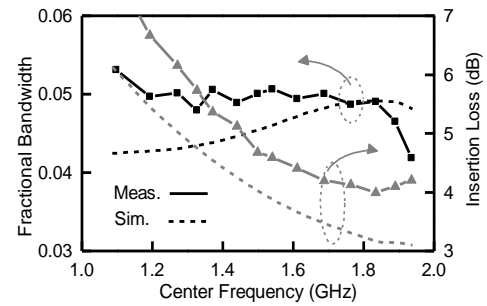


Fig. 19. The measured insertion loss and FBW of this filter.

Table 2: Comparison with recent cross-coupled tunable filters

Reference	Tuning Range (GHz)	Insertion Loss (dB)	Bandwidth	Number of Zeros
[13]	1.11~1.51	3.6~4.2	29±3MHz*, 1.8%~2.6%*	2
[14]	1.15~2	3.6~2.4	114±4MHz*, 9.9%~5.7%*	2
[15]	1.5~1.75	4.5~11	variable	2
[16]	1.25~2.1	3.5~8.5@FBW=4% 3.5~6.5@FBW=5.5%	variable	2
[19]	0.41~0.82	<6.5	9±1%	1
[30]	0.95~1.46	1.8~3.6	12.5±2%	3
[31]	1.36~1.78	2.8~5	93±7 MHz	2
This work	1.097~1.936	7.8~4	4.7±0.6%	3

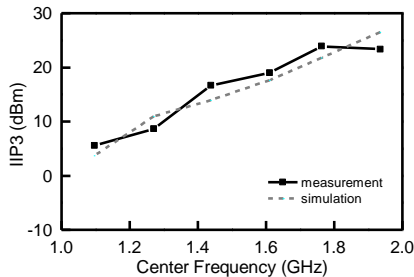


Fig. 20. The measured IIP3 compared with simulation.

It should be noted that the default bandwidth is 3dB bandwidth while the marked data using the symbol * is 1 dB bandwidth in Table 2. Different from the 3rd order filter in [30] with 3 transmission zeros, this

crossed coupled filter does not require additional coupling coefficient tuning elements. This is also an advantage when competing with 4th order filter in [15, 16]. Filter in [31] do not need additional capacitors, either, but it needs two different bias voltage values while in this filter only need one bias voltage value.

VI. CONCLUSION

In this paper, a cross coupled tunable trisection filter with source-load coupling is proposed. All magnetic coupling is employed in trisection structure while source and load are electrically coupled. Three transmission zeros that can effectively improve the frequency selectivity are generated due to the crossed coupled topology. *M* matrix is used to guide this design. The phase performance of the resonator is studied then

the computing formula of S parameters based on M is modified for this resonator. Energy relationship is utilized to analyze the coupling coefficients, which proves that the designed structures are able to satisfy the requirements of CFBW. According the theoretical analysis, coupling coefficients can be controlled and meet the desired values. Source-load coupling, and external quality factor are studied, optimized by simulation. The filter is fabricated on F4B-2 substrate and measured by a vector network analyzer. The measurement matches the simulation well. The tuning range is 1097 MHz to 1936 MHz, meaning that a 176% tuning ratio is achieved. The fractional bandwidth is keeping about 5%. In tuning range, the insertion loss varies from 7.8 dB to 4 dB.

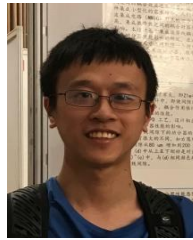
ACKNOWLEDGMENT

This work is supported by the National Natural Science Foundation of China (NSFC) under Grant 61771408, 61401375, 61531016, the Fundamental Research Funds for the Central Universities under Grant 2682014RC24, and the Sichuan Provincial Science and Technology Important Projects under Grant 2018GZ0139, 2017GZ0110.

REFERENCES

- [1] S. Nam, B. Lee, C. Kwak, and J. Lee, "A new class of k-band high-q frequency-tunable circular cavity filter," *IEEE Transactions on Microwave Theory and Techniques*, vol. 66, no. 3, pp. 1228-1237, 2018.
- [2] B. Yassini, M. Yu, and B. Keats, "A ka-band fully tunable cavity filter," *IEEE Transactions on Microwave Theory and Techniques*, vol. 60, no. 12, pp. 4002-4012, 2012.
- [3] H. Aghayari, N. Komjani, and N. M. Garmjani, "A novel integrated corrugated waveguide bandpass filter," *Applied Computational Electromagnetics Society Journal*, vol. 27, no. 1, pp. 67-73, Jan. 2012.
- [4] G. Zhang, J. P. Wang, H. Gu, and X. Xu, "60-ghz 3-d cavity bandpass filter for v-band gigabit wireless systems," *Applied Computational Electromagnetics Society Journal*, vol. 29, no. 11, pp. 928-933, Nov. 2014.
- [5] S. Zhang, L. Zhu, and R. Weerasekera, "Synthesis of inline mixed coupled quasi-elliptic bandpass filters based on $\lambda/4$ resonators," *IEEE Transactions on Microwave Theory and Techniques*, vol. 63, no. 10, pp. 3487-3493, 2015.
- [6] A. Anand and X. Liu, "Reconfigurable planar capacitive coupling in substrate-integrated coaxial-cavity filters," *IEEE Transactions on Microwave Theory and Techniques*, vol. 64, no. 8, pp. 2548-2560, 2016.
- [7] Y. C. Chiou and G. M. Rebeiz, "Tunable 1.55 - 2.1 ghz 4-pole elliptic bandpass filter with bandwidth control and > 50 db rejection for wireless systems," *IEEE Transactions on Microwave Theory and Techniques*, vol. 61, no. 1, pp. 117-124, 2013.
- [8] J. Hong, *Microstrip Filters for RF Microwave Applications*, 2nd Edition, NY:Wiley, New York, 2001.
- [9] T. Saito, S. Kodama, S. Ohshima, and A. Saito, "Design of high power handling filter using cascaded quadruplet superconducting bulk resonators," *IEEE Transactions on Applied Superconductivity*, vol. 28, no. 4, pp. 1-4, 2018.
- [10] X. Jun, H. Wei, and C. Zhe, "A compact quarter-wavelength stepped-impedance resonator bandpass filter with source-load coupling," *2015 IEEE International Wireless Symposium (IWS 2015)*, pp. 1-4, Mar. 30-Apr. 1, 2015.
- [11] B. Liu, Z. Guo, X. Wei, Y. Ma, R. Zhao, K. Xing, and L. Wu, "Quad-band bpf based on slrs with inductive source, and load coupling," *Electronics Letters*, vol. 53, no. 8, pp. 540-542, 2017.
- [12] N. M. Garmjani and N. Komjani, "Improved microstrip folded tri-section stepped impedance resonator bandpass filter using defected ground structure," *Applied Computational Electromagnetics Society Journal*, vol. 25, no. 11, pp. 975-983, Nov. 2010.
- [13] D. Tian, Q. Feng, and Q. Xiang, "A constant absolute bandwidth tunable band-pass filter based on magnetic dominated mixed coupling, and source-load electric coupling," *Journal of Electromagnetic Waves, and Applications*, vol. 30, no. 15, pp. 1953-1963, 2016.
- [14] D. Lu, N. S. Barker, and X. Tang, "A simple frequency-agile bandpass filter with predefined bandwidth and stopband using synchronously tuned dual-mode resonator," *IEEE Microwave and Wireless Components Letters*, vol. 27, no. 11, pp. 983-985, 2017.
- [15] C. Schuster, R. Hu, A. Wiens, M. Maasch, R. Jakob, and H. Maune, "Cross-coupled open-loop resonator bandpass filter with independently tunable center frequency and bandwidth," *2018 IEEE Radio and Wireless Symposium (RWS)*, pp. 52-55, 15-18 Jan. 2018.
- [16] T. Yang and G. M. Rebeiz, "Tunable 1.25-2.1-ghz 4-pole bandpass filter with intrinsic transmission zero tuning," *IEEE Transactions on Microwave Theory and Techniques*, vol. 63, no. 5, pp. 1569-1578, 2015.
- [17] L. Zhou, S. Liu, J. Duan, and M. Xun, "A novel tunable combline bandpass filter based on external quality factor and internal coupling tunings," *Applied Computational Electromagnetics Society Journal*, vol. 33, no. 6, pp. 690-696, Jun.

- 2018.
- [18] Z. Zhao, J. Chen, L. Yang, and K. Chen, "Three-pole tunable filters with constant bandwidth using mixed combline, and split-ring resonators," *IEEE Microwave and Wireless Components Letters*, vol. 24, no. 10, pp. 671-673, 2014.
- [19] M. Y. Fu, Q. Y. Xiang, D. Zhang, D. Y. Tian, and Q. Y. Feng, "A uhf 3rd order 5-bit digital tunable bandpass filter based on mixed coupled open ring resonators," *2016 Progress in Electromagnetic Research Symposium (PIERS)*, pp. 3460-3463, 8-11 Aug. 2016.
- [20] Y. C. Chiou and G. M. Rebeiz, "A tunable three-pole 1.5-2.2-ghz bandpass filter with bandwidth, and transmission zero control," *IEEE Transactions on Microwave Theory and Techniques*, vol. 59, no. 11, pp. 2872-2878, 2011.
- [21] Y. Chu-Chen, and C. Chi-Yang, "Microstrip cascade trisection filter," *IEEE Microwave and Guided Wave Letters*, vol. 9, no. 7, pp. 271-273, 1999.
- [22] R. Kaushik, M. G. Madhan, and K. Jagadeeshvelan, "Design and development of microstrip trisection filter for dth applications," *2014 International Conference on Communication and Network Technologies*, pp. 8-10, 18-19 Dec. 2014.
- [23] Q. Xiang, Q. Feng, and X. Huang, "Tunable bandstop filter based on split ring resonators loaded coplanar waveguide," *Applied Computational Electromagnetics Society Journal*, vol. 28, no. 7, pp. 591-596, Jul. 2013.
- [24] R. J. Cameron, "Advanced coupling matrix synthesis techniques for microwave filters," *IEEE Transactions on Microwave Theory and Techniques*, vol. 51, no. 1, pp. 1-10, 2003.
- [25] R. J. Cameron, "General coupling matrix synthesis methods for chebyshev filtering functions," *IEEE Transactions on Microwave Theory and Techniques*, vol. 47, no. 4, pp. 433-442, 1999.
- [26] R. J. Cameron, "Advanced filter synthesis," *IEEE Microwave Magazine*, vol. 12, no. 6, pp. 42-61, 2011.
- [27] A. C. Guyette, "Alternative architectures for narrowband varactor-tuned bandpass filters," *2009 European Microwave Integrated Circuits Conference (EuMIC)*, pp. 475-478, 28-29 Sept. 2009.
- [28] M. Ohira and Z. Ma, "A parameter-extraction method for microwave transversal resonator array bandpass filters with direct source/load coupling," *IEEE Transactions on Microwave Theory and Techniques*, vol. 61, no. 5, pp. 1801-1811, 2013.
- [29] T. Lin, K. K. W. Low, R. Gaddi, and G. M. Rebeiz, "High-linearity 5.3-7.0 ghz 3-pole tunable bandpass filter using commercial rf mems capacitors," *2018 48th European Microwave Conference (EuMC)*, pp. 555-558, 23-27 Sept. 2018.
- [30] D. Jia, Q. Feng, X. Huang, and Q. Xiang, "Tunable microstrip bandpass filter with constant fractional bandwidth based on cascade triplet topology," *International Journal of Electronics*, vol. 104, no. 10, pp. 1646-1657, 2017.
- [31] S. Wang, Q. Xiang, and Q. Feng, "A fourth order constant absolute bandwidth tunable bandpass filter with cross-coupling," *2019 IEEE MTT-S International Wireless Symposium (IWS)*, pp. 1-3, 19-22 May 2019.



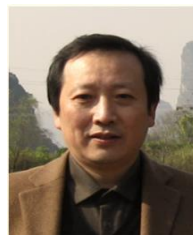
RFIC design.

Mingye Fu received the B.S. degree from Southwest Jiaotong University, Chengdu, China in 2017. He is now studying for Ph.D. degree in Southwest Jiaotong University, focusing on the microwave technology. His research interests include the reconfigurable/tunable RF circuits, MMIC/



Qianyin Xiang received the B.Eng. degree in Communication Engineering, and Ph.D. degree in Communication, and Information Systems from Southwest Jiaotong University (SWJTU), Chengdu, China, in 2005 and 2013, respectively. Xiang is member of *Applied Computational Electromagnetics Society*, *Institute of Electrical and Electronics Engineers (IEEE)*, and *IEEE Microwave Theory and Techniques Society (MTT-S)*. His research interests include Analog/RF circuits and systems, tunable/software defined devices, MMIC/RFIC.

Quanyuan Feng received the M.S. degree in Microelectronics, and Solid Electronics from University of Electronic Science and Technology of China (UESTC), and the Ph.D. degree in Electromagnetic Field and Microwave Technology from Southwest Jiaotong University (SWJTU), Chengdu, China, in 1991 and 2000, respectively. Prof. Feng has been honored as the "Excellent Expert" and the "Leader of Science and Technology" of Sichuan for his outstanding contribution. His research interests include antennas and propagation, integrated circuits design, electromagnetic compatibility and environmental electromagnetics, microwave materials and devices.



An Improved E-Plane Waveguide Power Divider Design for 94GHz Dual-Pyramidal Horn Antenna

Xiaoyan Zhang^{1,2}, Yuting Chen^{1*}, Yan Xie^{1,3}, and Lingfeng Liu¹

¹School of Information Engineering
East China Jiaotong University, Nanchang, 330013, China
xyzhang3129@ecjtu.jx.cn, *cytztgao@qq.com, 195915348@qq.com, lingfeng.liu@163.com

²State Key Laboratory of Millimeter Waves, Nanjing, 210096, China

³Beibo (Xiamen) Intelligent Technology Co., Ltd., Xiamen, 361006, China

Abstract — In this paper, a waveguide power divider is proposed for a 94 GHz horn antenna. The entire structure was machined using 3D printing technology, and is comprised of two pyramidal horn antennas, a one to two E-plane waveguide power divider, three waveguide bends, and a flange. By introducing a wedge-shaped groove, two trapezium taper ports, and a $\lambda/2$ extension on the T-junction of the waveguide, we found improved impedance matching of the power divider, and the two output ports had the same phase. Our results show that the bandwidth of the antenna was 3.2% (3 GHz), its gain was higher than 21.2 dBi with an approximately 10° half power beam width at 94 GHz, and it could be applied to a precise location at close range (6 m to 10 m), which is suitable for automotive radar applications.

Index Terms — 3D printing, automotive, one dimensional range profile, pyramidal horn, waveguide power divider.

I. INTRODUCTION

As a key element in an automotive radar system, anti-collision radar usually works using a millimeter wave band, such as 24 GHz [1] or 77 GHz [2, 3]. These two bands are usually used for Long Range Radar (LRR) and Medium Range Radar (MRR). At a short range, 94 GHz radar is commonly used because it has a small wavelength (3.19 mm) that can detect small obstacles and locate targets more accurately [4, 5].

The antennas for the 94 GHz radar are mainly patch antennas [6], substrate integrated waveguide (SIW) antennas [7, 8], and horn antennas [9, 10]. Generally, in order to achieve a high gain, the patch antenna and the SIW antenna have to be made into an array, inevitably producing a large physical size. In [6] and [7], the maximum size of two antenna arrays was more than 20 times and 30 times that of their respective in order to maintain a gain greater than 20 dBi. However, other

research using horn antenna aperture less than 10 times the wavelength generated more than 20 dBi gain [8, 9]. Traditionally, horn antenna structures include an E-plane sectorial horn, a H-plane sectorial horn [10], a conical horn [11], and a pyramidal horn [12]. Among them, the pyramidal horn antenna can achieve a higher gain with the same aperture size. According to design requirements, different E- and H-plane beams can be obtained by changing the aperture size of the pyramidal horn antenna.

The feed of the horn antenna is mainly a coaxial feed [13], used only for feeding a single horn; a waveguide slot feed [14], which is more suitable for feeding a large waveguide slot array with more than four horns; a waveguide power divider feed [15], which can feed multiple horns and has the advantages of a smaller volume and less transmission loss in high frequencies than the waveguide slot feed. Based on the above general characteristics, the waveguide power divider should be a suitable choice for the 94 GHz horn antenna feed.

The general waveguide power divider is improved on the basis of the traditional E- or H-plane T junction waveguide, which has a discontinuous structure leading to strong reflection and attenuation of electromagnetic waves [16]. In order to reduce the return loss of waveguide power dividers, some structures such as a step impedance transformer [17] and a step-shaped groove [18] have been added in the T junctions to counteract their discontinuity. However, the S_{11} of the power dividers was only reduced to about -25 dB at 94 GHz [19]. Importantly, the two output ports of the divider have opposite phases [20]. In this paper, we propose an E-plane T junction waveguide power divider for a 94 GHz dual-pyramidal horn antenna. A wedge-shaped groove and two trapezium taper ports were added to improve impedance matching. Additionally, a length of $\lambda/2$ was extended to one trapezium taper port to allow the two output ports to share the same phase.

This paper is arranged as follows. In Section II, the configuration of the proposed antenna and the waveguide power divider are described in detail. In Section III, we present our results. In Section IV, a conclusion is made.

II. ANTENNA CONFIGURATION AND DESIGN

A. Waveguide power divider design

The proposed E-plane waveguide power divider is shown in Fig. 1. This was designed based on a T junction waveguide. As Fig. 1 (a) shows, a wedge-shaped groove and the trapezium taper ports were added on the T junctions. The trapezoidal sections have a smaller waveguide height “n” than WR-10 at the T-junction and then taper to the standard WR-10 height at the ports. Each port is a standard rectangular waveguide WR-10. Originally, the two output ports were on both sides, so two 90° bends are added to put the port2 and port3 in the same side as shown in Fig. 1 (b). In addition, a length of $\lambda_g/2$ was extended to the right trapezium taper port. Here λ_g is the guided wavelength, which can be calculated by:

$$\lambda_g = \lambda_0 / \left[1 - \left(\frac{\lambda_0}{\lambda_c} \right)^2 \right]^{1/2}, \quad (1)$$

where, λ_0 and λ_c are the operating wavelength and the cutoff wavelength, respectively.

To investigate the efficiency of the proposed T junction in Fig. 1 (a), the simulated S_{11} was compared in four cases (as shown in Table 1) and, as shown in Fig. 2 (a), the wedge-shaped groove and the trapezium taper port reduce the electromagnetic reflection of the waveguide. Among these characteristics, the introduction of the wedge-shaped groove led to the greatest improvement in impedance matching. Obviously, our proposed T junction has a minimum S_{11} in the whole working frequency band. Thus, the proposed design has better impedance matching than the other three cases.

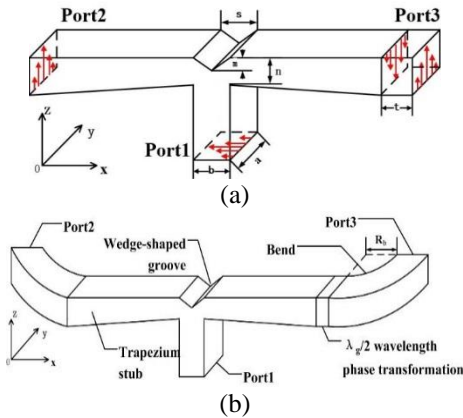


Fig. 1. Configuration of the E-plane T junction waveguide power divider: (a) $a=2.54$ mm, $b=1.27$ mm, $t=2.05$ mm, and (b) overall geometry ($R_b=2$ mm).

Table 1: The different structure of waveguide power divider

Index	Type		Graph
	Wedge Groove	Trapezoidal Port	
Case1	×	×	
Case2	×	✓	
Case3	✓	×	
Case4	✓	✓	

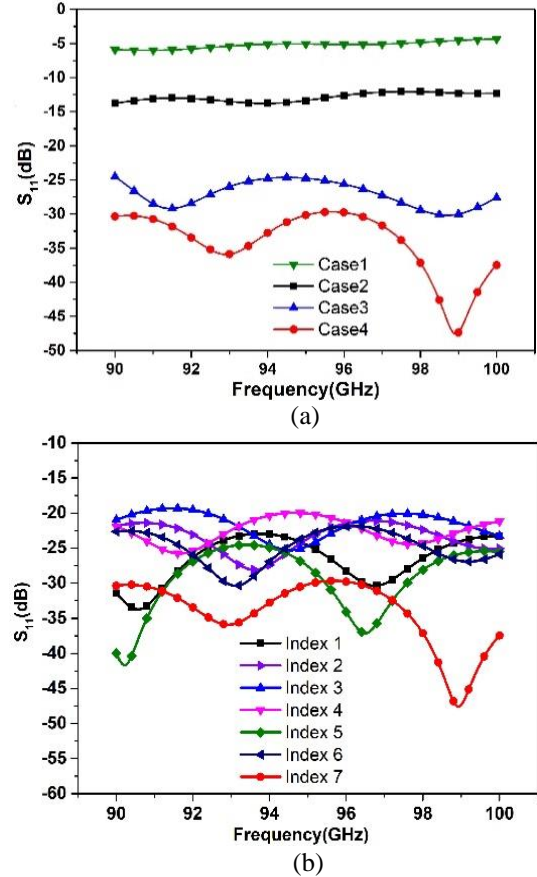


Fig. 2. Simulated S_{11} of the power dividers: (a) with different structure and (b) with different parameters.

The influence of the parameters of the wedge-shaped groove and the trapezium taper ports were studied by changing the values of s , m , and n . Figure 2 (b) illustrates the simulated S_{11} results of the antennas in case 4. We found that the performance of the waveguide was highly sensitive to changes in these parameters. The optimized parameters of the power divider are shown in Table 2, which were obtained by optimization using HFSS15.1 software. Clearly, the S_{11} curve represented by Index 7 is optimal at 94 GHz.

Table 2: The parameter scan




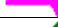


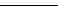
Index	Symbol	Parameter / mm		
		<i>s</i>	<i>m</i>	<i>n</i>
1		0.7	0.6	0.6
2		1.1	0.6	0.6
3		0.9	0.5	0.6
4		0.9	0.7	0.6
5		0.9	0.6	0.5
6		0.9	0.6	0.7
7		0.9	0.6	0.6

Figure 3 (a) gives the simulated S_{11} , S_{21} , S_{31} , and S_{23} of Fig. 1 (b). In the range of 90-100 GHz, S_{11} of our design was less than -30 dB, S_{23} was about -6 dB and its S_{21} and S_{31} were both at -3 dB. We found an excellent impedance matching and a good power allocation of the proposed power divider (Fig. 3 (a)). Figure 3 (b) shows the phases of port 2 and port 3. We found that they were nearly identical.

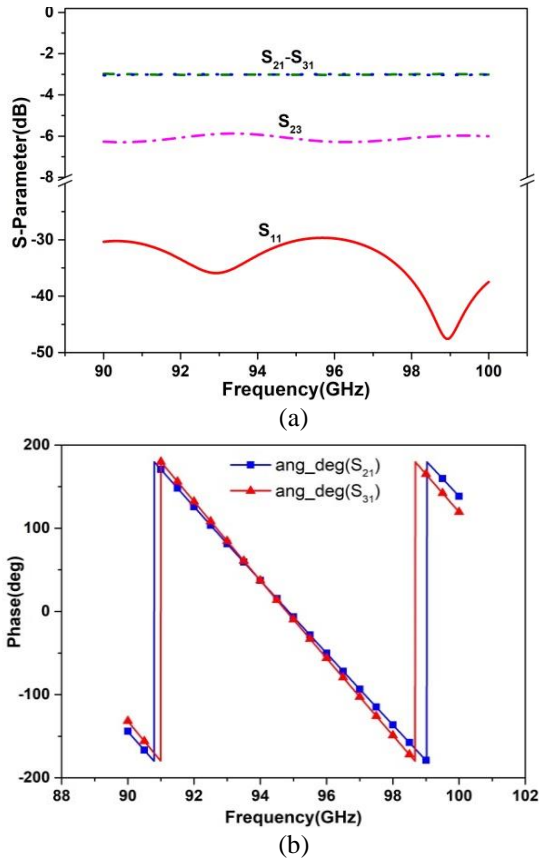


Fig. 3. Simulated results of T junction waveguide power divider: (a) S-parameters and (b) phase of the output ports.

The current distribution of the waveguide power divider is shown in Fig. 4. The wedge groove is used to realize the E-field transition between the output port

waveguide and the main waveguide and to maintain the uniform distribution of E-field in two trapezium taper ports.

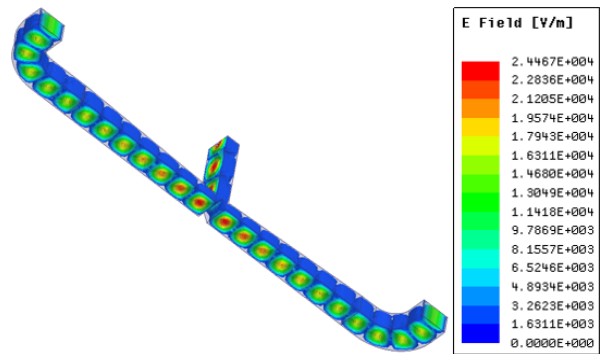


Fig. 4. Simulated E-field distribution at 94 GHz.

B. 94 GHz antenna design

The basic geometry of the proposed 94 GHz antenna is shown in Fig. 5. Its radiation characteristics are essentially a combination of the E- and H-plane sectorial horns. Figures 5 (a) and (b) show the xz-plane (H-plane) and the yz-plane (E-plane) of the pyramidal horn antenna, respectively. The optimal gain calculated for this horn antenna is proposed in [13]. The optimized parameters of the horn antenna can be obtained by:

$$A^4 - aA^3 + \frac{3bG\lambda^2}{8\pi\epsilon_{ap}}A = \frac{3G^2\lambda^4}{32\pi^2\epsilon_{ap}^2}, \quad (2)$$

and are listed in Table 3.

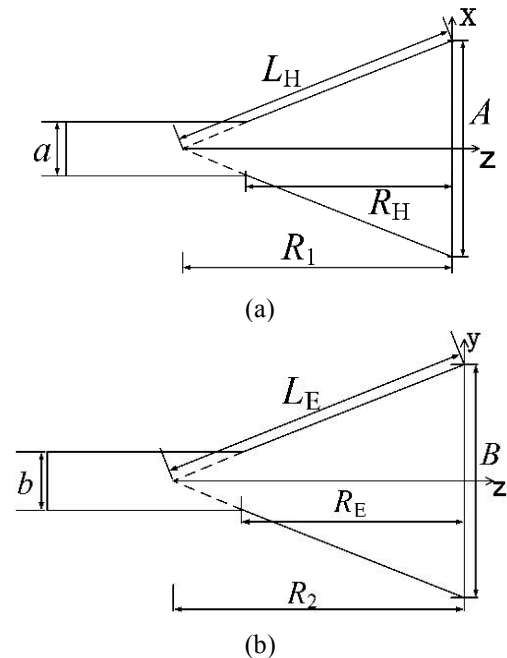


Fig. 5. The pyramidal horn antenna: (a) cross section of the xz-plane and (b) cross section of the yz-plane.

Table 3: Dimensions of the horn antenna

Parameter	Length/mm	Parameter	Length/mm
A	25.06	R_1	65.57
B	20.06	R_2	63.03
a	2.54	L_E	63.82
b	1.27	L_H	66.76
R_E	59.03	R_H	58.95

Figure 6 demonstrates the trend between radiation pattern and length. In order to achieve a >20 dB gain and >10° wider beam to improve the field of view (FOV), the length of the horn antenna was reduced. The length of R_H was 40 mm, while the gain was greater than 20 dBi and HPBW is 9.4° in the E-plane. However, the performance of a single antenna could not meet the design requirements, so a dual-pyramidal horn antenna with waveguide power divider was made.

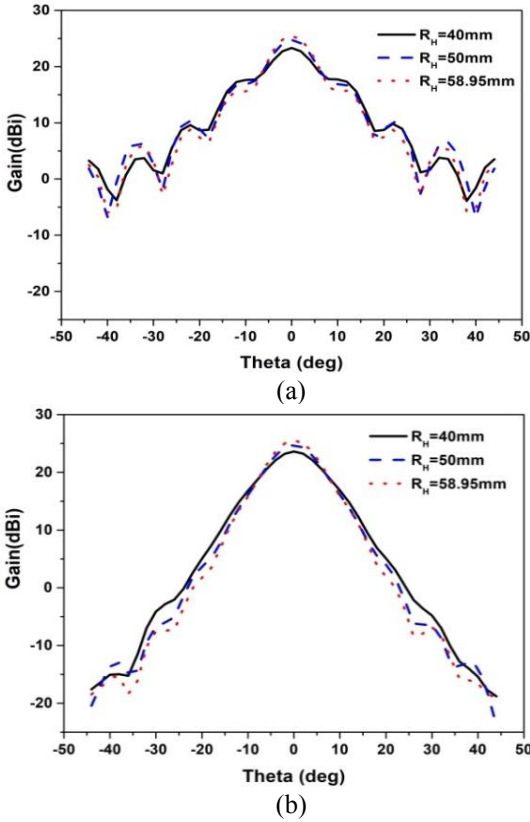


Fig. 6. The influence of length R_H on the proposed antenna: (a) E -plane and (b) H -plane.

The application of the antenna is shown in Fig. 7. H is the height of the antenna, and θ_{min} is the minimal degree in elevation. In the test environment, the height is fixed at a distance of 200 mm from the ground. According to the half power beam width of the antenna, the minimum detection range R_{min} of radar is estimated by:

$$R_{min} = H / \tan \theta_{min}. \quad (3)$$

A wider beam could improve the FOV. The maximum gain required by the radar prototype is greater than 20 dB, therefore reducing the length of the horn antenna would result in a reduction in gain, but we can achieve a smaller physical size, wider beam width and satisfactory gain.

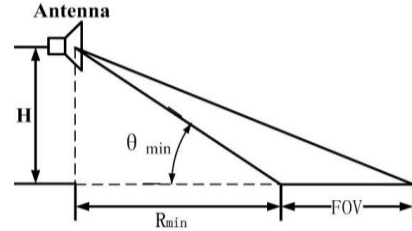


Fig. 7. Scenario for radar detection on the road.

C. Flange and overall structure

Figure 8 shows the 3D structural model of the proposed antenna. Considering that the interface of the radar machine is a wave port, we integrated the design of the antenna and the flange. The material used for the entire structure was *AlSi10Mg* and the model of the machine was a *SLM 125 Metal 3D Printer*. The type of flange was FUGP900. A 90° bend was used to connect the waveguide divider and the flange.

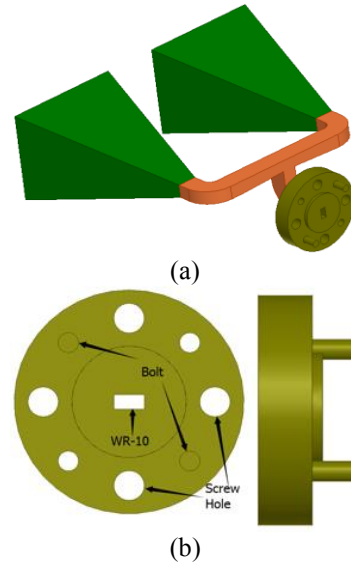


Fig. 8. 3D structure model of antenna: (a) overall structure and (b) flange.

III. EXPERIMENTAL RESULTS AND DISCUSSION

The proposed antenna was fabricated by 3D printing technology. Figure 9 shows the photographs of the fabricated antenna.

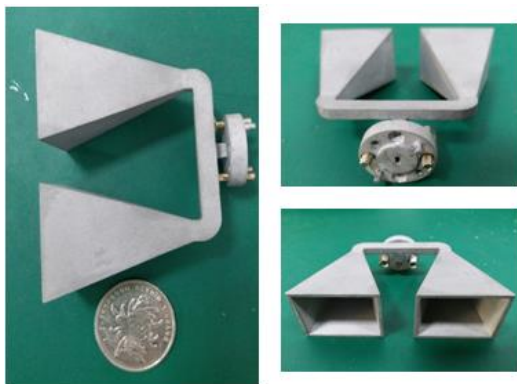


Fig. 9. Fabrication of the proposed antenna.

Figure 10 (a) shows the measured S_{11} of the proposed antenna. We found that the -10 dB impedance bandwidth of the proposed antenna was 3.3% (92.77-95.87 GHz). The antenna has another operating band of 3.4% (81.48-84.32 GHz), but this is not required. Figure 10 (b) shows the measured radiation pattern at 94 GHz. The data reveal that the peak gain of the antenna is higher than 21.2 dBi and the HPBW in E - and H -plane are 10.1° and 2.3° , respectively. The wider E -plane beam has advantages in obtaining higher azimuth resolution, while the narrower H -plane beam provides more accurate range resolution. All tests were performed in a microwave anechoic chamber.

As shown in Fig. 11 (a), the antenna was then assembled on a 94 GHz radar for application testing. A metal triangular trihedral corner reflector (TTCR) was used as a test target. The result of the test environment without TTCR is shown in Fig. 11 (b). It was placed at a distance from radar of both 6 m and 10 m. Figures 11 (c) and (d) show the normalized one-dimensional range profile of the reflector as measured by the radar. We found that although the ground clutter and other objects in the surrounding environment can create disruptive signals, an obvious peak can still indicate the detection of the target, providing evidence that our proposed antenna works on the 94 GHz radar.

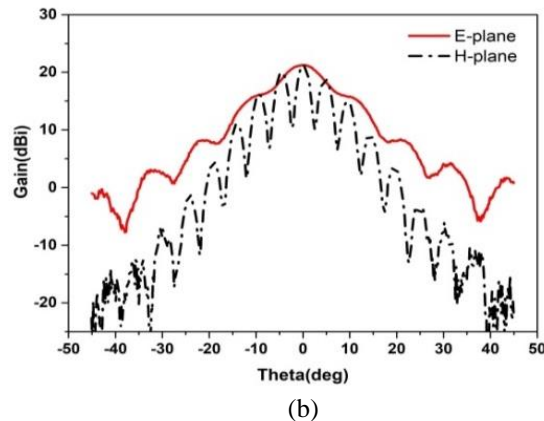
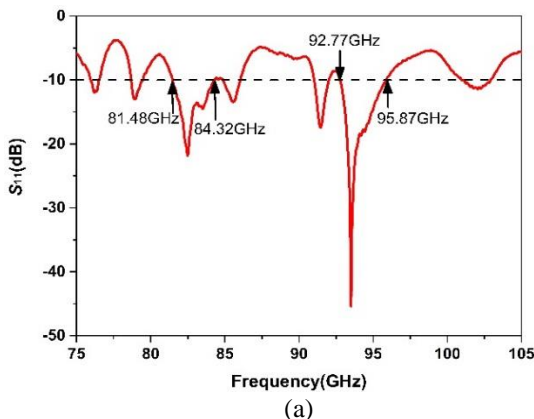
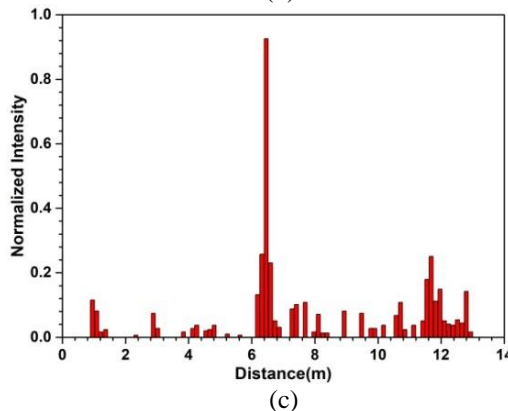
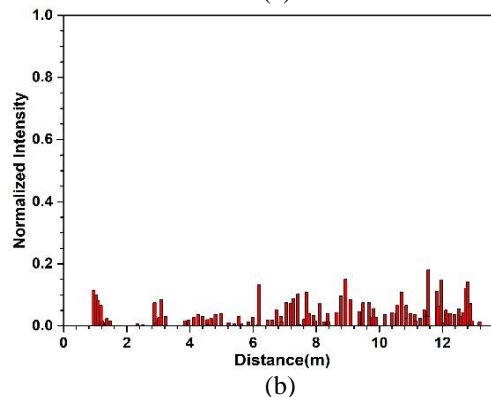
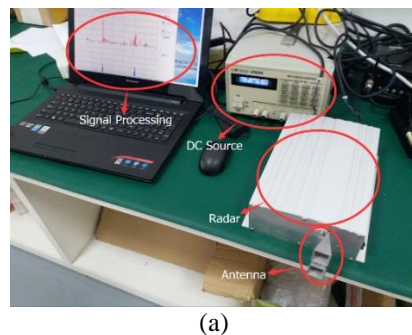


Fig. 10. Measured results of the antenna: (a) S_{11} of the proposed dual-horn antenna and (b) the radiation pattern at 94 GHz.



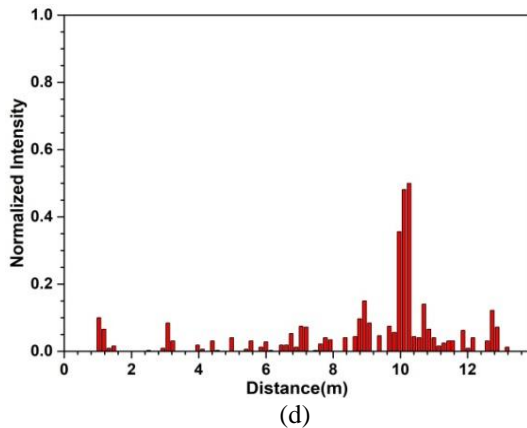


Fig. 11. Experimentally measured and normalized one-dimensional range profile of a metal TTCR. The experimental environment and background radiation measurement are shown in (a) and (b). Results at 6 m and 10 m are shown in (c) and (d).

IV. CONCLUSION

This paper describes the design and measurement of an improved waveguide power divider for dual-pyramidal horn antenna. The use of a waveguide power divider allowed for good impedance matching and matched phase for two output ports. The antenna showed characteristics of high gain, directivity, and a wide beam. The antenna structure created by 3D metal printing technology was strong and stable. A peak gain of 21.2 dBi and 10.1° beam in the E-plane was achieved. The performance of this design was also assessed in outdoor tests. We believe this design is an excellent fit for 94 GHz automotive application.

ACKNOWLEDGEMENT

The authors wish to acknowledge the support of the National Natural Science Foundation of China (Grants #61761017), Natural Science Foundation of Jiangxi Province (Grants #20192BAB207007), the Open Project of State Key Laboratory of Millimeter Wave (Grant #K201829) and Social science planning project of Jiangxi Province (Grant #17BJ40).

REFERENCES

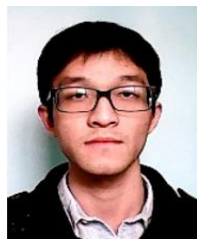
- [1] F. Xu, X. Chen, and X. A. Wang, "K-band microstrip antenna array applied in anti-collision radar," *2010 IEEE 12th International Conference on Communication*, pp. 1240-1243, 2010.
- [2] J. Xu, W. Hong, H. Zhang, G. L. Wang, Y. R. Yu, and Z. H. Jiang, "An array antenna for both long and medium range 77GHz automotive radar application," *IEEE Transactions and Antennas Propagation*, vol. 65, no. 12, pp. 7207-7216, 2017.
- [3] Y. R. Yu, W. Hong, H. Zhang, J. Xu, and Z. H. Jiang, "Optimization and implementation of SIW slot array for both medium and long range 77GHz automotive radar application," *IEEE Transactions on Antennas and Propagation*, vol. 66, no. 7, pp. 3769-3774, 2018.
- [4] D. G. Macfarlane and D. A. Robertson, "A real time close range millimeter wave exhibition radar," *35th International Conference on Infrared, Millimeter, and Terahertz Waves*, pp. 1-2, 2010.
- [5] W. D. Hu, Y. Y. Zhao, H. Ren, J. J. Ji, M. D. Wu, and X. Lv, "Design and implementation of a 94GHz high resolution stepped frequency radar," *2016 IEEE International Conference on Microwave and Millimeter Wave Technology*, vol. 2, pp. 916-918, 2016.
- [6] Y. J. Cheng, Y. X. Guo, and Z. G. Liu, "W-band large-scale high-gain planar integrated antenna array," *IEEE Transactions on Antennas and Propagation*, vol. 62, no. 6, pp. 3370-3373, 2014.
- [7] Y. J. Cheng, W. Hong, and K. Wu, "94 GHz substrate integrated monopulse antenna array," *IEEE Transactions on Antennas and Propagation*, vol. 60, no. 1, pp. 121-129, 2012.
- [8] S. Ramesh and T. R. Rao, "High gain dielectric loaded exponentially tapered slot antenna based on substrate integrated waveguide for V-band wireless communications," *ACES Journal*, vol. 29, no. 11, pp. 870-880, 2014.
- [9] C. Migliaccio, J. Y. Dauvignac, L. Brochier, J. L. Le Sonn, and C. Pichot, "W-band high gain lens antenna for metrology and radar applications," *Electronics Letters*, vol. 40, pp. 1394-1396, 2004.
- [10] J. Wang, J. X. Ge, Y. Zhou, H. Xia, and X. Z. Yang, "Design of a high-isolation 35/94-GHz dual-frequency orthogonal-polarization cassegrain antenna," *IEEE Antennas and Wireless Propagation Letters*, vol. 16, pp. 1297-1300, 2017.
- [11] D. Sun and J. Xu, "Compact phase corrected H-plane horn antenna using slow-wave structures," *IEEE Antennas and Wireless Propagation Letters*, vol. 16, pp. 1032-1035, 2017.
- [12] Y. Wu, B. Zhang, K. Ding, and R. Li, "A metallic 3D printed K-band ridged horn antenna," *ACES Conference: Advanced Manufacturing Technologies for Microwave Devices*, 2017.
- [13] H. B. Zhan, Y. Li, Y. C. Zuo, Q. L. Hu, and Y. H. Wang, "A 10-100-GHz double-ridged horn antenna and coax launcher," *IEEE Transactions on Antennas and Propagation*, vol. 63, pp. 3417-3422, 2015.
- [14] D. H. Park, "Design of millimeter-wave monopole Yagi-Uda-Fed waveguide pyramidal horn antennas," *International Conference on Platform Technology and Service*, pp. 1-5, 2017.
- [15] Y. C. Ou and G. M. Rebeiz, "On-chip slot-ring and high-gain horn antennas for millimeter-wave wafer-scale silicon systems," *IEEE Transactions*

on *Microwave Theory and Techniques*, vol. 59, pp. 1963-1972, 2011.

- [16] T. Sehm, A. Lehto, and A. V. Raisanen, "A large planar 39-GHz antenna array of waveguide-fed horns," *IEEE Transactions on Antennas and Propagation*, vol. 46, pp. 1189-1193, 1998.
- [17] K. C. Hwang, "Design and optimization of a broadband waveguide magic-T using a stepped conducting cone," *IEEE Microwave and Wireless Components Letters*, vol. 19, pp. 539-541, 2009.
- [18] P. Zhao, Q. Y. Wang, F. Zhang, and X. He, "An integratable planar waveguide power divider with anti-phases and full bandwidth," *IEEE Microwave and Wireless Components Letters*, vol. 26, pp. 583-585, 2018.
- [19] S. Y. Hu, K. J. Song, F. Zhang, Y. Zhu, and Y. Fan, "A novel compact wideband four-way W-band waveguide power divider with low insertion loss," *2016 IEEE MTT-S International Microwave Workshop Series on Advanced Materials and Processes for RF and THz Applications*, pp. 1-3, 2016.
- [20] W. J. Feng, W. Q. Che, and K. Deng, "Compact planar magic-T using E-plane substrate integrated waveguide (SIW) power divider and slotline transition," *IEEE Microwave and Wireless Components Letters*, vol. 20, pp. 1-3, 2010.



Xianyan Zhang received the B.S. degree in Applied Physics and M.S. degree in Physical Electronics from Yunnan University, Kunming, China, in 2001 and 2004 respectively, and the Ph.D. degree in Electromagnetic Field and Microwave Technology from Institute of Electronics, Chinese Academy of Sciences in 2007. Her research interests include electromagnetic computation, antenna design and wireless power transmission structure design.



Yuting Chen received the B.S. degree in School of Information Engineering from East China Jiaotong University, Nanchang, China, in 2013, and the M.S. degree in Information and Communication Engineering from East China Jiaotong University, Nanchang, China, in 2019. His research interests include electromagnetic band-gap structure, antenna design.



Yan Xie was born in Nanchang, Jiangxi, China in 1987. He received the B.S. degree in Electronic Information Engineering and M.S. degree in Signal and Information Processing and the Ph.D. degree in Electromagnetic Field and Microwave Technology from Beijing University of Aeronautics and Astronautics, Beijing, China, in 2007, 2010, and 2014, respectively. His research interests include the development of microwave and millimeter wave system, radio frequency circuit and algorithm simulation.



Lingfeng Liu received his B.S. degree in Electronic Information Engineering from Wuhan University, China, in 2005, his M.S. degree in Signal and Information Processing in Communications from Aalborg University, Denmark, in 2007, and his Ph.D. degree in Electrical Engineering from the Universite Catholique de Louvain (UCL) and the Universite Libre de Bruxelles (ULB), Belgium, in 2012. From 2007 to 2012 he was a Research Assistant at ICTTEAM Electrical Engineering (UCL). Since 2012, he has been working as a Lecturer and later Associate Professor at the School of Information Engineering of the East China JiaoTong University, China. His research interests cover channel characterization and modeling in body area networks, MIMO channel estimation and modeling, and cooperative communication networks.

Electric Field and SAR Distribution in the Vicinity of Orthodontic Brace Exposed to the Cell Phone Radiation

Dejan B. Jovanovic¹, Dragan Dj. Krasic², Vladimir B. Stankovic³, Nenad N. Cvetkovic¹, and Dragan D. Vuckovic¹

¹ Faculty of Electronic Engineering
University of Nis, Nis, 18000, Serbia
dejan.jovanovic@elfak.ni.ac.rs, nenad.cvetkovic@elfak.ni.ac.rs, dragan.vuckovic@elfak.ni.ac.rs

² Faculty of Medicine
University of Nis, Nis, 18000, Serbia
dragan.krasic@medfak.ni.ac.rs

³ Faculty of Occupational Safety
University of Nis, Nis, 18000, Serbia
vladimir.stankovic@znrak.ni.ac.rs

Abstract — The aim of this study is to investigate the impact of orthodontic brace on the electric field distribution and amount of the absorbed energy from the cell phone within the teeth. A comparative analysis of the models (child and adult) with and without brace has been carried out due to different morphological and tissue characteristics of child's and adult's head. The 3D realistic models of the child's and adult's head, with the jaw having the orthodontic brace, have been designed. The shapes and features of the child and adult head model, as well as the distance between the electromagnetic source and the exposed object, have an important role in the evaluation of the Specific Absorption Rate (SAR). The applied procedure is based on the numerical solution of the electromagnetic waves propagation equations. The numerical analysis has been performed at the frequency of 3G (0.9GHz). The obtained results are represented within the teeth positioned on the side of the electromagnetic radiation source. Based on the obtained results, one can conclude that the presence of orthodontic brace affects the increase of electric field and SAR within the teeth.

Index Terms— Adult's head model, cellphone, child's head model, electric field distribution, orthodontic braces, specific absorption rate.

I. INTRODUCTION

Orthodontic treatment deals with the correction of inborn and gained anomalies in teeth position. That includes using dental braces in order to ensure alignment in a natural way by the movement of the teeth. The main goal of dental braces usage is to provide the proper

function of teeth and to improve dental health. There are different types of aesthetic brace systems as well as the different materials for producing the orthodontic braces. Most commonly, metal wires are inserted into orthodontic braces made from stainless steel.

According to previous studies, one can find that the metal objects can significantly increase the amount of absorbed energy. The authors in [1] have found that the SAR values can be several times greater in the presence of metal object. The effect of electromagnetic radiation from mobile phone on nickel release from orthodontic brackets has been taken into consideration in study [2]. It is found that the concentration of nickel in the artificial saliva in the exposure group was significantly higher than that of the control group. The level of the nickel released in this investigation was far below the toxic level but maybe enough that can lead to allergic reaction in humans. One of the previously studies [3] reported the involuntary movements of the subjects, which had gold (metal) alloy dental inlay, caused by electromagnetic waves.

As it is well known, cell phones and communication systems have been developed at an astounding rate. This brings significantly increased exposure to electromagnetic (EM) cell phone radiation, which turned the focus towards researching of the impact of electromagnetic waves on human organism and estimation of human health risk.

Despite the concerns about the health effects of long-term exposure to RF radiation, the popularity of wireless devices among the children is growing rapidly. Today's children will certainly have much more exposure to cell phone radiation than adults [4].

The safety measures that prescribe the maximum allowable levels for exposure to electromagnetic fields have been adopted in safety standards [5-8]. Moreover, the electromagnetic field has been characterized as potentially carcinogenic to humans and classified as a group 2B carcinogen [9].

Numerous studies, which refer to the impact of the electromagnetic radiation from the cell phones, deal with the numerical analysis of electric field and SAR distribution within the biological tissues inside the human head [10-17], but not in the oral region.

The main aim of this study is to determine the orthodontic brace impact on the electric field distribution and SAR values inside the certain teeth, while using the cell phone. Moreover, these results take into account the age of the cell phone user. Therefore, the paper deals with the comparative analysis of these results when orthodontic braces are embedded in child's and adult's head model.

Hence, numerical analysis of electric field distribution, as well as values of the absorbed energy in the vicinity of an orthodontic brace (metal object positioned at the surface of teeth), has been performed and presented in this paper. For this purpose, the actual smartphone, as a source of EMF radiation, has been modeled for this study.

The shapes of the head model, its features and the distance between the electromagnetic source and the exposed object, have an important role in the evaluation of the amount of the absorbed electromagnetic energy. The numerical calculations of the electric field and SAR values have been performed by using the Computer Simulation Technology (CST) software package [18]. Numerical analysis has been performed at the frequency of 3G mobile network –0.9GHz.

II. METHOD AND MODELING

A. Model

In order to determine the electric field and SAR distribution in the vicinity of orthodontic brace exposed to the cell phone radiation, the 3D realistic models of the child's and adult's head as well as the jaw with the orthodontic brace have been developed. In addition to the essential differences in size and shape of the head of adults and child [4, 19-26], the differences in morphology and composition of tissues are also included as parameters in this investigation (Fig. 1, Table 1 and Table 2). This primarily refers to the amount of water content in tissues, and the growth of various organs with age [27]. Anatomical and morphological characteristics of head models correspond to the seven year old child and an average adult person (Fig. 1). Both models (child and adult) have the same construction, consisting of the following tissues and biological organs: Cortical Bones, Brain, Cerebrospinal Fluid, Fat, Cartilage, Pituitary Gland, Spinal Cord, Muscle, Eyes, Skin, Tongue and

Teeth. The cross-section of the 3D realistic child's and adult's head model with biological tissues and organs is shown in Fig. 1.

The whole process of head models design was performed in few stages. First, it is necessary to design the external looks of the biological organs and tissues, whose shape replicates the actual human head appearance. Then, they are used as a base for creating the head models for numerical analysis. Also, during the process of creating the head models, it is important that the biological organs are modelled such that they don't overlap each other. In this way, it is possible to consider the boundary conditions at the separation area between two tissues during the propagation of EM waves from one tissue into another.

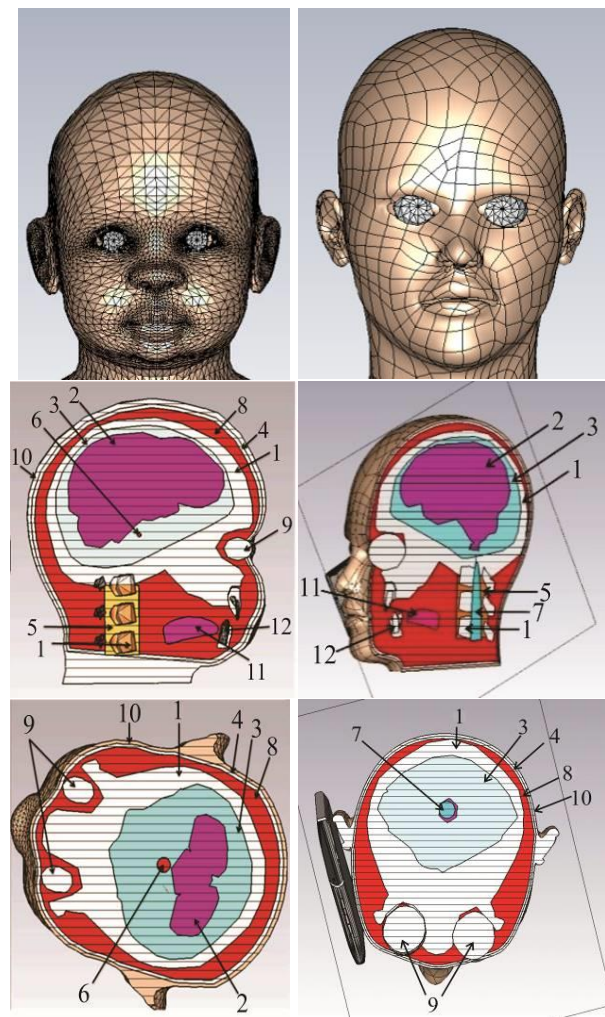


Fig. 1. External appearance and cross-section of the child's head model (left) and adult's head model (right).

The detailed knowledge of the electromagnetic properties (permittivity, conductivity and density) is necessary in order to understand the interaction between

electromagnetic radiation and the exposed object. The effects of propagation, reflection and attenuation of electromagnetic waves within the human body depend on the electromagnetic properties of biological tissues and organs. These parameters are highly dependent on the tissue type and the frequency.

Also, the age dependence of dielectric properties of biological tissues mainly relies on the fact that the permittivity and electrical conductivity can be expressed as a function of water content in the tissue.

The concentration of the water varies depending on the age of tissue. As the content of the water in the tissue increases, the conductivity equally increases. As the frequency increases, the conductivity also increases, but the permittivity decreases. It should be noted that the relative magnetic permeability is assumed to be 1.

The values of electromagnetic properties for an adult person and a child [27-31], for the above mentioned frequencies, are shown in Table 1 and Table 2 respectively. Numerical designations for electromagnetic properties for tissues and organs from Tables correspond to those from Fig. 1.

In addition, the most frequently used material for orthodontic brace is the stainless steel (FeCrNi), containing 18–20% of chromium and 8–10% of nickel [32], due to the stainless steel with the electrical resistivity $\rho=7.2 \times 10^{-7} \Omega\text{m}$, which has been used in simulation.

In order to obtain the most accurate results, the assembled model (orthodontic brace model and jaw model) shown in Fig. 2 (b), has been designed so that its characteristics replicate the real state as close as possible. Jaw model has been designed according to the real one (Fig. 2 (a)) created by the dentist prosthodontist. Generally, the dimensions of the jaw vary and depend on an individual person. In this study, the dimensions of the jaw model (Fig. 2 (b)) are adjusted for the child's head model as well as for the adult's head model. In addition, this jaw model was positioned inside child's and adult's models as shown in Fig. 2 (c).

The model of an actual smartphone has been developed as a source of electromagnetic radiation (Fig. 3). The cell phone model contains the following parts: the display, cell phone housing and planar inverted F antenna (PIFA). The PIFA, as a source of electromagnetic radiation, was modelled with the output power $P=1 \text{ W}$ [33] and the impedance $Z=50 \Omega$. The PIFA antenna consists of a radiating patch, ground plane, feed and shorting strip. The detailed description and PIFA dimensions can be found in [16]. The return loss characteristic of PIFA is shown in Fig. 3.

It should be noted that the smartphone with PIFA antenna, used in this study, is positioned in the microphone area (at the user mouth level). The mobile phone is positioned on the right side of the head model

and slanted towards the face, Fig. 4. This position of mobile phone is typical for conversation scenario.

Table 1: Electromagnetic properties of tissues and organs for an adult person

Biological Tissue		3G 0.9GHz	4G 2.6GHz	5G 28GHz	$\rho[\text{kgm}^{-3}]$	
1	Cortical Bones	ϵ_r	12.45	11.3	5.17	1908
		$\sigma [\text{Sm}^{-1}]$	0.143	0.424	4.94	
2	Brain*	ϵ_r	49.4	44.5	19.2	1046
		$\sigma [\text{Sm}^{-1}]$	1.26	2.2	27.6	
3	Cerebrospinal Fluid	ϵ_r	68.60	66	28.2	1007
		$\sigma [\text{Sm}^{-1}]$	2.410	3.6	43.8	
4	Fat	ϵ_r	11.30	10.8	6.09	911
		$\sigma [\text{Sm}^{-1}]$	0.109	0.28	5.04	
5	Cartilage	ϵ_r	42.70	38.4	13.2	1100
		$\sigma [\text{Sm}^{-1}]$	0.782	1.87	20	
6	Pituitary Gland	ϵ_r	59.70	57	24.5	1053
		$\sigma [\text{Sm}^{-1}]$	1.040	2.09	36.2	
7	Spinal Cord	ϵ_r	32.50	30	13.9	1075
		$\sigma [\text{Sm}^{-1}]$	0.574	1.15	17.6	
8	Muscle	ϵ_r	55.00	52.5	24.4	1090
		$\sigma [\text{Sm}^{-1}]$	0.943	1.84	33.6	
9	Eyes*	ϵ_r	49.60	47.55	20.15	1060
		$\sigma [\text{Sm}^{-1}]$	0.994	2.08	30.87	
10	Skin	ϵ_r	41.40	37.8	16.6	1109
		$\sigma [\text{Sm}^{-1}]$	0.867	1.54	25.8	
11	Tongue	ϵ_r	55.30	52.4	22.7	1090
		$\sigma [\text{Sm}^{-1}]$	0.936	1.92	33	
12	Teeth	ϵ_r	12.50	11.3	5.17	2180
		$\sigma [\text{Sm}^{-1}]$	0.143	0.424	4.94	

* Characteristics of tissues are defined as an average value.

In order to create numerical models with correctly associated electromagnetic properties of biological tissues and organs and determine the spatial distribution of the electromagnetic field (that originates from a cell phone) within the model, the Computer Simulation Technology (CST) software package is used. This software is based on the FIT (Finite Integration Technique) method [34]. The simulation is realized in time domain using Transient Solver included into CST package and the source is modelled as discrete port.

Before any computation it is necessary to define appropriate boundary conditions that define the electromagnetic wave propagation within the environment of the model. Open (add space) boundary conditions, that assume perfectly matched microwave absorber material at the boundary, have been applied in order to insure that the closest fields is not in the contact with the boundary, since the best results are obtained in

that way.

When using the CST software package, the key step before computation is to create the mesh of elements. A finer mesh means a greater number of elements, which makes the results more accurate. On the other hand, a finer mesh requires more powerful hardware and computational time (that can last for days for some applications). Therefore, it is essential to find the proper balance between the result accuracy and computation time. For numerical analysis presented in this paper, it was necessary to perform the test of convergence in order to demonstrate that the results do not depend on appropriate number of required mesh elements.

With mesh created in this way, for computation of electromagnetic field propagation and SAR, the computer resources with the following specifications have been used: RAM-32 GB, processor-4 core (3.20 GHz).

Table 2: Electromagnetic properties of tissues and organs for a child

Biological Tissue		3G 0.9GHz	4G 2.6GHz	5G 28GHz	ρ [kgm ⁻³]	
1	Cortical Bones	ϵ_r	14.79	13.42	6.12	1908
		σ [Sm ⁻¹]	0.180	0.53	6.21	
2	Brain*	ϵ_r	55.24	53.67	23.15	1046
		σ [Sm ⁻¹]	1.39	2.76	34.56	
3	Cerebrospinal Fluid	ϵ_r	81.84	78.74	33.64	1007
		σ [Sm ⁻¹]	2.93	4.38	53.25	
4	Fat	ϵ_r	13.48	12.88	7.26	911
		σ [Sm ⁻¹]	0.132	0.34	6.11	
5	Cartilage	ϵ_r	49.11	44.16	15.18	1100
		σ [Sm ⁻¹]	0.899	2.15	22.3	
6	Pituitary Gland	ϵ_r	62.09	59.28	25.48	1053
		σ [Sm ⁻¹]	1.082	2.17	37.65	
7	Spinal Cord	ϵ_r	38.77	35.79	16.54	1075
		σ [Sm ⁻¹]	0.697	1.39	21.296	
8	Muscle	ϵ_r	62.32	59.48	27.57	1090
		σ [Sm ⁻¹]	1.065	2.08	37.97	
9	Eyes*	ϵ_r	59.17	56.72	24.04	1060
		σ [Sm ⁻¹]	1.212	2.54	37.66	
10	Skin	ϵ_r	51.58	47.09	20.67	1109
		σ [Sm ⁻¹]	1.078	1.91	31.48	
11	Tongue	ϵ_r	55.30	52.4	22.7	1090
		σ [Sm ⁻¹]	0.936	1.92	33	
12	Teeth	ϵ_r	14.79	13.37	6.11	2180
		σ [Sm ⁻¹]	0.180	0.533	6.17	

* Characteristics of tissues are defined as an average value.

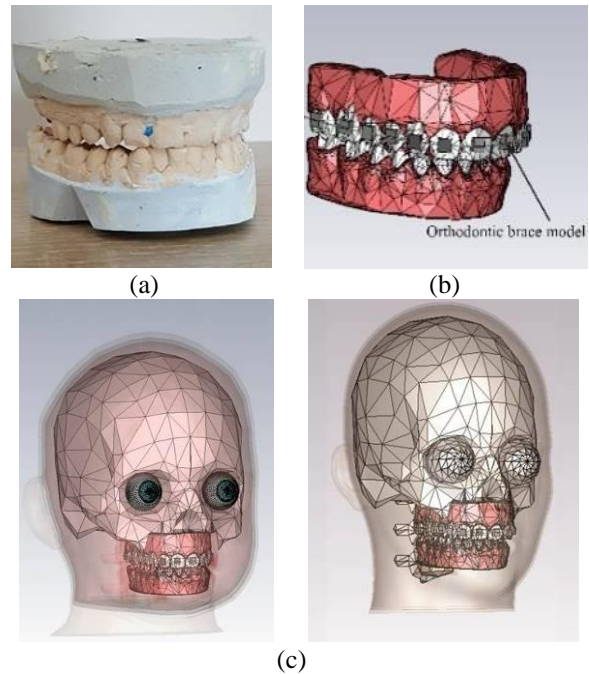


Fig. 2. External appearance of the jaw: (a) artificial human jaw created by dentist prosthetics, (b) assembled model of the jaw and orthodontic brace used for simulation, and (c) position of the assembled model inside the child's head model (left) and adult's head model (right).

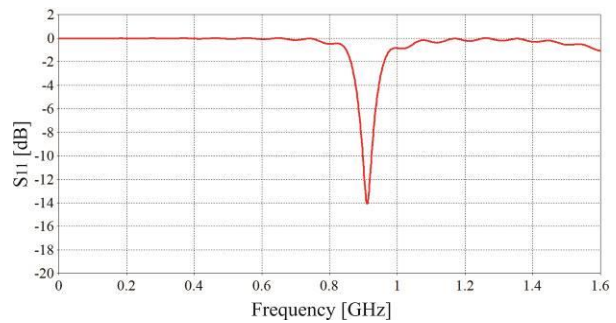


Fig. 3. Return loss of the PIFA antenna (dB).

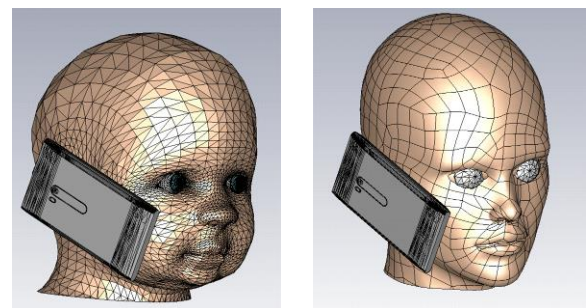


Fig. 4. The external look of the smartphone and its position.

B. SAR calculation

The SAR is a measure of the radio frequency (RF) energy rate absorbed by the body, in terms of watts per kilogram (W/kg) averaged over a small sample of tissue. SAR is defined as the speed of power dissipation normalised by the density of the material, and can be described by the following equation [35]:

$$\text{SAR} = \frac{\sigma}{\rho} |E|^2, \quad (1)$$

where σ is the electrical conductivity (S/m) and ρ is the density of tissue (kg/m^3). It should be also noted that the electric field E (V/m) is the r.m.s. value.

In addition, the averaged SAR can be defined as the ratio of the power absorbed in the tissue and the weight of that biological tissue. The averaged SAR is obtained by integrating SAR value over the observed volume:

$$\text{SAR}_{\text{av}} = \frac{1}{V} \int_V \text{SAR} dV = \frac{1}{V} \int_V \frac{\sigma}{\rho} |E|^2 dV. \quad (2)$$

Mass averaged SAR in this study is calculated for a sample of 1g ($\text{SAR}_{1\text{g}}$) and a sample of 10g ($\text{SAR}_{10\text{g}}$).

III. RESULTS

In this section, electric field and SAR distribution will be shown at the cross-sections of both models (child and adult) at the level of the orthodontic brace. Comparative analysis of the obtained results for models with and without orthodontic brace will be carried out using child head and adult head model.

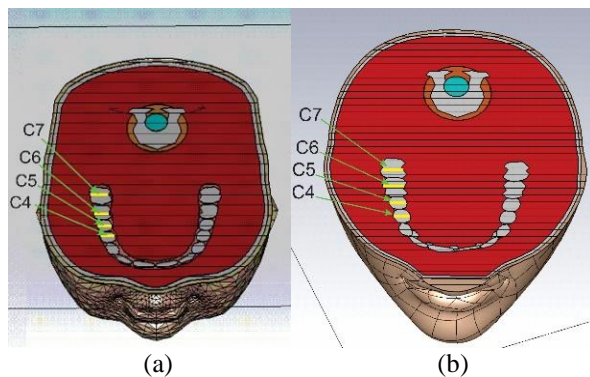


Fig. 5. Cross-section and curves for evaluating electric field and SAR distribution: (a) child and (b) adult.

The obtained results of electric field within the teeth are represented as a function of the distance from the radiation source along the curves shown in Fig. 5. Numerical labels of the curves from Fig. 5 correspond to the teeth labels (Table 3 – Table 5). The results for electric field strength and amount of absorbed energy are represented for the teeth that are on the same side as the

source of electromagnetic radiation (cell phone). These teeth are the most exposed to the electromagnetic radiation. All curves are located in the same planes with the orthodontic brace.

Also it should be noted that the maximum value of electric field as well as SAR value in the colour palette on the right side of the figures is set to be the same for both models and for all frequencies, in order to enable the easier comparison.

A. Electric field distribution

This section deals with a comparative analysis of the electric field distribution in the vicinity of the orthodontic brace, positioned in the child's and adult's model, at the frequency of 3G mobile networks.

It should be mentioned that the allowable values for the electric field are: 41 V/m at 0.9 GHz [5-8].

The spatial distribution of the electric field for the horizontal cross-section located at the mouth level, is shown in Fig. 6.

The peak of electric field strength exists in the vicinity of the orthodontic brace (Figs. 6 (b) and (d)) in the case of both models (child and adult). The obtained results for maximum values of electric field strength within certain teeth, for the models with and without the orthodontic brace, are represented in Table 3 (labels of the teeth correspond to the ones from Fig. 6).

The dependence of the electric field along the curves (Fig. 5) within the teeth, as a function of a distance from the radiation source, for the models with and without the orthodontic brace, is given in Figs. 7 and 8.

According to these figures, the differences in the values of the electric field can be noted. It is evident that the value of the electric field is significantly greater in the presence of an orthodontic brace for both models. Based on the results shown in Figs. 6-8, as well as the results given in Table 3, the overall conclusion is that the presence of an orthodontic brace increases the electric field strength within the teeth.

Also it is noticeable that the electric field strength in the case of a child is higher comparing to the adult case. This was expected due to the differences between the dielectric characteristics and also because of the differences in dimensions.

B. Specific absorption rate

This section presents the impact of orthodontic brace on the SAR values, in the case of the child's head and adult's head model. The dependence of the $\text{SAR}_{1\text{g}}$ and $\text{SAR}_{10\text{g}}$, along the curves within teeth, versus the distance from the radiation source and for different frequencies, is represented.

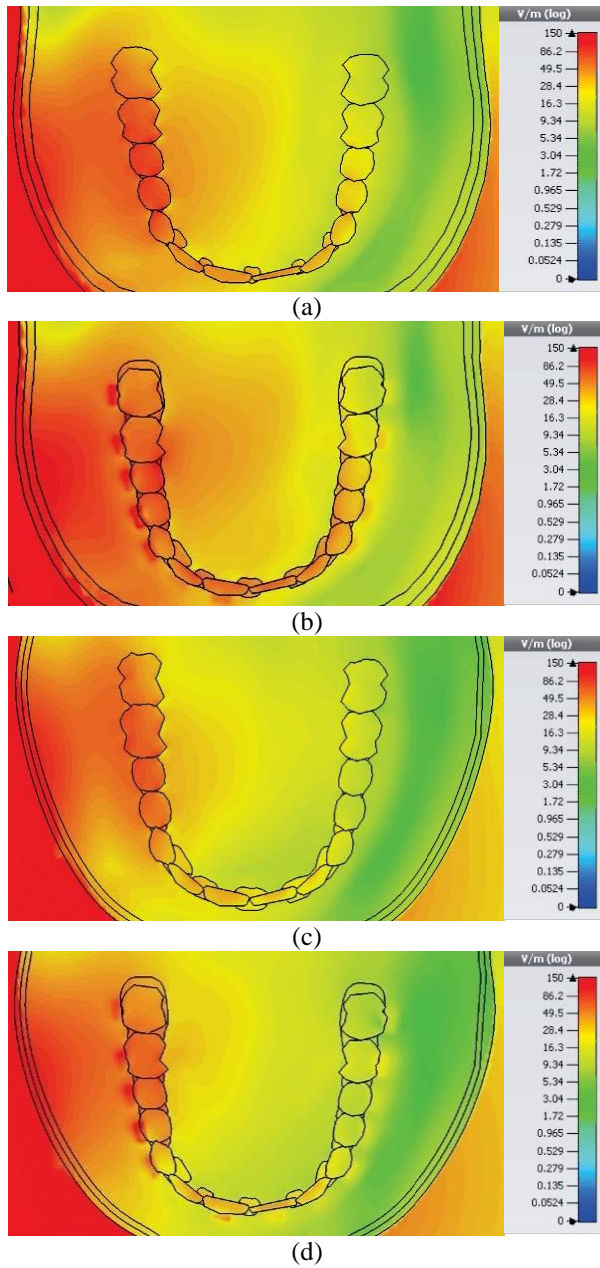


Fig. 6. Spatial distribution of electric field within the models: (a) child without orthodontic brace, (b) child with orthodontic brace, (c) adult without orthodontic brace, and (d) adult with orthodontic brace.

Table 3: Maximum value of the electric field strength within teeth - E [V/m]

Tooth	Child without Orthodontic Brace	Child with Orthodontic Brace	Adult without Orthodontic Brace	Adult with Orthodontic Brace
No. 4	79.89	128.93	52.92	115.88
No. 5	87.41	223.76	71.63	129.94
No. 6	83.25	194.52	67.54	121.62
No. 7	62.67	130.07	46.49	90.01

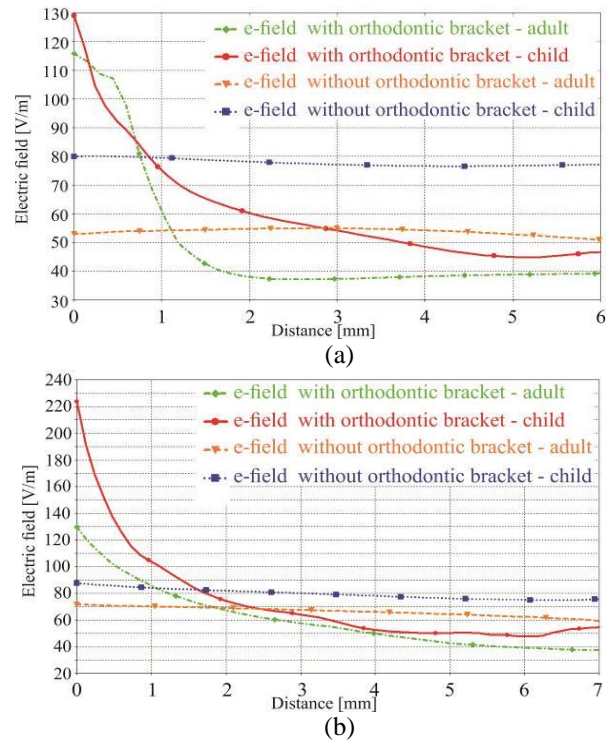


Fig. 7. Electric field strength along the curves: (a) C4 and (b) C5.

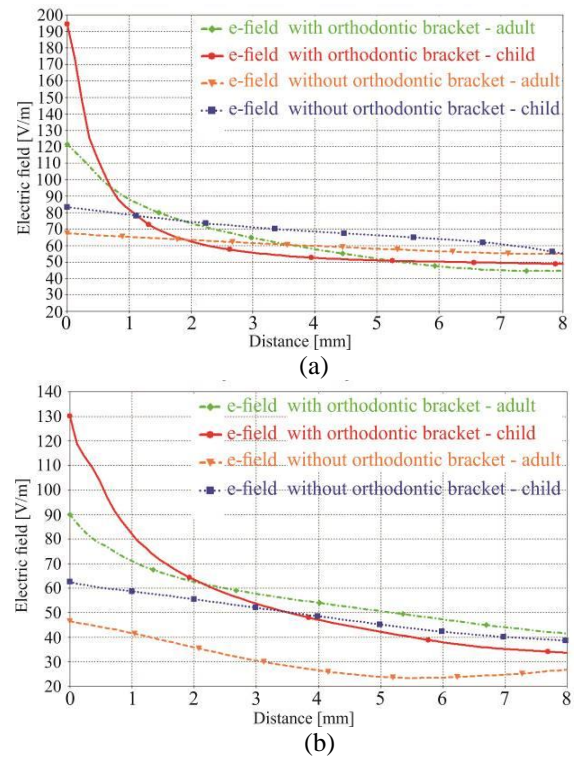


Fig. 8. Electric field strength along the curves: (a) C6 and (b) C7.

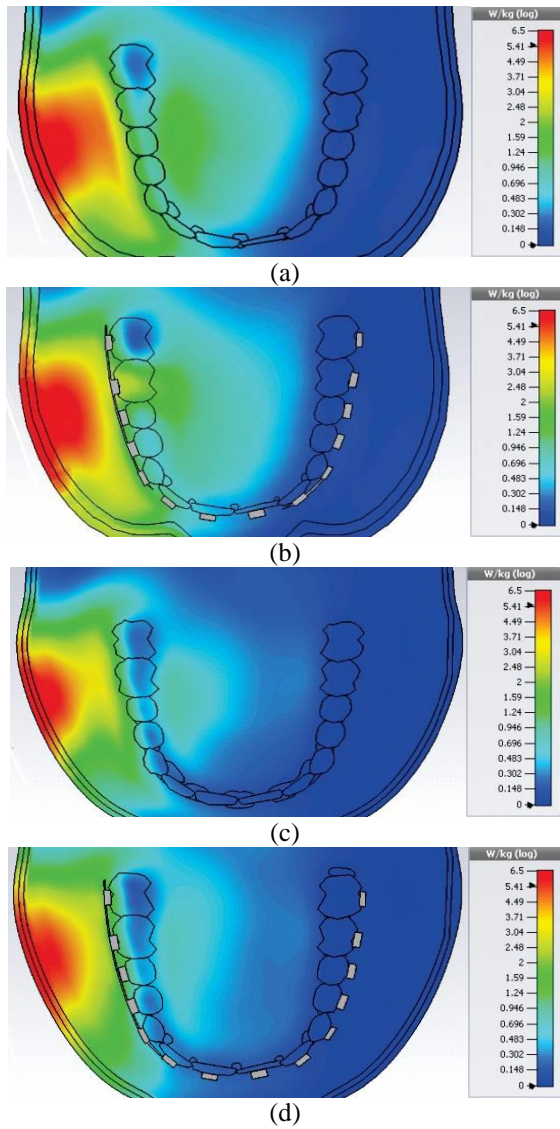


Fig. 9. Spatial distribution of SAR_{1g} : (a) child without orthodontic brace, (b) child with orthodontic brace, (c) adult without orthodontic brace, and (d) adult with orthodontic brace.

It should be mentioned that, according to appropriate safety standards, the limit of SAR for public exposure from cell phones is 1.6 watts per kilogram (1.6 W/kg) for SAR_{1g} and 2 watts per kilogram (2 W/kg) for SAR_{10g} [5].

The spatial distribution of SAR averaged for 1g (SAR_{1g}) within the models (with and without orthodontic brace) in the case of child and adult is represented in Fig. 9. The maximum value of SAR in the colour palette is set to be the same for both models.

The dependence of the SAR_{1g} and SAR_{10g} along the curves within teeth, versus the distance from the radiation source, for the model (child and adult) with and without the orthodontic brace, is given in Figs. 10-13.

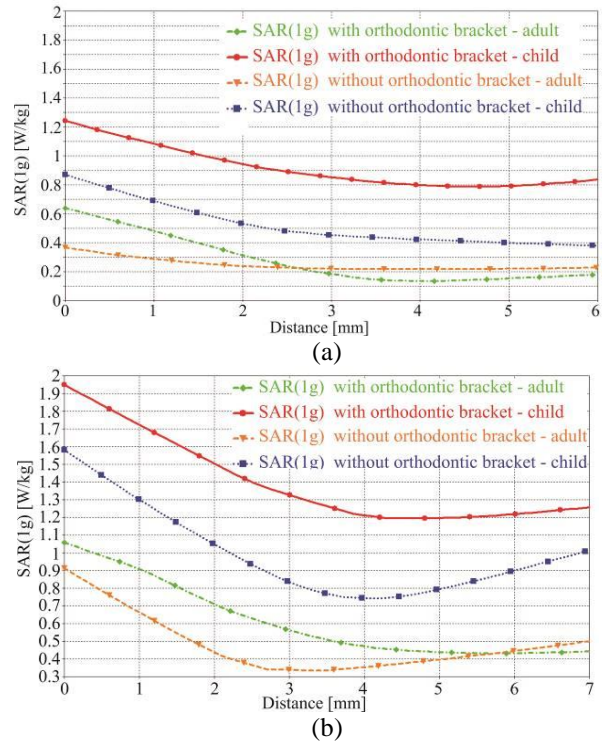


Fig. 10. Specific absorption rate - SAR_{1g} along the curves: (a) C4 and (b) C5.

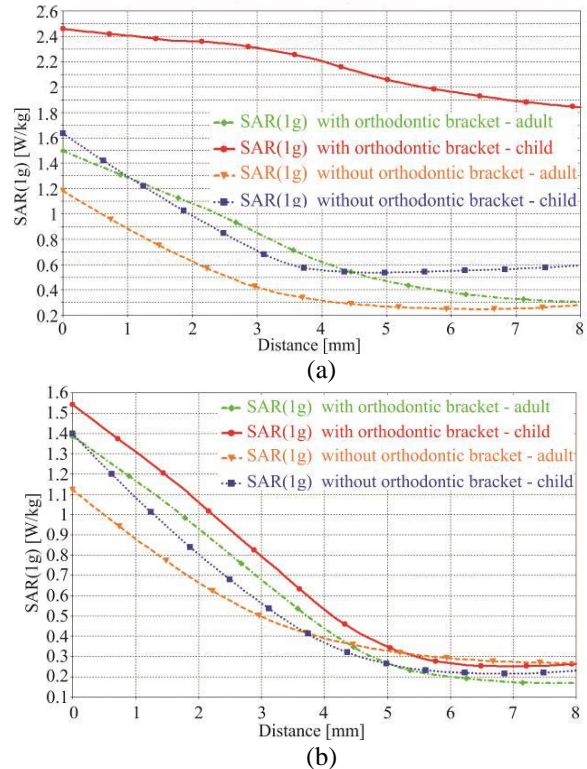


Fig. 11. Specific absorption rate - SAR_{1g} along the curves: (a) C6 and (b) C7.

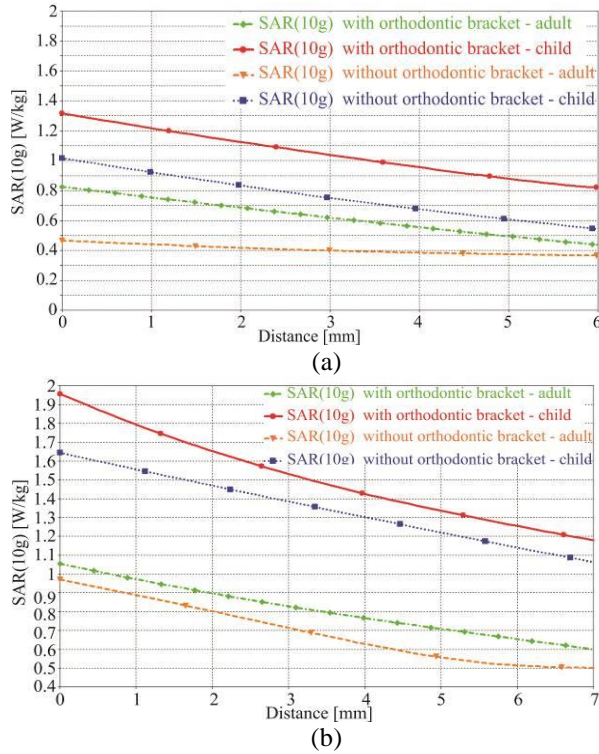


Fig. 12. Specific absorption rate - SAR_{10g} along the curves: (a) C4 and (b) C5.

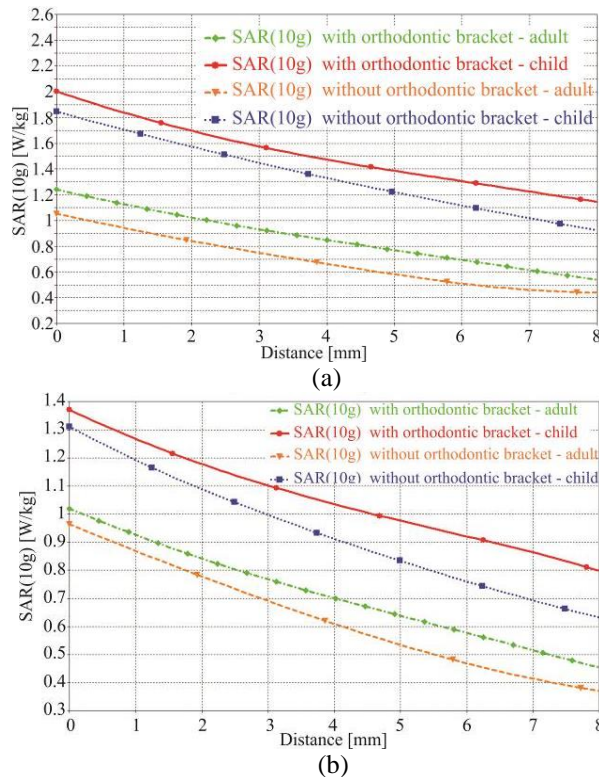


Fig. 13. Specific absorption rate - SAR_{10g} along the curves: (a) C6 and (b) C7.

The maximum values of the SAR_{1g} and SAR_{10g} within certain teeth, for the models with and without orthodontic brace, are represented in Tables 4 and 5, respectively.

Table 4: Maximum value of SAR_{1g} [W/kg]

Tooth	Child without Orthodontic Brace	Child with Orthodontic Brace	Adult without Orthodontic Brace	Adult with Orthodontic Brace
No. 4	0.88	1.27	0.37	0.64
No. 5	1.58	1.95	0.91	1.06
No. 6	1.73	2.46	1.18	1.49
No. 7	1.4	1.55	1.14	1.38

Table 5: Maximum value of SAR_{10g} [W/kg]

Tooth	Child without Orthodontic Brace	Child with Orthodontic Brace	Adult without Orthodontic Brace	Adult with Orthodontic Brace
No. 4	1.01	1.32	0.46	0.825
No. 5	1.64	1.96	0.95	1.05
No. 6	1.84	2.01	1.05	1.24
No. 7	1.21	1.37	0.96	1.02

Based on the results represented in Figs. 10-13 and results shown in Table 4 and Table 5, the increase of the SAR_{1g} and SAR_{10g} values can be noticed in the presence of the orthodontic brace. Also, it can be seen that the SAR_{1g} and SAR_{10g} values are higher in the case of child's head model.

V. DISCUSSION

According to the obtained results for the electric field distribution, in the vicinity of the orthodontic brace exposed to the cell phone radiation, the maximum value of electric field is greater in the presence of the orthodontic brace in the case of child as well as in the case of adult head model. This can be seen from Figs. 6 – 8 and Table 3.

Based on the results given in Table 3, one can see that the highest value of the electric field strength was found in the tooth No. 5. This value in the case of child is 223.76 V/m, which is about 155% higher comparing to the child model without orthodontic brace and 72% higher comparing to the adult with orthodontic brace (129.94 V/m).

The significant deviation of the electric field strength can be also noted within the tooth No. 6. Nevertheless, the impact of orthodontic brace on the electric field cannot be neglected within other teeth.

Since the referent value for the electric field, prescribed by adequate standards at 0.9 GHz, is 41 V/m, comparing the results obtained by numerical calculation with values prescribed by safety standards, it is evident that obtained results exceed the referent levels inside all teeth in both models (with and without the orthodontic brace). However, it should be kept in mind that in the case of model with orthodontic brace the values are many times greater than the allowable values.

Regarding the obtained results for SAR within the teeth, in the presence of an orthodontic brace, a significant increase in the amount of absorbed energy can be observed. The maximum of SAR_{1g} occurs in the tooth No. 6 in the case of a child (2.46W/kg). This value is about 65% higher comparing to the adult with orthodontic brace and 45% higher comparing to the results obtained for a child without orthodontic brace. In this tooth and tooth No. 5, the SAR_{1g} overcomes the safety values but only in the case of child in the presence of the orthodontic brace. The amount of absorbed energy inside the other teeth satisfies basic restriction. However, the increase in the amount of absorbed energy in the presence of an orthodontic brace is not negligible.

Based on the results, obtained for SAR_{10g} , (Table 5) it can be noticed that the SAR_{10g} overcomes the safety values but only in tooth No. 6 and only in the case of child with the orthodontic brace. Hence, the increase in the SAR_{10g} value can be noticed in the presence of the orthodontic brace.

VI. CONCLUSION

This study deals with the electric field distribution and the amount of absorbed energy within teeth, in the presence of an orthodontic brace, exposed to the electromagnetic radiation from the cell phone. The numerical calculation was performed for the frequency of 3G mobile network (0.9GHz).

The comparative analysis is presented for two models, child's head model and adult's head model.

Based on the obtained results, one can conclude that the presence of orthodontic brace causes increase of electric field and SAR within the teeth. In some cases, those values overcome referent limits for electric field strength, i.e., safety limits for SAR values. In addition, it is important to note that the obtained results are valid for investigated specific scenario, which is based on simulation model presented in this study.

Also, according to the results obtained by numerical calculation using child head model as well as adult head model, it can be concluded that certain variations in the values of electric field and SAR exist.

Because of the mentioned before and the fact that each standard contains specific safety limits of exposure to electromagnetic fields but they have been developed based on the research for adults, it should be established if they are sufficiently valid also in case of children.

The future researches should be focused on the impact of orthodontic brace on the electric field strength and amount of absorbed energy at the frequency of LTE-4G, and the latest generation of mobile networks – 5G.

The results obtained in this research can represent a good base for multidisciplinary studies involving medical professionals. It is the proper way of studying the biological effects due to the influence of orthodontic

brace presence exposed to the electromagnetic radiation from a cell phone.

ACKNOWLEDGMENT

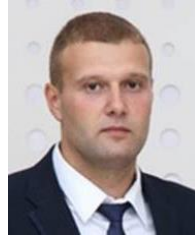
The research presented in this paper is financed by the Ministry of Education, Science and Technological Development of the Republic of Serbia under the project TR33035.

REFERENCES

- [1] W. G. Whittow, R. M. Edwards, C. J. Panagamuwa, and J. C. Vardaxoglou, "Effect of tongue jewellery and orthodontist metallic braces on the sar due to mobile phones in different anatomical human head models including children," *2008 Loughborough Antennas and Propagation Conference*, Loughborough, UK, pp. 293-296, 2008.
- [2] S. M. Mortazavi, M. Paknahad, I. Khaleghi, and M. Eghlidospour, "Effect of radiofrequency electromagnetic fields (RF-EMFS) from mobile phones on nickel release from orthodontic brackets: An in vitro study," *International orthodontics*, vol. 16, no. 2, pp. 562-570, 2018.
- [3] Y. Fujii, "Gold alloy dental inlay for preventing involuntary body movements caused by electromagnetic waves emitted by a cell phone," *Open Journal of Antennas and Propagation*, vol. 2, no. 4, pp. 37-43, 2014.
- [4] O. P. Gandhi, "Yes the children are more exposed to radiofrequency energy from mobile telephones than adults," *IEEE Access*, vol. 3, pp. 985-988, 2015.
- [5] Council of the European Union, "Council recommendation of 12 July 1999 on the limitation of exposure of the general public to electromagnetic fields (0 Hz to 300 GHz)," (1999/519/EC 1999), *Official Journal of European Communities*, L 199/59-70, 1999.
- [6] IEEE - Institute of Electrical and Electronics Engineers, "IEEE Standard for safety levels with respect to human exposure to radio frequency electromagnetic fields, 3 kHz to 300 GHz," *Inc. C95.1-2005*, 2006.
- [7] Ministarstvo prostornog planiranja i životne sredine Republike Srbije [Ministry of Spatial Planning and Environment of the Republic of Serbia], "Pravilnik o granicama izlaganja nejonizujućim zračenjima [Rulebook on limits of exposure to non-ionizing radiation]," *Službeni glasnik Republike Srbije [Official Gazette of Republic of Serbia]*, 104/09, [in Serbian], 2009.
- [8] International Commission on Non-ionizing Radiation Protection, "ICNIRP statement on the guidelines for limiting exposure to time-varying electric, magnetic, and electromagnetic fields (up

- to 300 GHz,” *Health Physics*, vol. 74, no. 4, pp. 494-522, 1998.
- [9] International Agency for Research on Cancers, “IARC classifies radiofrequency electromagnetic fields as possibly carcinogenic to humans,” *Press Release*, no. 208, 2008.
- [10] R. Hirt and G. Schmid, “Numerical analysis of specific absorption rate in the human head due to a 13.56 MHz RFID-based intra-ocular pressure measurement system,” *Physics in Medicine & Biology*, vol. 58, no. 18, pp. 267-277, 2013.
- [11] F. Schaumburg and F. A. Guarnieri, “Assessment of thermal effects in a model of the human head implanted with a wireless active microvalve for the treatment of glaucoma creating a filtering bleb,” *Physics in Medicine & Biology*, vol. 62, no. 9, pp. 191-203, 2017.
- [12] C. Buccella, V. De Santis, and M. Feliziani, “Numerical prediction of SAR and thermal elevation in a 0.25-mm 3-D model of the human eye exposed to handheld transmitters,” *IEEE International Symposium on Electromagnetic Compatibility*, Honolulu, HI, USA, pp. 1-6, 2007.
- [13] V. Stankovic, D. Jovanovic, D. Krstic, V. Markovic, and N. Cvetkovic, “Temperature distribution and specific absorption rate inside a child’s head,” *International Journal of Heat and Mass Transfer*, vol. 104, pp. 559-565, 2017.
- [14] V. Stankovic, D. Jovanovic, D. Krstic, V. Markovic, and M. Dunjic, “Calculation of electromagnetic field from mobile phone induced in the pituitary gland of children head model,” *Vojnosanitetski Pregled*, vol. 74, no. 9, pp. 854-861, 2017.
- [15] F. Kaburcuk and A. Z. Elsherbeni, “Temperature rise and SAR distribution at wide range of frequencies in a human head due to an antenna radiation,” *ACES Journal*, vol. 33, no. 4, pp. 367-372, 2018.
- [16] M. I. Hossain, M. R. I. Faruque, and M. T. Islam, “A new design of cell phone body for the SAR reduction in the human head,” *ACES Journal*, vol. 30, no. 7, pp. 792-798, 2015.
- [17] F. Kaburcuk, “Effects of a brain tumor in a dispersive human head on SAR and temperature rise distributions due to RF sources at 4G and 5G frequencies,” *Electromagnetic Biology and Medicine*, vol. 38, no. 2, pp. 168-176, 2019.
- [18] Dassault Systèmes, CST (Computer Simulation Technology) Studio Suite, 2009.
- [19] M. Martinez-Burdalo, A. Martin, M. Anguiano, and R. Villar, “Comparison of FDTD-calculated specific absorption rate in adults and children when using a mobile phone at 900 and 1800 MHz,” *Physics in Medicine and Biology*, vol. 49, pp. 345-354, 2004.
- [20] J. Keshvari and S. Lang, “Comparison of radio frequency energy absorption in ear and eye region of children and adults at 900, 1800 and 2450 MHz,” *Physics in Medicine and Biology*, vol. 50, pp. 4355-4369, 2005.
- [21] A. A. de Salles, G. Bulla, and C. E. Rodriguez, “Electromagnetic absorption in the head of adults and children due to mobile phone operation close to the head,” *Electromagnetic Biology and Medicine*, vol. 25, pp. 349-360, 2006.
- [22] J. Wiart, A. Hadjem, M. F. Wong, and I. Bloch, “Analysis of RF exposure in the head tissues of children and adults,” *Physics in Medicine and Biology*, vol. 53, pp. 3681-3695, 2008.
- [23] A. Christ, M. C. Gosselin, S. Kühn, and N. Kuster, “Impact of pinna compression on the RF absorption in the heads of adult and juvenile cell phone users,” *Bioelectromagnetics*, vol. 31, pp. 406-412, 2010.
- [24] O. P. Gandhi, L. L. Morgan, A. A. de Salles, Y. Y. Han, R. B. Herberman, and D. L. Davis, “Exposure limits: The underestimation of absorbed cell phone radiation, especially in children,” *Electromagnetic Biology and Medicine*, vol. 31, pp. 34-51, 2012.
- [25] L. L. Morgan, S. Kesari, and D. L. Davis, “Why children absorb more microwave radiation than adults: The consequences,” *Journal of Microscopy and Ultrastructure*, vol. 2, pp. 197-204, 2014.
- [26] A. Christ, M. C. Gosselin, M. Christopoulou, S. Kühnand, and N. Kuster, “Age-dependent tissue-specific exposure of cell phone users,” *Physics in Medicine and Biology*, vol. 55, pp. 1767-1783, 2010.
- [27] J. Wang, O. Fujiwara, and S. Watanabe, “Approximation of aging effect on dielectric tissue properties for SAR assessment of mobile telephones,” *IEEE Transactions on Electromagnetic Compatibility*, vol. 48, pp. 408-413, 2006.
- [28] A. Peyman, A. A. Rezazadeh, and C. Gabriel, “Changes in the dielectric properties of rat tissue as a function of age at microwave frequencies. Corrections to Peyman et al. (2001),” *Physics in Medicine and Niology*, vol. 47. pp. 2187-2188, 2002.
- [29] G. Schmid and R. Uberbacher, “Age dependence of dielectric properties of bovine brain and ocular tissue in the frequency range of 400 MHz to 18 GHz,” *Physics in Medicine and Biology*, vol. 50, pp. 4711-4720, 2005.
- [30] ITIS Foundation, Dielectric properties of tissues, Available at: <https://goo.gl/76SnEN>
- [31] C. R. Fernández, G. Bulla, A. C. Pedra, and A. A. de Salles, “Comparison of electromagnetic absorption characteristics in the head of adult and a children for 1800 MHz mobile phones,” *International Conference on Microwave and*

- Optoelectronics*, Brasilia, Brazil, pp. 523-528, 2005.
- [32] S. M. Castro, M. J. Ponces, J. D. Lopes, M. Casconcelos, and M. C. F. Pollmann, "Orthodontic wires and its corrosion—The specific case of stainless steel and beta-titanium," *Journal of Dental Sciences*, vol. 10, no. 1, pp. 1-7, 2015.
- [33] IEEE - Institute of Electrical and Electronics Engineers, "IEEE recommended practice for measurements and computations of radio frequency electromagnetic fields with respect to human exposure to such fields, 100kHz-300GHz," *Inc. C95.3-2002*, 2002.
- [34] M. Clemens and T. Weiland, "Discrete electromagnetism with the finite integration technique," *Progress in Electromagnetic Research*, vol. 32, pp. 65-87, 2001.
- [35] M. A. Ebrahimi-Ganjeh and A. R. Attari, "Interaction of dual band helical and PIFA handset antennas with human head and hand," *Progress in Electromagnetic Research*, vol. 77, pp. 225-242, 2007.



Dejan Jovanovic was born in Prokuplje, Serbia. He obtained M.Sc. degree at the Faculty of Electronic Engineering, University of Nis, Serbia in 2013. Jovanovic is a Ph.D. student at Faculty of Electronic Engineering, University of Nis. His main areas of research include numerical methods for electromagnetic field calculation and electromagnetic radiations.

Miniaturized Frequency Selective Radome Operating in the X-Band with Wideband Absorption

Hamza Ahmad¹, MuhibUr Rahman^{2*}, Shahid Bashir³, Wajid Zaman⁴,
and Fauziahanim Che Seman⁵

¹ Gandhara Institute of Science and Technology, Peshawar, Pakistan

^{2*}Department of Electrical Engineering, Polytechnique Montreal, Montreal, QC H3T 1J4, Canada

³University of Engineering and Technology, Peshawar, Pakistan

⁴National University of Sciences & Technology (NUST), Islamabad, Pakistan

⁵Research Center of Applied Electromagnetics, Universiti Tun Hussein Onn Malaysia, Batu Pahat, Malaysia

Abstract — In this work, a miniaturized frequency selective radome with wideband absorption is presented. The proposed design consists of a bandpass FSS and a resistive FSS. Both FSS's are combined together through a foam spacer. A slotted miniaturized form of the conventional Jerusalem cross structure is employed as the bandpass FSS. A meandered form of the basic square loop with lumped resistors incorporated in each side of the loop is used as the resistive FSS. The bandpass FSS ensures the transmission in the X-band, which is the operating band of the radome. The resistive FSS absorbs the out-of-band signals and thus reduces RCS at higher frequencies. The proposed design operates in the frequency range of 8.88-10.85 GHz and absorbs between 18.8-28.35 GHz. The insertion loss at the center frequency of the operating band is 0.82 dB. The thickness of the entire structure is $0.07 \lambda_0$ with respect to center frequency (10 GHz) of the operating band. The overall size of a unit cell of the miniaturized design is $0.2 \lambda_0$ that ensure angular stability for different polarizations and incident angles.

Index Terms — Bandpass FSS, Frequency Selective Surface (FSS), radome, resistive FSS, wideband absorption.

I. INTRODUCTION

A radome is usually made up of weatherproof material and used as a shield for an antenna to protect it from the physical environment. It is necessary for a radome to have a negligible effect on the operating frequency of encircled antenna so that electrical performance of antenna may not be disturbed. Radomes having frequency selective abilities have attracted the designers in recent years. Such radomes have the

tendency to prevent coupling from nearby antenna without disturbing radiation characteristics of the antenna [1,2]. Frequency selective surfaces (FSSs) are employed for this purpose. FSSs possesses spatial filtering properties and usually have a periodic structure. A radome is normally considered as a bandpass FSS which permits the passage of operating signal with negligible insertion loss and blocks the unwanted signal [3,4].

The radar cross section (RCS) of an object is its equivalent area which if scattered isotropically would result in the same scattered power density. With the development of the radar detection and stealth technology, how to reduce RCS has been of great military and practical significance. Over the years, there has been a growing attraction in the design of stealthy radome for many applications. Stealth technology requires the reduction of radar cross section of the antenna without affecting its radiation capabilities [5]. An antenna contributes in the in-band RCS and out-of-band RCS, depending on the radome reflection characteristics and its geometry. The RCS of the antenna can be reduced when frequency selective radome, designed with proper geometry, reflects the incident out of band signal in specular directions. Monostatic RCS of antenna which has not additional scatterers in its proximity can be reduced through this technique [6-7]. However, this technique cannot reduce the bistatic RCS because the reflected signal can be collected by bistatic radars.

An ideal condition for low RCS radome is that the desired signal must have minimum attenuation, whereas the incident unwanted signal should be absorbed. In [8], this concept has been proposed by introducing an absorbing layer in the structure. However, the qualitative

results are not provided. A bandpass filter is achieved by a conductive FSS while the absorption of out of band signal is achieved through bandstop resistive FSS [9]. The bandpass and resistive FSS are providing wideband absorption with different geometries. In [10], a conductive FSS and a resistive FSS with lumped resistors are used to form a composite structure. In [11], two resonators are coupled to miniaturize a bandstop FSS for wideband rejection.

In [12], they have proposed a novel FSS reflector for a dipole array to mitigate RCS within operating frequency range. The proposed FSS possesses good bandstop characteristics and is designed on quasi fractal geometrical approach which is quite complex to implement. Similarly in [13], FSS radome is designed using binary particle swarm optimization (BPSO) algorithm by the combination of pixel overlap technique. The proposed technique is quite attractive, however the manufacturability of this design become limited as the lattice points in FSS element are difficult to avoid from neighboring conductors, which in fact creates the overlapping problem. In [14], a switchable wideband FSS absorber/reflector is designed for C-band applications operating within 4-8 GHz frequency range. The proposed FSS has innovative characteristics by combining switchable performance with wideband absorption. In [15], a wideband rasorber is designed which operates at 3.8-10.3 GHz with and incorporates the switching of transmission and reflection bands using pin diodes. Triple-layer FSS has been used in [16] for a wide transmission band with a resistive sheet for absorption at lower frequencies. Another design with similar operation has been presented in [17] using dipole arrays. An FSS based rasorber with meander line square loop having lumped resistors has been presented in [18] while a dual absorption band has been achieved in [19]. A frequency selective radome for the X-band has been designed by combining a bandpass FSS and an absorbing FSS using the surface resistive technique [20].

In this work, an FSS based radome with frequency selective capabilities is designed. The proposed design consists of a miniaturized bandpass FSS that permits the operating signal to pass through the structure unattenuated while reflecting any out-of-band signal. The proposed design also consists of a miniaturized resistive FSS with lumped resistors to absorb the unwanted signal. This aids in minimizing the RCS of antenna that would be enclosed in the proposed radome. The operating band is chosen to be X-band which is used in radar applications and space communication. The absorption band covers frequencies above the X-band to make the antenna, enclosed in the radome, invisible to a potential target. This design is better than [20] due to several reasons. Firstly, a parametric analysis of the

design parameters is presented in this work. Secondly, the equivalent circuit for the proposed design is given with the values of circuit elements. Finally, the angular stability for this design is better than [20] and thus can give desired response even for oblique incident signals.

II. PROPOSED DESIGN

The proposed unit cell design is demonstrated in Fig. 1. A resistive FSS is placed on the front side while a bandpass FSS is placed on the back side of the structure. The bandpass and the resistive FSS are designed separately on two identical substrates. The material employed as substrate is RT/Duroid 5880 ($\epsilon_r = 2.2$) with a thickness of 0.127mm. Both the FSSs are separated by a foam spacer. The overall thickness and periodicity of the proposed design have been carefully optimized.

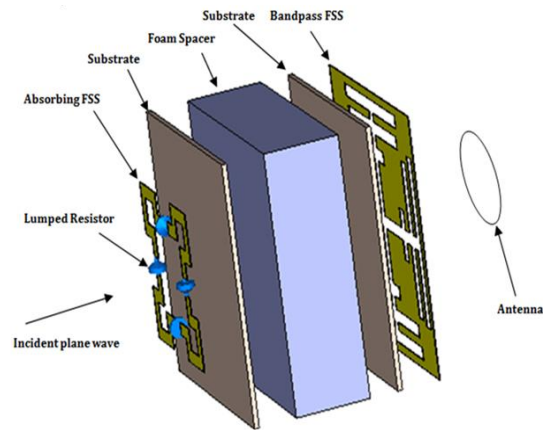


Fig. 1. Proposed unit cell structure of the FSS based radome.

The presented design is represented by the equivalent circuit illustrated in Fig. 2. The bandpass FSS is represented by a parallel LC circuit while the resistive FSS is represented by a series RLC circuit. The thickness of the foam spacer is represented by a transmission line of length d . The resistance, R comes from the resistors inserted in the four sides of the resistive FSS. Absorption of signals requires that there is no reflected signal from the proposed structure. Therefore, the input impedance of the proposed structure should be equal to the free space impedance, Z_0 . The controlling parameters to achieve this goal are the resistance R and the thickness d of the foam spacer. Initially, the bandpass FSS and resistive FSS are designed. The resistance and thickness of the foam spacer are then optimized so that the imaginary part of the input impedance of the proposed design becomes zero while the real part becomes close to 377Ω to ensure perfect absorption in the required band.

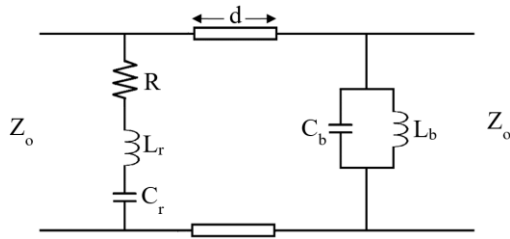


Fig. 2. Equivalent circuit of the proposed design.

III. BANDPASS FSS

We need to design the bandpass FSS in such a way that it has a passband in the operating frequency of the proposed structure and also a wide reflection bandwidth. The unit cell structure for the bandpass FSS is illustrated in Fig. 3 which is a modified form of the conventional slotted Jerusalem cross structure [2]. It is designed to give a passband in the X-band and reflects higher frequencies. The Jerusalem Cross resonates when the end to end length is approximately $\lambda/2$. Starting from this, the element is modified and miniaturized to resonate at the desired frequency but with a small size. The greater inter-element spacing and smaller periodicity of this miniaturized structure prevent grating lobes and make the structure narrowband.

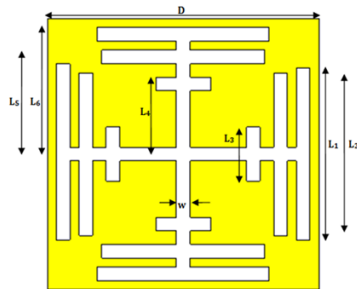


Fig. 3. Unit cell of the bandpass FSS. $D = 6$ mm, $L_1 = 3.8$ mm, $L_2 = 3.6$ mm, $L_3 = 1.2$ mm, $L_4 = 1.7$ mm.

IV. RESISTIVE FSS

In order to achieve a large bandwidth in the absorption band, the preferred element for the resistive FSS is the basic square loop [2]. While designing the resistive FSS, it must be ensured that the insertion loss in the operating band of the antenna does not increase. The basic loop resonates when the circumference of the loop is approximately one wavelength. For absorption at lower frequencies, the size of the square loop is to be kept large, but this causes an increase in the insertion loss in the operating band. This complication can be catered by miniaturizing the basic square loop structure via meandering [21] as shown in Fig. 4. The absorption capability in this bandstop FSS is achieved by incorporating lumped resistors into the four sides of the loop.

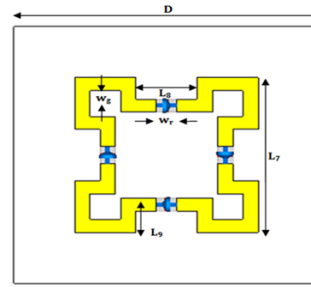


Fig. 4. Unit cell of the resistive FSS. $D = 6$ mm, $L_7 = 3.6$ mm, $L_8 = 1.2$ mm, $L_9 = 0.7$ mm, $w_r = 0.4$ mm, $w_g = 0.3$ mm.

V. ANALYSIS AND RESULTS

The proposed design is simulated in CST microwave studio using unit cell boundary conditions. The structure needs to be analyzed both in transmitting and receiving modes for the performance of a practical radome. For an incoming wave on the front side of the design, the transmission and reflection coefficients for both modes are shown in Fig. 5. The operating band is from 8.88-10.85 GHz. The center frequency is 10 GHz where the insertion loss is only 0.82dB. The frequency band between 18.8-28.35 GHz is the absorption band of the radome. The absorption band can be shifted to a lower frequency at the cost of increased insertion loss in the operating band. The transmission coefficient in the transmitting and receiving modes are exactly the same which is the case for every passive device. However, the reflection coefficients of both the modes are different from each other. The reason for this phenomenon is that the out-of-band signal is absorbed in receiving mode while it is totally reflected in transmitting mode.

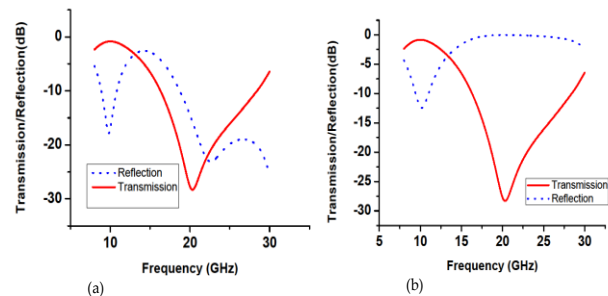


Fig. 5. Transmission and reflection coefficient of radome: (a) receiving mode and (b) transmitting mode.

Figure 6 exhibits the absorption percentages for transmitting and receiving modes. It is evident that absorption is greater than 80% between 18.8-28.35 GHz in the receiving mode. Absorption is negligible in the same band for transmitting mode. These results confirm the absorption performance of the proposed radome. A practical radome requires that the passband transmission is stable with the incidence angle. The small periodicity

of the structure guarantees passband stability, but the absorption properties are degraded with the incidence angle.

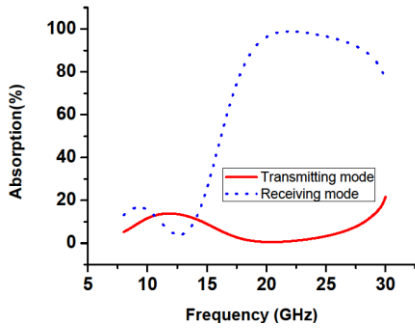


Fig. 6. Absorption percentage of radome.

Figure 7 manifests the transmission and reflection coefficients in receiving mode of the radome for various incident angles of TE and TM polarizations. The reflection and transmission coefficients are stable up to 45°. The stability can be improved for higher incidence angles by increasing the lumped resistance. This, unfortunately, increases the insertion loss in the passband. The operating band is stable for both TE and TM polarizations. The absorbing bandwidth decreases with increase in angle of incidence. For TM polarization, the absorbing bandwidth is reduced much drastically as compared to TM polarization as the incidence angle goes higher.

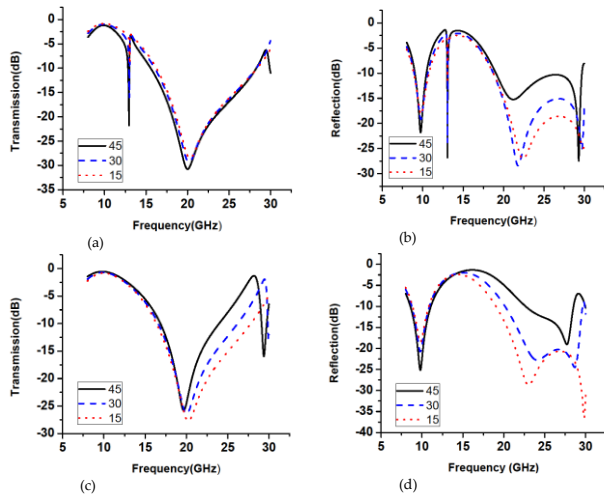


Fig. 7. Transmission and reflection coefficients for oblique incidence angles: (a) transmission for TE polarization, (b) reflection for TE polarization, (c) transmission for TM polarization, and (d) reflection for TM polarization.

The value of the lumped resistance for the proposed design is optimized to 120 Ω through parametric sweeps.

Figure 8 shows the effect of different values of ‘R’ on reflection and transmission coefficients in receiving mode of the radome. We need to choose that value of resistance which gives us smaller insertion loss in the working band and larger absorption in the absorption band. For resistance values less than 120 Ω, the insertion loss is smaller but the reflection coefficient is higher in the absorption band as compared to values greater than 120Ω. Therefore, the value of 120 Ω is a good compromise keeping in view all the aspects.

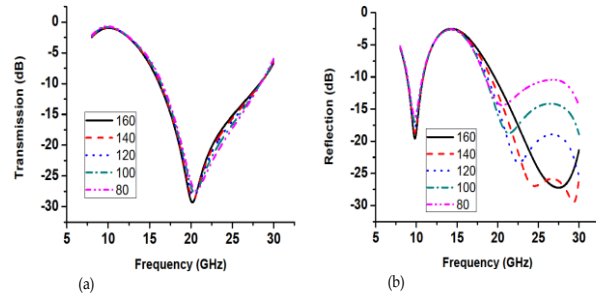


Fig. 8. Effect of different values of lumped resistance, R: (a) transmission and (b) reflection.

The thickness, *d*, of the foam spacer is critical to the performance of the proposed design. Figure 9 shows the effect of different values of the thickness of the spacer on the transmission and reflection coefficients. For our design, we require that the transmission coefficient in the operating band be closer to 0 dB. At the same time, we need the absorption bandwidth to be as large as possible. Careful observation of Fig. 9 indicates that a thickness of 2mm is the best choice to meet our criteria.

The thickness of the overall design is only 2.3mm and the periodicity of the unit cell is 6mm. The values of the circuit components at the center frequency of the operating band have been found to be $L_b = 0.26$ nH, $C_b = 0.98$ pF, $d = 2$ mm, $L_r = 1.61$ nH, $C_r = 0.16$ pF, $R = 120$ Ω. Table 1 gives a performance comparison of our work with some of the designs reported previously in literature

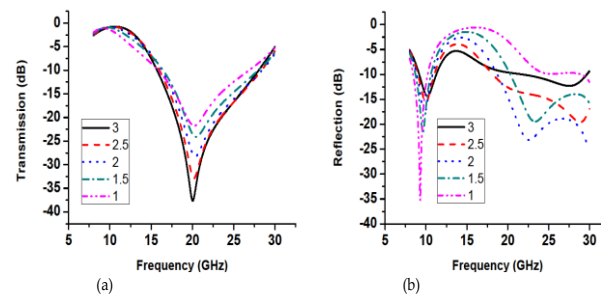


Fig. 9. Effect of different values of spacer thickness “d”: (a) transmission and (b) reflection.

Table 1: Performance comparison of several FSS

Ref.	Transmission Band (GHz)	Absorption Band (GHz)	Polarization	FSS Type
[9]	3 - 5	10 - 18	Double	Interdigital Jerusalem Cross elements
[10]	0.85 - 0.95	3 - 9	Double	Incurved square loops loaded with lumped resistors
[15]	2.80 - 2.90	3.8 - 10.3	Double	Square loop with lumped resistors and PIN diodes
[16]	8.3 - 11.07	2.4 - 7.1	Double	Circular spiral resonators with lumped resistors
[17]	5.2 - 5.8 GHz	2.8 - 5.0	Double	Crossed dipole with lumped resistor
[22]	23.5 GHz to 24.6 GHz	0 to 30 GHz excluding 23.5 to 24.6 GHz	Double	Slotted rings
[23]	4.09 - 4.90	1.98 - 4.70	Double	Square loop with lumped resistors
[24]	4.6 - 5.8	2.3 - 7.2	Single	Four leg loaded cross element
[25]	4.68 - 5.36	2.66 - 4.5 5.66 - 8.56	Single	Tripole loop and tripole slots
Our work	10 GHz	18.8 - 28.3 GHz	Double	Meandered square loop with lumped resistors

VI. EXPERIMENTAL SETUP

The proposed radome was measured in an anechoic chamber by using Keysight N5234A with the time-domain gating. The aperture of two horn antennas for testing is 65mm×65mm. The space between transmitting antenna (TX) or receiving antenna (RX) and the radome was 0.8 m. Due to the measurement setup limitation, the far-field condition was hard to meet for the entire frequency range. Our prototype was positioned on the far field of the TX antennas so that the transmission can be considered similar to the simulation. As a result, some discrepancy could arise concerning the reflection effects at the higher frequencies. The radome was surrounded with absorbent foam to reduce the effect of the edge diffraction. The corresponding unit cell prototype and measured transmission and reflection coefficient of radome in receiving and transmitting mode is shown in Figs. 10 (a) and (b), respectively.

VII. CONCLUSION

A frequency selective radome having a miniaturized unit cell with broadband absorption has been presented. The operating band of the proposed design is X-band while the absorption occurs at higher frequencies. An alteration of the basic Jerusalem cross structure is used as a bandpass FSS for transmission. For absorption, the basic square loop is miniaturized and meandered consisting of lumped resistors, is used as a resistive FSS. The operating band is from 8.88-10.85 GHz. The center frequency is 10 GHz where the insertion loss is only 0.82dB. The frequency band between 18.8-28.35 GHz is the absorption band of the radome. At the operating frequency of the proposed design, the thickness is $0.07 \lambda_0$. The periodicity of the unit cell of the proposed design

is kept small in order to suppress grating lobes in the absorption band. The angular stability for the proposed design is up to 45° for each TE and TM polarizations.

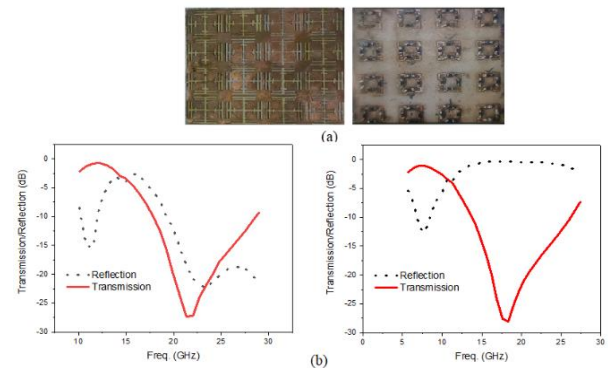
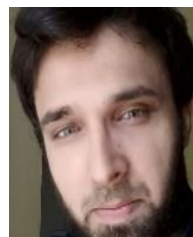


Fig. 10. (a) Unit cell prototype, and (b) measured transmission and reflection coefficient of radome in receiving and transmitting mode.

REFERENCES

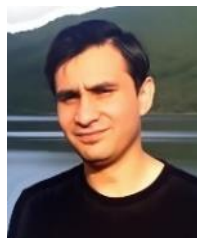
- [1] D. J. Kozakoff, *Analysis of Radome-Enclosed Antennas*. Norwood, MA: Artech House, 1997.
- [2] B. A. Munk, *Frequency Selective Surfaces: Theory and Design*. New York, NY, USA: Wiley, 2000.
- [3] P. C. Kim, D. G. Lee, I. S. Seo, and G. H. Kim, "Low-observable radomes composed of composite sandwich constructions and frequency selective surfaces," *Composites Science and Technology*, vol. 68, pp. 2163-2170, 2008.
- [4] H. Chen, X. Hou, and L. Deng, "Design of frequency selective surfaces radome for a planar slotted waveguide antenna," *IEEE Antennas and*

- Wireless Propagation Letters*, vol. 8, pp. 1231-1233, 2009.
- [5] Y.C. Chang, "Low radar cross section radome," US Patent 6,639,567B2.
- [6] E. L. Pelton and B. A. Munk, "A streamlined metallic radome," *IEEE Transactions on Antennas and Propagation*, vol. 22, pp. 799-803, 1974.
- [7] H. Zhou, S. Qu, B. Lin, J. Wang, H. Ma, and Z. Xu, "Filter-antenna consisting of conical FSS radome and monopole antenna," *IEEE Transactions on Antennas and Propagation*, vol. 60, pp. 3040-3045, 2012.
- [8] W. S. Arceneaux, R. D. Akins, and W. B. May, "Absorptive/transmissive radome," US Patent 5,400,043, 1995.
- [9] F. Costa and A. Monorchio, "A frequency selective radome with wideband absorbing properties," *IEEE Transactions on Antennas and Propagation*, vol. 60, no. 6, pp. 2740-2747, June 2012.
- [10] Q. Chen, J. Bai, L. Chen, and Y. Fu, "A miniaturized absorptive frequency selective surface," *IEEE Antennas and Wireless Propagation Letters*, vol. 14, pp. 80-83, 2015.
- [11] S. Abbasi, J. Nourinia, C. Ghobadi, M. Karamirad, and B. Mohammadi, "A sub-wavelength polarization sensitive bandstop FSS with wide angular response for X- and Ku-bands," *International Journal of Electronics and Communications*, 2018.
- [12] W. T. Wang, S. X. Gong, X. Wang, H. W. Yuan, J. Ling, and T. T. Wan, "RCS reduction of array antenna by using bandstop FSS reflector," *Journal of Electromagnetic Waves and Applications*, vol. 23, nos. 11-12, pp. 1505-1514, 2009.
- [13] N. Liu, X. Sheng, C. Zhang, J. Fan, and D. Guo, "Design of FSS radome using binary particle swarm algorithm combined with pixel-overlap technique," *Journal of Electromagnetic Waves and Applications*, vol. 31, no. 5, pp. 522-531, 2017.
- [14] P. Kong, X. W. Yu, M. Y. Zhao, Y. He, L. Miao, and J. J. Jiang, "Switchable frequency selective surfaces absorber/reflector for wideband applications," *Journal of Electromagnetic Waves and Applications*, vol. 29, no. 11, pp. 1473-1485, 2015.
- [15] C. Bakshi, D. Mitra, and S. Ghosh, "A frequency selective surface based reconfigurable rasorber with switchable transmission/reflection band," *IEEE Antennas and Wireless Propagation Letters*, vol. 18, no. 1, pp. 29-33, Jan. 2019.
- [16] Q. Chen, D. Sang, M. Guo, and Y. Fu, "Miniaturized frequency-selective rasorber with a wide transmission band using circular spiral resonator," in *IEEE Transactions on Antennas and Propagation*, vol. 67, no. 2, pp. 1045-1052, Feb. 2019.
- [17] Z. Wang, et al., "A high-transmittance frequency-selective rasorber based on dipole arrays," in *IEEE Access*, vol. 6, pp. 31367-31374, 2018.
- [18] W. Yu, et al., "Dual-polarized band-absorptive frequency selective rasorber using meander-line and lumped resistors," in *IEEE Transactions on Antennas and Propagation*, vol. 67, no. 2, pp. 1318-1322, Feb. 2019.
- [19] Y. Zhang, B. Li, L. Zhu, Y. Tang, Y. Chang, and Y. Bo, "Frequency selective rasorber with low insertion loss and dual-band absorptions using planar slotline structures," in *IEEE Antennas and Wireless Propagation Letters*, vol. 17, no. 4, pp. 633-636, Apr. 2018.
- [20] H. Ahmad, M. U. Khan, F. A. Tahir, and R. A. Bhatti, "A miniaturized frequency selective radome with wide absorption response above X-band," *Progress in Electromagnetics Research Symposium*, Singapore, vol. 2017, pp. 1424-1427, 2017.
- [21] H. Ahmad, M. U. Khan, F. A. Tahir, R. Hussain, and M. S. Sharawi, "Microwave absorber using single-layer FSS with wideband operation above the x-band," *12th European Conference on Antennas and Propagation (EuCAP 2018)*, London, pp. 1-3, 2018.
- [22] W. Wu, Y. Ma, X. Zhang, C. Li, and N. Yuan, "An ultrathin and narrow bandpass frequency selective radome with wide reflection bands," *AEU - International Journal of Electronics and Communications*, vol. 102, pp. 35-40, Apr. 2019.
- [23] P. Xiao, J. Xu, and Y. Han, "Design of dual-polarized frequency selective absorbers," in *2018 International Applied Computational Electromagnetics Society Symposium - China (ACES)*, pp. 1-2, 2018.
- [24] Y. Li, Q. Guo, L. Chen, and Z. Li, "Design of a frequency selective surface with a transmissive window and two bidirectional absorptive bands," in *2018 International Applied Computational Electromagnetics Society Symposium - China (ACES)*, pp. 1-3, 2018.
- [25] Q. Guo, Z. Li, J. Su, L. Y. Yang, and J. Song, "Dual-polarization absorptive/transmissive frequency selective surface based on tripole elements," *IEEE Antennas and Wireless Propagation Letters*, vol. 18, no. 5, pp. 961-965, May 2019.



Hamza Ahmad received a bachelor's degree in Electrical (Communication) Engineering from the University of Engineering and Technology, Peshawar, Pakistan, in September 2014, an M.S. degree in Electrical Engineering from NUST Islamabad, Pakistan in 2017. He was also a

Research Fellow at RIMMS NUST, Islamabad, Pakistan from September 2016 to August 2017. Currently he is a Lecturer at Gandhara Institute of Science and Technology Peshawar, Pakistan.



MuhibUr Rahman received a bachelor's degree in Electrical (Communication) Engineering from the University of Engineering and Technology, Peshawar, Pakistan, in September 2014, an M.S. degree in Electrical Engineering from NUST Islamabad, Pakistan in March 2016.

He worked as a Research Assistant in Lahore University of Management Sciences, and Dongguk University, Seoul, South Korea. Currently, he is working toward his Ph.D. degree in Polytechnique Montreal, Canada. He published a number of index journals and taken various patents. He is an active reviewer of various well reputed antenna and microwave journals.



Shahid Bashir received the B.Sc. degree in Electrical Engineering from the University of Engineering and Technology Peshawar (UET Peshawar), Peshawar, Pakistan, and the Ph.D. degree in Mobile Communications from Loughborough University, Loughborough, U.K., in

2009. He is currently an Assistant Professor with the Electrical Engineering Department, UET Peshawar. He has published in various reputed journals and conferences.



proceedings.

Wajid Zaman received an M.S. degree in Electrical Engineering from NUST Islamabad, Pakistan in 2017. His research interest includes multi-band antennas, wide band antennas, and radome. He published various antenna papers in well reputed journals and conference



Fauziahanim Che Seman received the degree in Electrical Communication Engineering from Universiti Teknologi Malaysia in 2001, the master's degree from Universiti Tun Hussein Onn Malaysia in 2003, and the Ph.D. degree from the Queen's University of Belfast, U.K., in 2011.

After the Master's degree, she joined the Faculty of Electrical Engineering, Universiti Tun Hussein Onn Malaysia as a Lecturer, where she is currently an Associate Professor with the Research Center of Applied Electromagnetic. She has published number of index journals and conference proceedings and taken various patents.

Eddy Currents Induced in Two Parallel Round Conductors

Tomasz Szczegielniak¹, Paweł Jabłoński¹, Dariusz Kusiak¹, and Zygmunt Piątek²

¹Department of Automation, Electrical Engineering and Optoelectronics, Faculty of Electrical Engineering Czestochowa University of Technology, Armii Krajowej 17, 42-200 Czestochowa, Poland
 tomasz.szczegielniak@pcz.pl, pawel.jablonski@pcz.pl, dariusz.kusiak@pcz.pl

²Czestochowa University of Technology, Poland
 zygmunt.piatek@interia.pl

Abstract — The paper presents a method of analysis of eddy currents induced in a system of two parallel round conductors by a transverse alternating magnetic field generated by a current in one of them. The magnetic field is represented by means of magnetic vector potential as expansion into Fourier series. Using the Laplace and Helmholtz equations as well as the classical boundary conditions we determine analytically the current density induced due to the proximity effect. Power transmission lines with round conductors are widely used in distribution networks. Therefore, although the paper is theoretical, the determination of electromagnetic parameters of the power transmission lines is of huge practical significance.

Index Terms — Current density, eddy currents, proximity effect, round conductor.

I. INTRODUCTION

A system of two or more round wires is very often used in power transmission lines. For example, in a three phase cable line there are often three round wires as a three-core cable or three single-core cables in the trefoil or the flat formation [1]. In each conductor, eddy currents are induced by magnetic field generated by neighboring alternating currents. The eddy currents induced in the conductors affect considerably the physical quantities related with the wires, such as impedances, electromagnetic field and power losses [2-4].

In order to calculate the current density induced in a twin line built from solid conductors of circular cross section a series of analytical [5-9] and numerical methods [10-13] are used. One of them consists in replacing the source wire with a current filament placed on the axis of the wire. Then the eddy currents induced in the second round wire may be determined analytically, e.g., they can be deduced from the solution for tubular, screen [14-16] after assuming that the inner radius equals zero.

In this paper we propose the method of successive approximations for calculating eddy currents induced in the round conductor using the magnetic vector potential. The determined current densities can be used to calculate impedances, magnetic field and power losses resulting from induced eddy currents.

The geometry of the system under consideration is shown in Fig. 1. The radii of the conductors are R_1 and R_2 respectively and the distance between the conductor axes is d . A sinusoidal current of angular frequency ω and complex r.m.s. value I_1 flows through the first (source) conductor.

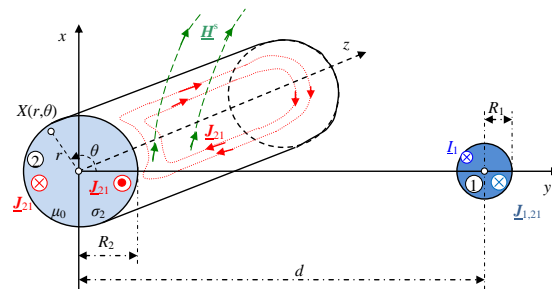


Fig. 1. Eddy currents induced in a round conductor (on the left) by the magnetic field of the neighboring conductor (on the right).

There are two kinds of induced eddy currents. The first one consists in inducing eddy currents $J_{21}(r, \theta) = \mathbf{1}_z J_{21}(r, \theta)$ in the second conductor by time harmonic magnetic field $H^s(r_{XY})$ (“source field”) generated by current I_1 in the first conductor. The second one is the current density $J_{1,21}(\rho, \varphi)$ induced in the first tubular conductor by previously induced current density $J_{21}(r, \theta)$.

In [9] current I_1 in the first round conductor was assumed to be located at the wire axis as a filament current. Then the magnetic field of the first conductor was represented by means of the magnetic vector

potential expanded into Fourier series. In the non-conducting external region, the Laplace equation was used to determine the magnetic field strength with taking into account the reverse reaction of the eddy currents induced in the considered conductor. The Helmholtz equation supplemented with classical boundary conditions was used to determine the eddy current density. The final formulas obtained in this procedure are as follows:

- The current density in the second round conductor induced by current I_1 flowing through the first one:

$$\underline{J}_{21}(r, \theta) = -\frac{\underline{\Gamma}_2 \underline{I}_1}{\pi R_2} \sum_{n=1}^{\infty} \left(\frac{R_2}{d}\right)^n \frac{I_n(\underline{\Gamma}_2 r)}{I_{n-1}(\underline{\Gamma}_2 R_2)} \cos n\theta, \quad (1)$$

in which I_{n-1} and I_{n+1} are the modified Bessel functions of the first kind of orders $n-1$ and n , respectively;

- The complex propagation constant:

$$\underline{\Gamma}_2 = \sqrt{j\omega\mu_2\sigma_2} = \sqrt{\omega\mu_2\sigma_2} \exp\left(j\frac{\pi}{4}\right), \quad (2)$$

where σ_2 is the conductivity and μ_2 is the permeability of the second round conductor;

- By analogy, the current density in the first tubular conductor induced by current I_2 flowing through the second one is:

$$\underline{J}_{12}(r, \theta) = -\frac{\underline{\Gamma}_1 \underline{I}_2}{\pi R_1} \sum_{n=1}^{\infty} \left(-\frac{R_1}{d}\right)^n \frac{I_n(\underline{\Gamma}_1 r)}{I_{n-1}(\underline{\Gamma}_1 R_1)} \cos n\theta, \quad (3)$$

in which the complex propagation constant of the first round conductor is defined by the formula:

$$\underline{\Gamma}_1 = \sqrt{j\omega\mu_1\sigma_1} = \sqrt{\omega\mu_1\sigma_1} \exp\left(j\frac{\pi}{4}\right), \quad (4)$$

where σ_1 is the conductivity and μ_1 the permeability of the first round conductor.

However, it should be realized that the induced current given by Eq. (1), from now on denoted as $\underline{J}_{21}^{(1)}(r, \theta)$ and called the first approximation of the total induced current density in wire 2, induces also a current of density $\underline{J}_{1,21}^{(1)}(\rho, \varphi)$ in the first conductor, which in turn induces the current density $\underline{J}_{21}^{(2)}(r, \theta)$ which adds to $\underline{J}_{21}^{(1)}(r, \theta)$ in the second conductor. Hence, the current density in the second conductor can be regarded as the following sum:

$$\underline{J}_{21}(r, \theta) = \sum_{m=1}^{\infty} \underline{J}_{21}^{(m)}(r, \theta), \quad (5)$$

where $\underline{J}_{21}^{(m)}$ is the m^{th} term of current density induced in the second round conductor. In previous works, e.g., [9, 14-16], the focus was directed on $\underline{J}_{21}^{(1)}(r, \theta)$. In this paper, the aim is to determine the second approximation.

II. THE FIRST APPROXIMATION

Let us consider two round parallel conductors.

Conductor 1 of conductivity σ_1 and radius R_1 leads a time harmonic current of r.m.s. I_1 and angular frequency ω . The second conductor of conductivity σ_2 and radius R_2 is affected by the magnetic field generated by the first conductor (Fig. 2).

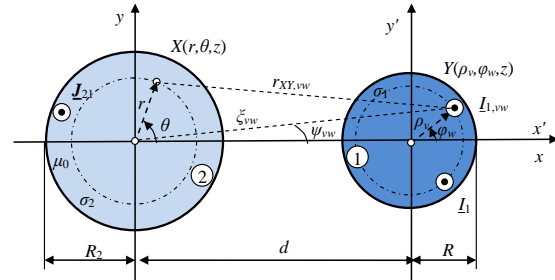


Fig. 2. Conductor 2 (on the left) in non-uniform magnetic field due to current I_1 in conductor 1 (on the right).

In general, the current density in the first conductor is non-uniform. Therefore, the cross section of the first round conductor is divided into elementary segments of radial dimension:

$$\Delta\rho = \frac{R_1}{V}, \quad (6)$$

and angular span:

$$\Delta\varphi = \frac{2\pi}{W}, \quad (7)$$

as shown in Fig. 3.

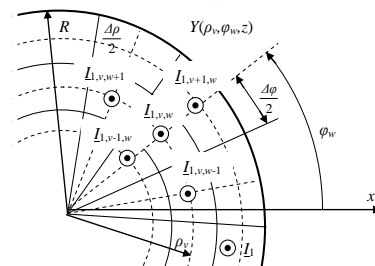


Fig. 3. Division of conductor 1 into segments.

For low frequency, we can assume that the total current I_1 is represented by a set of $V \times W$ filament currents distributed discretely at points $Y(\rho_v, \varphi_w)$ in cylindrical coordinates system determined by radius:

$$\rho_v = (2v-1)\frac{\Delta\rho}{2}, \quad (8)$$

and angle:

$$\varphi_w = (2w-1)\frac{\Delta\varphi}{2}, \quad (9)$$

where $v = 1, 2, \dots, V$ and $w = 1, 2, \dots, W$. The area of such a segment equals:

$$S_{vw} = \rho_v \Delta\rho \Delta\varphi. \quad (10)$$

Then the current in segment (v, w) is:

$$\underline{I}_{1vw}^{(0)}(\rho_v, \varphi_w) = S_{vw} \underline{J}_1^{(0)}(\rho_v, \varphi_w), \quad (11)$$

where $\underline{J}_1^{(0)}$ is an initial approximation of current density in conductor 1. For example, it can be a DC density as follows:

$$\underline{J}_1^{(0)} = \frac{\underline{I}_1}{\pi R_1^2}, \quad (12)$$

but it is more reasonable to use formula with the skin effect taken into account as follows:

$$\underline{J}_1^{(0)} = \frac{\underline{I}_2 \underline{I}_2}{2\pi R_2} \frac{I_0(\underline{I}_2 r)}{I_1(\underline{I}_2 R_2)}. \quad (13)$$

The magnetic vector potential generated by current \underline{I}_1 has only one component parallel to the conductor's axis (z component) as follows:

$$\underline{A}^s(r_{XY}) = \underline{1}_z \underline{A}^s(r_{XY, vw}). \quad (14)$$

It is the source potential with respect to the first conductor and it is given by following formula:

$$\underline{A}^s(r_{XY}) = \sum_{v=1}^V \sum_{w=1}^W \frac{\mu_0 \underline{I}_{1, vw}}{2\pi} \ln \frac{1}{r_{XY, vw}} + \underline{A}_0, \quad (15)$$

where the constant \underline{A}_0 can be freely assumed.

The above magnetic vector potential can be expressed in local cylindrical system of co-ordinates (r, θ, z) related with the second conductor. From Fig. 2 it follows that:

$$r_{XY, vw}^2 = r^2 + \xi_{vw}^2 - 2r\xi_{vw} \cos(\theta - \psi_{vw}), \quad (16)$$

where

$$\xi_{vw}^2 = \rho_v^2 + d^2 + 2\rho_v d \cos \varphi_w, \quad (17)$$

and

$$\psi_{vw} = \arcsin \left(\frac{\rho_v}{\xi_{vw}} \sin \varphi_w \right). \quad (18)$$

Thus, the total vector potential becomes:

$$\underline{A}^w(r_{XY}) = \sum_{v=1}^V \sum_{w=1}^W \frac{\mu_0 \underline{I}_{1, vw}}{2\pi} \times \ln \frac{1}{\sqrt{r^2 + \xi_{vw}^2 - 2r\xi_{vw} \cos(\theta - \psi_{vw})}} + \underline{A}_0. \quad (19)$$

The expression under the square root can be rewritten as follows:

$$\frac{r_{XY, vw}^2}{\xi_{vw}^2} = 1 + \left(\frac{r}{\xi_{vw}} \right)^2 - 2 \frac{r}{\xi_{vw}} \cos(\theta - \psi_{vw}). \quad (20)$$

Hence,

$$\ln \frac{r_{XY, vw}}{\xi_{vw}} = \frac{1}{2} \ln \left[1 + \left(\frac{r}{\xi_{vw}} \right)^2 - 2 \frac{r}{\xi_{vw}} \cos(\theta - \psi_{vw}) \right], \quad (21)$$

and by expanding the right-hand side of equation (21) into Fourier series¹ it follows that:

$$\ln \frac{r_{XY, vw}}{\xi_{vw}} = - \sum_{n=1}^{\infty} \frac{1}{n} \left(\frac{r}{\xi_{vw}} \right)^n \cos n(\theta - \psi_{vw}), \quad (22)$$

for $r < \xi_{vw}$. Hence,

$$\ln \frac{1}{r_{XY, vw}} = \ln \frac{1}{\xi_{vw}} + \sum_{n=1}^{\infty} \frac{1}{n} \left(\frac{r}{\xi_{vw}} \right)^n \cos n(\theta - \psi_{vw}), \quad (23)$$

and the magnetic vector potential (19) at point $X(r, \theta)$ such that $r < \xi_{vw}$ can be rewritten as follows:

$$\underline{A}^s(r, \theta) = \frac{\mu_0}{2\pi} \sum_{v=1}^V \sum_{w=1}^W \underline{I}_{1, vw}^{(0)} \left[\ln \frac{1}{\xi_{vw}} + \sum_{n=1}^{\infty} \frac{1}{n} \left(\frac{r}{\xi_{vw}} \right)^n \cos n(\theta - \psi_{vw}) \right] + \underline{A}_0. \quad (24)$$

In order to determine the density of the current induced in conductor 2 we may apply the analytical procedure shown in [9, 14-16]. Finally, the first approximation of the current density induced in the second round conductor by the current \underline{I}_1 in the first round conductor takes the following form:

$$\underline{J}_{21}^{(1)}(r, \theta) = - \frac{\underline{I}_2}{\pi R_2} \sum_{v=1}^V \sum_{w=1}^W \underline{I}_{1, vw}^{(0)} \times \sum_{n=1}^{\infty} \left(\frac{R_2}{\xi_{vw}} \right)^n \frac{I_n(\underline{I}_2 r)}{I_{n-1}(\underline{I}_2 R_2)} \cos n(\theta - \psi_{vw}). \quad (25)$$

The distributions of magnitude of this current density on the surface of this conductor for various discretization parameters are shown in Fig. 4.

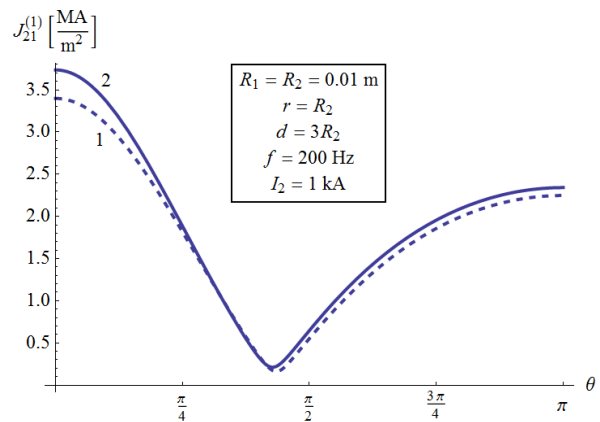


Fig. 4. Magnitude of the first approximation of the current density given by (25) for $V = 4$ and $W = 2$ (solid curve 1), $W = 180$ (dotted curve 2).

¹ Reference [17] provides formula (1.514):

$$\ln(1 + x^2 - 2x \cos \alpha) = -2 \sum_{n=1}^{\infty} \frac{1}{n} x^n \cos n\alpha.$$

The results calculated via (25) marginally depend on the number of radial division (V). Their dependence on angular division (W) is rather slight – in practice, the results remain the same for $W > 18$. The magnitude of the density of the induced eddy currents acquires the highest values at the point closest to the neighboring conductor, i.e., for $\theta = 0^\circ$. It strongly depends on frequency, which is shown in Fig. 5.

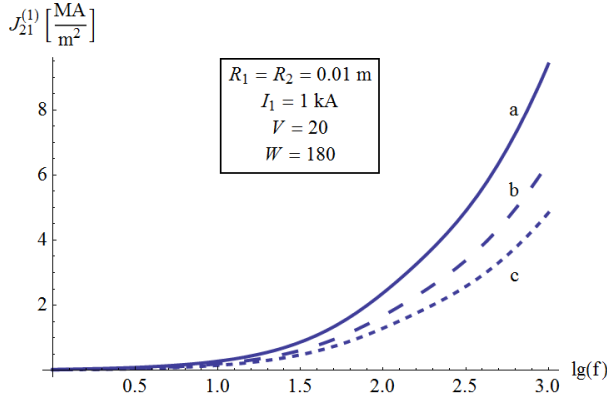


Fig. 5. Magnitude of current density given by (25) at point $r = R_1$, $\theta = 0^\circ$ vs. frequency f for $d = 3R_2$ (solid curve a), $d = 4R_2$ (dashed curve b), $d = 5R_2$ (dotted curve c); calculations performed for $V = 20$ and $W = 180$.

The same results are obtained when applying (1). So, the first approximation given by (25) describes the current density induced in conductor 2 as if current I_1 was located on the axis of conductor 1.

The first approximation of current density, $J_{21}^{(1)}(r, \theta)$, strongly depends on the distance d , which is shown in Fig. 6.

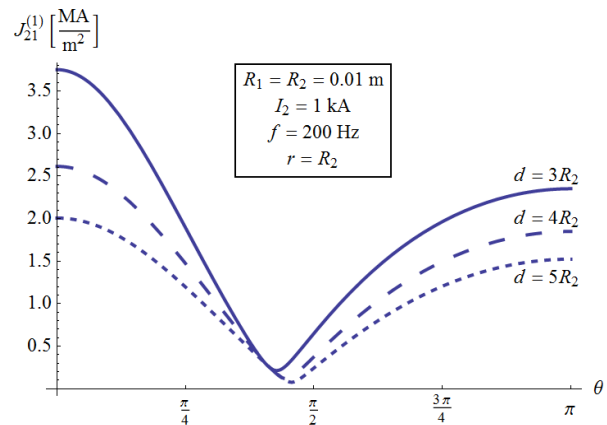


Fig. 6. Magnitude of current density given by (25) on the surface of conductor 2 for various distances d .

The argument of current density, $\varphi_{21}^{(1)}(r, \theta)$, also depends on distance d – see Fig. 7.

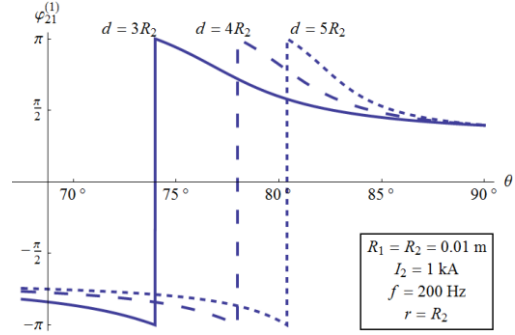


Fig. 7. Argument of the current density given by (25) on the surface of conductor 2 for various distances d .

A similar procedure can be applied, when the second conductor carries current I_2 which induces eddy currents in the first conductor (Fig. 8).

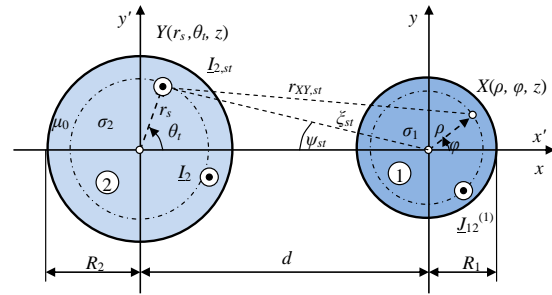


Fig. 8. Quantities used for calculating the current density induced in conductor 1 due to magnetic field generated by current I_2 in conductor 2.

In general, the current density in the second conductor is non-uniform as well. Therefore, the cross section of conductor 2 is divided into polar segments of radial dimension:

$$\Delta r = \frac{R_2}{S}, \tag{26}$$

and angular span:

$$\Delta \theta = \frac{2\pi}{T}, \tag{27}$$

as shown in Fig. 9.

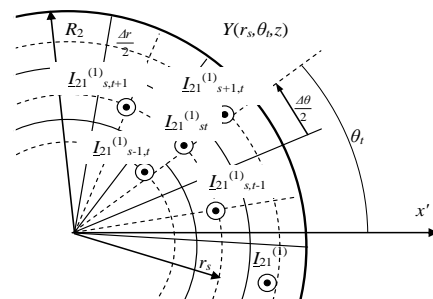


Fig. 9. Division of conductor 2 into polar segments.

Current of density $\underline{J}_2(r_s, \theta_t)$ is approximated by a system of filaments located at points $Y(r_s, \theta_t)$ in the cylindrical co-ordinates associated with conductor 2, where:

$$r_s = (2s-1) \frac{\Delta r}{2}, \quad (28)$$

and

$$\theta_t = (2t-1) \frac{\Delta \theta}{2}, \quad (29)$$

where $s = 1, 2, \dots, S$ and $t = 1, 2, \dots, T$.

The area of the segment equals:

$$S_{st} = r_s \Delta r \Delta \theta. \quad (30)$$

Then from Fig. 8 it follows that:

$$\begin{aligned} r_{XY, st}^2 &= \rho^2 + \zeta_{st}^2 + 2\rho\zeta_{st} \cos(\varphi + \psi_{st}) = \\ &= \rho^2 + \zeta_{st}^2 - 2\rho\zeta_{st} \cos(\pi - \varphi - \psi_{st}), \end{aligned} \quad (31)$$

where

$$\zeta_{st}^2 = r_s^2 + d^2 - 2r_s d \cos \theta_t, \quad (32)$$

and

$$\psi_{st} = \arcsin\left(\frac{r_s}{\zeta_{st}} \sin \theta_t\right). \quad (33)$$

Hence, the current in each segment equals:

$$\begin{aligned} \underline{I}_{2, st}^{(0)} &= S_{st} \underline{J}_2^{(0)}(r = r_s, \theta = \theta_t) = \\ &= \frac{\underline{I}_2 \underline{I}_2 r_s \Delta r \Delta \theta}{2\pi R_2} \frac{I_0(\underline{I}_2 r_s)}{I_1(\underline{I}_2 R_2)}. \end{aligned} \quad (34)$$

Applying the procedure given above in (19)-(25) for the second conductor, the following formula representing the first approximation of the eddy current density induced in the first conductor by current \underline{I}_2 in conductor 2 is obtained:

$$\begin{aligned} \underline{J}_{12}^{(1)}(\rho, \varphi) &= -\frac{\underline{I}_1}{\pi R_1} \sum_{s=1}^S \sum_{t=1}^T \sum_{n=1}^{\infty} \underline{I}_{2, st}^{(0)} (-1)^n \left(\frac{R_1}{\zeta_{st}}\right)^n \times \\ &\times \frac{I_n(\underline{I}_1 \rho)}{I_{n-1}(\underline{I}_1 R_1)} \cos n(\varphi + \psi_{st}) = \\ &= J_{12}^{(1)}(\rho, \varphi) \exp[j\varphi_{12}^{(1)}(\rho, \varphi)]. \end{aligned} \quad (35)$$

In case of two identical conductors the distributions of current density magnitude and argument will be symmetrical to those given by (25) – see Fig. 10 and Fig. 11.

The proposed method was compared with finite element method (FEM) – Table 1.

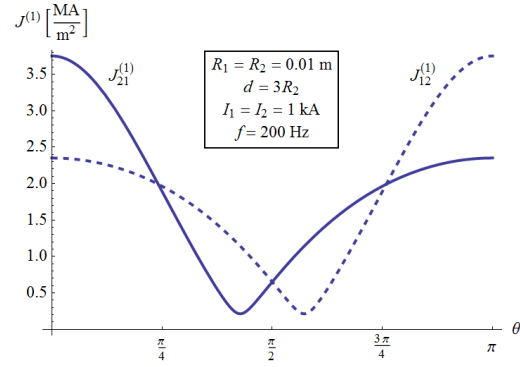


Fig. 10. Distributions of magnitude of eddy current densities given by (25) on the surfaces of two same conductors due to currents in the neighboring conductor.

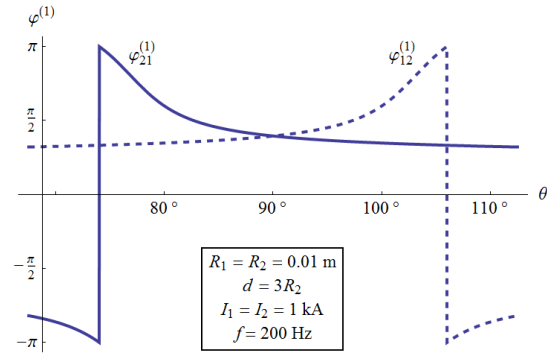


Fig. 11. Distributions of argument of eddy current densities given by (25) on the surfaces of two same conductors due to currents in the neighboring conductor.

Table 1: Magnitudes of the total current densities induced at characteristic points on the surfaces of two same conductors arranged in a twin line

		Proposed Method		FEM	
		$J^{(1)}$ kA·m ⁻²	J kA·m ⁻²	$J^{(1)}$ kA·m ⁻²	J kA·m ⁻²
Conductor 1 $\rho = R_1$	$\varphi = 0$	2352	2321		
	$\varphi = \pi/2$	650	650		
	$\varphi = \pi$	3753	3714		
Conductor 2 $r = R_2$	$\theta = 0$	3753	3714		
	$\theta = \pi/2$	650	650		
	$\theta = \pi$	2352	2321		

III. THE SECOND APPROXIMATION

The current of density $\underline{J}_{21}^{(1)}(r, \theta)$ induced in the second conductor by current \underline{I}_1 induces itself current of density $\underline{J}_{1,21}^{(1)}(\rho, \varphi)$ in the first conductor (this can be considered as a reverse reaction). However, $\underline{J}_{21}^{(1)}(r, \theta)$ is non-uniformly distributed - see (25) and Figs. 6 and 10. To determine $\underline{J}_{1,21}^{(1)}(\rho, \varphi)$, a set of filaments arranged in polar grid as in Fig. 9 can be used. The procedure is quite similar to that described by (26)-(35) with that difference that $\underline{J}_{21}^{(1)}(r, \theta)$ is used instead of $\underline{J}_2^{(0)}$. Hence,

$$\underline{I}_{21st}^{(1)} = S_{st} \underline{J}_{21}^{(1)}(r = r_s, \theta = \theta_t), \quad (36)$$

and the reverse reaction in conductor 1 can be written as:

$$\begin{aligned} \underline{J}_{1,21}^{(1)}(\rho, \varphi) = & -\frac{\underline{I}_1}{\pi R_1} \sum_{s=1}^S \sum_{t=1}^T \sum_{n=1}^{\infty} \underline{I}_{21st}^{(1)} (-1)^n \times \\ & \times \left(\frac{R_1}{\xi_{st}} \right)^n \frac{I_n(\underline{I}_1 \rho)}{I_{n-1}(\underline{I}_1 R_1)} \cos n(\varphi + \psi_{st}). \end{aligned} \quad (37)$$

The induced current of density $\underline{J}_{1,21}^{(1)}(\rho, \varphi)$ is then a source of further magnetic field which induces secondary eddy currents in conductor 2. To evaluate their density, the same polar grid as in Fig. 3 can be used, but this time the currents associated with the filaments are as follows:

$$\underline{I}_{1,21vw}^{(1)} = S_{vw} \underline{J}_{1,21}^{(1)}(\rho = \rho_v, \varphi = \varphi_w). \quad (38)$$

Each such a current contributes to the second correction to the eddy currents in a similar way as given by (25) so that:

$$\begin{aligned} \underline{J}_{21}^{(2)}(r, \theta) = & -\frac{\underline{I}_2}{\pi R_2} \sum_{v=1}^V \sum_{w=1}^W \sum_{n=1}^{\infty} \underline{I}_{1,21vw}^{(1)} \times \\ & \times \left(\frac{R_2}{\xi_{vw}} \right)^n \frac{I_n(\underline{I}_2 r)}{I_{n-1}(\underline{I}_2 R_2)} \cos n(\theta - \psi_{vw}). \end{aligned} \quad (39)$$

A similar procedure can be repeated for the second correction in conductor 1. To avoid extensive repetitions, only the key formulas are given below:

$$\underline{I}_{12vw}^{(1)} = S_{vw} \underline{J}_{12}^{(1)}(\rho = \rho_v, \varphi = \varphi_w), \quad (40)$$

$$\begin{aligned} \underline{J}_{2,12}^{(1)}(r, \theta) = & -\frac{\underline{I}_2}{\pi R_2} \sum_{v=1}^V \sum_{w=1}^W \sum_{n=1}^{\infty} \underline{I}_{12vw}^{(1)} \times \\ & \times \left(\frac{R_2}{\xi_{vw}} \right)^n \frac{I_n(\underline{I}_2 r)}{I_{n-1}(\underline{I}_2 R_2)} \cos n(\theta - \psi_{vw}), \end{aligned} \quad (41)$$

$$\underline{J}_{2,12st}^{(1)} = S_{st} \underline{J}_{2,12}^{(1)}(r = r_s, \theta = \theta_t), \quad (42)$$

and finally,

$$\begin{aligned} \underline{J}_{12}^{(2)}(\rho, \varphi) = & -\frac{\underline{I}_1}{\pi R_1} \times \sum_{s=1}^S \sum_{t=1}^T \sum_{n=1}^{\infty} \underline{I}_{2,12st}^{(1)} \times \\ & \times \left(\frac{R_1}{\xi_{st}} \right)^n (-1)^n \frac{I_n(\underline{I}_1 \rho)}{I_{n-1}(\underline{I}_1 R_1)} \cos n(\varphi + \psi_{st}). \end{aligned} \quad (43)$$

In a similar way the corrections of third and higher orders can be found. But numerical calculations show they are very low compared to the first one even for high frequency. So, they can be often neglected.

IV. THE TOTAL INDUCED CURRENT DENSITY

The total current density induced in the neighboring conductor is a sum of all the corrections. As mentioned above, the third and higher order terms can be often neglected so that the results can be limited to the first two terms. Hence, the total induced current density can be approximated as follows:

- In conductor 2:

$$\underline{J}_{21}(r, \theta) = \underline{J}_{21}^{(1)}(r, \theta) + \underline{J}_{21}^{(2)}(r, \theta), \quad (44)$$

- And in conductor 1:

$$\underline{J}_{12}(\rho, \varphi) = \underline{J}_{12}^{(1)}(\rho, \varphi) + \underline{J}_{12}^{(2)}(\rho, \varphi). \quad (45)$$

Figures 12 and 13 show the magnitude and argument of \underline{J}_{21} given by (44) on the surface of conductor 2, whereas Figures 14 and 15 show the quantities for \underline{J}_{21} and \underline{J}_{12} for some exemplary values of geometrical and excitation parameters.

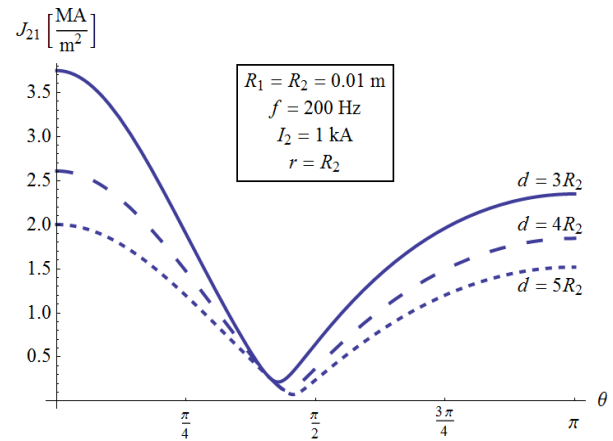


Fig. 12. Magnitude of current density given by (44) on the surface of conductor 2 for various distances d .

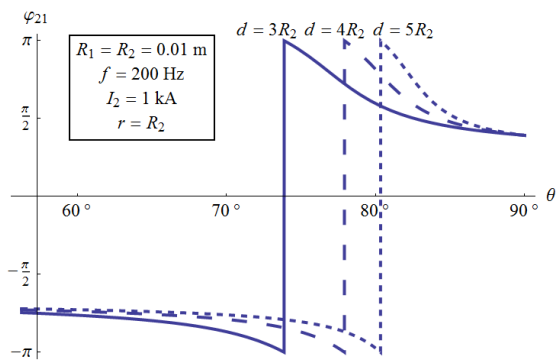


Fig. 13. Argument of current density given by (44) on the surface of conductor 2 for various distances d .

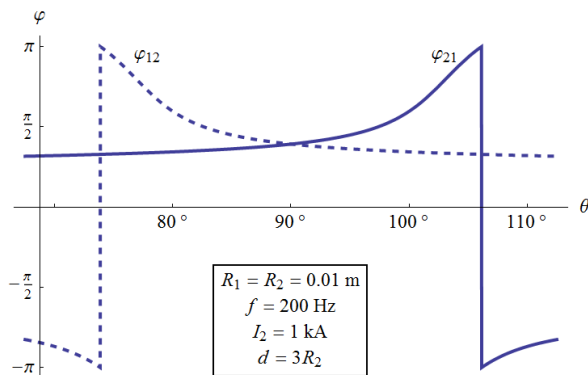


Fig. 15. Argument of current densities given by (44) and (45) on the surface of conductors for various distances d .

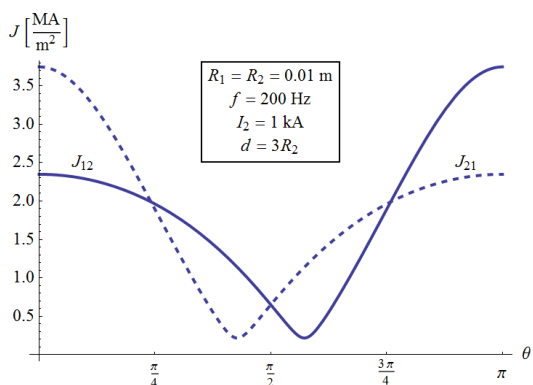


Fig. 14. Magnitude of current densities given by (44) and (45) on the surface of conductors for various distances d .

Table 2 presents a comparison of the results obtained via the proposed method and finite elements.

Table 2: Magnitudes of the total current densities induced at characteristic points on the surface of the conductors induced by the currents $I_1 = I_2 = 1$ kA – the first and the second approximations

$R_1 = R_2 = 0.01$ m; $d = 3R_2$; $\sigma_1 = \sigma_2 = 55 \cdot 10^6$ S/m $I = 1$ kA; $f = 200$ Hz		Proposed Method		FEM
		$J^{(1)}$ kA·m ⁻²	J kA·m ⁻²	J kA·m ⁻²
Conductor 1 $\rho = R_1$	$\varphi = 0$	2352	2354	2321
	$\varphi = \pi/2$	650	652	650
	$\varphi = \pi$	3753	3756	3714
Conductor 2 $r = R_2$	$\theta = 0$	3753	3756	3714
	$\theta = \pi/2$	650	652	650
	$\theta = \pi$	2352	2354	2321

V. CONCLUSION

An analytical-numerical method for determination of the current density induced in a round conductor by magnetic field generated by a sinusoidal current in a neighboring round parallel conductor was presented in the paper. The total current density was expressed as a series of successive corrections. The solution was given in the form of infinite Fourier series.

Based on the performed calculations it can be stated the current density induced in a round conductor (without current) by current in the neighboring round conductor can be limited to the second correction. This statement seems valid even for high frequency.

Besides, the current density induced in “source” conductor by the current density previously induced in considered conductor makes an important impact on distribution of the “source” current and should not be neglected.

The proposed method can be used for any dimensions and electrical properties of the conductors and any distance between them. It is shown that the induced currents can be neglected when the distance between conductors amounts to at least four conductor diameters.

The results shown in Tables 1 and 2 confirm that the current densities calculated via the proposed method and those determined by FEMM software agree very well, indicating the correctness of the proposed approach.

The solutions for current density presented in the paper can be used to find impedances, magnetic fields, power losses and temperatures in a system of cylindrical conductors with taking into account the induced currents.

REFERENCES

- [1] R. Benato and A. Paoluci, *EHVAC Undergrounding Electrical Power: Performance and Planning*, Springer-Verlag London Limited, 2010.
- [2] O. Coufal, "Current density in two solid parallel conductors and their impedance," *Electrical Engineering*, vol. 96, pp. 287-297, 2014.
- [3] F. Capelli and J. R. Riba, "Analysis of formulas to calculate the AC inductance of different configurations of nonmagnetic circular conductors," *Electrical Engineering*, vol. 99, pp. 827-837, 2017.
- [4] A. Pagnetti, A. Xemard, F. Pladian, and C. A. Nucci, "An improved method for the calculation of the internal impedances of solid and hollow conductors with inclusion of proximity effect," *IEEE Trans. On Power Delivery*, vol. 27, pp. 2063-2072, 2012.
- [5] T. Dłabać and D. Filipović, "Integral equation approach for proximity effect in a two-wire line with round conductors," *Technicki Vjesnik*, vol. 22, no. 4, pp. 1065-1068, 2015.
- [6] D. Filipović and T. Dłabać, "Proximity effect in a shielded symmetrical three-phase line," *Serbian Journal of Electrical Engineering*, vol. 11, no. 4, pp. 585-59, 2014.
- [7] P. Rolicz, "Eddy currents generated in a system of two cylindrical conductors by a transverse alternating magnetic field," *Electric Power Systems Research*, vol. 79, pp. 295-300, 2009.
- [8] P. Jabłoński, "Cylindrical conductor in an arbitrary time-harmonic transverse magnetic field," *Przegląd Elektrotechniczny*, r. 87, no. 5, 2011.
- [9] Z. Piątek, "Method of calculating eddy currents induced by the sinusoidal current of the parallel conductor in the circular conductor (in Polish)," *ZN Pol. Śl. Elektryka*, no. 75, pp. 137-150, 1981.
- [10] J. R. Riba, "Analysis of formulas to calculate AC resistance of different conductors' configurations," *Electric Power Systems Research*, vol. 127, pp. 93-100, 2015.
- [11] J. R. Riba, "Calculation of AC to DC resistance ratio of conductive nonmagnetic straight conductors by applying FEM simulations," *European Journal of Physics*, vol. 36, no. 5, 2015.
- [12] A. Shendge, "A study on a conductor system for investigation of proximity effect," *Journal of Electromagnetic Analysis and Application*, no. 4, pp. 440-446, 2012.
- [13] H. A. Aebischer and H. Friedli, "Analytical approximation for the inductance of circularly cylindrical two-wire transmission lines with proximity effect," *Advanced Electromagnetic*, vol. 7, no. 1, pp. 25-34, 2018.
- [14] Z. Piątek, "Self and mutual impedances of a finite length gas-insulated transmission line (GIL)," *Electric Power Systems Research*, no. 77, pp. 191-201, 2007.
- [15] Z. Piątek, *Impedances of Tubular High Current Busducts*, Polish Acad. Sci. Committee Elect. Eng. Ser. Progress in High-Voltage Technique, vol. 28, Wyd. Pol. Czest., Czestochowa, 2008.
- [16] Z. Piątek, D. Kusiak, and T. Szczegielniak, "Electromagnetic field and impedances of high current busducts," in *Proceedings of the 2010 Proceedings of the International Symposium*, Wroclaw, Poland, 20-22 Sept. 2010.
- [17] I. S. Gradsztejn and I. M. Ryżyk, *Tables of Integrals, Sums, Series and Products*, (in Polish), PWN, Warsaw, 1972.



Tomasz Szczegielniak was born in Konskie, Poland on Feb. 26, 1981. He received the M.S. degree from the Czestochowa University of Technology in 2006 and the Ph.D. degree from the Silesian University of Technology in 2011. Currently he is an Assistant Professor at the Institute of Optoelectronics and Measurement Systems at the Czestochowa University of Technology. His special interests are power system analysis, electromagnetic field analysis and numerical methods in engineering. He has been author or co-author of about 150 scientific papers published in Poland and abroad in conference proceedings, as monographs and in journals.



Paweł Jabłoński was born on 25 Sept. 1971 in Olesno, Poland. In 1995 he graduated from the Faculty of Electrical Engineering of Czestochowa University of Technology, where in 2007 he received a Doctor's degree, and in 2013 a Habilitated Doctor's degree. Currently he is an Associate Professor at the Institute of Optoelectronics and Measurement Systems. His scientific interests are electromagnetic field theory and numerical methods in solving field problems. He has written over 100 works published as books, papers in journals and conference proceedings.



Dariusz Kusiak was born on 20 Jan. 1980 in Radomsko, Poland. He graduated from the Faculty of Electrical Engineering the Czestochowa University of Technology in 2004 and received the Ph.D. degree in 2008. Currently he is an Assistant Professor at the Institute of Optoelectronics and Measurement Systems. He has written and co-written 150 works published in numerous journals and materials for both domestic as well as international scientific conferences. His scholarly interests include matters of electromagnetic fields connected with high-current lines or busducts.



Zygmunt Piatek was born in Pajeczno, Poland, on June 29, 1947. In 1972 he graduated from the Faculty of Electrical Engineering of Silesian University of Technology in Gliwice, where in 1980 he received a Doctor's degree, and in 2000 a Habilitated Doctor's degree. Since Oct. 1, 2003 he has been a Researcher and

Professor at the Czestochowa University of Technology. His scientific interests include: issues referring to electromagnetic field in high current, overhead and cable low and high voltage transmission lines, earth-return circuits and impulse metal forming. He has been author or co-author of about 260 scientific papers published in Poland and abroad in conference proceedings, as monographs and in journals. He collaborates with academic and industrial centers in Poland, France, the Czech Republic and Ukraine.

Efficient Computational Model of Phase Noise and its Applicability to Assess the Performance of Digital Modulation Techniques

Asmaa E. Farahat and Khlaïd F. A. Hussein

Microwave Engineering Department
Electronics Research Institute, Cairo, 11843, Egypt
asmaa@eri.sci.eg, Khalid_elgabaly@yahoo.com

Abstract — Two methods are proposed to get a discrete-time model for a sinusoidal carrier signal affected by phase noise of a predetermined power spectral density (PSD). The proposed methods aim to calculate the instantaneous phase error at the discrete time samples. In the first method, uncorrelated uniformly distributed random numbers are generated at the discrete time samples and added to the angle of the carrier. These phase samples are, then, correlated along the time by enforcing the spectrum of the signal to take the magnitudes obtained from the predetermined PSD. In the second method, uniformly distributed random numbers are generated at the discrete frequencies which are uncorrelated along the frequency to represent the phase of the signal spectrum. In both methods, a subsequent application of the inverse Fourier transform results in the time domain waveform of the signal in which the time samples of the phase error appear as correlated random values. The instantaneous phase error is calculated for different ratios of the noise-to-carrier power. Experimental measurements of the PSD of the phase noise for some commercially available microwave generators are performed and the measurements are used to calculate the instantaneous phase error associating the output signal. In all the cases, the obtained phase noise model is used to study the effect of such a noise type on the performance of M-ary PSK communication systems where the dependence of the bit-error-rate on the noise-to-carrier power level is investigated.

Index Terms — M-ary PSK, phase error, phase noise.

I. INTRODUCTION

The growing capacity and quality demands in wireless communication systems imposed more stringent requirements on the accurate assessment and modeling of the phase noise of local oscillators. Even in the digital world, phase noise in the guise of jitter is important. Clock jitter directly affects timing margins and hence limits system performance. Phase noise causes spectral purity degradation which leads to channel interference in RF communication channels. In OFDM systems, Phase

noise has two detrimental effects on the performance. It rotates all the subcarriers in the same OFDM symbol with a common phase, which is called common phase error (CPE). The more important is that it destroys the orthogonality of the subcarriers by spreading the power from one subcarrier to the adjacent subcarriers which is called inert-carrier interference [1]. In digital modulation techniques specially those employing phase to encode data as in PSK communication systems, it reduces the distance between the symbols leading to higher error rates. Phase noise in oscillators is one of the hardware impairments that is becoming a limiting factor in high data rate digital communication systems. It limits the performance of systems that employ dense constellations. Moreover, the level of phase noise at a given offset frequency increases with increasing the carrier frequency, which means that the phase noise problems may be worse in systems with high frequency carriers [1].

Phase noise is random phase fluctuations in a waveform. The fluctuations are visualized as sidebands in the signal power spectrum spreading out on either side of the signal. It reduces in level with increasing offset from the carrier frequency and is typically measured in dBc/Hz [1]. Phase noise is of particular importance as it reduces the quality of the signal and thus increases the rate of error in a communication link.

Phase noise is a phenomenon that essentially spreads out the power in a carrier. The carrier has no longer a discrete line power spectrum but a continuous PSD. The phase noise plot is a single side spectrum indicating the noise power density in one hertz bandwidth with regard to the carrier power. It can be modeled using power-law noise processes [2-4]. Phase noise typically rises much faster closer to the carrier and falls away as we get far from the carrier [5]. Power law noise processes are characterized by their functional dependence on Fourier frequencies. The spectral density plot of a typical oscillator's output is usually a combination of different power-law noise processes. It is very useful and meaningful to categorize the noise processes. The first job in evaluating a spectral density plot is to determine which type of noise exists for a particular

range of Fourier frequencies.

Several attempts to model phase noise have been reported in literature [6]-[12]. In [6], the oscillator phase noise is represented as integration of two functions representing flicker noise and white noise assuming independent noise sources. In [7], the phase noise is modeled as accumulated and synchronous random phase deviations with Gaussian distribution. It also relates the PSD of a noisy periodic signal analytically to its phase deviations which can be estimated from the jitter of the signal. In [8], flicker noise is estimated from white noise using the method of fractional order of integration. In [9], the phase noise is modeled as a random walk stochastic process added as random phase term to a sine wave and the decrease in sideband power is calculated when the oscillator signal is coherently mixed with a time delay replica of itself. In [10], a non-linear equation for the phase error is derived which is solved for the random phase perturbations. In [11] a power law model is used to model the phase noise with Gaussian stochastic process to represent the noise sources and a random variable representing the slope of each process. In [12] an analytic model for phase noise is derived to account for two sources of phase noise, thermo-mechanical and white noise.

In this work, the phase error range is estimated explicitly for phase noise characterized by its single side band PSD. A mathematical model for the phase noise is developed which enables the determination of the phase error span and instantaneous time samples. All the sources of phase noise can be accounted for in the proposed phase noise model accurately. Each of the previously mentioned methods has modeled certain types of phase noise sources but not all the sources that can be present in practical cases. Experimental measurements of the PSD of the phase noise for some commercially available microwave generators are performed and the instantaneous phase error associating the output signal is calculated. The effects of the phase noise on the performance of communication systems employing PSK modulation techniques are studied. The bit error rate (BER) and symbol rate (SER) can then be estimated for specific PSD of the phase noise.

II. MODELING THE PHASE NOISE

There are several types of phase noise, each characterized by the slope of the PSD curve. Phase noise across a range of frequencies will be dominated by a specific noise process [13]. In the present work it is considered that the oscillator may suffer from all or some of the following causes of phase noise, (i) *Random walk FM noise* ($1/f^4$) found at lower offset frequencies, (ii) *flicker frequency noise* ($1/f^3$), (iii) *white frequency noise* ($1/f^2$) [14], (iv) *flicker PM noise* ($1/f$) [15], and (v) *white PM noise* ($1/f^0$), which is mainly caused by thermal noise and shot noise [3]. It is possible to consider

that all the five noise processes are generated from a single oscillator, but usually, only two or three noise processes are dominant. Figure 1 is a graph of single sideband PSD of a sinusoidal signal affected by phase noise on a log-log scale with all the five noise processes taken into consideration.

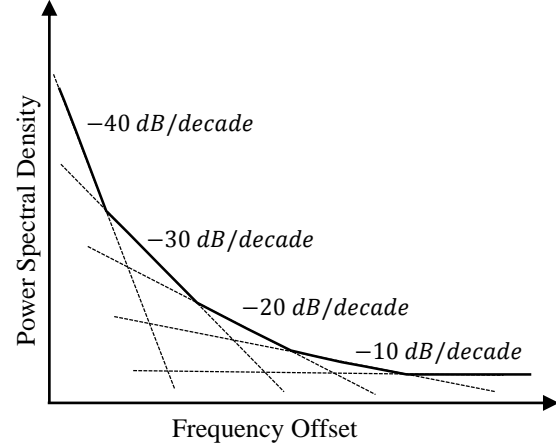


Fig. 1. Single side band PSD $L(f)$ describing phase noise characteristics.

The phase noise in the frequency domain is commonly characterized by the single side band PSD, $L(f)$, which is defined as the noise power in 1 Hz bandwidth at an offset frequency, f , from the carrier frequency relative to the carrier power [16, 17]:

$$L(f) = \frac{\text{Noise power in 1Hz bandwidth}}{P_c}, \quad (1)$$

where P_c is the carrier power.

The magnitudes of the spectrum of a carrier signal affected by phase noise can be obtained as follows:

$$A(f) = \sqrt{P_c L(f)}. \quad (2)$$

The spectrum of a pure sinusoidal signal is a Dirac delta function. The presence of phase noise will cause spectrum broadening as shown in Fig. 2. The noise-to-carrier power ratio (NCR) in a bandwidth Δf centered at the carrier frequency can be calculated as follows:

$$\text{NCR} = 2 \int_0^{\Delta f/2} L(f) df. \quad (3)$$

The PSD of the phase noise, $L(f)$ can be described by equation (1) according to the explained physical sources. This gives rise to the magnitude distribution $A(f)$ given by equation (2). However, the phase of the noisy signal, $\psi(f)$, and the instantaneous phase error in the time domain, $\varphi_e(t)$, are not known. The knowledge of the discrete-time phase errors, $\varphi_e(t_n)$, $n = 1, 2, 3, \dots, N$, are

necessary whenever it is required to assess communication system performance measure such as the bit error rate (BER). The next section aims to evaluate the phase errors as functions of the frequency and time as well.

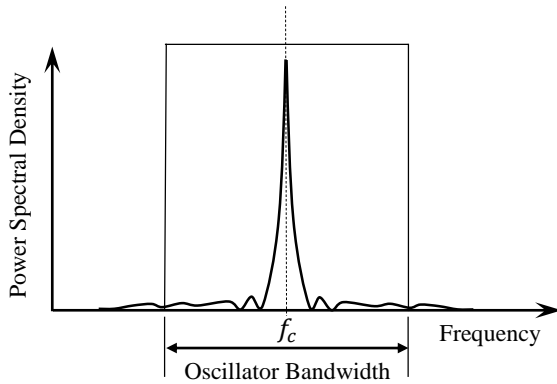


Fig. 2. Spectrum of a sinusoidal signal affected by phase noise.

For performance assessment in many applications including communication systems, it is necessary to determine the instantaneous phase error of a carrier signal subjected to phase noise. Modeling the phase noise means to get complete numerical information about a carrier signal affected by phase noise of a given PSD distribution. Complete information include the magnitude and phase distributions over the frequency for the carrier signal when affected by the phase noise, and also give the time samples of the signal from which the instantaneous phase error can be deduced.

In the first method, the phase noise is modeled through the following steps. First a random sequence of uniformly distributed random phase samples is generated and added to the angle of the carrier signal in time domain. The Fourier transformation is applied to the carrier signal where the magnitudes of the resulting signal spectrum are replaced by the magnitudes $A(f)$ which are obtained from $L(f)$ as given by (2). This process has the effect of correlating the random phase error samples along the time. The inverse Fourier transformation is, then, applied giving rise to the correlated time samples of the instantaneous phase error caused by the phase noise.

At high frequencies (in the gigahertz range) the above method may be impractical as it requires huge number of time and frequency samples to perform the Fourier transform which is memory and time consuming. An alternative procedure is proposed to construct the model of such a carrier signal with less computational complexity. This procedure starts with the construction of the magnitude and phase distribution in the frequency domain for the noisy carrier signal and then the inverse Fourier transform is applied to get the corresponding

time samples. It should be noted that the magnitudes are obtained from the $L(f)$ as given by (2) whereas the phases (of the signal spectrum) are constructed as uniformly distributed random numbers in the range $[-\pi, \pi]$, which are not correlated along the frequency.

The following subsections provide descriptions for the two methods mentioned above to construct a model for the phase noise when affects a carrier signal.

A. Modeling phase noise as correlated time sequence of random phase errors

Let the carrier signal $\xi(t)$ without the phase noise be expressed as:

$$\xi(t) = A_c e^{j(2\pi f_c t + \Psi)}, \quad (4)$$

where A_c is the carrier amplitude, f_c is the carrier frequency, and Ψ is a constant phase. When such carrier signal is affected by phase noise, it can be expressed as:

$$s(t) = A_c e^{j(2\pi f_c t + \Psi + \varphi_e(t))}, \quad (5)$$

where $\varphi_e(t)$ is the unknown instantaneous value of the phase error due to phase noise.

Let us consider a signal $x(t)$ similar to $s(t)$ except for one difference; the unknown phase error $\varphi_e(t)$ is replaced by random variable $\Phi(t)$ which represents the uniformly distributed random phases over the time. This means that,

$$x(t) = A_c e^{j(2\pi f_c t + \Psi + \Phi(t))}. \quad (6)$$

For discrete time $t_n = n \Delta t, n = 1, 2, \dots, N$, the signal $\xi(t)$ is discretized to get a sequence of N time samples:

$$\xi_n = \xi(t_n) = A_c e^{j(2\pi f_c t_n + \Psi)}, \quad n = 1, 2, \dots, N. \quad (7)$$

Initially, a sequence of N uncorrelated uniformly distributed random angles in the closed interval $[-\Phi_{\max}, \Phi_{\max}]$ is generated as follows:

$$\Phi_n = \Phi(t_n) = r_n \Phi_{\max}, \quad (8)$$

where r_n is a random number in the range $[-1, 1]$ and $0 < \Phi_{\max} < \pi$.

An expression for the discrete signal x_n can be obtained by adding discrete angle errors Φ_n to the phase of the discrete time samples ξ_n as follows:

$$x_n = x(t_n) = A_c e^{j(2\pi f_c t_n + \Psi + \Phi_n)}. \quad (9)$$

Applying the Fast Fourier Transform (FFT) to the discrete sequence x_n , one gets:

$$X_k = X(f_k) = \text{FFT}(x_n), \quad k = 0, 1, 2, \dots, K, \quad (10)$$

where $f_k = k \Delta f, k = 0, 1, 2, \dots, K$, and Δf is the discrete frequency step.

Let's define,

$$\alpha_k = |X_k|, \quad k = 0,1,2, \dots, K, \quad (11)$$

$$\psi_k = \text{phase}(X_k), \quad k = 0,1,2, \dots, K. \quad (12)$$

Let us write the discrete form of $L(f)$ as:

$$L(f_k) = L_k, \quad k = 1, 2, \dots, K. \quad (13)$$

To get the desired PSD $L(f)$, the discrete spectrum X_k should be modified by replacing the magnitudes α_k by A_k where,

$$A_0 = A_c, \quad (14-a)$$

$$A_k = \sqrt{P_c L_k} = A_c \sqrt{L_k}, \quad k = 1, 2, \dots, K. \quad (14-b)$$

Thus, the final form of the carrier $S(f)$ affected by the phase noise signal can be constructed using the magnitudes A_k and the phases ψ_k as follows:

$$S_k = S(f_k) = A_k e^{j\psi_k}, \quad k = 0,1,2, \dots, K. \quad (15)$$

The distribution of the discrete magnitudes of the Fourier transform of a carrier signal affected by the phase noise with the discrete frequencies seems like that shown in Fig. 3. It is worth noting that the spectrum is broadened due to the phase noise and that the carrier power is reduced. It is also important to note that irrespective of the value of Φ_{\max} , the phases ψ_k given by (12) have uniform random distribution in the interval $[-\pi, \pi]$ and the carrier phase is equal to Ψ .

The corresponding time sequence of the carrier signal, can be obtained by applying the Inverse Fast Fourier Transform (IFFT) to the frequency samples, S_k :

$$s_n = s(t_n) = \text{IFFT}(S_k). \quad (16)$$

The discrete-time phase error due to phase noise, φ_{e_n} which is the phase error at each time sample $\varphi_{e_n} = \varphi_e(t_n)$, can be obtained as follows:

$$\varphi_{e_n} = \tan^{-1} \left[\frac{\text{imag}(s_n)}{\text{real}(s_n)} \right] - (2\pi f_c t_n + \Psi). \quad (17)$$

Thus, the discrete time sequences of carrier signal affected by phase noise can be expressed as:

$$s_n = s(t_n) = A e^{j(2\pi f_c t_n + \Psi + \varphi_{e_n})}. \quad (18)$$

It may be interesting to notice that even though the sequences Φ_n are uncorrelated random samples with time, the samples φ_{e_n} are sequentially correlated. Actually, the correlation effect is attributed to the imposed magnitude distribution, A_k , that replaces the magnitudes α_k corresponding to the uncorrelated sequences.

It may be worth to recall that the number of time/frequency samples for IFFT is restricted by $N =$

$\frac{1}{\Delta f \Delta t}$. The main drawback of this method is that the requirement of 1 Hz resolution of the resulting phase noise model in the frequency domain means the application of IFFT on a huge number of frequency samples. Quantitatively speaking, for $\Delta f = 1$ Hz and assuming the time sampling is to be performed with the Nyquist rate, $\Delta t = 1/2f_c$, one gets:

$$N = 2f_c. \quad (19)$$

It should be noted that (19) gives the minimum value of N . Larger values of N result in better accuracy of the obtained model of the phase noise. Nevertheless, this leads to computational complexity which may be unaffordable for high carrier frequency.

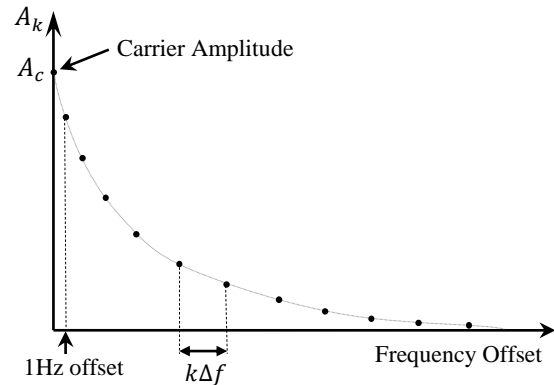


Fig. 3. Magnitudes of the spectrum of the noisy carrier signal, $S(f)$.

B. Modeling phase noise as uncorrelated random phases in the frequency domain

As mentioned above, the method introduced in the previous section leads to high computational complexity for high frequency carrier. In this section, a more computationally efficient method alternative to that described in the last section is introduced. This method starts constructing the phase noise model directly in the frequency domain by generating the phases ψ_k as uniformly distributed random numbers in the range $[-\pi, \pi]$ in one hand, and, in the other hand, using the magnitudes A_k given by (14) to construct the discrete frequency samples S_k as expressed in (15). The phase at the carrier frequency (zero frequency offset) is set equal to phase of the carrier in the absence of phase noise (Ψ).

The discrete frequency domain samples S_k of the carrier signal are constructed using the magnitudes A_k and the random phases ψ_k according to the following expression:

$$S_k = S(f_k) = A_k e^{j\psi_k}. \quad (20)$$

At a specific discrete time index, n , the sample s_n can be calculated by applying the Discrete Inverse Fourier Transform (DIFT) as follows:

$$s_n = s(t_n) = \text{DIFT}(S_k). \quad (21)$$

The corresponding phase error φ_{e_n} due to phase noise is calculated using (17). Note that the time step Δt for DIFT calculation is set arbitrarily; it doesn't obey the restriction for the relation between Δf and Δt as in the IFFT. This enables computationally efficient calculation of the phase error samples over a large time span with arbitrary time resolution. Also, this method enables computationally efficient construction of the spectrum of the noisy carrier signal over an arbitrary frequency range centered at the carrier frequency with high frequency resolution (1 Hz).

III. RESULTS AND DISCUSSIONS

Recall that the purpose of constructing a phase noise model is to get complete description of a carrier signal affected by phase noise. In this section, a model is constructed for such a carrier signal given the PSD distribution of the phase noise. Such a model describes the time samples of the carrier as well as the samples of the instantaneous phase errors encountered due to the phase noise. Two oscillators of carrier frequencies 1 MHz and 1 GHz are considered and the corresponding signal models are constructed by following the procedures explained in Sections II.A and II.B, respectively. For each carrier signals, the time samples of the phase error are calculated over a time span of 1 second. For experimental assessment, the frequency-domain method proposed in the present work is applied to obtain the models of the noisy carrier signals output from two commercially available microwave generators. A vector signal analyzer (VSA) is used for measuring the PSD of the encountered phase noise for the two microwave generators. Finally, the performance assessment of M -ary PSK communication systems subjected to phase noise is achieved regarding the BER and SER for $M = 4$ and 8.

A. Modeling phase noise as correlated sequential random phase errors

For carrier signals of relatively low frequency (a few megahertz) affected by phase noise, it is appropriate to apply the method described in Section II.A to construct the phase noise model by correlating random sequence of uncorrelated phases in the time domain. Such uncorrelated random sequence is generated as uniformly distributed random numbers. In the present section, this method is applied to obtain the noise model for a 1 MHz carrier signal affected by phase noise having a predetermined PSD distribution over the frequency.

A.1 Construction of the frequency spectrum magnitudes of the noisy signal

Let the PSD, $L(f)$, for a range of 1 MHz offset from the carrier frequency be that shown in Fig. 4. In the first and second decades: (1 Hz – 10 Hz), (10 Hz – 100 Hz),

the $L(f)$ curve has slopes of -40 and -30 dB/decade, respectively. In the third and fourth decades: (100 Hz – 1 kHz), (1 kHz – 10 kHz), it has slope of -20 dB. In the fifth decade: (10 Hz – 100 kHz), it has slope of -10 dB. For frequencies higher than 100 kHz, the $L(f)$ curve has a zero-slope corresponding to white phase noise level of -130 dBc/Hz. The maximum of the PSD is -10 dBc/Hz at 1 Hz offset from the carrier. If a carrier signal of 1 MHz is affected by phase noise of such a PSD, the corresponding magnitudes of the signal spectrum can be obtained by (14). Figure 5 shows a plot of the resulting signal spectrum magnitudes for a single side span of 100 Hz offset from the carrier frequency.

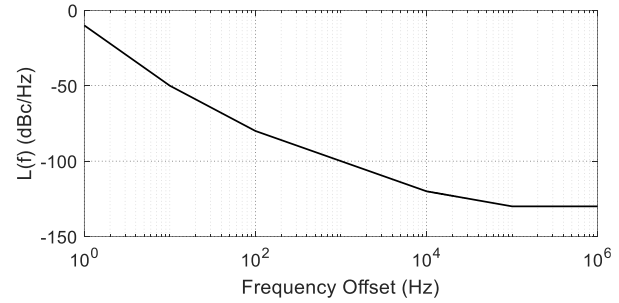


Fig. 4. Power spectral density $L(f)$ of the phase noise.

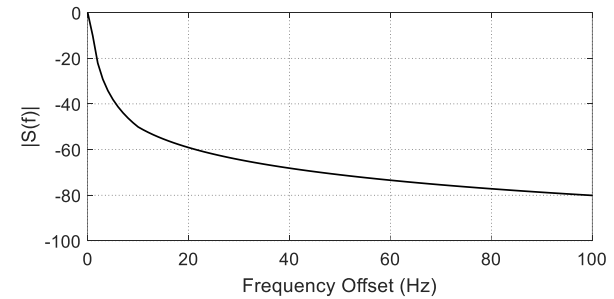


Fig. 5. Amplitude spectrum of the synthesized model, $S(f)$, for a 1 MHz carrier affected by phase noise of the PSD given in Fig. 4.

A.2 Phases of the frequency spectrum of the noisy signal

The time-domain carrier signal is discretized so that each cycle of the sinusoid has 16 time samples. Thus, for one second duration of this signal, the total number of samples is $N = 16M$ samples with time resolution of $\Delta t = \frac{1}{N}$ (as $\Delta f = 1$ Hz). The uncorrelated uniformly distributed random sequence of phase samples $\Phi(t)$ are generated as described in section II.A according to (8) with $\Phi_{\max} = \frac{\pi}{2}$. The application of the FFT operation on the discrete-time carrier signal x_n given by (9) with the imposed phase samples, Φ_n , results in a spectrum whose magnitudes and phases in the frequency domain are α_k and ψ_k , respectively. The phases, ψ_k , are found to be random numbers which are uniformly distributed in

the range $[-\pi, \pi]$. The plot of such phases with the frequency is presented in Fig. 6 for an offset frequency span of 100 Hz from the carrier frequency.

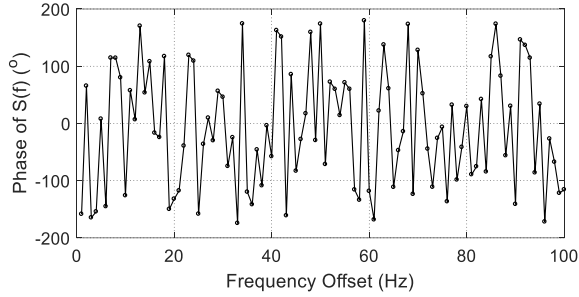


Fig. 6. Distribution of the discrete phases of $S(f)$ with the frequency for a carrier signal affected by phase noise.

A.3 The phase error time samples

It should be mentioned that the phase error is calculated by continuing the steps achieved in Section A.2, according to the procedure explained in Section II.A. The α_k magnitudes are, then, replaced by A_k which are given by (14) to obtain the frequency spectrum, $S_k \equiv S(f_k)$, of the noisy carrier signal as described by (15). The IFFT is, then, applied to the discrete frequency samples, S_k , to get the discrete time samples $s_n \equiv s(t_n)$. The time samples of the instantaneous phase error φ_{e_n} are obtained using (17). The calculated time samples of φ_{e_n} for a time span of one second are plotted against the time and shown in Fig. 7. It is clear that the sequential samples of the phase error are temporally correlated over the one-second span of the time. The swing of the phase error, which is the difference between the maximum and minimum, is about 65° .

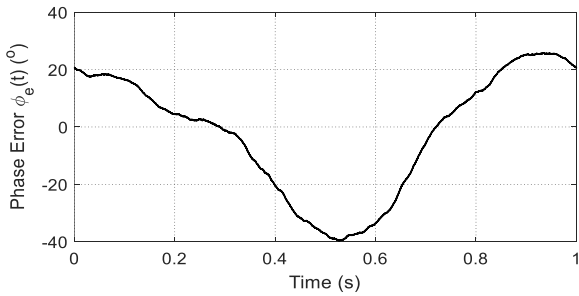


Fig. 7. Time samples of the instantaneous phase error of a carrier signal affected by phase noise of the PSD described by the curve $L(f)$ presented in Fig. 4 with $\Psi = 0^\circ$.

B. Modeling phase noise as uncorrelated random phases in the frequency domain

For carrier signals of relatively high frequency (gigahertz) affected by phase noise, it is appropriate to apply the method described in Section II.B to construct the phase noise model by generating uncorrelated

random sequence of phases in the frequency domain. In the present section, this method is applied to obtain the phase noise model for a 1 GHz carrier signal of 0dBm power and 0° phase. This signal is affected by phase noise of the PSD distribution presented in Fig. 4 which is defined over the frequency offset range 1 Hz to 1 MHz with a frequency step $\Delta f = 1$ Hz.

The spectrum of the noisy signal is obtained by calculating the distribution of the magnitudes and phases over the frequency range $(f_c - 1 \text{ MHz})$ to $(f_c + 1 \text{ MHz})$. The magnitudes are obtained from the PSD distribution, $L(f)$, as given by (14) and by setting $A_{-k} = A_k$ to get symmetrical sidebands. This results in the magnitudes distribution presented in Fig. 8 over the offset frequency range $(-4 \text{ kHz to } 4 \text{ kHz})$ from f_c .

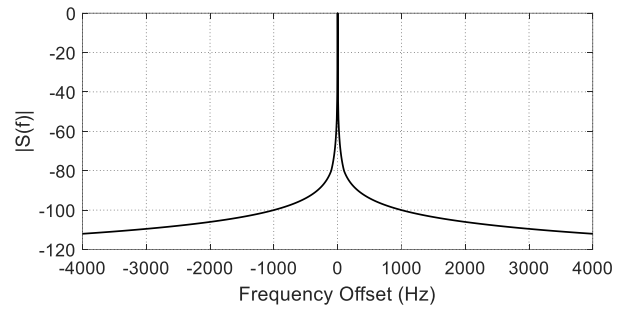


Fig. 8. Magnitudes of the spectrum for a 1 GHz carrier signal affected by phase noise of the PSD distribution presented in Fig. 4.

It should be noticed that to cover the entire frequency band, $(f_c - 1 \text{ MHz})$ to $(f_c + 1 \text{ MHz})$, a number of 2 mega samples of the frequency samples plus the carrier frequency sample are required. The frequency domain phases, ψ_k , are generated as uniformly distributed random numbers in the interval $[-\pi, \pi]$.

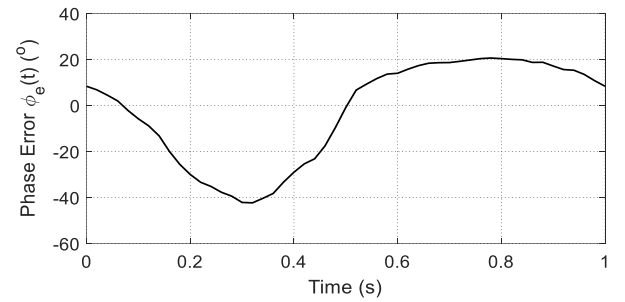


Fig. 9. Calculated instantaneous phase error for a 1 GHz carrier due to phase noise with the PSD shown in Fig. 4.

The phase error at each time sample is calculated as given by (17) with time step $\Delta t = 5\text{ms}$ and plotted over a time period of one second as shown in Fig. 9. It can be seen in the figure that the mean of the phase error is 0° and the swing is about 65° . The time samples φ_n are

calculated over a time span of one second.

C. Dependence of the time-variance of the phase error on phase noise power

It has been shown, in the previous discussions of the results concerning the time variation of the phase error, that it can be considered as a time-correlated sequence of random angles with zero-mean and a variance that may be dependent on the power of the phase noise. The dependence of the time-variance of the resulting phase error on the power of a phase noise having a spectral density distribution as shown in Fig. 4 and affecting a 1 GHz carrier signal is studied. It may be worth noting that, referring to Fig. 4, the area under the $L(f)$ curve within the operational bandwidth, gives half the ratio of noise power to the carrier power. In Fig. 10 the standard deviation of the phase error and the corresponding span are calculated for different NCR within a 10 MHz bandwidth for a 1 GHz carrier frequency having 0 dBm power. It is clear that as the NCR increases the phase error variance and, consequently, its span increase monotonically.

D. Experimental assessment for phase error variance for commercially available oscillators

Experimental data are usually plotted on log-log scales that make the power laws appear as straight lines where the slopes and, hence, the corresponding types of noise can be easily recognized. In this section, the phase noise associated with some commercially available oscillators are measured and modeled to obtain the time samples of the oscillator output.

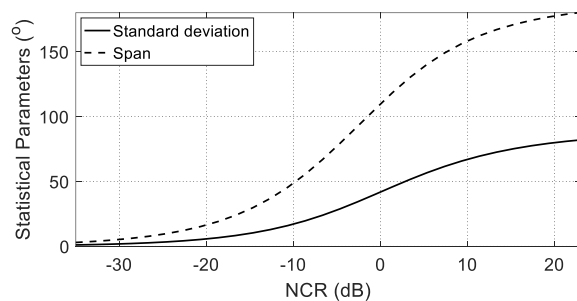


Fig. 10. Span and standard deviation of the phase error for different values of the carrier-to-noise power ratio.

D.1. Modeling the phase noise of the Agilent Vector Signal Generator (VSG) E8267D

The Agilent VSG model E8267D is precise, well-fabricated and commercially available for scientific research purposes. It operates in the frequency band 250 KHz to 44 GHz. The spectrum of the output signal and the phase noise PSD for 1 GHz frequency and 0 dBm power are measured using the Agilent Vector Signal Analyzer (VSA) model N9010A. The experimental setup is shown in Fig. 11 where the E8267D output is connected

to N9010A input through a Pasternack coaxial cable PE300-24 (cable length: 60 cm, insertion loss 0.36 dB/m at 1GHz). The phase noise is measured in the offset frequency range 1Hz – 1MHz from the carrier frequency. Front-panel screen shots of the VSG and VSA showing the settings and measurement data are shown in Figs. 12 (a) and 12 (b), respectively. The measured raw data and the averaged curve of the phase noise are plotted as shown in Fig. 13. The spectrum of the output signal is measured using the VSA with resolution bandwidth (RBW) of 1 Hz and video bandwidth (VBW) of 1 KHz over a 100 Hz span. The measured power spectrum is plotted as shown in Fig. 14.

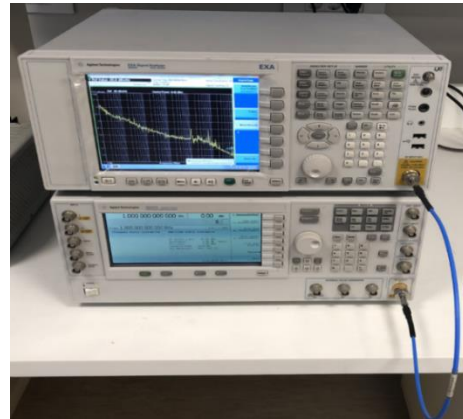
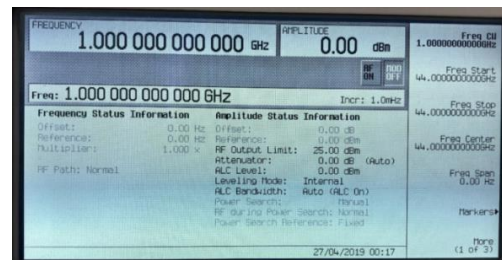
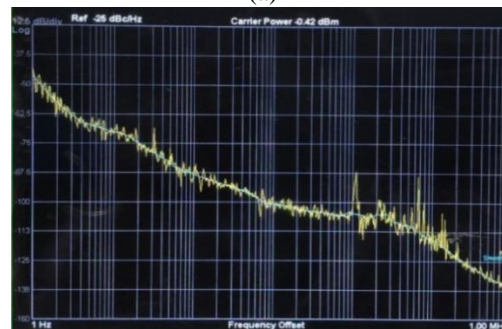


Fig. 11. Experimental setup for measuring the phase noise of the Agilent VSG model E8267D.



(a)



(b)

Fig. 12. Screen shots of (a) VSG E8267D showing the oscillator settings, and (b) VSA N9010A, showing the corresponding phase noise measurements.

The power spectrum of the output signal from such a VSG can be calculated from the PSD of the associated phase noise over a span of 100 Hz using (14) as described in Section II.A. In this way, the measured PSD of phase noise shown in Fig. 13, is used to numerically obtain the power spectrum of the output signal which is plotted and compared with the measured spectrum as shown in Fig. 14. As shown in the figure the calculated power spectrum agrees with the measured one over the entire frequency band, which ensures the accuracy of the developed model.

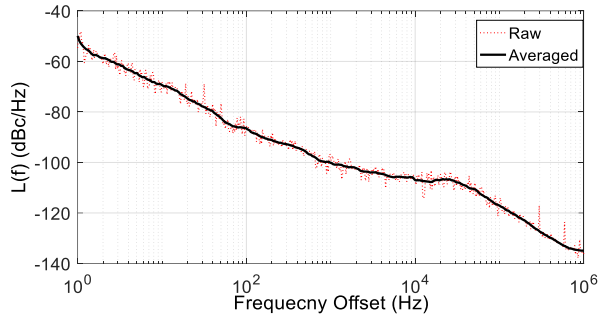


Fig. 13. Measured PSD of the phase noise for Agilent VSG model E8267D for 1 GHz frequency and 0 dBm power.

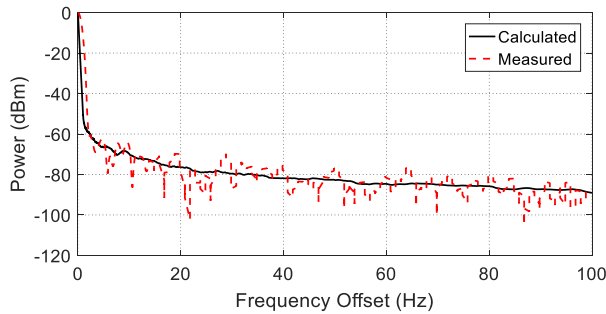


Fig. 14. Power spectrum of the 1 GHz, 0 dBm output signal of the Agilent VSG model E8267D.

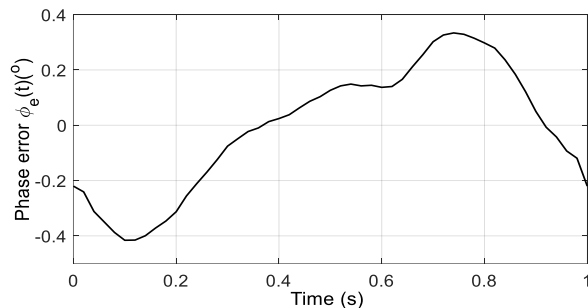


Fig. 15. Instantaneous phase error associating the output signal of the Agilent VSG model E8267D.

Following the procedure explained in Section II.B, the magnitudes A_k of the spectrum is obtained from the

measured phase noise PSD shown in Fig. 13. On the other hand, the phases ψ_k are generated as uniformly distributed random numbers in the interval $[-\pi, \pi]$. The DIFT is applied to the constructed signal spectrum to get the time samples of the phase error over a time span of 1 second with resolution $\Delta t = 5\text{ms}$. The results are plotted in Fig. 15.

It is clear that the Agilent VSG model E8267D has very low level of phase noise and, consequently, the span of the phase error is about 0.7° and the corresponding variance is 0.02.

D.2 Modeling the phase noise of the Agilent SG N9310A

The Agilent SG model N9310 is commercially available and operates in the frequency band 9 KHz to 3 GHz. The PSD of the phase noise associating an output signal of 1 GHz frequency and 0 dBm power is measured in the offset frequency range 1Hz – 1MHz using the same experimental setup described in Section III.D.1 and shown in Fig. 16. The measured data of the phase noise and the averaged curve are plotted as shown in Fig. 17. The instantaneous phase error is obtained from the PSD of the phase noise using the procedure explained in Section II.B and is plotted versus time as shown in Fig. 18.

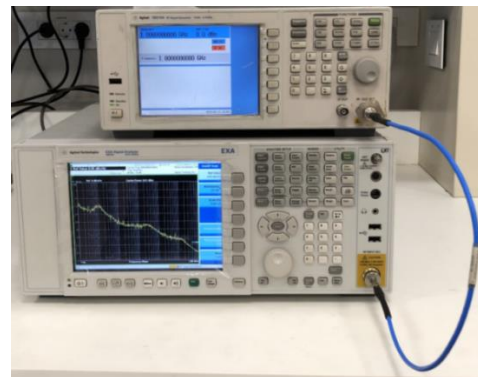


Fig. 16. Experimental setup for measuring the phase noise of the Agilent SG model N9310.

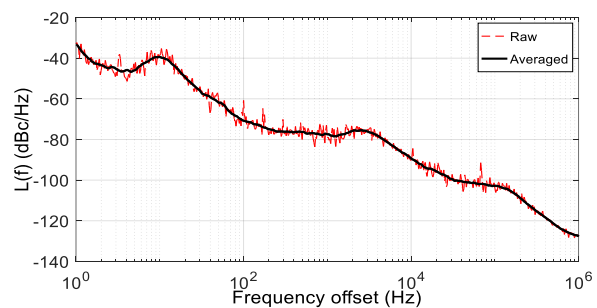


Fig. 17. Measured PSD of the phase noise for Agilent SG model N9310 for an output signal of 1 GHz frequency and 0 dBm power.

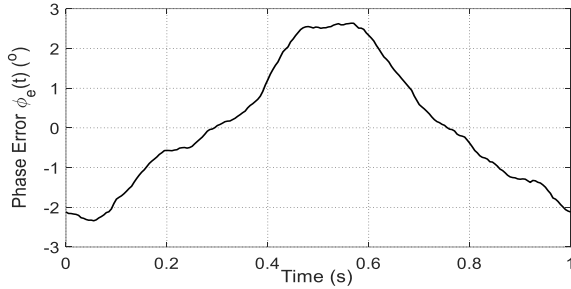


Fig. 18. Instantaneous phase error associating the output signal of the Agilent SG model N9310 for a frequency of 1 GHz and output power of 0 dBm.

E. Performance assessment of M -ary PSK communication systems using the proposed model of the phase noise

In this section, the proposed phase noise model is used to assess the performance of the communication systems employing M -ary PSK modulation techniques in the presence of phase noise. The swing of the instantaneous phase error obtained as described in Section II is used to study the effect of the phase noise on the BER for different levels of the noise power. The procedure is performed with 1 Hz frequency resolution. It should be noted that, in the following presentations and discussions, the phase noise is assumed to have the PSD described in Fig. 4. The BER and SER are calculated for $M = 4$ and 8 at different values of the NCR through numerical simulation of the communication process where 10 M symbols are to be received. The symbol rate is assumed to be 10 Mps. The time samples of the phase error are obtained for each value of the NCR following the procedure explained in Section II.B. At the time of receiving a symbol, the instantaneous value of phase error is added to the phase of this symbol. The calculated BER and SER for $M = 4$ and 8 are plotted versus the NCR as shown in Figs. 19 and 20, respectively. The constellation diagrams are plotted in Figs. 21 and 22 for phase error spans of 20° ($NCR \approx -28$ dB) and 30° ($NCR \approx -22$ dB), respectively for M -ary PSK systems with $M = 4$ and 8.

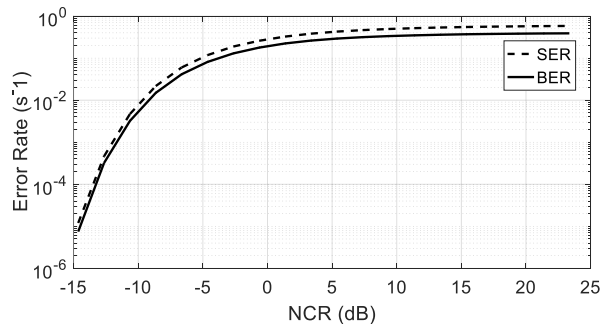


Fig. 19. BER versus NCR for M -ary PSK system with $M = 4$.

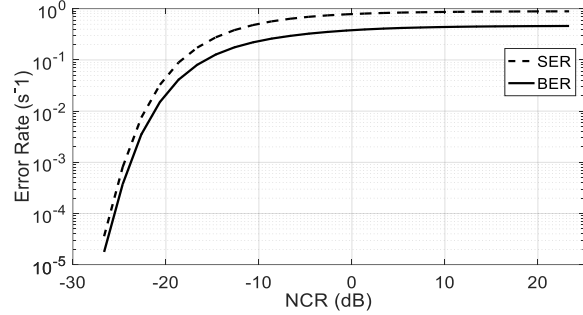


Fig. 20. BER versus NCR for M -ary PSK system with $M = 8$.

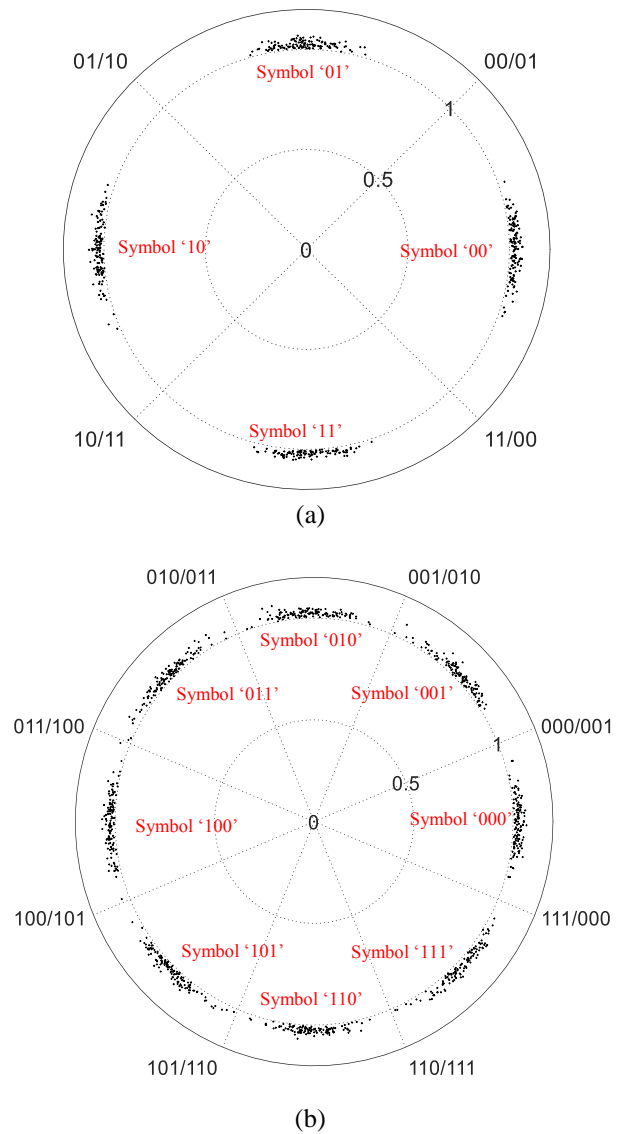


Fig. 21. Constellation diagram for M -ary PSK system affected by phase noise at phase error swing of 20° : (a) $M = 4$ and (b) $M = 8$.

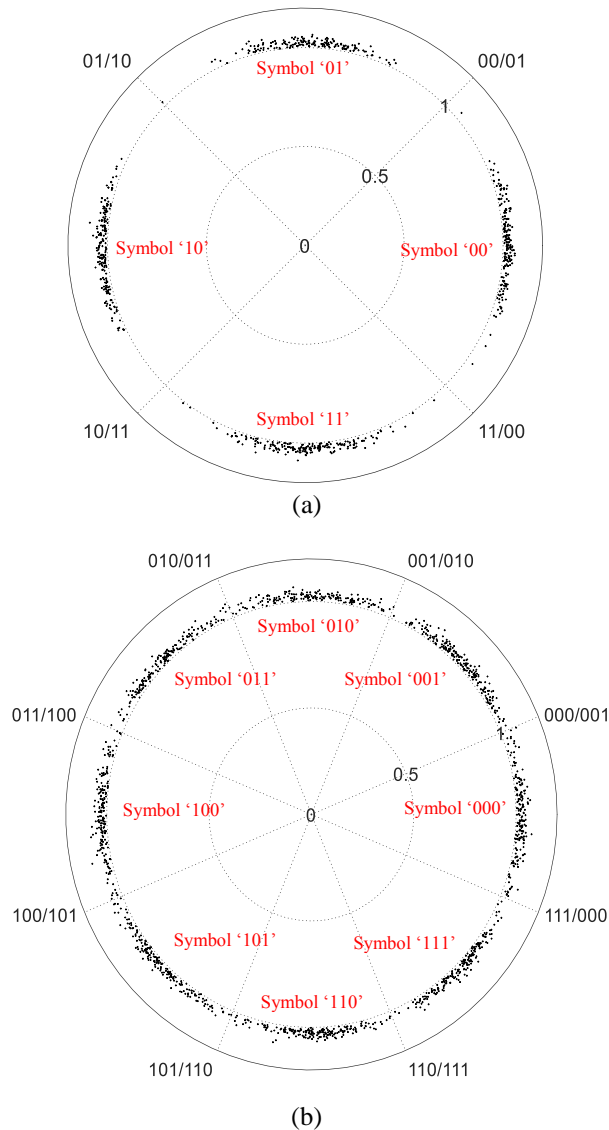


Fig. 22. Constellation diagram for M -ary PSK for phase error range of 30° : (a) $M = 4$ and (b) $M = 8$.

IV. CONCLUSION

Numerical models of the oscillator phase noise using two mathematical procedures to calculate the resulting instantaneous phase error are introduced. Experimental measurements of the PSD of the phase noise encountered in some commercially available oscillators have been performed and the time samples of the corresponding phase error are calculated. To demonstrate the importance and applicability of the proposed model of the phase noise, the effect of the resulting phase error on some performance measures of the M -ary PSK modulation techniques, such as the SER and BER, is investigated for $M = 4$ and 8.

REFERENCES

- [1] M. Reza Khanzadi, "Phase Noise in communication Systems Modeling, Compensation, and Performance Analysis", Thesis for degree of Doctor of Philosophy, *Chalmers University of Technology*, Nov. 2015.
- [2] Study Programme 3B/7, "Characterization of frequency and phase noise", *International Radio Consultative Committee*, pp. 142-150, 1986.
- [3] J. Rutman, "Characterization of phase and frequency instabilities in precision frequency sources: Fifteen years of progress," *Proceeding of the IEEE*, vol. 66, no. 9, Sep. 1978.
- [4] M. Jankovic, "Phase Noise in Microwave Oscillators and Amplifiers," *University of Colorado, Department of Electrical, Computer and Energy Engineering*, 2010.
- [5] E. Rubiola, E. Salik, S. Huang, N. Yu, and L. Maleki, "Photonic-delay technique for phase-noise measurement of microwave oscillators," *Journal of the Optical Society of America B*, vol. 22, no. 5, pp. 987-997, 2005.
- [6] M. Reza. Khanzadi, "Modeling and Estimation of Phase Noise in Oscillators with Colored Noise Sources," Thesis for degree of Licentiate of Engineering, *Chalmers University of Technology*, August 2013.
- [7] F. Brandonisio and M. P. Kennedy, *Noise Shaping all Digital Phase Locked Loops*, ch. 7, Springer 2014.
- [8] J. A. Barnes and D. W. Allan, "A statistical model of flicker noise," *Proceedings of the IEEE*, vol. 54, no. 2, Feb. 1966.
- [9] J. J. Podesta, "Phase noise cancellation in a mixer circuit: Analysis using a random phase function," *Technical Report ARFSD-TR-95016*, Jan. 1996.
- [10] A. Demir, A. Mehrotra, and J. Roychowdhury, "Phase noise in oscillators: A unifying theory and numerical methods for characterization," *IEEE Transactions on Circuits and Systems-I: Fundamental Theory and Applications*, vol. 47, no. 5, May 2000.
- [11] P. Vu, A. M. Haimovich, and B. Himed, "Effect of phase noise on spatial processing by sensors with independent oscillators," *IEEE Radar Conference*, 2018.
- [12] C. Mathai, S. A. Bhawe, and S. Tallur, "Modeling the colors of phase noise in optomechanical oscillators," *OSA Continuum*, vol. 2, no. 7, July 2019.
- [13] D. A. Howe, "Frequency domain stability measurements: A tutorial introduction," *National Bureau of Standards (NBS)*, Technical Note 679, Mar. 1976.

- [14] R. F. Lacey, A. L. Helgesson, and J. H. Holloway, "Short-Term stability of passive atomic frequency standards," *Proceedings of the IEEE*, vol. 54, no. 2, Feb. 1966.
- [15] D. Halford, A. E. Wainwright, and I. A. Barnes, "Flicker noise of phase in RF amplifiers and frequency multipliers: Characterization, cause and cure," (summary), in *Proc. 22nd Annu. Frequency Control Symp.*, Atlantic-City, NJ, pp. 340-341, Apr. 1968.
- [16] L. Dickstein "Introduction to phase noise in signal generators," white paper, *Giga-Tronics*, 2012.
- [17] A. Hajimiri and T. H. Lee, "A general theory of phase noise in electrical oscillators," *IEEE Journal of Solid-State Circuits*, vol. 33, no. 2, Feb. 1998.